

Influence of graphene reinforcement distribution on thermomechanical instability and vibration
of delaminated structures

by

Seyed Farzad Nikrad

A thesis submitted in partial fulfillment of the requirements for the degree of

Doctor of Philosophy

Department of Mechanical Engineering
University of Alberta

© Seyed Farzad Nikrad, 2024

Abstract

Over the last two decades, the realm of nanoscience has experienced exceptional expansion, positioning nanotechnology at the forefront of advancements across various sectors such as computing, sensors, biomedicine, and a plethora of additional applications. Within this landscape, the identification and incorporation of graphene into polymer nanocomposites mark a pivotal advancement in nanoscience. Graphene, characterized by its single layer of carbon atoms arranged in a hexagonal lattice, is renowned for its array of extraordinary attributes.

Research into functionally graded graphene-reinforced composite (FG-GRC) laminated plates has revealed significant limitations, especially in understanding how interlaminar defects and delamination affect their thermal postbuckling performance and overall instability responses. While the addition of graphene is proven to increase the stiffness and strength of polymeric composite laminates, delamination remains a major obstacle, jeopardizing these improvements. The first two chapters of this thesis thoroughly explore the challenges of graphene distribution within the laminates, highlighting those inconsistencies in the structural integrity and mechanical performance of materials caused by delamination areas and can lead to unexpected buckling mode shapes under different scenarios.

In the first chapter, this study conducts a thorough assessment of how diverse distributions of graphene reinforcement can counteract the negative effects of delamination, employing a refined semi-analytical strategy that leverages the third-order shear deformation theory (TSDT) and the Rayleigh-Ritz approximation method. This approach enables to investigate the complex delamination cases, moving from basic shape assumptions in the past to circular and elliptical shapes of delamination. The study provides insights into local and global buckling in composite delaminated plates, focusing on how graphene distribution patterns, delamination configurations,

and external conditions impact thermal instability responses. Chapter two delves into how graphene distribution affects the energy release rate (ERR) around delamination edges in graphene-reinforced laminates. It examines multiple delamination scenarios, which partition the laminate into segments with varied graphene reinforcement patterns. This analysis is key to understanding how these patterns influence the laminate's vulnerability to delamination by studying the ERR across different regions.

Moreover, this chapter seeks to understand the effect of both symmetrical and asymmetrical graphene distribution patterns, in conjunction with specific delamination configurations, on the fundamental frequencies of FG-GRC plates in both pre- and post-buckled thermal states, highlighting the complex interplay between material distribution, structural imperfections, and their combined effects on the performance of the laminated plate.

Recent advancements in manufacturing technologies have transformed the fabrication of composite laminates. This innovation offers enhanced design flexibility, customization options, and improved production efficiency. The integration of advanced manufacturing with composite materials has opened up new possibilities for constructing complex and functional engineering structures with unique material characteristics, such as thin-walled composite laminated struts. Nonetheless, it is crucial to consider local buckling as a pivotal design factor for these types of structures, regardless of their cross-sectional shape.

The final two chapters of this thesis introduce a novel study on the application of graphene sheet reinforcements within composite laminated channel section structures, one of the most practical types of the thin-walled struts. This investigation aims to determine how the integration of graphene, in a variety of symmetric and asymmetric patterns, can enhance the structural

performance of channel section struts when subjected to compressive mechanical and thermal loading, while eliminating the need for additional intermediate stiffeners.

The method used to study the instability and thermally induced vibration of FG-GRC channel section struts employs the von Karman geometrical nonlinearity and relies on the layerwise, third-order shear deformation theory (LW-TSDT). For the purpose of confirming the precision of the outcomes derived from the LW-TSDT and assessing its computational efficiency, a three-dimensional (3D) finite element model is constructed for comparison, utilizing ABAQUS software.

This thesis delivers pivotal numerical insights for solid mechanic designers, highlighting the critical need to weave these findings into their design simulations for augmented performance and enhanced reliability. Specifically, it was found that the application of the FG-X graphene distribution pattern in channel section struts increases their critical buckling resistance by 30%, whereas the FG-O pattern leads to a reduction of about 26% when compared to a uniform graphene dispersion. These results highlight the critical impact of graphene distribution on the mechanical integrity and buckling resilience of composite materials, stressing the value of optimizing material distribution.

Preface

This thesis, authored by Seyed Farzad Nikrad, constitutes a significant original contribution to the solid mechanics.

The research within this thesis was conducted under the supervision of Prof. Zengtao Chen and co-supervised by Dr. Hamid Akbarzadeh at the University of Macgill, along with Dr. Mahdi Hamidinejad at the University of Alberta. Their guidance and expertise profoundly influenced both the content and methodology of this study.

Chapters 2 through 5 of the thesis have been published as journal papers, thus extending the dissemination of the research findings.

I am appreciative of the reviewers and editorial teams involved in this process for their invaluable contributions.

Acknowledgements

First and foremost, I extend my deepest gratitude to my esteemed supervisors, Prof. Zengtao Chen, Prof. Hamid Akbarzadeh, and Prof. Mahdi Hamidinejad, for their invaluable guidance, unwavering support, and exceptional mentorship throughout my doctoral studies. Their steadfast commitment to scholarly excellence has profoundly inspired me and set a remarkable example of academic integrity. The successful completion of this research endeavor would not have been feasible without their insightful feedback, dedicated efforts, and constant encouragement.

I am profoundly thankful to my family, especially my parents and brother, for their enduring love, support, and firm belief in my potential. Their foundational role in shaping my character and their relentless support over the years have been crucial to my personal and academic achievements.

Most importantly, I owe a debt of gratitude to my wife, Sara, for her boundless love and unwavering support during this journey. Her companionship during countless late nights and early mornings, along with her role as my muse, editor, proofreader, and confidant, has been instrumental in maintaining my focus and well-being. Her presence has been a source of strength and inspiration, for which I am eternally grateful.

Table of Contents

Abstract.....	ii
Preface	v
Acknowledgements	vi
1. Introduction.....	1
1.1. Graphene as a composite reinforcement.....	1
1.2. Composite laminates with delamination zones.....	1
1.3. Delamination propagation	2
1.4. Thin-walled composite laminated struts	2
1.5. Motivations and objectives.....	3
2. Nonlinear thermal postbuckling of functionally graded graphene reinforced composite laminated plates with circular or elliptical delamination.....	7
2.1. Introduction	7
2.2. Theoretical formulations.....	13
2.2.1. Structural model.....	13
2.2.2. Thermomechanical characteristics of GRC laminates	16
2.3. Modelling of GRC laminated plate.....	18
2.3.1. GRC laminated plate with circular and elliptical embedded delamination zones	18
2.3.2. GRC laminated plate with a single edge delamination zone	24
2.4. Results and discussion	27
2.4.1. Comparative study	30
2.4.2. Parametric study.....	32
2.5. Concluding remarks.....	57
3. Effect of graphene reinforcement distribution on energy release rate and vibration of thermally pre/post-buckled delaminated composite plates	60
3.1. Introduction	61
3.2. Theoretical formulations.....	66
3.2.1. Basic parameters of the FG-GRC laminated plates.....	66
3.3. Structural model	68
3.3.1. FG-GRC laminated plate with a single through-the-width delamination.....	69
3.3.2. FG-GRC laminated plate with double through-the-width delaminations	78
3.3.3. Energy expressions for FG-GRC laminated plates with delamination.....	84
3.4. Determination of energy release rate (ERR) using crack tip element (CTE) method.....	88
3.5. Results and discussion	91
3.5.1. FG-GRC laminated plate with a single through-the-width delamination.....	91
3.5.2. FG-GRC laminated plate with multiple through-the-width delaminations	108
3.6. Concluding remarks.....	116

4. Effects of functionally graded graphene reinforcements on nonlinear post-local buckling and axial stiffness of laminated channel section struts	119
4.1. Introduction	120
4.2. Theoretical formulation	123
4.3. Structural modelling of channel section struts.....	126
4.3.1. Modelling based on the LW-TSDT.....	126
4.3.2. Modelling based on the finite element simulation	136
4.4. Results and discussion	138
4.4.1. GRC laminated channel section strut with UD graphene pattern.....	138
4.4.2. Comparison analysis on the nonuniform graphene distribution patterns	142
4.4.3. Parametric study on the channel section struts with FG-X, UD, and FG-O graphene distribution patterns	152
4.5. Concluding remarks.....	166
5. Imperfection sensitivity of free vibration of FG-GRC laminated channel section struts in thermally pre- and post-buckling equilibrium states.....	169
5.1. Introduction	170
5.2. Theoretical formulation	171
5.3. Structural modelling of channel section struts.....	172
5.3.1. Modelling based on the LW-TSDT.....	172
5.3.2. Modelling based on the finite element simulation	176
5.4. Results and discussion	177
5.4.1. GRC laminated channel section strut with UD graphene pattern.....	177
5.4.2. Influence of different graphene distribution patterns on the thermal post-buckling equilibrium paths and vibration characteristics of channel section struts.....	181
5.4.3. Imperfection sensitivity of post-buckling equilibrium paths and free vibration of FGX channel section struts	194
5.5. Concluding remarks.....	201
6. Conclusions and future perspectives.....	204
6.1. Conclusions	204
6.2. Recommendations for future work	207
References	210
Appendix A.....	218
Appendix B.....	219
Appendix C.....	222
Appendix D	224

List of tables

Table 2-1 Mathematical expressions of displacement and rotation at different edges of the perfect FG-GRC plate (SSSS and CCCC)	21
Table 2-2 Mathematical expressions of displacement and rotation at different edges of GRC laminated plate with a single edge delamination (SSSF).....	21
Table 2-3 Thermomechanical properties of single layer graphene sheet with geometrical characteristics.....	27
Table 2-4 Coefficients P_i associated to the fourth order interpolation (Eq. (2.25)) for various thermomechanical properties [67]	28
Table 2-5 The efficiency parameters $\eta_i, i = 1,2,3$ for different volume fractions of graphene sheets at three different levels of temperature [28, 29, 31].	29
Table 3-1 Lay-up arrangements of the FG-GRC laminated plates with different graded graphene distributions.....	67
Table 3-2 Mathematical expressions of the boundary conditions at longitudinal ends of the FG-GRC plate with single delamination.....	73
Table 3-3 The buckled configurations of clamped and simply-supported FG-GRC laminated composite plates with single through-the-width delamination zone and several graphene graded patterns.....	97
Table 3-4 Buckled configurations of the FGX and FGA laminated composite plates with double through-the-width delaminations at $T=350$ K and $T=500$ K.	112
Table 4-1 Mathematical expressions of the boundary conditions at longitudinal ends of the FG-GRC channel section struts	127
Table 4-2 Comparison of computing time and CPU usage in performed simulations and computational performance of proposed methodology (UD, $bfbw = 0.25, tftw = 1$).....	141
Table 4-3 Influence of different shape factors and compressive end-shortening loads on the buckling mode-shapes of FG-X channel section struts where $tftw = 1$	162
Table 5-1 schematic of local imperfections applied to flange and web of channel section struts.....	173
Table 5-2. Comparison of computing time and CPU usage in performed simulations and computational performance of proposed methodology (UD, $bfbw = 0.2, tftw = 1, CCC-CCC$).....	181

List of figures

Figure 2-1 FG-GRC laminated plate	13
Figure 2-2 Four types of graphene distributions in GRCs	14
Figure 2-3 Segmentation of the GRC laminated plate with embedded delamination	19
Figure 2-4 Segmentation of the FG-GRC plate with edge delamination	25
Figure 2-5 Thermal postbuckling of temperature dependent of GRC laminated plates.....	31
Figure 2-6 Non-dimensional out-of-plane displacement versus the non-dimensional end-shortening.....	32
Figure 2-7 Effect of the boundary conditions of FG-GRC laminated plates on: (a) Thermal postbuckling deflection and (b) Variation of the bending moment at the center of the plates	34
Figure 2-8 The influence of graphene reinforcement distribution on the thermal equilibrium paths of FG-GRC laminated plates with embedded circular delamination, $AD/A=0.25$, CCCC.....	36
Figure 2-9 The influence of graphene reinforcement distribution on the thermal equilibrium paths of FG-GRC laminated plates with embedded circular delamination, $AD/A=0.25$, SSSS	36
Figure 2-10 Influence of clamped and simply-supported boundary conditions on the thermal equilibrium paths of FG-A laminated plates with embedded circular delamination, $AD/A=0.25$	38
Figure 2-11 Buckled configuration of the FG-X laminated plate with a circular embedded delamination zone, $AD/A=0.25$, SSSS	39
Figure 2-12 Comparison of deflection through the sublamine and baselamine of FG-X plate with embedded circular delamination	40
Figure 2-13 Comparison of normal Stress (σ_{11}) through the sublamine and baselamine of FG-X plate with embedded circular delamination.....	41
Figure 2-14 The influence of graphene reinforcement distribution on the thermal equilibrium paths of FG-GRC laminated plates with embedded elliptical delamination, $AD/A=0.25$, CCCC	43
Figure 2-15 The influence of graphene reinforcement distribution on the thermal equilibrium paths of FG-GRC laminated plates with embedded elliptical delamination, $AD/A=0.25$, SSSS.....	43
Figure 2-16 Local postbuckling equilibrium paths of FG-GRC laminated plate with single edge delamination at $T=300$ K, $AD/A=0.23$	46
Figure 2-17 The influence of graphene reinforcement distribution on the thermomechanical equilibrium paths of FG-GRC laminated plates with single edge delamination, $AD/A=0.23$, SSSF.....	46
Figure 2-18 Variation of the normal stress through the top surface of the FG-GRC laminate plates with single edge delamination, $U=0.3$ (a) FG-X, (b) UD, (c) FG-O, $AD/A=0.23$, SSSF	48
Figure 2-19 The influence of the delamination area on the thermomechanical equilibrium path of the delaminated plate with FG-X graphene distribution patterns, $R=AD/A$	49
Figure 2-20 The impact of the delamination size on the load-carrying capacity of the FG-X delaminated plate subjected to both thermal and compressive loading, $R=AD/A$	50

Figure 2-21 Influence of the delamination area on the out-of-plane displacement of the FG-X delaminated plate through the Y direction at $X=0$, $R=AD/A$	51
Figure 2-22 Thermomechanical equilibrium paths of the FG-X delaminated plate $R=AD/A=0.23$, SSSF. (a) without contact constraint. (b) with contact.....	53
Figure 2-23 Effect of contact constraint on the free-edge's buckling mode shape of the FG-X delaminated plate.....	54
Figure 2-24 Influence of sublaminates thickness on the (a) thermomechanical instability behavior of FG-X delaminated plate. (b) Load-carrying capacity, SSSF	56
Figure 2-25 Impact of the length to thickness ratio of the graphene sheets on the postbuckling responses of the FG-X delaminated plate, SSSF	57
Figure 3-1 Division of the FG-GRC laminated plate with a single through-the-width delamination into four regions along the X and Z axis	71
Figure 3-2 Segmentation of the FG-GRC laminated plate with a single through-the-width delamination into fifteen numerical layers along the Z axis	71
Figure 3-3 Segmentation of the FG-GRC laminated plate with two equal length through-the-width delaminations into five regions along the X axes.....	79
Figure 3-4 Segmentation of the FG-GRC laminated plate with multiple through-the-width delaminations into fifteen numerical layers along the Z axis	79
Figure 3-5 three-dimensional crack tip element	88
Figure 3-6 Free-body diagram for a delaminated plate above and below the crack plane.....	89
Figure 3-7 Influence of boundary conditions and several symmetric graphene distribution patterns on the thermal postbuckling deflection of the composite laminated plates with single through-the-width delamination.	93
Figure 3-8 Influence of boundary conditions and several asymmetric graphene distribution patterns on the thermal postbuckling deflection of the composite laminated plates with single through-the-width delamination.	95
Figure 3-9 Distribution of the in-plane displacements through the thickness direction of the FG-GRC laminated composite plates	96
Figure 3-10 Influence of the boundary conditions and several graphene distributions on the load-bearing capacity of the FG-GRC laminated composite plates	99
Figure 3-11 Variation of the ERR (Modes I and II) along the delamination edge of the FG-GRC laminated composite plates.....	101
Figure 3-12 Variation of the ERR (Modes I and II) along the delamination front of the FG-GRC laminated composite plates with different asymmetric graphene distribution patterns.	102
Figure 3-13 Effect of different kinds of graphene graded patterns and boundary conditions on the variation of total ERR along the delamination edge of FG-GRC laminated composite plates.	104
Figure 3-14 Effect of FGX and FGA graded patterns and boundary conditions on thermally pre- and post-buckled vibration of delaminated and perfect GRC plates.....	107
Figure 3-15 Effect of several symmetric and asymmetric functionally graded patterns on thermally pre- and post-buckled vibration of perfect and delaminated GRC plates.	108

Figure 3-16 Influence of the double same size through-the-width delaminations with different configurations on the thermal postbuckling deflection paths of the FGX and FGA laminated composite plates	111
Figure 3-17 Influence of several delamination configurations on the distribution of total ERR along their edges ...	115
Figure 3-18 Effect of several delamination configurations on thermally pre- and post-buckled vibration of delaminated FGX and FGA graphene reinforced plate with CFC.....	116
Figure 4-1 (a) A schematic FG-GRC laminated channel section struts with their local coordinate systems (b) detailed view half of the piecewise functionally graded graphene reinforced cross-section.....	124
Figure 4-2 Schematic depiction of the cross-section with an FG-X graphene distribution pattern within both the flanges and the web.....	125
Figure 4-3 A typical channel section strut and segmentation of the flanges and web (a) Separation of flanges and web, (b) Discretization of flanges and web through their thickness based on the layerwise theory	128
Figure 4-4 A typical channel section strut modelled based on the finite element simulation (a) Implementing loading and boundary conditions, (b) Diagrammatic representation of the mesh for the channel section strut	138
Figure 4-5 Variation of the critical buckling end-shortening with the shape factor	140
Figure 4-6 Nonlinear postbuckling equilibrium paths of flange and web in a channel section strut with UD graphene distribution pattern.....	142
Figure 4-7 Comparison of nonuniform symmetric graphene distribution patterns of the flanges on (a) nonlinear postbuckling response and (b) load-bearing capacity of the FG-GRC channel section struts with web: UD.....	145
Figure 4-8 Comparison of nonuniform asymmetric graphene distribution patterns of the flanges on (a) nonlinear postbuckling response and (b) load-bearing capacity of the FG-GRC channel section struts with web: UD.....	146
Figure 4-9 Influence of the nonuniform graphene distribution pattern of the web on the critical buckling end-shortening of the FG-GRC channel section struts (a) Flanges with FG-X, (b) Flanges with FG-O.....	149
Figure 4-10 Influence of the nonuniform graphene distribution pattern of the web on the postbuckling behavior of the FG-GRC channel section struts	151
Figure 4-11 Influence of the nonuniform graphene distribution pattern of the web on the postbuckling behavior of the FG-GRC channel section struts	152
Figure 4-12 Comparison the influence of FG-X, UD, and FG-O graphene distribution patterns on (a) nonlinear postbuckling response, (b) load-bearing capacity, (c) postbuckling compressional stiffness ratio of the channel section strut.....	154
Figure 4-13 Local deflection at the crest of the buckle for channel section struts with different graphene distribution patterns	155
Figure 4-14 Influence of various graphene distribution patterns on the longitudinal membrane stress distribution at (a) buckle crest, (b) quarter length of the strut, (c) buckle nodes.....	158
Figure 4-15 Influence of various graphene distribution patterns and geometrical parameters on the critical buckling end-shortening of FG-GRC channel section struts (a) $tftw = 1$, (b) $tftw = 0.5$, (c) $tftw = 2$	161
Figure 4-16 Influence of different flange to web thickness ratios on (a) nonlinear postbuckling equilibrium paths, and (b) load-bearing capacity of the FG-X channel section strut.....	165

Figure 5-1 Typical channel section strut modelled based on the finite element simulation (a) implementing clamped boundary conditions, (b) diagrammatic representation of the mesh for the channel section strut	177
Figure 5-2 Comparison the nonlinear thermal equilibrium paths of flange and web in a channel section strut with UD graphene distribution pattern	180
Figure 5-3 Investigation the influence of various kinds of graphene distribution patterns and boundary conditions on the critical buckling temperatures and fundamental natural frequencies of laminated channel section struts	184
Figure 5-4 Investigation the boundary conditions and various graphene distribution patterns on the thermal equilibrium paths of laminated channel section struts	187
Figure 5-5 Influence the boundary conditions and various graphene distribution patterns on the variation of bending moment at the center of the web (a) clamped (b) simply-supported.....	188
Figure 5-6 Influence of different graphene distribution patterns on variations of thermally induced pre- and post-buckling vibration of laminated channel section struts.....	192
Figure 5-7 Influence of various graphene distribution patterns and geometrical parameters on the fundamental frequencies of FG-GRC channel section struts.....	194
Figure 5-8 Influence of geometrical imperfection on the thermal post-buckling equilibrium paths of the FGX channel section struts (a) clamped boundary condition (b) simply-supported boundary condition	197
Figure 5-9 Influence of geometrical imperfection on the local deflection at the buckle crest of FGX channel section struts (a) clamped boundary condition (b) simply-supported boundary condition	198
Figure 5-10 Influence of geometrical imperfections on variations of thermally induced pre- and post-buckling vibrations of FGX laminated channel section struts	201

1. Introduction

1.1. Graphene as a composite reinforcement

As a two-dimensional lattice of carbon atoms, graphene has gained much attention in recent years because of its outstanding thermal, mechanical, and electrical properties in tandem with its applicability for developing reconfigurable nanoscale materials [1–19]. Graphene is referred as a sheet of carbon stacked tightly together in a hexagonal ring configuration. Based on the molecular dynamic (MD) simulation, it is confirmed that the anisotropic mechanical properties of graphene sheets are unaffected by their size [12]. With their broad range of application and high yield strength, graphene sheets now become ready for practical applications for fabrication of high-performance polymer nanocomposites [16]. Contrary to carbon fiber reinforced composites, which can contain a high proportion of carbon fibers (<50 wt%), GRCs can only incorporate a small amount of weight fraction of carbon nanofillers (about 0.05–5%) [17,18] since adding more carbon nanofillers can degrade the mechanical properties of the nanocomposites due to formation of agglomerates or clusters, which can cause stress concentrations in the composite material and result in the initiation and propagation of cracks. This can ultimately reduce the composite's toughness and increase its propensity for fracture [19].

1.2. Composite laminates with delamination zones

Over the last few decades, composite laminates have been widely used in a variety of applications where a relatively high stiffness/strength-to-weight ratio is required. However, these materials are susceptible to a wide variety of flaws and degradation, which can result in severe stiffness and strength loss. When laminated composites are subjected to compressive loads, delamination becomes a restriction in composite design.

A significant proportion of research in delamination analysis has focused on the evaluation of linear and nonlinear buckling and vibration behavior of laminated composite plates and beams, through experimental methods. Such studies have investigated the characteristics of both single and multiple delamination zones within rectangular geometries [20–24]. Pekbay and Sayman [21] conducted a comprehensive study on the buckling behavior of single-delaminated, glass-fiber composite laminates using both experimental measurements and numerical simulations. In their research, they utilized a unique approach of introducing a pre-macro defect, in the form of a delamination, by strategically placing rectangular teflon films with a thickness of 13 mm between plies of varying orientations during the manufacturing process of the test samples.

1.3. Delamination propagation

Notably, none of the aforementioned papers predict the delamination propagation while investigating the influence of this interlaminar flaw on the nonlinear thermal or mechanical instability behavior of laminated composite structures. However, due to the devastating effect of growth of delamination which most likely happens in the postbuckling regime, it is a great necessity to precisely estimate the possibility of delamination growth under different loading conditions, which most commonly is done by calculating the energy release rate (ERR) at the delamination edge. A brief literature review on this topic was provided hereinafter [25].

1.4. Thin-walled composite laminated struts

In recent years, use of composite laminates has experienced substantial growth in various industries, owing to their capacity to provide a beneficial balance between stiffness, strength, and weight. Moreover, significant progress has been witnessed in manufacturing techniques, which has revolutionized the production of composite laminates, presenting numerous benefits in terms of design adaptability, customization, and manufacturing efficiency. By combining the advantages of

both advanced manufacturing and composite materials, a groundbreaking approach has unlocked fresh opportunities for fabricating complex and functional engineering structures with intriguing material properties, including thin-walled composite laminated struts [26,27]. These structures are commonly utilized in scenarios involving in-plane compressive loading, particularly in the aerospace industry. The industry's focus on developing efficient and lightweight structures requires considering the potential occurrence of local buckling/post buckling at designated load levels. The precise analysis of compressive instability is crucial for these structures, considering the substantial reduction in compressive stiffness and load-bearing capacity during the post-local-buckling phase [28]. As a result, extensive research involving numerical simulations, analytical methods, and experimental investigations has been conducted on thin-walled open- and closed-section struts for varied sectional geometries composed of diverse isotropic and anisotropic materials [29].

1.5. Motivations and objectives

Upon conducting an extensive review of the literature, it has become evident that a significant research gap exists concerning the impact of varying distribution patterns of graphene sheet reinforcement on the thermal postbuckling response of laminated composite plates with single or multiple interface delaminations in diverse shapes, such as embedded circular and elliptical delaminations, as well as edge and through-the-width rectangular delaminations. While incorporating graphene reinforcements into polymeric composite laminates has proven to enhance their stiffness and strength, the presence of delamination can significantly reduce these desirable properties. Hence, assessing which graphene distribution patterns can effectively counteract the adverse effects of delamination is essential. This assessment is achieved through an in-depth examination of the thermal and mechanical instabilities of FG-GRC plates with delamination.

Another objective of this thesis is to conduct a comprehensive investigation on the distribution of ERR along the delamination edges of FG-GRC laminated plates to examine how graphene distribution can affect the delamination propagation. The specific parts of the damaged area within the composite laminate will be identified that are more susceptible to propagation under varying graphene distribution patterns and boundary conditions. An additional objective of this study is to assess the impact of various symmetric and asymmetric graphene distribution patterns in combination with distinct delamination configurations on the fundamental frequencies of thermally pre- and post-buckled FG-GRC plates.

Moreover, based on an extensive literature review, it is evident that local buckling should be regarded as a critical design consideration for thin-walled struts, irrespective of their cross-sectional profile. Local buckling significantly impacts the axial compressive stiffness and, subsequently, the load-bearing capacity in an adverse manner. Consequently, it is imperative to prioritize the resolution of this pivotal concern in this type of practical and extensively utilized engineering structures by diligently exploring diverse avenues to identify effective solutions.

Considering the established improvements in stiffness and strength resulting from the addition of graphene reinforcements to polymeric composite laminates, as another motivation, this thesis represents an initial exploration in utilizing graphene as a reinforcement in composite laminated channel-section struts to assess how the symmetric and asymmetric distributions of graphene of various pattern can improve the performance of channel section struts under compressive loads (uniform end-shortening and thermal), while avoiding the addition of intermediate stiffeners.

The final objective of this thesis involves undertaking extensive efforts on perfect and geometrically imperfect FG-GRC channel section struts to pinpoint the particular arrangements of graphene patterns that significantly improve the critical buckling temperature, as well as the

fundamental and second-order frequencies, in both pre- and post-buckling states.

This thesis is organized in a paper-based format, comprising six chapters. The introductory and concluding remarks are confined to the first and final chapters, respectively. Chapters 2 through 4 have been successfully published in peer-reviewed journals. Additionally, Chapter 5, another scholarly paper emanating from this thesis, has been submitted to a journal and is under review right now. The details of chapters are briefed as follows:

- Chapter 2 of this thesis has been published as S.F. Nikrad, Z.T. Chen, A.H. Akbarzadeh “Nonlinear thermal postbuckling of functionally graded graphene reinforced composite laminated plates with circular or elliptical delamination”, *Acta Mechanica*. [Link](#) In this chapter the nonlinear thermal instability responses of FG-GRC laminated plates with embedded circular and elliptical delamination as well as edge delamination, subjected to a uniform temperature rise and a variety of mechanical boundary conditions is investigated.
- Chapter 3 of this thesis has been published as Paper No. 2: S.F. Nikrad, Z.T. Chen, A.H. Akbarzadeh “Effect of graphene reinforcement distribution on energy release rate and vibration of thermally pre/post-buckled delaminated composite plates”, *Thin-Walled Structures*. [Link](#) In this chapter the nonlinear thermal instability responses of FG-GRC laminated plates with single or multiple through-the-width delaminations, are investigated. The possibility of delamination growth is also evaluated using the three-dimensional crack tip element (3D-CTE) method, which determines the ERR at the delamination edge. Furthermore, the influence of delamination configurations and the types of graphene reinforcement distribution patterns on the free vibration of FG-GRC delaminated plates in thermally pre/post-buckled regimes is evaluated.

- Chapter 4 of this thesis has been published as S.F. Nikrad, A.H. Akbarzadeh, M. Hamidinejad, Z.T. Chen “Effects of functionally graded graphene reinforcements on nonlinear post-local buckling and axial stiffness of laminated channel section struts”, *Thin-Walled Structures*. [Link](#) It explores the potential improvements in the postbuckling characteristics of polymeric composite laminated channel section struts subjected to a progressive end-shortening by employing multi-layer graphene sheets reinforcements. The solution methodology incorporates the von Karman geometrical nonlinearity and is based on the layerwise third-order shear deformation theory (LW-TSDT).
- Chapter 5 of this thesis has been submitted to *Composite Structures* as S.F. Nikrad, A.H. Akbarzadeh, M. Hamidinejad, Z.T. Chen “Imperfection sensitivity of free vibration of FG-GRC laminated channel section struts in thermally pre- and post-buckling equilibrium conditions” *Composite Structures* (Under Review). In this chapter, an extensive analysis of nonlinear thermal instability in perfect and geometrically imperfect FG-GRC laminated channel section struts is undertaken to discern the graphene distribution patterns that are most and least effective in elevating the critical buckling temperature and natural frequencies through pre- and post-buckling conditions.

2. Nonlinear thermal postbuckling of functionally graded graphene reinforced composite laminated plates with circular or elliptical delamination¹

This research investigates the nonlinear thermal instability responses of functionally graded graphene reinforced composite (FG-GRC) laminated plates with embedded circular and elliptical delamination as well as edge delamination, subjected to a uniform temperature rise and a variety of mechanical boundary conditions. The thermomechanical properties of the GRCs are estimated using the extended Halpin-Tsai micromechanical model that incorporates efficiency parameters to take into account nanoscale size and surface effects of the graphene reinforcement. The von Karman geometrical nonlinearity is adopted in a solution based on the third-order shear deformation theory. The nonlinear equilibrium equations derived by the minimum total potential energy principle are solved using the Ritz method in conjunction with the Newton–Raphson iterative procedure. Parametric studies reveal that the types of graphene distribution pattern and geometry of delamination zones have a substantial effect on the thermal equilibrium paths and buckling temperature of the GRC delaminated plates. FG-X graphene sheet pattern raises the critical buckling temperature and compressive strength of the baselaminate and reduces the nonlinear thermal postbuckling deflection; however, it causes a significant increase in normal stress distribution at the top and the bottom surfaces of the delaminated plates.

2.1. Introduction

Because of the technological limitations, fabrication of a perfect (with no defects) functionally graded material (FGM) where the mixture of two distinct material phases changes continuously is difficult. The ideal alternative to FGMs is a multilayer structure composed of several layers with a layer-wise variation in the mixing ratio of matrix and nano reinforcements [30]. To fabricate a

¹ A version of this chapter is published in the journal of Acta Mechanica, 5999-6039, 2023,

multilayer functionally graded composite reinforced by graphene platelets (GPLs), which consist of stacked parallel two-dimensional graphene layers, epoxy with specified weight fraction of GPLs should be combined followed by casting the well-mixed nanocomposite liquid into a mold to create the first layer of graphene reinforced composite. This procedure is repeated to produce other nanocomposite layers with varying GPL weight fractions that are then bonded together via hot pressing to form multilayer nanocomposites [30].

Several experiments have been conducted on the graphene/epoxy laminated nanocomposite beams; it has been observed that slight increase of the weight fraction of graphene considerably improves the critical buckling load of the nanocomposite beam. As a result, with only 0.1% weight fraction of graphene platelets, the critical buckling load is increased by 52% compared to a pure epoxy beam [31]. Parashar and Mertiny [32] utilized finite element method (FEM) to study the buckling behaviour of a single layer graphene/epoxy composite plate subjected to a uniaxial compressive load. According to their findings, adding 6% volume fraction graphene increases the critical buckling load of the nanocomposite plate by 26%. Yang and co-authors [33–35] analyzed the bending, postbuckling, and dynamic instability of functionally graded polymer nanocomposite beams reinforced with graphene platelets (GPLs), using the Timoshenko beam theory and by employing the von-Karman nonlinear strain-displacement relationship. They also conducted free and forced vibration analyses of functionally graded polymer composite plates reinforced with graphene with temperature independent material properties [36]. The most significant conclusion from these research works is that multi-layer nanocomposite structures with a higher proportion of GPLs in their top and bottom layers compared to their middle layers exhibit a superior static and dynamic performance.

Recently many research topics have been focused on the static and dynamic responses of different FG-GRC structures, including beams, plates, cylindrical panels, and shells [37–48]. Shen and colleagues [38] applied a two-step perturbation approach to examine the nonlinear bending behavior of FG-GRC laminated plates resting on an elastic foundation. According to their findings, the laminated composite plate with the highest volume fraction of graphene in its top and bottom layers, referred to as the FG-X type, has the lowest load-deflection curve but the largest central bending moment. A numerical study was conducted to evaluate the compressive instability response of FG-GRC plates subjected to a uniaxial compression force in thermal environment. The governing differential equations for the plate postbuckling analysis were derived according to the higher order shear deformation theory. It was found that the buckling load and postbuckling strength of the laminated composite plate with the greatest volume fraction of graphene in the middle layer, named the FG-O type, is lower than those of other graphene distributions [41]. Ma and Jin [47] suggested an improved plate theory capable of satisfying the interlaminar shear stress between layers of a thick FG-GRC laminate subjected to compressive load.

Chen et al. [49,50] recently examined the compressive and thermal postbuckling behavior of sandwich plates and cylindrical shells with an auxetic graphene-reinforced metal matrix composite (GRMMC) core. The auxetic GRMMC core with a negative Poisson's ratio (NPR) is expected to be functionally graded (FG) piecewise by varying the graphene volume fraction across the thickness direction of the core. Temperature-dependent material properties are assumed for both the metal face sheets and the GRMMC core. The results confirmed that the FG pattern of the graphene sheets affects the compressive and thermal postbuckling equilibrium paths.

Over the last few decades, composite laminates have been widely used in a variety of applications requiring a relatively high stiffness/strength-to-weight ratio. However, these materials

are susceptible to a wide variety of flaws and degradation, which can result in severe stiffness and strength loss. When laminated composites are subjected to compressive loads, delamination becomes a composite design restriction.

A significant proportion of research in delamination analysis has focused on the evaluation of linear and nonlinear buckling and vibration behavior of laminated composite plates and beams, through experimental methods. Such studies have investigated the characteristics of both single and multiple delamination zones within rectangular geometries [20–22,24,51]. Pekbay and Sayman [21] conducted a comprehensive study on the buckling behavior of single-delaminated glass-fiber composite laminates using both experimental measurements and numerical solutions. In their research, they utilized a unique approach of introducing a pre-macro defect, in the form of a delamination, by strategically placing rectangular teflon films with a thickness of 13 mm between plies of varying orientations during the manufacturing process.

Recently a new laminate partitioning scheme was proposed to analyze the postbuckling behavior of the composite laminate with a single through-the-width delamination. The advantage of this approach is offering a better displacement consistency at the edge of the delamination zone and providing access to the interlaminar tractions [52]. Static and dynamic response of a laminated composite plate reinforced with curvilinear fibers with an embedded delamination zone were studied by Sharma [53] based on the FEM. There are also several research focus on delamination propagation through implementing the isogeometric cohesive elements under static and transient dynamic loads [54–56]. Based on the proposed method the cohesive elements are generated from CAD data and implemented in MIGFEM. The technique accurately represents composite laminates using NURBS elements and allows seamless design integration between CAD and analysis.

The presence of interface cracks and delamination within composite materials introduces unique challenges that can be effectively mitigated using the extended finite element method (XFEM). Composite materials consist of distinct layers or constituents, such as fibers and matrices, which are interconnected at interfaces. The occurrence of cracks or delamination at these interfaces can significantly compromise the structural integrity and mechanical performance of the composite. XFEM, an advanced numerical technique, offers a compelling solution for accurately modeling and simulating the intricate behavior of interface cracks and delamination in composite materials [57–59]

Nikrad et al. [60,61] has explored the effect of lay-ups, boundary conditions, and delamination zone on the thermal instability of laminated composite plates with embedded and through-the-width delamination. Their analysis revealed that delaminated composite plate may buckle in a local, global, or mixed mode, depending on the lay-ups and types of the edge supports. Furthermore, using layerwise theory, a computational analysis was performed to examine the compressive instability response and delamination propagation of composite plates with multiple off-center through-the-width delamination zones. It was discovered that the near-to-surface delamination zone leads to the local mode of buckling [62].

Kharazi et al. [63,64] established a novel layerwise theory based on the first order shear deformation theory, verified by the results of FEM, to evaluate the critical buckling load and compressive instability response of composite plates with multiple through-the-width delaminations. Ovesy [65,66] investigated the compressive instability of composite plates with various types of delamination zones including through-the-width and embedded delaminations. They considered the von-Karman nonlinear strain-displacement relationship and applied the single-layer plate theories such as classical plate theory (CLPT) and first order shear deformation

theory (FSDT) to derive the instability equations. They discovered that the length and position of the delamination zones can influence the postbuckling mode and load carrying capacity.

The literature review has demonstrated a significant research gap concerning the investigation of interlaminar flaws and delamination, and their impact on the thermal postbuckling and/or buckling behavior of FG-GRC laminated plates. Although the incorporation of graphene reinforcements into polymeric composite laminates has proven to be an effective strategy for enhancing their stiffness and strength, the presence of a delamination zone can lead to a significant reduction in these properties. Furthermore, despite the specified and well-arranged graphene distribution pattern in the FG-GRC laminated plate, the top sublaminates and bottom baselaminates may exhibit irregular graphene dispersion based on the location of delamination. This irregularity can cause unexpected responses and different buckling mode shapes under several loading and boundary conditions, emphasizing the need for further investigation of these issues. The critical objective of this study is to assess the efficacy of graphene sheet reinforcements with alternative graphene reinforcement distribution patterns in mitigating the adverse effects of the delamination on the thermal instability responses of the sublaminates and baselaminates.

Most delamination analyses conducted in the literature using the Rayleigh-Ritz approximation technique assumed simple shapes like square and rectangular for delamination to facilitate the definition of corresponding shape functions and avoid continuity challenges that may arise from more complex shapes. However, in this paper, a more realistic scenario is considered by investigating the FG-GRC laminates with embedded delamination regions that have circular and elliptical shapes. To accomplish this, an analytical approach based on the higher-order shear deformation theory is developed using the Rayleigh-Ritz approximation technique and implementing simple and complete polynomial series. The proposed method can evaluate both

sublaminates local buckling and baselaminates global buckling; additionally, there are no restrictions on the type of boundary conditions that can be handled by the introduced procedure. The effect of different graphene reinforcement distributions, size of the graphene sheets, position and the geometry of the delamination zone, and boundary conditions on the thermal equilibrium paths, thermal bifurcation points of baselaminates, stress distribution, and load-carrying capacity of the GRC delaminated plates are investigated in this paper.

2.2. Theoretical formulations

2.2.1. Structural model

The current research considers a multilayer laminated composite plate comprised of N_L layers having a total thickness h , length L_1 , and width b_1 and between any two arbitrary layers, different kinds of delamination zones may occur. A Cartesian coordinate is defined where X and Y are in the midplane and Z defines along the upward normal direction. The origin of the reference coordinate system is in the center of the midplane as shown in Fig 2.1.

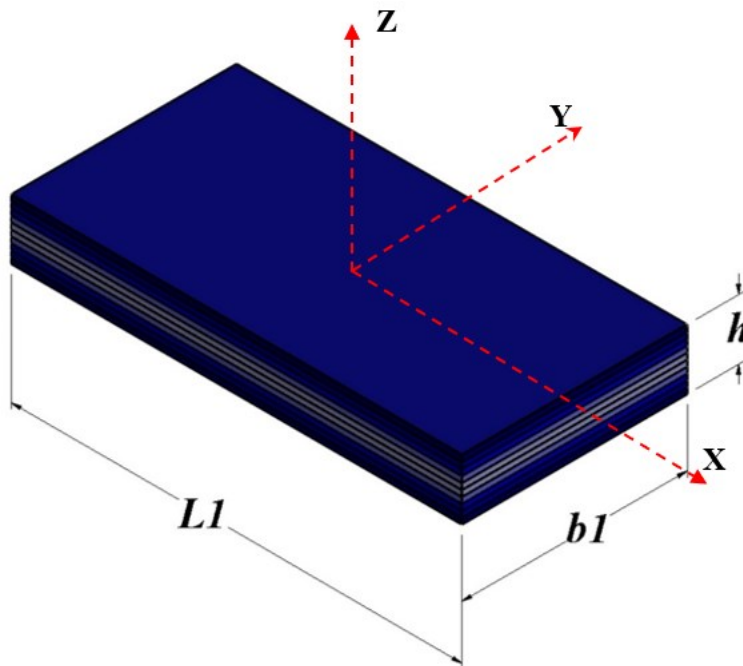


Figure 2-1 FG-GRC laminated plate

The thickness of all plies is assumed to be the same. Each ply is formed from a polymeric matrix reinforced by graphene sheets and may contain a distinct volume fraction of graphene. When the graphene volume fraction in layers varies, a piece-wise FG-GRC laminated plate is formed. In the present study, two types of graphene reinforcement layers: zigzag (referred to as 0° -ply) or armchair (referred to as 90° -ply) are considered. Four different graphene distribution patterns of GRCs are studied in this paper, including three non-uniform distributions (FG-X, FG-O, and FG-A) and one symmetric and uniform graphene distribution (UD), As illustrated in Fig 2.2.

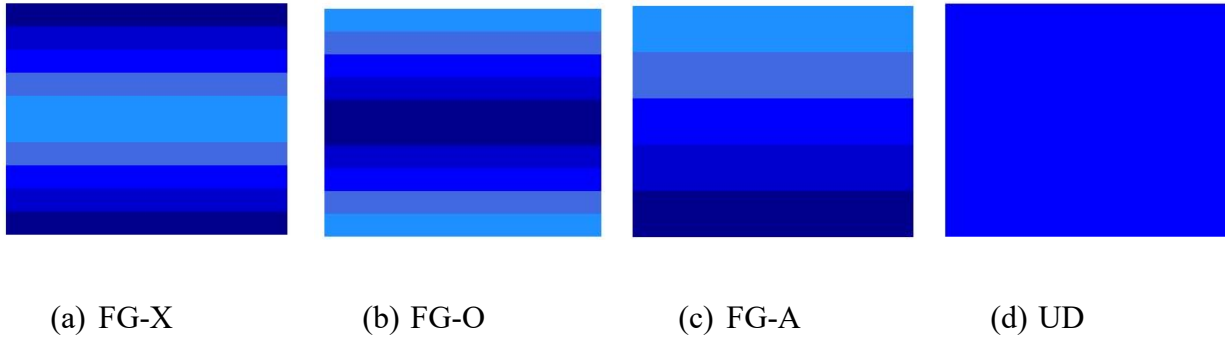


Figure 2-2 Four types of graphene distributions in GRCs with graphene contents increasing with darkness

There are various higher order shear deformation plate theories for determining the displacement fields. The third order shear deformation plate theory (TSDT) is employed in this study. The reason for increasing the displacements up to the cubic term in the thickness coordinate is to obtain a quadratic variation of the transverse shear strains and stresses throughout the plate thickness. The assumption of straightness and normality of a transverse normal after deformation of a plate is relaxed in TSDT by expanding the displacements u and v as cubic functions of the thickness coordinate. The displacement fields for the FG-GRC laminated composite plate is expressed according to the TSDT by [61]:

$$u(x, y, z) = u_0(x, y) + z\varphi_x(x, y) - \frac{4z^3}{3h^2} \left(\varphi_x(x, y) + \frac{\partial w_0}{\partial x} \right)$$

$$\begin{aligned}
v(x, y, z) &= v_0(x, y) + z\varphi_y(x, y) - \frac{4z^3}{3h^2} \left(\varphi_y(x, y) + \frac{\partial w_0}{\partial y} \right) \\
w(x, y, z) &= w_0(x, y)
\end{aligned} \tag{2-1}$$

where u_0 , v_0 , and w_0 represent the displacement components defined at the midplane of the plate; φ_x and φ_y are the middle surface rotations about the y and x axes, respectively. The displacement fields in Eq. (2.1) show that once the plate deforms, a straight line perpendicular to the undeformed middle plane becomes a cubic curve. For small strain and moderate rotating deformation, the von-Karman nonlinear strain–displacement relation, as given in Appendix A, is adopted.

As noted previously, the main objective of this research is to perform a thermal instability analysis on the FG-GRC delaminated plate subjected to a uniform temperature rise that can act as a compressive load when the boundary conditions are constrained along the in-plane directions. By assuming linear stress-strain relations and using T_0 as a reference temperature and T as a temperature distribution over the plate, we have [67]:

$$\begin{bmatrix} \sigma_{xx} \\ \sigma_{yy} \\ \tau_{yz} \\ \tau_{xz} \\ \tau_{xy} \end{bmatrix} = \begin{bmatrix} \bar{Q}_{11} & \bar{Q}_{12} & 0 & 0 & \bar{Q}_{16} \\ \bar{Q}_{21} & \bar{Q}_{22} & 0 & 0 & \bar{Q}_{26} \\ 0 & 0 & \bar{Q}_{44} & \bar{Q}_{45} & 0 \\ 0 & 0 & \bar{Q}_{45} & \bar{Q}_{55} & 0 \\ \bar{Q}_{61} & \bar{Q}_{62} & 0 & 0 & \bar{Q}_{66} \end{bmatrix} \left(\begin{bmatrix} \varepsilon_{xx} \\ \varepsilon_{yy} \\ \gamma_{yz} \\ \gamma_{xz} \\ \gamma_{xy} \end{bmatrix} - (T - T_0) \begin{bmatrix} \alpha_{xx} \\ \alpha_{yy} \\ 0 \\ 0 \\ 2\alpha_{xy} \end{bmatrix} \right) \tag{2-2}$$

where α_{ij} indicates the thermal expansion coefficients. Based on the transformation rule in the fiber reinforced composite materials, \bar{Q}_{ij} denotes the transformed elastic constants.

According to TSDT, the stress resultants N_{ij} , M_{ij} , P_{ij} , Q_{ij} , and R_{ij} are defined by:

$$\begin{aligned}
\begin{Bmatrix} \{N\} \\ \{M\} \\ \{P\} \end{Bmatrix} &= \begin{bmatrix} [A] & [B] & [E] \\ [B] & [D] & [F] \\ [E] & [F] & [H] \end{bmatrix} \begin{Bmatrix} \{\varepsilon^0\} - \{\varepsilon^{th}\} \\ \{\varepsilon^1\} \\ \{\varepsilon^3\} \end{Bmatrix} \\
\begin{Bmatrix} \{Q\} \\ \{R\} \end{Bmatrix} &= \begin{bmatrix} [As] & [Ds] \\ [Ds] & [Fs] \end{bmatrix} \begin{Bmatrix} \{\gamma^0\} \\ \{\gamma^2\} \end{Bmatrix}
\end{aligned} \tag{2-3}$$

The stiffness matrices in Eq. (2.3) are defined as:

$$(A_{ij}, B_{ij}, D_{ij}, E_{ij}, F_{ij}, H_{ij}) = \int_{-\frac{h}{2}}^{\frac{h}{2}} \bar{Q}_{ij}(1, z, z^2, z^3, z^4, z^6) dz, \quad (i, j = 1, 2, 6)$$

$$(A_{Sij}, DS_{ij}, FS_{ij}) = \int_{-\frac{h}{2}}^{\frac{h}{2}} \bar{Q}_{ij}(1, z^2, z^4) dz, \quad (i, j = 4, 5) \quad (2-4)$$

In addition, $\{\varepsilon^{th}\}$ is the thermal strain and is defined as follows:

$$\begin{Bmatrix} \varepsilon_{xx} \\ \varepsilon_{yy} \\ \gamma_{xy} \end{Bmatrix}^{th} = \sum_{K=1}^N \int_{h_{K-1}}^{h_K} \begin{bmatrix} \cos^2(\theta_K) & \sin^2(\theta_K) \\ \sin^2(\theta_K) & \cos^2(\theta_K) \\ 2\cos(\theta_K)\sin(\theta_K) & -2\cos(\theta_K)\sin(\theta_K) \end{bmatrix} \begin{Bmatrix} \alpha_{11} \\ \alpha_{22} \end{Bmatrix} (T - T_0) dz \quad (2-5)$$

where θ_K is the ply angle in the Kth lamina.

As previously stated, the minimal total potential energy principle is used to investigate the thermomechanical instability performance of the FG-GRC delaminated composite plate. The following equation provides the strain energy per unit volume as follows:

$$\begin{aligned} U &= \int \frac{1}{2} \bar{\sigma}^T \bar{\varepsilon} dV \\ &= \frac{1}{2} \int_{-\frac{b_1}{2}}^{\frac{b_1}{2}} \int_{-\frac{L_1}{2}}^{\frac{L_1}{2}} \left(\{\varepsilon^{(0)}\}[A]\{\varepsilon^{(0)}\}^T + 2\{\varepsilon^{(0)}\}[B]\{\varepsilon^{(1)}\}^T + \{\varepsilon^{(1)}\}[D]\{\varepsilon^{(1)}\}^T + 2\{\varepsilon^{(0)}\}[E]\{\varepsilon^{(3)}\}^T + \{\varepsilon^{(1)}\}[F]\{\varepsilon^{(3)}\}^T + \right. \\ &\quad \left. \{\varepsilon^{(3)}\}[H]\{\varepsilon^{(3)}\}^T + \{\gamma^{(0)}\}[As]\{\gamma^{(0)}\}^T + 2\{\gamma^{(0)}\}[Ds]\{\gamma^{(2)}\}^T + \{\gamma^{(2)}\}[Fs]\{\gamma^{(2)}\}^T - 2\{\varepsilon^T\}[A]\{\varepsilon^{(0)}\}^T - \right. \\ &\quad \left. 2\{\varepsilon^T\}[B]\{\varepsilon^{(1)}\}^T - 2\{\varepsilon^T\}[E]\{\varepsilon^{(3)}\}^T + \{\varepsilon^T\}[A]\{\varepsilon^T\}^T \right) \end{aligned} \quad (2-6)$$

Because the plate is under thermal loading as a compressive load, the total potential energy of the plate is equal to the strain energy.

$$\Pi = U \quad (2-7)$$

2.2.2. Thermomechanical characteristics of GRC laminates

The thermomechanical properties of GRCs are critical for studying the performance of these structures. MD has been used to precisely determine the thermomechanical properties of a graphene reinforced polymer nanocomposite [68]. The comparison of the MD simulation results with the predictions of the rule of mixture [69] and Halpin-Tsai model [68] reveals that due to the nano size effect and surface effect, these micromechanical models cannot be used directly to predict the effective material properties of GRCs and modifications are required [38]. The Halpin-

Tsai mathematical model is modified by considering efficiency parameters $\eta_i, i = 1,2,3$ obtained by matching the MD simulation results to those of the Halpin-Tsai model. Based on this approach the elasticity and shear module of composite media reinforced by graphene sheets may be evaluated by [37,39,40]:

$$\begin{aligned}
 E_{11} &= \eta_1 \frac{1 + 2 \left(\frac{a^G}{h^G} \right) \gamma_{11} V^G}{1 - \gamma_{11} V^G} E^m \\
 E_{22} &= \eta_2 \frac{1 + 2 \left(\frac{b^G}{h^G} \right) \gamma_{22} V^G}{1 - \gamma_{22} V^G} E^m \\
 G_{12} &= \eta_3 \frac{1}{1 - \gamma_{12} V^G} G^m
 \end{aligned} \tag{2-8}$$

where a^G , b^G , and h^G , represent the length, width, and effective thickness of the graphene sheet, respectively. The remaining supplementary parameters are as defined by:

$$\begin{aligned}
 \gamma_{11} &= \frac{\left(\frac{E_{11}^G}{E^m} \right) - 1}{\left(\frac{E_{11}^G}{E^m} \right) + 2 \left(\frac{a^G}{h^G} \right)} \\
 \gamma_{22} &= \frac{\left(\frac{E_{22}^G}{E^m} \right) - 1}{\left(\frac{E_{22}^G}{E^m} \right) + 2 \left(\frac{b^G}{h^G} \right)} \\
 \gamma_{12} &= \frac{\left(\frac{G_{12}^G}{E^m} \right) - 1}{\left(\frac{G_{12}^G}{E^m} \right)}
 \end{aligned} \tag{2-9}$$

It should be noted that E^m and G^m represent the elasticity and shear moduli of the homogeneous isotropic matrix, respectively. Additionally, in Eq. (2.9), E_{11}^G, E_{22}^G , and G_{12}^G denote the graphene sheet elasticity and shear moduli. As noted previously, each layer of the GRC laminates is composed of graphene and matrix; thus, in Eq. (2.8), V^G refers to the graphene volume fraction and $V^m = 1 - V^G$ indicates the matrix volume proportion. Graphene efficiency parameters $\eta_j (j = 1,2,3)$, developed in the extended Halpin-Tsai approach, are found by comparing the

results of the MD simulations to those derived from the micromechanical models. The Schapery model [64] is one of the most extensively used methods for determining the thermal expansion coefficients of composite media such as carbon nanotube reinforced composites. This model is also applicable to GRC materials:

$$\alpha_{11} = \frac{V^G E_{11}^G \alpha_{11}^G + V^m E^m \alpha^m}{V^G E_{11}^G + V^m E^m}$$

$$\alpha_{22} = (1 + \nu_{12}^G) V^G \alpha_{22}^G + (1 + \nu^m) V^m \alpha^m - \nu_{12} \alpha_{11} \quad (2-10)$$

where α_{11}^G , α_{22}^G and α^m are the thermal expansion coefficients, and ν_{12}^G and ν^m are the Poisson's ratios respectively, of the graphene sheet and matrix. The Poisson's ratios of the GRCs can be explained in terms of the Poisson' ratios of constituents according to the standard rule of mixes. As a result, one may arrive at:

$$\nu_{12} = V^G \nu_{12}^G + V^m \nu^m \quad (2-11)$$

2.3. Modelling of GRC laminated plate

2.3.1. GRC laminated plate with circular and elliptical embedded delamination zones

Utilizing the minimum total potential energy is one of the recommended methods for solving nonlinear problems. Obviously, this requires the displacement field to describe the variation of u, v, w, ϕ_x , and ϕ_y across the middle surface. As mentioned, delamination separates GRC laminated plates into distinct zones through their thickness and longitudinal directions. In this circumstance, it is necessary to define suitable displacement and rotation functions for each zone, taking into account the continuity conditions between the boundaries of several divided regions. Plate boundary conditions are an additional important requirement that must be satisfied by the displacement and rotation functions. As illustrated in Fig 2.3, circular and elliptical embedded delamination zones at the center of the square GRC laminated plates separate them into two distinct regions along their thickness directions, and into three different zones along their longitudinal

directions. Fig 2.3 demonstrates that the radius of the circular embedded delamination is equal to R , and dimensions of the major and minor axes of the elliptical delamination are, respectively, $2a$ and $2b$. The boundaries of the circular and elliptical delamination are defined in the following equations, respectively:

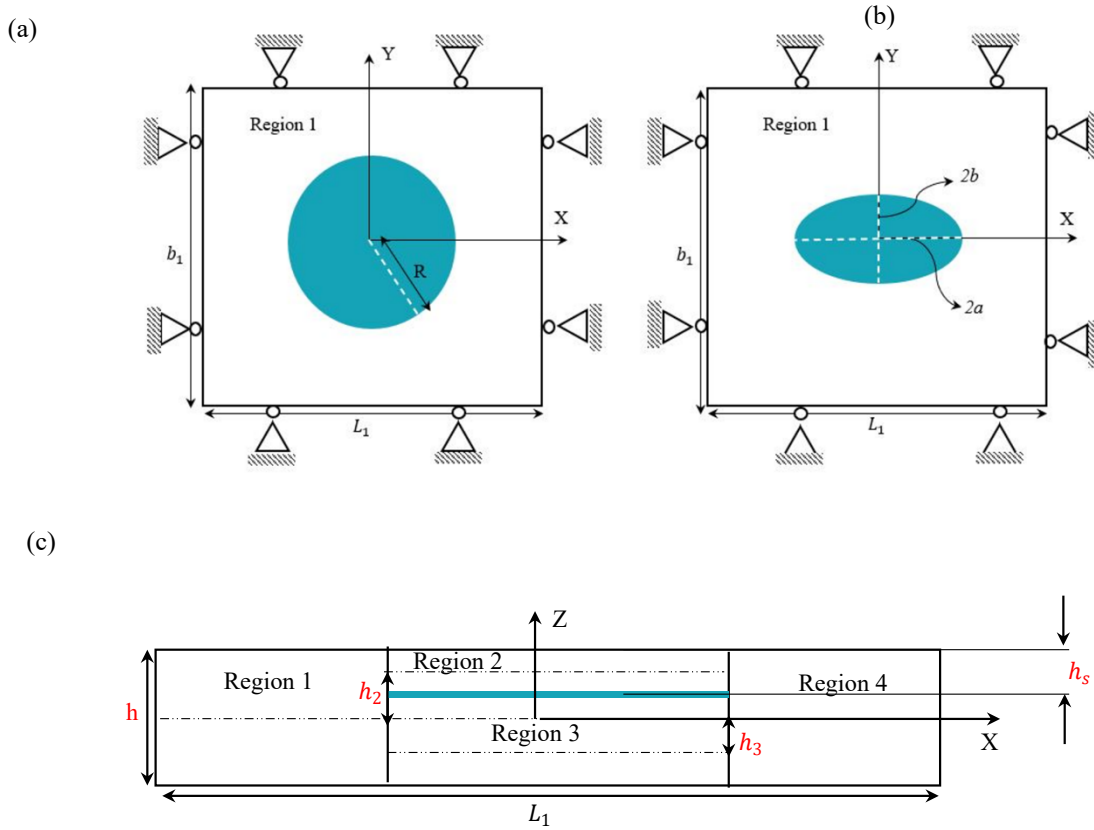


Figure 2-3 Segmentation of the GRC laminated plate with embedded delamination into subdomains (a) circular delamination (b) elliptical delamination (c) divided regions alongside the X axes

$$C_{circle} = x^2 + y^2 - R^2 \quad (2-12)$$

$$C_{ellipse} = \frac{x^2}{a^2} + \frac{y^2}{b^2} - 1 \quad (2-13)$$

The essential continuity conditions of displacement and rotation functions at the boundaries of delamination zones with arbitrary geometry, C , are therefore expressed as follows:

$$W_0^{(1)}|_C = W_0^{(2)}|_C = W_0^{(3)}|_C, \frac{\partial W_0^{(1)}}{\partial x}|_C = \frac{\partial W_0^{(2)}}{\partial x}|_C = \frac{\partial W_0^{(3)}}{\partial x}|_C, \frac{\partial W_0^{(1)}}{\partial y}|_C = \frac{\partial W_0^{(2)}}{\partial y}|_C = \frac{\partial W_0^{(3)}}{\partial y}|_C$$

$$\begin{aligned}
U_0^{(2)}|_c &= U_0^{(1)}|_c + h_2 \varphi_x^{(1)}|_c - h_2^3 C_1^{(1)} (\varphi_x^{(1)}|_c + W_{,x}^{(1)}|_c) \\
U_0^{(3)}|_c &= U_0^{(1)}|_c + h_3 \varphi_x^{(1)}|_c - h_3^3 C_1^{(1)} (\varphi_x^{(1)}|_c + W_{,x}^{(1)}|_c) \\
V_0^{(2)}|_c &= V_0^{(1)}|_c + h_2 \varphi_y^{(1)}|_c - h_2^3 C_1^{(1)} (\varphi_y^{(1)}|_c + W_{,y}^{(1)}|_c) \\
V_0^{(3)}|_c &= V_0^{(1)}|_c + h_3 \varphi_y^{(1)}|_c - h_3^3 C_1^{(1)} (\varphi_y^{(1)}|_c + W_{,y}^{(1)}|_c) \\
\varphi_x^{(2)}|_c &= \varphi_x^{(1)}|_c - 3h_2^2 C_1^{(1)} (\varphi_x^{(1)}|_c + W_{,x}^{(1)}|_c) \\
\varphi_x^{(3)}|_c &= \varphi_x^{(1)}|_c - 3h_3^2 C_1^{(1)} (\varphi_x^{(1)}|_c + W_{,x}^{(1)}|_c) \\
\varphi_y^{(2)}|_c &= \varphi_y^{(1)}|_c - 3h_2^2 C_1^{(1)} (\varphi_y^{(1)}|_c + W_{,y}^{(1)}|_c) \\
\varphi_y^{(3)}|_c &= \varphi_y^{(1)}|_c - 3h_3^2 C_1^{(1)} (\varphi_y^{(1)}|_c + W_{,y}^{(1)}|_c)
\end{aligned} \tag{2-14}$$

In Eq. (2.14), h_2 and h_3 denote the distances between the midplanes of the region 2 and 3 and the midplane of the whole plate, as shown in Fig 2.3. Additionally, $U^{(i)}$, $V^{(i)}$, and $W^{(i)}$ represent the displacement fields of the i^{th} region alongside the X, Y, and Z directions of the plate, respectively; $\varphi_x^{(i)}$ and $\varphi_y^{(i)}$ also indicate the rotation of the midplane of the i^{th} region around the y and x axes. Additionally, the constant $C_1^{(1)}$ can be expressed as follows: $C_1^{(1)} = \frac{4}{3h^2}$, where h represents the total thickness of the plate, as illustrated in Fig 2.3. In this work, two different types of boundary conditions are considered for the GRC laminated plates with embedded delamination zones including immovable simply supported (SSSS) and clamped (CCCC) at all edges. In the case of the GRC laminated plate with a single edge delamination, however, due to the presence of this damage area along one of the plate's longitudinal edges, the stated edge is assumed to be unrestricted, while the other three edges are subjected to simply-supported boundary conditions (SSSF). The mathematical formulas for different kinds of boundary conditions applied to GRC delaminated plates are mentioned in Tables (2.1) and (2.2), respectively. According to the continuity and boundary conditions mentioned in Eq. (2.14) and Tables (2.1) and (2.2), the displacement and rotation functions are assumed to be polynomial. For brevity, hereinafter, the

admissible functions for the GRC laminated plate with a circular embedded delamination zone and simply supported boundary conditions are provided. It should be noted that the admissible displacement and rotation functions of the GRC laminated plate with an elliptical embedded delamination are given in Appendix B for simply supported and clamped boundary conditions.

Table 2-1 Mathematical expressions of displacement and rotation at different edges of the perfect FG-GRC plate (SSSS and CCCC)

Type of B.C	Out-of-plane displacement	In-plane displacement	Rotation
Simply Supported	$W _{x=-\frac{L_1}{2}} = W _{x=\frac{L_1}{2}} = 0$	$U _{x=-\frac{L_1}{2}} = U _{x=\frac{L_1}{2}} = 0$	-
	$W _{y=-\frac{b_1}{2}} = W _{y=\frac{b_1}{2}} = 0$	$V _{y=-\frac{b_1}{2}} = V _{y=\frac{b_1}{2}} = 0$	
Clamped	$W _{x=-\frac{L_1}{2}} = W _{x=\frac{L_1}{2}} = 0$	$U _{x=-\frac{L_1}{2}} = U _{x=\frac{L_1}{2}} = 0$	$\varphi_x _{x=-\frac{L_1}{2}} = \varphi_x _{x=\frac{L_1}{2}} = 0$
	$W _{y=-\frac{b_1}{2}} = W _{y=\frac{b_1}{2}} = 0$	$V _{y=-\frac{b_1}{2}} = V _{y=\frac{b_1}{2}} = 0$	$\varphi_y _{y=-\frac{b_1}{2}} = \varphi_y _{y=\frac{b_1}{2}} = 0$

Table 2-2 Mathematical expressions of displacement and rotation at different edges of GRC laminated plate with a single edge delamination (SSSF)

Type of B.C	Out-of-plane displacement	In-plane displacement
Simply Supported	$W _{x=-\frac{L_1}{2}} = W _{x=\frac{L_1}{2}} = 0$	$U _{x=-\frac{L_1}{2}} = U _{x=\frac{L_1}{2}} = \text{End shortening}$
	$W _{y=\frac{b_1}{2}} = 0$	$V _{y=\frac{b_1}{2}} = 0$

Out-of-Plane displacements

$$W^{(1)} = \sum_{m=0}^{M_1} \sum_{n=0}^{N_1} \left(x - \frac{L_1}{2}\right) \left(x + \frac{L_1}{2}\right) \left(y - \frac{b_1}{2}\right) \left(y + \frac{b_1}{2}\right) W_{mn}^{(1)} x^m y^n$$

$$W^{(2)} = W^{(1)} + \sum_{m=0}^{M_2} \sum_{n=0}^{N_2} (x^2 + y^2 - R^2)^2 W_{mn}^{(2)} x^m y^n$$

$$W^{(3)} = W^{(1)} + \sum_{m=0}^{M_3} \sum_{n=0}^{N_3} (x^2 + y^2 - R^2)^2 W_{mn}^{(3)} x^m y^n \quad (2-15)$$

In-plane displacements

$$U^{(1)} = \sum_{p=0}^{P_1} \sum_{q=0}^{Q_1} \left(x - \frac{L_1}{2}\right) \left(x + \frac{L_1}{2}\right) U_{pq}^{(1)} x^p y^q$$

$$U^{(2)} = U^{(1)} - \frac{4h_3^3}{3h_1^2} \left(\varphi_x^{(1)} + \frac{\partial W^{(1)}}{\partial x}\right) + h_2 \varphi_x^{(1)} + \sum_{p=0}^{P_2} \sum_{q=0}^{Q_2} (x^2 + y^2 - R^2) U_{pq}^{(2)} x^p y^q$$

$$U^{(3)} = U^{(1)} - \frac{4h_3^3}{3h_1^2} \left(\varphi_x^{(1)} + \frac{\partial W^{(1)}}{\partial x}\right) + h_3 \varphi_x^{(1)} + \sum_{p=0}^{P_3} \sum_{q=0}^{Q_3} (x^2 + y^2 - R^2) U_{pq}^{(3)} x^p y^q$$

$$V^{(1)} = \sum_{s=0}^{S_1} \sum_{r=0}^{R_1} \left(y - \frac{b_1}{2}\right) \left(y + \frac{b_1}{2}\right) V_{sr}^{(1)} x^s y^r$$

$$V^{(2)} = V^{(1)} - \frac{4h_2^3}{3h_1^2} \left(\varphi_y^{(1)} + \frac{\partial W^{(1)}}{\partial y}\right) + h_2 \varphi_y^{(1)} + \sum_{s=0}^{S_2} \sum_{r=0}^{R_2} (x^2 + y^2 - R^2) V_{sr}^{(2)} x^s y^r$$

$$V^{(3)} = V^{(1)} - \frac{4h_3^3}{3h_1^2} \left(\varphi_y^{(1)} + \frac{\partial W^{(1)}}{\partial y}\right) + h_3 \varphi_y^{(1)} + \sum_{s=0}^{S_3} \sum_{r=0}^{R_3} (x^2 + y^2 - R^2) V_{sr}^{(3)} x^s y^r \quad (2-16)$$

Rotational functions

$$\varphi_x^{(1)} = \sum_{j=0}^{J_1} \sum_{k=0}^{K_1} \varphi_{x_{jk}}^{(1)} x^j y^k$$

$$\varphi_x^{(2)} = \varphi_x^{(1)} - \frac{4h_2^2}{h_1^2} \left(\varphi_x^{(1)} + \frac{\partial W^{(1)}}{\partial x}\right) + \sum_{j=0}^{J_2} \sum_{k=0}^{K_2} \varphi_{x_{jk}}^{(2)} (x^2 + y^2 - R^2) x^j y^k$$

$$\varphi_x^{(3)} = \varphi_x^{(1)} - \frac{4h_3^2}{h_1^2} \left(\varphi_x^{(1)} + \frac{\partial W^{(1)}}{\partial x}\right) + \sum_{j=0}^{J_3} \sum_{k=0}^{K_3} \varphi_{x_{jk}}^{(3)} (x^2 + y^2 - R^2) x^j y^k$$

$$\varphi_y^{(1)} = \sum_{i=0}^{I_1} \sum_{t=0}^{T_1} \varphi_{y_{it}}^{(1)} x^i y^t$$

$$\varphi_y^{(2)} = \varphi_y^{(1)} - \frac{4h_2^2}{h_1^2} \left(\varphi_y^{(1)} + \frac{\partial W^{(1)}}{\partial y}\right) + \sum_{i=0}^{I_2} \sum_{t=0}^{T_2} \varphi_{y_{it}}^{(2)} (x^2 + y^2 - R^2) x^i y^t$$

$$\varphi_y^{(3)} = \varphi_y^{(1)} - \frac{4h_3^2}{h_1^2} \left(\varphi_y^{(1)} + \frac{\partial W^{(1)}}{\partial y}\right) + \sum_{i=0}^{I_3} \sum_{t=0}^{T_3} \varphi_{y_{it}}^{(3)} (x^2 + y^2 - R^2) x^i y^t \quad (2-17)$$

In Eqs. (2.15), (2.16), and (2.17), the second series is defined to fulfill the continuity conditions that arise due to the delamination. It is worth noting that an unacceptable physical phenomenon

known as penetration may occur between the sublaminates and baselaminates where the GRC delaminated plate is subjected to compressive loads. The size and location of the delamination zone, graphene reinforcement distribution pattern, and type of boundary condition all play essential roles in the occurrence of penetration. In this study, the penalty constraint is used to prevent penetration violation. By establishing a restriction on the equations, this strategy results in equal displacements in the overlapped areas. To do this, various virtual linear springs are assumed throughout the contact regions, and the contact stiffness of the corresponding springs (i.e. K_f) is changed to assure the consistency of the contact region's displacements. Thus, the estimated strain energy of the assumed virtual springs might be calculated as [64]:

$$U_{contact} = \int \frac{1}{2} K_f (W^{(i)} - W^{(i+1)})^2 ds \quad (2-18)$$

This study presents novel polynomial series as displacement and rotation functions for each region of the GRC delaminated plate, which includes circular and elliptical delamination zones, as outlined in Eqs. (2.12)-(2.17) and Appendix B. These functions are derived using the higher-order shear deformation theory. After defining the displacement and rotation fields and applying the minimum total potential energy principle, we obtain a system of nonlinear equations. The total potential energy, which is the sum of the strain energy in each region, can be evaluated by substituting the displacement and rotation functions (Eqs. (2.15), (2.16), and (2.17)) into Eq. (2.6).

In addition to the strain energy in each region, we need to consider the strain energy of the assumed springs in the contact zone as presented in Eq. (2.18). This ensures that the contact zone between the delaminated regions is correctly modeled. By incorporating these equations, we can obtain a comprehensive understanding of the thermal instability behavior of the FG-GRC delaminated plate.

$$U^{total} = \sum_{j=1}^J U^j$$

$$\Pi = U^{total} + U_{contact} \quad (2-19)$$

Following this stage, the total potential energy should be minimized using the unknown displacement and rotation coefficients as shown in Eq. (2.20). [60]

$$\frac{\partial \Pi}{\partial \chi} = 0 \quad (2-20)$$

where χ is the vector of unknowns $\chi = \{U_{pq}^{(i)}, V_{sr}^{(i)}, W_{mn}^{(i)}, \varphi_{xjk}^{(i)}, \varphi_{yit}^{(i)}\}$. The Eq. (2.20) leads to the following matrix representation of the equilibrium equations [60]:

$$[K(T, \chi)]\{\chi\} = \{F(T)\} \quad (2-21)$$

where $[K(T, \chi)]$ and $\{F(T)\}$ are the stiffness matrix and force vector, respectively. Eq. (2.21) shows a system of nonlinear equation that is solved using the generalized Newton-Raphson iterative method.

2.3.2. GRC laminated plate with a single edge delamination zone

In Section 3.1, we centered our attention on circular and elliptical embedded delaminations. It is noteworthy that the displacement and rotation functions developed for these cases can be adapted with minor modifications to model plates with semi-circular or elliptical edge delaminations. To expand the scope of our findings and enable the modeling of a broader range of delamination geometries, we made the deliberate decision to alter the shape of the edge delamination to a rectangular configuration. Similar to the circular and elliptical embedded delamination shown in Fig 2.3, the edge delamination also separates the composite plate into two distinct regions along the thickness direction, one of which is thicker than the other region and is referred to as baselaminate, while the other part is thinner and is called to as sublaminates. Additionally, this delamination zone divides the prescribed GRC laminated plate into three different zones running parallel to the longitudinal direction of the plate, as displayed in Fig 2.4. This figure also shows that the plate is still symmetric around the Y axis despite the presence of

the rectangular delamination zone, which means that delamination is positioned at the center of the free edge.

As stated in the preceding section, it is necessary to consider the continuity boundary conditions between the different areas established through the longitudinal direction of the delaminated plate. The essential displacement and rotation continuity conditions that must be satisfied at the edge delamination boundaries are expressed in Appendix C.

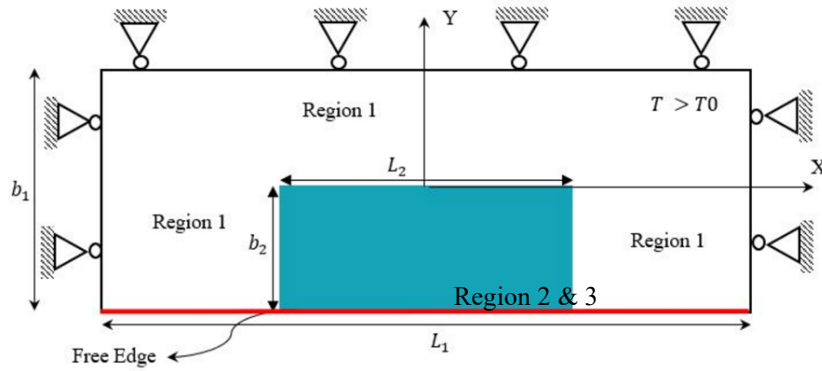


Figure 2-4 Segmentation of the FG-GRC plate with edge delamination into subdomains (regions)

Based on the continuity and boundary conditions stated in Appendix C and table (2.2), respectively, the displacement and rotation functions of the GRC laminated plate with a single edge delamination that has SSSF boundary conditions are just mentioned below.

Out-of-plane displacements

$$W^{(1)} = \sum_{m=0}^{M_1} \sum_{n=0}^{N_1} \left(x - \frac{L_1}{2}\right) \left(x + \frac{L_1}{2}\right) \left(y - \frac{b_1}{2}\right) W_{mn}^{(1)} x^m y^n$$

$$W^{(2)} = W^{(1)} + \sum_{m=0}^{M_2} \sum_{n=0}^{N_2} \left(x - \frac{L_2}{2}\right)^2 \left(x + \frac{L_2}{2}\right)^2 (y - b_2)^2 W_{mn}^{(2)} x^m y^n$$

$$W^{(3)} = W^{(1)} + \sum_{m=0}^{M_3} \sum_{n=0}^{N_3} \left(x - \frac{L_2}{2}\right)^2 \left(x + \frac{L_2}{2}\right)^2 (y - b_2)^2 W_{mn}^{(3)} x^m y^n \quad (2-22)$$

In-plane displacements

$$U^{(1)} = -\varepsilon \cdot x + \sum_{p=0}^{P_1} \sum_{q=0}^{Q_1} \left(x - \frac{L_1}{2}\right) \left(x + \frac{L_1}{2}\right) U_{pq}^{(1)} x^p y^q$$

$$U^{(2)} = U^{(1)} - \frac{4h_2^3}{3h_1^2} \left(\varphi_x^{(1)} + \frac{\partial W^{(1)}}{\partial x}\right) + h_2 \varphi_x^{(1)} + \sum_{p=0}^{P_2} \sum_{q=0}^{Q_2} \left(x - \frac{L_2}{2}\right) \left(x + \frac{L_2}{2}\right) (y - b_2) U_{pq}^{(2)} x^p y^q$$

$$U^{(3)} = U^{(1)} - \frac{4h_3^3}{3h_1^2} \left(\varphi_x^{(1)} + \frac{\partial W^{(1)}}{\partial x}\right) + h_3 \varphi_x^{(1)} + \sum_{p=0}^{P_3} \sum_{q=0}^{Q_3} \left(x - \frac{L_2}{2}\right) \left(x + \frac{L_2}{2}\right) (y - b_2) U_{pq}^{(3)} x^p y^q$$

$$V^{(1)} = \sum_{s=0}^{S_1} \sum_{r=0}^{R_1} \left(y - \frac{b_1}{2}\right) V_{sr}^{(1)} x^s y^r$$

$$V^{(2)} = V^{(1)} - \frac{4h_2^3}{3h_1^2} \left(\varphi_y^{(1)} + \frac{\partial W^{(1)}}{\partial y}\right) + h_2 \varphi_y^{(1)} + \sum_{s=0}^{S_2} \sum_{r=0}^{R_2} \left(x - \frac{L_2}{2}\right) \left(x + \frac{L_2}{2}\right) (y - b_2) V_{sr}^{(2)} x^s y^r$$

$$V^{(2)} = V^{(1)} - \frac{4h_3^3}{3h_1^2} \left(\varphi_y^{(1)} + \frac{\partial W^{(1)}}{\partial y}\right) + h_3 \varphi_y^{(1)} + \sum_{s=0}^{S_3} \sum_{r=0}^{R_3} \left(x - \frac{L_2}{2}\right) \left(x + \frac{L_2}{2}\right) (y - b_2) V_{sr}^{(3)} x^s y^r \quad (2-23)$$

In the case of a GRC laminated plate with a single edge delamination zone, end-shortening strain as a compressive mechanical load is anticipated in addition to the uniform temperature rise. This assumption will allow us to assess the impact of various graphene distribution patterns on the nonlinear thermomechanical responses of this structure. Therefore, it is required to consider $-\varepsilon \cdot x$, $\varepsilon = \frac{\Delta L_1}{L_1}$, for the in-plane function through the X direction for applying the end-shortening strain.

Rotational functions

$$\varphi_x^{(1)} = \sum_{j=0}^{J_1} \sum_{k=0}^{K_1} \varphi_{x_{jk}}^{(1)} x^j y^k$$

$$\varphi_x^{(2)} = \varphi_x^{(1)} - \frac{4h_2^2}{h_1^2} \left(\varphi_x^{(1)} + \frac{\partial W^{(1)}}{\partial x}\right) + \sum_{j=0}^{J_2} \sum_{k=0}^{K_2} \varphi_{x_{jk}}^{(2)} \left(x - \frac{L_2}{2}\right) \left(x + \frac{L_2}{2}\right) (y - b_2) x^j y^k$$

$$\varphi_x^{(3)} = \varphi_x^{(1)} - \frac{4h_3^2}{h_1^2} \left(\varphi_x^{(1)} + \frac{\partial W^{(1)}}{\partial x}\right) + \sum_{j=0}^{J_3} \sum_{k=0}^{K_3} \varphi_{x_{jk}}^{(3)} \left(x - \frac{L_2}{2}\right) \left(x + \frac{L_2}{2}\right) (y - b_2) x^j y^k$$

$$\varphi_y^{(1)} = \sum_{i=0}^{I_1} \sum_{t=0}^{T_1} \varphi_{y_{it}}^{(1)} x^i y^t$$

$$\varphi_y^{(2)} = \varphi_y^{(1)} - \frac{4h_2^2}{h_1^2} \left(\varphi_y^{(1)} + \frac{\partial W^{(1)}}{\partial y} \right) + \sum_{i=0}^{l_2} \sum_{t=0}^{T_2} \varphi_{y_{it}}^{(2)} \left(x - \frac{L_2}{2} \right) \left(x + \frac{L_2}{2} \right) (y - b_2) x^i y^t$$

$$\varphi_y^{(2)} = \varphi_y^{(1)} - \frac{4h_3^2}{h_1^2} \left(\varphi_y^{(1)} + \frac{\partial W^{(1)}}{\partial y} \right) + \sum_{i=0}^{l_3} \sum_{t=0}^{T_3} \varphi_{y_{it}}^{(3)} \left(x - \frac{L_2}{2} \right) \left(x + \frac{L_2}{2} \right) (y - b_2) x^i y^t \quad (2-24)$$

2.4. Results and discussion

Here, the approach described in the preceding sections is used to investigate the nonlinear thermal and thermomechanical instability of composite laminated plates with various types of delamination zones reinforced by graphene sheets. It is well established that when the temperature dependency of material properties is taken into account, more accurate results can be obtained [70,71]. For this reason, temperature-dependent material properties are considered in this paper. Poly (methyl methacrylate), so-called PMMA, is selected for the matrix with material properties $E^m = (3.52 - 0.0034T) \text{ GPa}$, $\nu^m = 0.34$, and $\alpha^m = 45 \times 10^{-6} (1 + 0.0005(T - T_0)) \text{ } 1/K$ and the graphene sheets with effective thickness $h^G = 0.188 \text{ nm}$ are selected as reinforcement of each layer. Because the material properties of graphene sheets are also highly dependent on temperature variation, Lin et al. [69] employed MD simulation to obtain the material properties of graphene sheets at various temperatures, which are illustrated in Table (2.3).

Table 2-3 Thermomechanical properties of single layer graphene sheet with geometrical characteristics

$$a^G = 14.76 \text{ nm}, b^G = 14.77 \text{ nm}, h^G = 0.188 \text{ nm} [69]$$

$T [K]$	$E_{11}^G [TPa]$	$E_{11}^G [TPa]$	$G_{12}^G [TPa]$	ν_{12}^G	$\alpha_{11}^G [10^{-6}/K]$	$\alpha_{22}^G [10^{-6}/K]$
300	1.812	1.807	0.683	0.177	-0.9	-0.95
400	1.769	1.763	0.691	0.177	-0.35	-0.4
500	1.748	1.735	0.700	0.177	-0.08	-0.08
700	1.737	1.721	0.676	0.177	0.25	0.3
1000	1.660	1.646	0.645	0.177	0.32	0.32

Because of the temperature dependency, it is desirable to obtain continuous functions for the material properties of graphene sheets in terms of temperature that can be described using a fourth-order polynomial [72]

$$P = P_0 + P_1 \left(\frac{T}{T_0}\right) + P_2 \left(\frac{T}{T_0}\right)^2 + P_3 \left(\frac{T}{T_0}\right)^3 + P_4 \left(\frac{T}{T_0}\right)^4 \quad (2-25)$$

where $T_0 = 300 K$ is the reference temperature and the coefficients P_i are specific to each thermomechanical properties as presented in Table (2.4). The out of plane shear moduli of graphene sheets can be estimated by $G_{13} = G_{23} = 0.5G_{12}$ (37)

Table 2-4 Coefficients P_i associated to the fourth order interpolation (Eq. (2.25)) for various thermomechanical properties [72]

P	P_0	P_1	P_2	P_3	P_4
$E_{11}(GPa)$	2.1560	-0.5531	2.4378×10^{-1}	-3.3879×10^{-2}	-8.6786×10^{-4}
$E_{22}(GPa)$	1.9590	-0.0824	-1.5645×10^{-1}	1.0440×10^{-1}	-1.7550×10^{-2}
$G_{12}(GPa)$	0.9633	-0.7672	7.2866×10^{-1}	-2.7761×10^{-1}	3.5839×10^{-2}
ν_{12}	0.1770	0	0	0	0
$\alpha_{11}(10^{-6}/K)$	-7.3133	12.4823	-8.3291	2.5511	-2.9089×10^{-1}
$\alpha_{22}(10^{-6}/K)$	-6.0633	9.3930	-5.8005	1.7154	-1.9446×10^{-1}

As illustrated in Eq. (2.8), the extended Halpin-Tsai approach was proposed to improve the accuracy of the material properties of GRC laminated plates obtained from the Halpin-Tsai. This approach includes some efficiency parameters, $\eta_i, i = 1,2,3$. Shen et al. [38,39,41] evaluated these parameters for five distinct graphene volume fractions at three different temperatures as shown in Table (2.5).

Table 2-5 The efficiency parameters $\eta_i, i = 1,2,3$ for different volume fractions of graphene sheets at three different levels of temperature [38,39,41]

T (K)	V_G	η_1	η_2	η_3
300	0.03	2.929	2.855	11.842
	0.05	3.068	2.962	15.944
	0.07	3.013	2.966	23.575
	0.09	2.647	2.609	32.816
	0.11	2.311	2.260	33.125
400	0.03	2.977	2.896	13.928
	0.05	3.128	3.023	15.229
	0.07	3.060	3.027	22.588
	0.09	2.701	2.603	28.896
	0.11	2.405	2.337	29.527
500	0.03	3.388	3.382	16.712
	0.05	3.544	3.414	16.018
	0.07	3.462	3.339	23.428
	0.09	3.058	2.936	29.754
	0.11	2.736	2.665	30.773

In all cases studied in this work, the specified GRC laminated plates consist of ten plies stacked in the sequence $[0,90,0,90,0]_s$. Four different types of graphene distributions are considered to reinforce the specified composite plate, including FG-X, FG-O, FG-A, and UD. The graphene volume fraction varies symmetrically as $[0.11,0.09,0.07,0.05,0.03]_s$ in the FG-X distribution from top to bottom of the plate. In this functionally grading arrangement, the top and bottom layers have the highest volume fraction of graphene reinforcement while the layer located at the midplane has the lowest volume fraction. The symmetric arrangement of $[0.03,0.05,0.07,0.09,0.11]_s$ is referred to as FG-O. Unlike the FG-X distribution, the top and bottom layers contain the least

amount of graphene, while the layer at the midplane contains the most amount of this reinforcement. FG-A is an asymmetric FG-GRC laminated plate in which the lowest graphene volume fraction is dedicated to the two top layers of the plate, and the graphene volume fraction increases in the thickness direction until it reaches its maximum at the two bottom layers, which can be shown like: $[(0.03)_2, (0.05)_2, (0.07)_2, (0.09)_2, (0.11)_2]_a$. Here subscript “2” indicates the number of layers sharing the same volume fraction of graphene from top to bottom, whilst subscript “s” and “a” indicate the symmetric and asymmetric distribution of graphene reinforcement in the FG-GRC plate, respectively. Uniform distribution, UD, is another symmetric configuration of GRC laminate, in which all layers have the same volume fraction of graphene; in this study, $V_G = 0.07$ is considered for UD, thus, the two cases of FG-GRC and UD-GRC laminated plates will have equal values of the total volume fraction of graphene.

2.4.1. Comparative study

The thermal instability analysis of a GRC plate with simply supported boundary conditions was studied by Shen et al [31] using a two-step perturbation approach. The thermal postbuckling behavior of the GRC laminated plate with three different graphene distribution patterns, including FG-X, FG-O, and UD, are compared in Fig 2.5. It is observed that our results are in an excellent agreement with those reported in the reference [31]. Given that the primary objective of this paper is to assess the nonlinear thermal behavior of GRC delaminated plate, it is also necessary to compare the results of our method to that of another reliable source on plates with delamination. The verification is presented in Fig 2.6, which shows the instability equilibrium path of a composite plate with a single through-the-width delamination and clamped boundary conditions at the both longitudinal ends subjected to a non-dimensional end-shortening strain. The top sublaminates and the bottom baselaminates have lay ups of $[0,90,90,0]$ and $[0,90,90,0]_3$. As shown

in Fig 2.6, the current results are in close agreement with findings reported in reference [58] by using FEM.

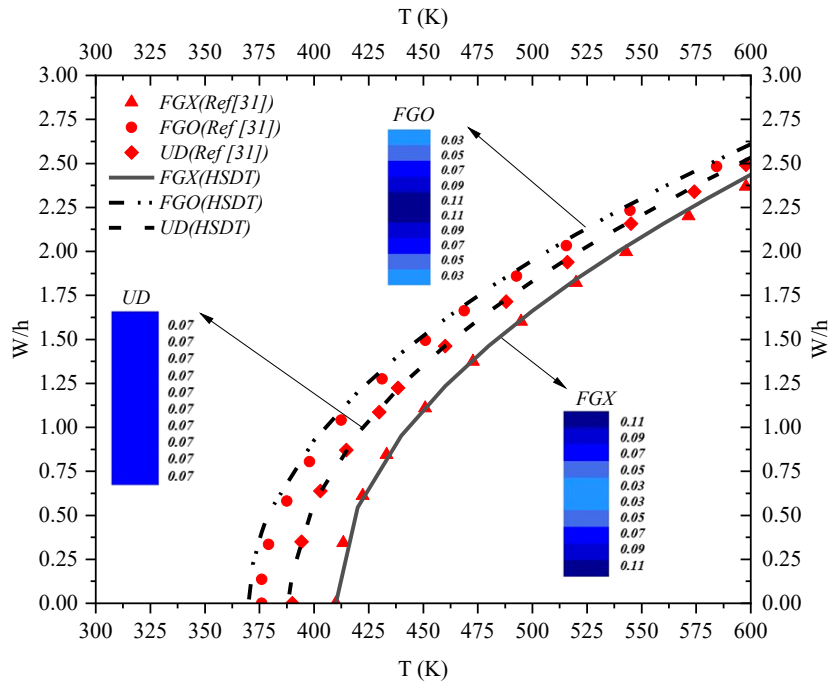


Figure 2-5 Thermal postbuckling of temperature dependent of GRC laminated plates: comparison of the results of the current study and those provided by Shen et al. [31]

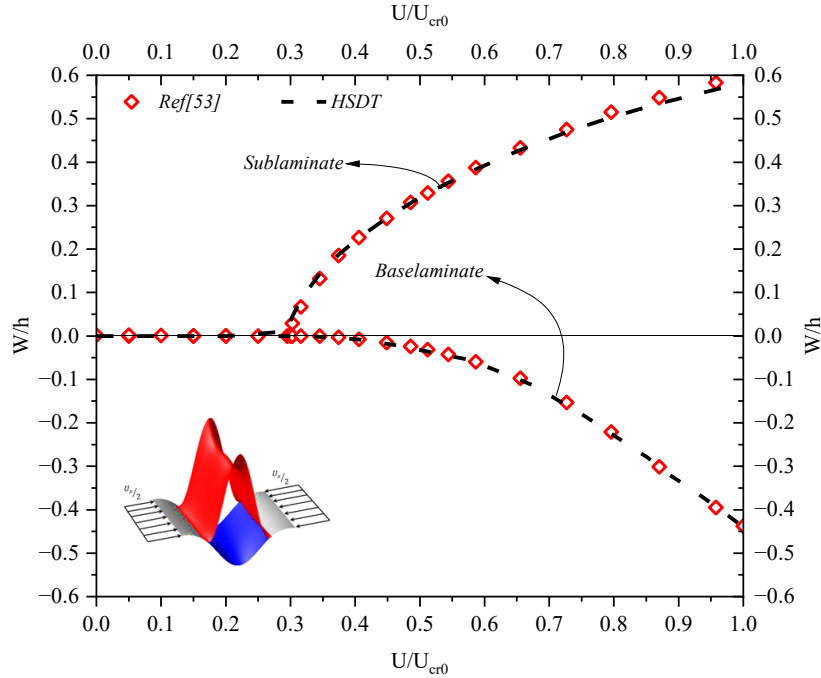


Figure 2-6 Non-dimensional out-of-plane displacement versus the non-dimensional end-shortening: comparison of the results of the current study and those finite element results provided by Kharazi et al. [53]

2.4.2. Parametric study

2.4.2.1. Thermal instability analysis of GRC laminated plate

Fig 2.7(a) indicates the effect of boundary conditions on the thermal equilibrium path of FG-GRC laminated plates ($L_1/b_1 = 1, L_1/h = 20$) without delamination zone for two distinct graphene reinforcement distribution patterns, FG-X and FG-A, one is symmetric and the other asymmetric, additionally, Fig 2.7(b) illustrates the effect of simply-supported and clamped boundary conditions on the variation of the total bending moment at the center of the FG-GRC laminated plates. As illustrated in Fig 2.7(a), the thermal equilibrium paths of the FG-X laminated plates for both simply-supported and clamped boundary conditions are primary-secondary, showing that there exist bifurcation points indicating the critical buckling temperatures. Also, Fig 2.7(b) shows that the total bending moment of the FG-X laminated plates are equal to zero in the vicinity of the critical buckling temperature. The thermal instability response of the FG-A

laminated plate with clamped edges, on the other hand, differs dramatically from that of the FG-A laminated plate with simply-supported boundary conditions. When the FG-A laminated plate is subjected to thermal loading, non-zero thermal moments are generated through the plate due to the asymmetric stretching-bending coupling, as shown in Fig 2.7(b). A simply-supported edge does not have the potential to apply an extra moment to keep the FG-A laminated plate flat, as opposed to the clamped boundary condition, which can. For this reason, the thermal equilibrium path of the FG-A laminated plate with simply supported edges is of the unique and stable nonlinear bending type, whereas the response of the FG-A laminated plate with clamped boundary conditions is of the primary-secondary path.

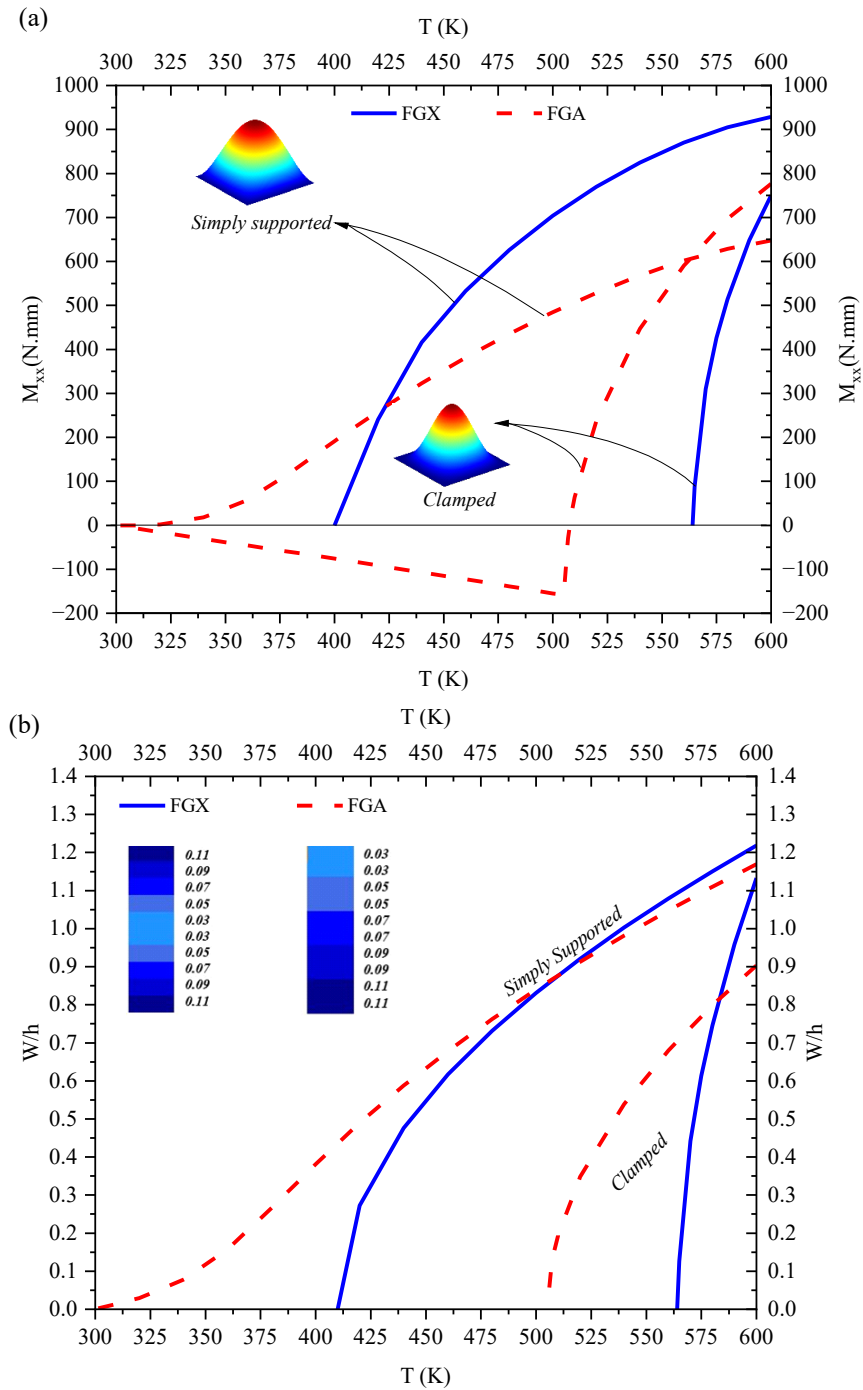


Figure 2-7 Effect of the boundary conditions of FG-GRC laminated plates subjected to a uniform temperature rise on: (a) Thermal postbuckling deflection and (b) Variation of the bending moment at the center of the plates

2.4.2.2. Thermal stability analysis of GRC laminated plate with an embedded delamination zone

The influence of the clamped and simply-supported boundary conditions on the nonlinear thermal equilibrium paths of the GRC laminated plate ($L_1/b_1 = 1, L_1/h = 40$) with a single circular embedded delamination zone reinforced by various types of functionally graded and uniform graphene sheets are illustrated in Figs 2.8 and 2.9, respectively. The ratio of the delamination area (A_D) to the total area of the plate (A) is 0.25 and the thickness ratio of the sublaminates (h_s) to the total thickness of the plate (h) is 0.2. As indicated, an increase in temperature leads to the local buckling of the top sublaminates during the initial thermal loading phases. This phenomenon occurs because the top sublaminates are thinner than the bottom baselaminates and have a lower graphene volume fraction compared to the thicker segment, resulting in reduced flexural rigidity and compressive strength. Therefore, the postbuckling response of the top sublaminates is restrained by the bottom baselaminates for further lateral deflection. Regardless of the boundary condition types and graphene sheet distributions, the negative out-of-plane displacement of the baselaminates grows as the temperature rises, and this thicker segment pulls the top sublaminates towards the negative direction of Z during its deflection. For instance, in Fig 2.8, by increasing the temperature up to $T = 430$ K, the deflection of the top sublaminates and bottom baselaminates of the FG-X plate increases along the positive and negative directions of Z , respectively, which is referred to as mixed-mode buckling. After $T = 430$ K, the deflection of the thicker segment of the FG-X laminated plate further increases in the negative direction and pulls down the top sublaminates.

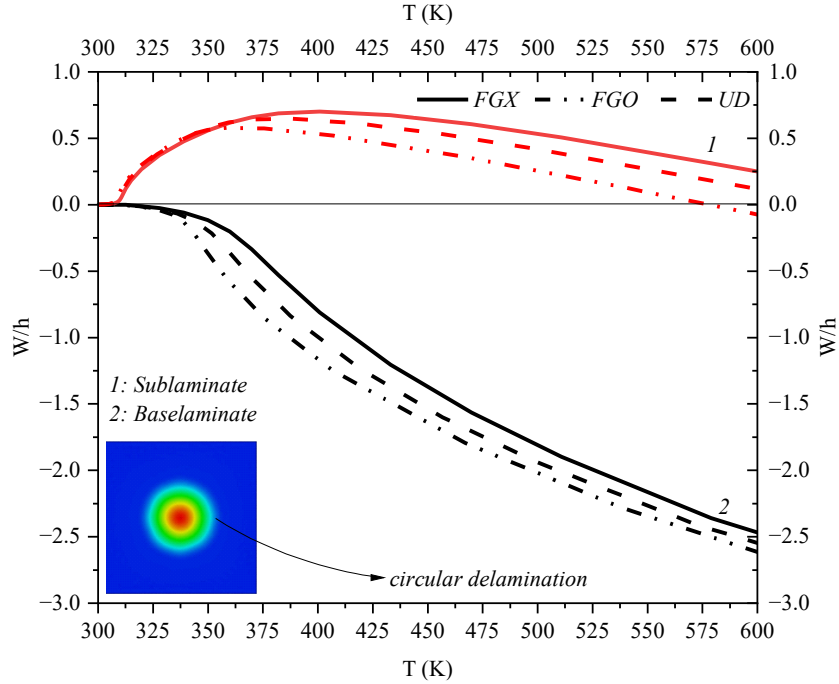


Figure 2-8 The influence of graphene reinforcement distribution on the thermal equilibrium paths of FG-GRC laminated plates with embedded circular delamination, $AD/A=0.25$, $h_s/h = 0.2$, CCCC

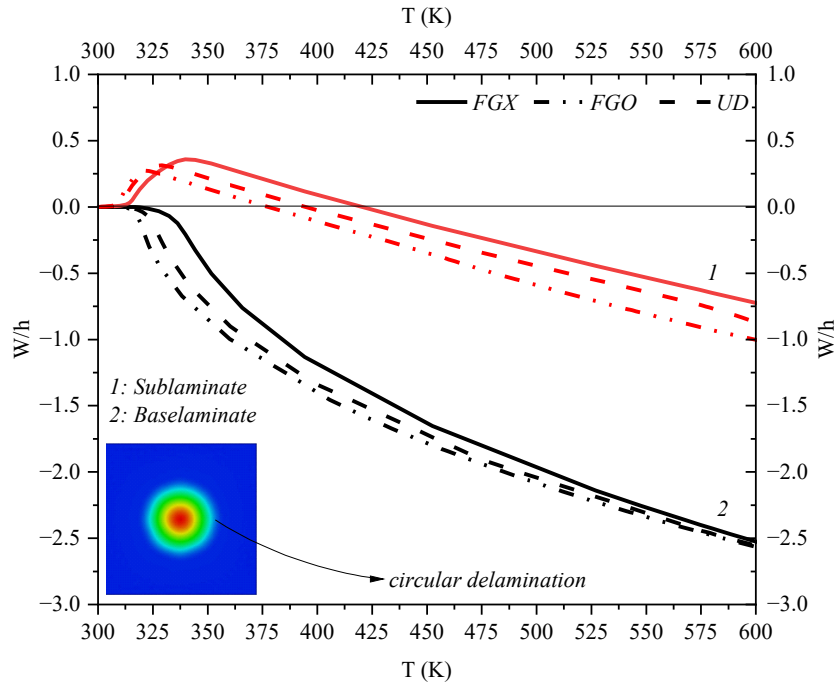


Figure 2-9 The influence of graphene reinforcement distribution on the thermal equilibrium paths of FG-GRC laminated plates with embedded circular delamination, $AD/A=0.25$, $h_s/h = 0.2$, SSSS

The nonlinear thermal responses of the FG-A laminated plate as an asymmetric graphene distribution pattern, containing an embedded circular delamination zone are compared in Fig 2.10 for different boundary conditions. In clamped boundary condition, the top sublamine and bottom baselamine deflect in opposite directions to create a mixed-mode buckling similar to those of plates with symmetric graphene dispersion patterns discussed in Fig 2.8. However, under the simply supported boundary condition, the out-of-plane displacements of the top sublamine and bottom baselamine are identical from the initial step of thermal loading until $T = 600$ K and are alongside the negative direction of Z . We should note that in this case the penalty constraint was considered across the delamination zone to prevent the occurrence of unacceptable physical penetration of sublamine and baselamine. The stiffness of the virtual springs used in this case is $K = 500 \text{ N/mm}^3$. According to the reasons stated about Fig 2.7, the thermal postbuckling deflection of the FG-A delaminated plate with clamped boundary conditions is primary-secondary and has a bifurcation point at approximately 350 K temperature for its bottom baselamine. However, the thermal postbuckling equilibrium path for the same plate with simply-supported boundary conditions is unique.

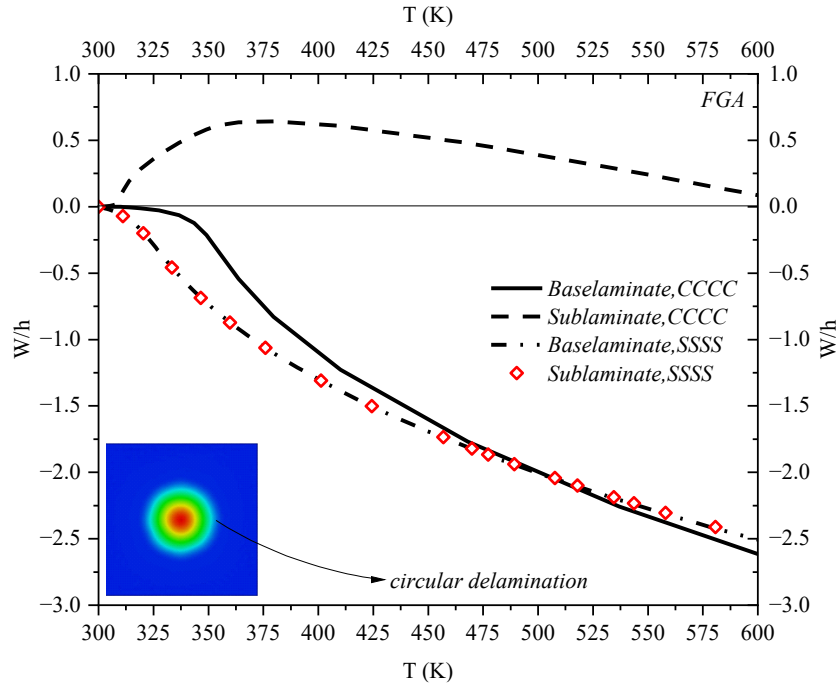


Figure 2-10 Influence of clamped and simply-supported boundary conditions on the thermal equilibrium paths of FGA laminated plates with embedded circular delamination, $AD/A=0.25$, $h_s/h = 0.2$

Figure 2.11 displays the mixed-mode buckling phenomenon of a composite plate. The plate includes a circular embedded delamination and a distribution pattern of FG-X graphene that has been optimized to boost its compressive strength. The graph reveals that, at a temperature of 620 K, the entire plate experiences a negative deflection. However, the top sublaminate deflects locally in the opposite direction to that of the baselaminate.

Figures 2.12 and 2.13 indicate the contour of deflection variation and normal stress distribution across the top and bottom surfaces of the FG-X delaminated plate at various thermal loading levels. Although the loading and boundary conditions through the X and Y in-plane directions of the plate are symmetric, the presence of near-surface embedded circular delaminations can result in a significant difference in the postbuckling behavior of various segments of the FG-GRC laminated plate, including the top sublaminate and bottom baselaminate. As shown in Fig 2.11, the FG-GRC laminated plate with a circular embedded delamination experiences mixed-mode buckling during

the postbuckling phase. This means that the bottom baselaminate deflects downward by the increase of temperature, while the top sublamine has an opposite out-of-plane displacement, resulting in different stress distributions through the top and bottom surfaces of the FG-GRC laminated plate. As illustrated in Fig 2.13, the top surface is under the compressive stress, except for the top sublamine, which is locally subjected to tensile stress. For example, at the maximum temperature, $T=600$ K, the average compressive stress at the top surface is approximately -1500 MPa, while the level of stress at the top sublamine is roughly 800 MPa. However, the entire of the bottom baselamine undergoes the compressive stress. According to the results shown in Figs 2.8, 2.9, and 2.13, despite the fact that the FG-X graphene distribution pattern reduces the thermal postbuckling deflection of the delaminated plate, the level of normal stress increases significantly on the top and bottom surfaces which contain the highest volume fraction of graphene, exposing them to failure.

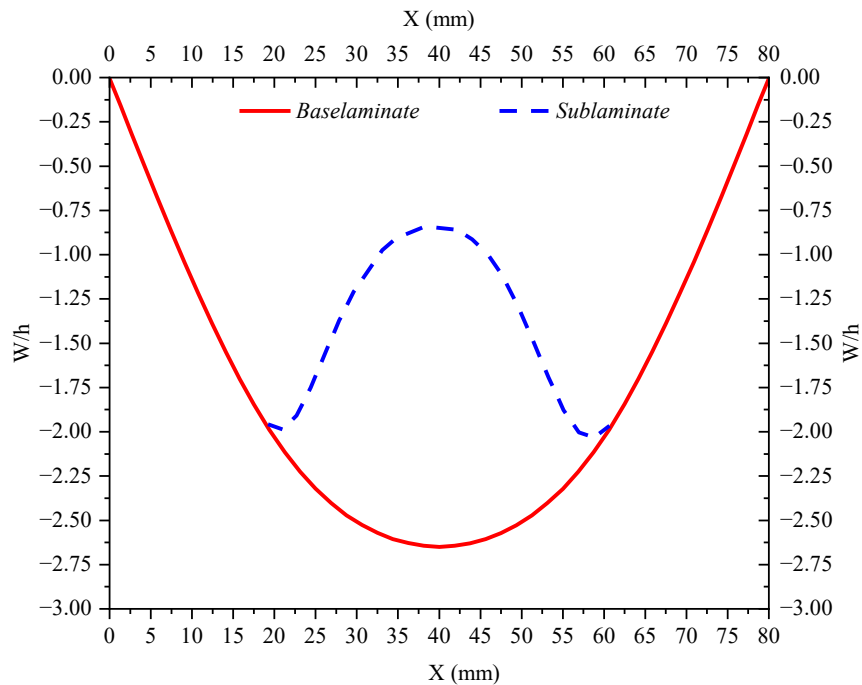


Figure 2-11 Buckled configuration of the FG-X laminated plate with a circular embedded delamination zone,

$$AD/A=0.25, h_s/h = 0.2, SSSS$$

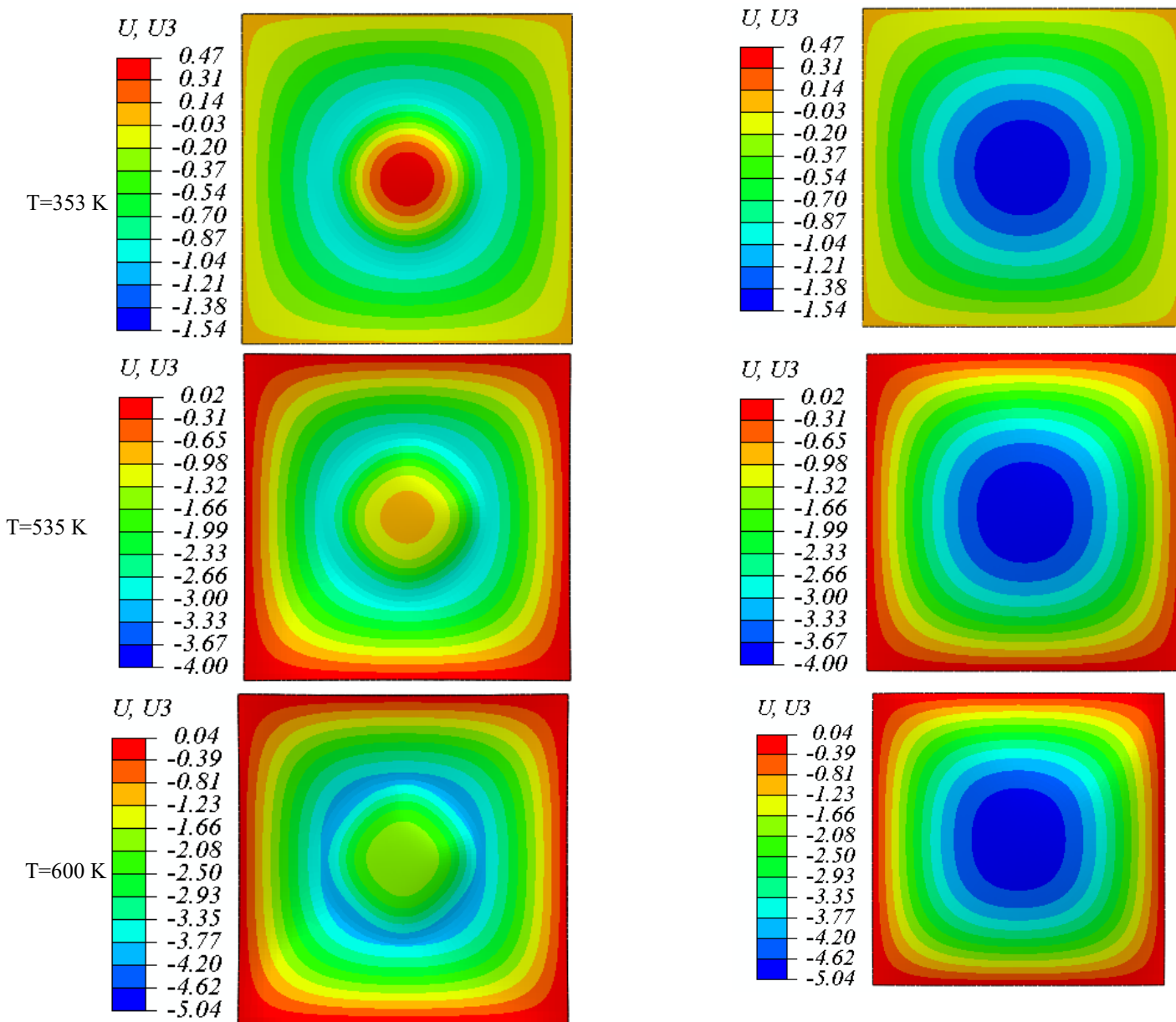


Figure 2-12 Comparison of deflection through the sublaminates and baselaminates of FG-X plate with embedded circular delamination at three different temperatures $AD/A=0.25$, SSSS. (a) Sublaminates (b) Baselaminates, deflection reported in mm

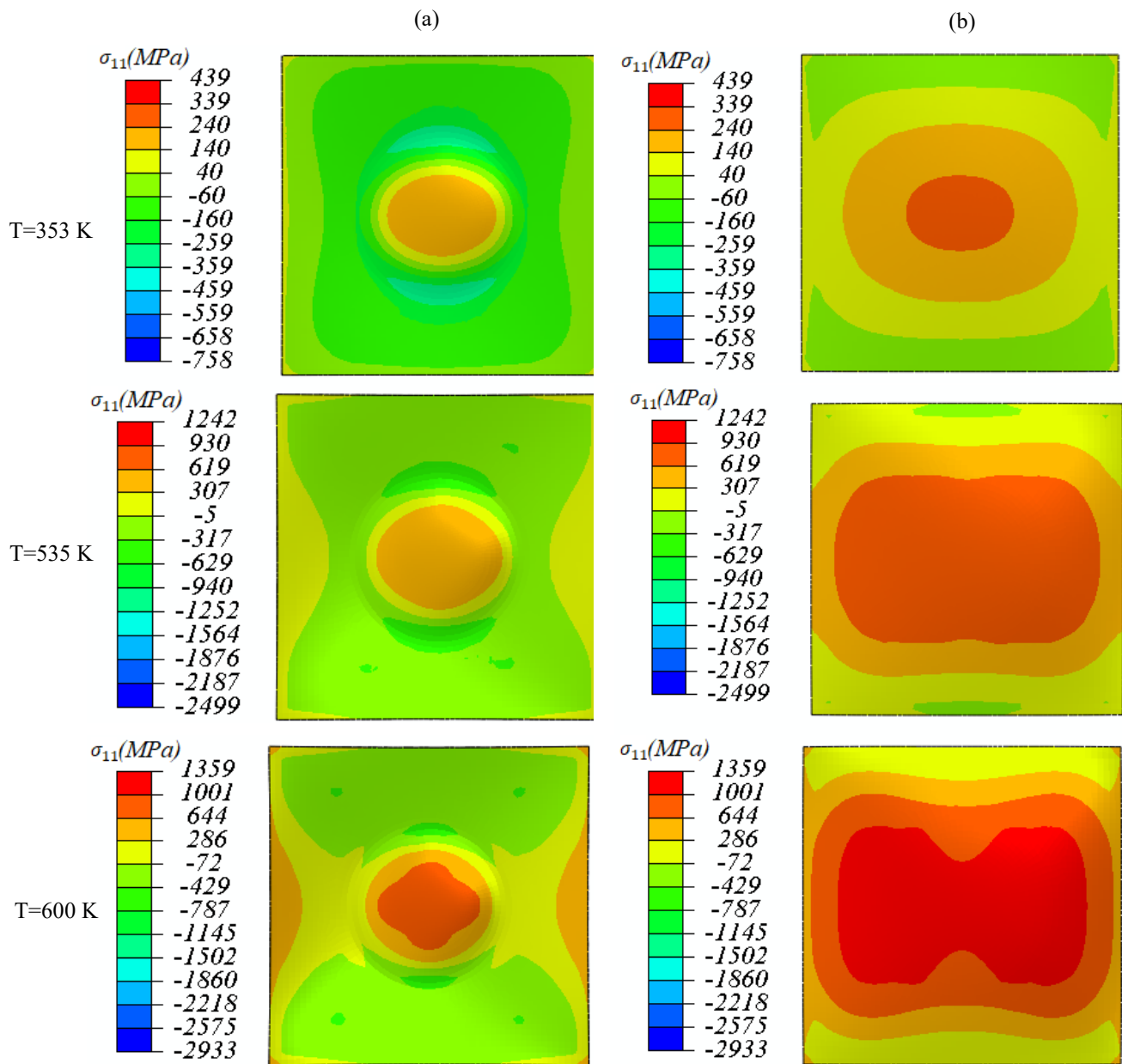


Figure 2-13 Comparison of normal Stress (σ_{11}) through the sublaminates and baselaminates of FG-X plate with embedded circular delamination at three different temperatures AD/A=0.25, SSSS. (a) Sublaminates (b) Baselaminates

To better understand the influence of the delamination zone on the nonlinear thermal responses of the GRC laminated plates, the plate ($L_1/b_1 = 1, L_1/h = 40$) is assumed to have an elliptical embedded delamination zone rather than a circular one. Figs 2.14 and 2.15 illustrate the thermal instability behavior of that GRC delaminated plate with clamped and simply-supported boundary conditions, respectively. For both types of boundary conditions, the top sublaminates and bottom baselaminates deflect in the same direction while adhering to one another and acting as one GRC laminated plate, which is known as the global buckling mode, as contrasted to the circular embedded delamination, which exhibited mixed-mode buckling under the same loading and boundary conditions. Notably, the penetration phenomenon likely occurs in the global buckling mode. To eliminate this undesirable occurrence and obtain realistic results, the penalty constraint is adopted for all cases, and the constant spring stiffness is set to $K = 500 \text{ (N/mm}^3\text{)}$. For the sake of brevity, additional results about the GRC laminated plate with an embedded elliptical delamination zone were attached to Appendix D.

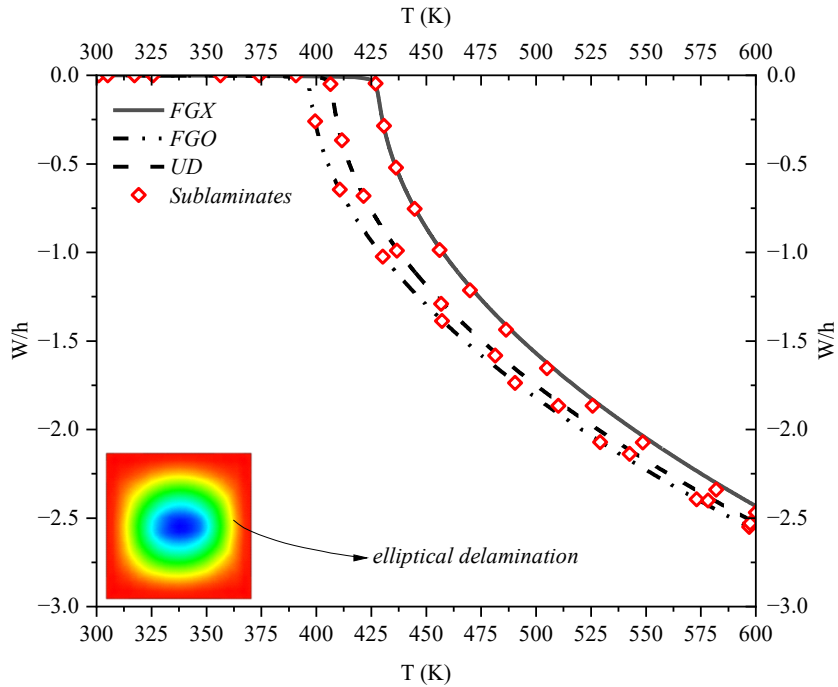


Figure 2-14 The influence of graphene reinforcement distribution on the thermal equilibrium paths of FG-GRC laminated plates with embedded elliptical delamination, $AD/A=0.25$, $h_s/h = 0.2$, CCCC

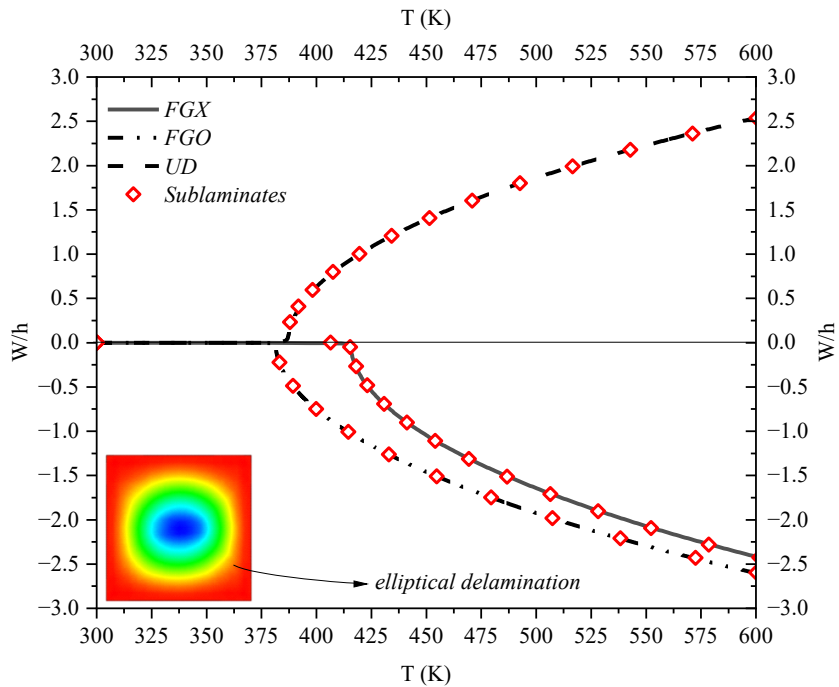


Figure 2-15 The influence of graphene reinforcement distribution on the thermal equilibrium paths of FG-GRC laminated plates with embedded elliptical delamination, $AD/A=0.25$, $h_s/h = 0.2$, SSSS

2.4.2.3. Thermomechanical analysis of GRC laminated plate with an edge delamination

Fig 2.16 demonstrates the effect of various graphene reinforcement distributions on the mechanical postbuckling deflection path of functionally graded and uniform GRC delaminated plates ($L_1/b_1 = 2, L_1/h = 20$). The edge delamination is located along one of the longitudinal edges of the plate. The lay ups sequence of the top sublaminates and bottom baselaminates are $[0,90]$ and $[0,90,0,0,90,0,90,0]$, respectively. The ratio of the delamination area (AD) to the overall area of the plate (A) is equal to 0.23. In this case, the GRC delaminated plate is just subjected to a compressive stress in the form of end-shortening strain at $T_0=300$ K. The boundary conditions applied to this delaminated plate is SSSF, as previously stated. As illustrated, for three types of graphene distribution patterns, when the value of the applied end-shortening equals to $U=0.3$, only the sublaminates buckle through the positive direction of the Z axis, while the baselaminates remain flat with no obvious out-of-plane displacement. This condition is known as local buckling mode, which happens since the baselaminates are four times thicker than the sublaminates and contain a higher volume fraction of the graphene reinforcements, resulting in greater stiffness. It can also be concluded that the postbuckling strength of the plate with FG-X distribution pattern is higher than that with FG-O and UD distribution patterns. In other words, when the same end-shortening strain is applied to the plate with different graphene distributions, the sublaminates deflection of the FG-X plate is less than that of the FG-O and UD.

Fig 2.17 also shows the thermomechanical postbuckling behavior of the same plate studied in Fig 2.16. When exposed to the constant end-shortening strain, $U=0.3$, the temperature of the functionally graded and uniform GRC delaminated plates rises uniformly. This value of the end-shortening strain causes local buckling of the GRC delaminated plate, as seen in Fig 2.16. It can be inferred from Fig 2.17 that increasing the temperature from $T_0=300$ K to $T=600$ K leads to

substantial deflection of both the sublaminates and baselaminates of the GRC plate. Moreover, the delaminated plate with FG-X graphene distribution pattern has a higher thermomechanical postbuckling strength than the other graphene distributions. Another feature of Fig 2.17 is the distinction between the sublaminates and baselaminates postbuckling equilibrium paths. The sublaminates restrained by the rest of the GRC plate are initiated to buckle at the reference temperature $T_0=300$ K due to the presence of the compressive load, constant end-shortening strain, and has a unique type of equilibrium path without any bifurcation point, however this end-shortening strain is not able to cause deflection in the thicker baselaminates at this temperature. As the temperature increases, the thicker and stiffened segment of the delaminated plate starts to deflect considerably and has a primary-secondary equilibrium path with a bifurcation point. Fig 2.17 also clearly shows that the critical buckling temperature of the baselaminates of FG-X plate is greater than the other distribution patterns. This is because the baselaminates layers in the FG-X plate are enriched with more graphene fillers, resulting in increased baselaminates stiffness. Figures 2.16 and 2.17 show the deflections of the points located at the center of the free edge.

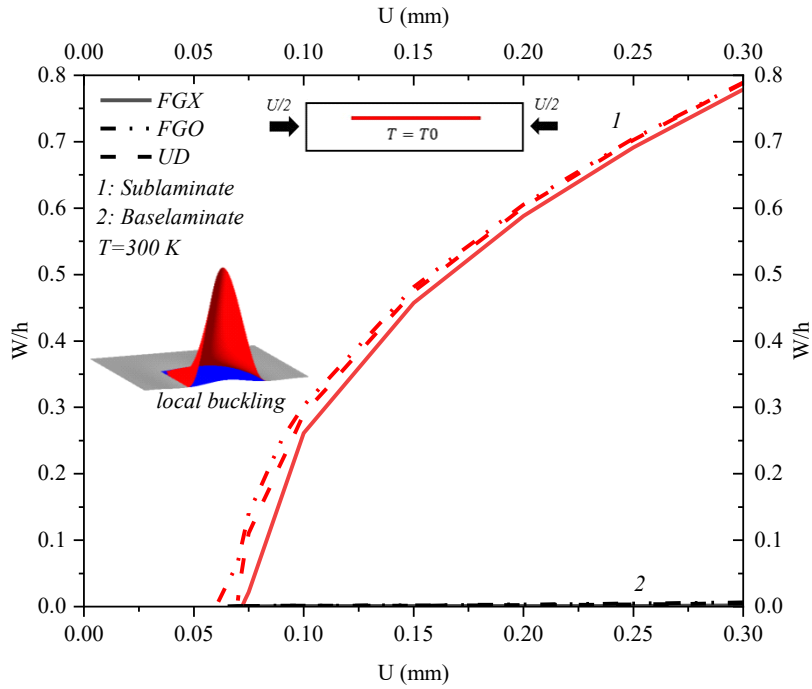


Figure 2-16 Local postbuckling equilibrium paths of FG-GRC laminated plate with single edge delamination at $T=300\text{ K}$, $AD/A=0.23$, $h_s/h = 0.2$

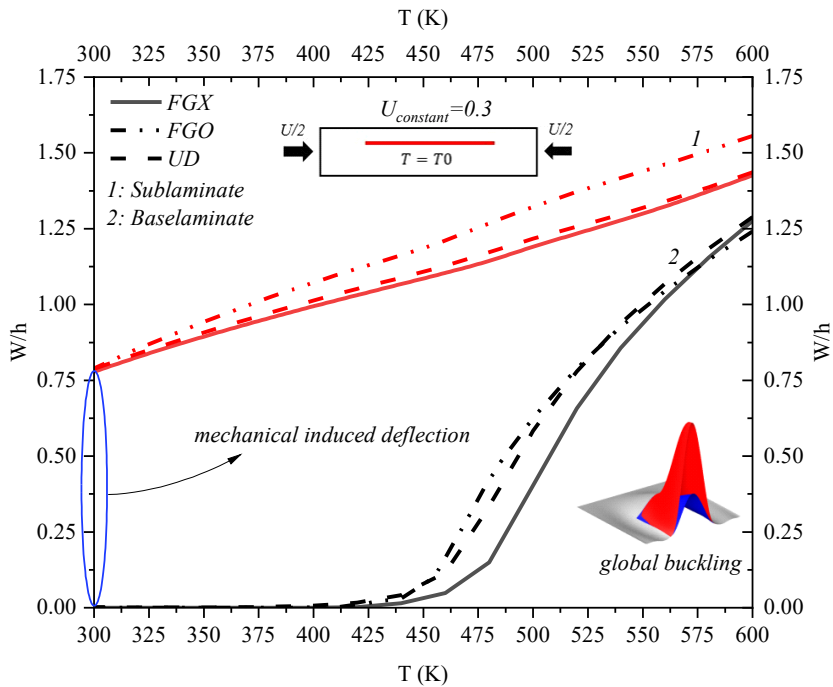


Figure 2-17 The influence of graphene reinforcement distribution on the thermomechanical equilibrium paths of FG-GRC laminated plates with single edge delamination, $AD/A=0.23$, $h_s/h = 0.2$, SSSF

The normal stress distribution at the top surfaces of the GRC delaminated plates ($L_1/b_1 = 2$, $L_1/h = 20$, $A_D/A = 0.23$, SSSF) subjected to the constant end-shortening strain ($U=0.3$) at $T_0=300$ K ($\Delta T = 0$) and $T=600$ K ($\Delta T = 300$) are shown in Fig 2.18. As illustrated, there is a noticeable difference in the normal stress distribution across the top surface of FG-X and FG-O graphene patterns when there is no thermal-induced stress at $T_0=300$ K. As previously mentioned, FG-X and FG-O possess vastly dissimilar graphene distributions, with the former's top layer containing 0.11 graphene and the latter's containing 0.03 volume percentage of graphene. Consequently, these two layers have different bending stiffness, which results in different stress levels. The FG-X delaminated plate's maximum normal stress is 350 MPa, whereas that of FG-O is approximately 180 MPa. Additionally, when $T=600$ K and the normal stress is generated due to the thermomechanical compressive loads, the highest difference in the normal stress is also observed between the FG-X and FG-O graphene distribution patterns. It is important to note that since the thermal loading and the end-shortening strain are applied simultaneously, the level of the stress in the current cases is significantly higher than those just under the end-shortening strain. The similarity of all six contours is that the maximum stress happens near the center of the free edge, where there is the greatest deflection due to the edge delamination. Moreover, the stress levels of FG-X and UD do not differ considerably.

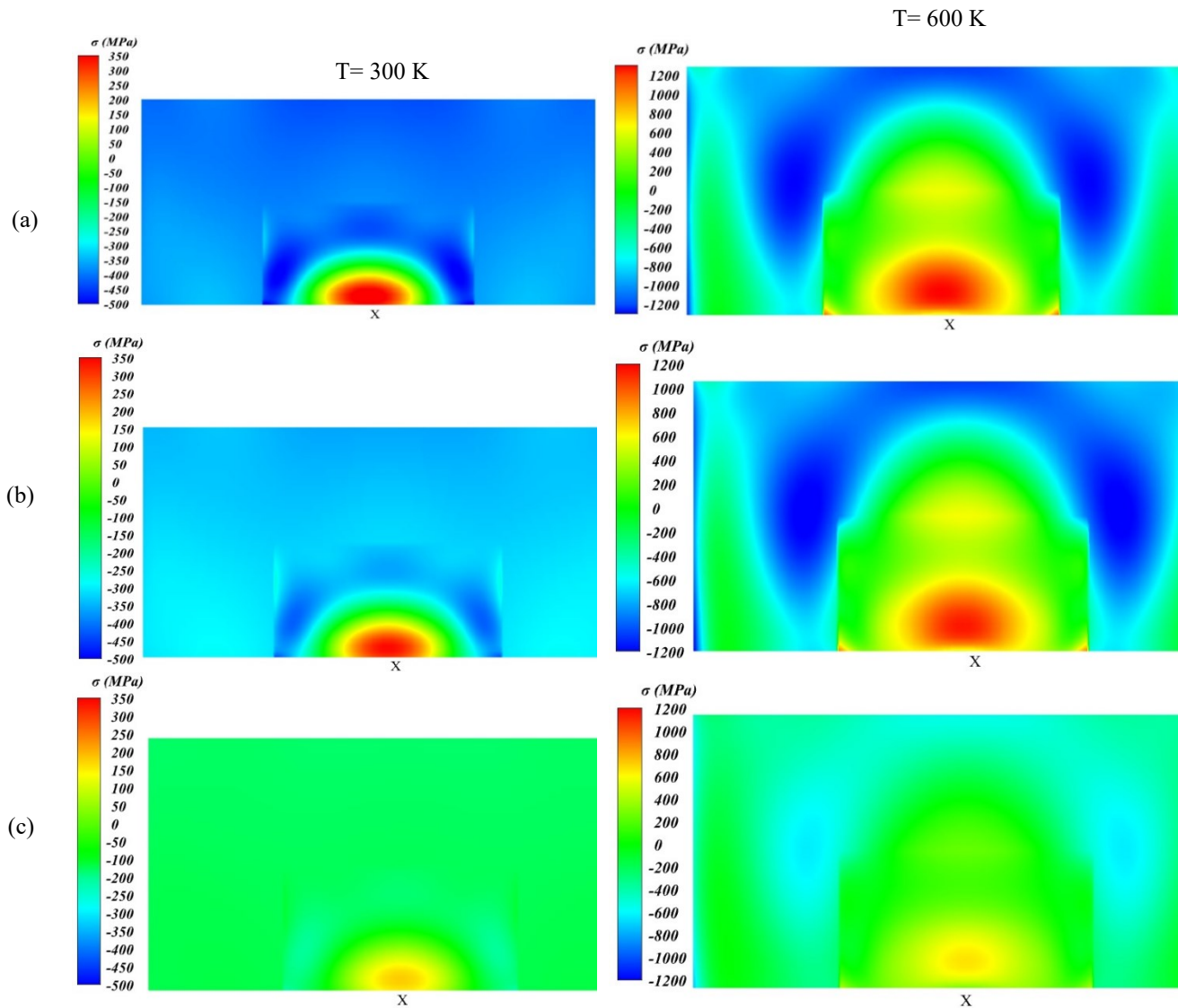


Figure 2-18 Variation of the normal stress through the top surface of the FG-GRC laminate plates with single edge delamination, $U=0.3$ (a) FG-X, (b) UD, (c) FG-O, $AD/A=0.23$, $\frac{h_s}{h} = 0.2$, SSSF

The following parametric studies aim to examine the effect of edge delamination area and depth on the nonlinear thermomechanical instability behavior of the FG-X laminated plate, the best graphene distribution in enhancing the compressive strength of the plate.

Fig 2.19 indicates the thermomechanical deflection curves for three distinct ratios of the delamination area (AD) to the plate area (A). In this figure, the delamination size influence is examined by maintaining a constant length of the delamination along the free edge of the plate, shown in Fig 2.4, while altering the width of the delamination zone for each case. It is essential to

note that the boundary and loading conditions, the layups and delamination thickness coordinate are precisely similar to those analyzed in Fig 17. Based on this assumption, at the reference temperature, the out-of-plane deflections of the baselaminates are equal to zero for all three different areas; however, the sublaminates experience varying deflections, which directly relate to the area of the delamination zone. As demonstrated in this figure, in every case, both the upper sublaminates and lower baselaminates exhibit positive deflection along the Z-axis. At each temperature, the out-of-plane displacement of the upper sublaminates (solid lines) is consistently greater than that of the lower baselaminates (dash lines). This observation confirms the absence of any penetration between these regions, thereby eliminating the need for contact constraints in these instances.

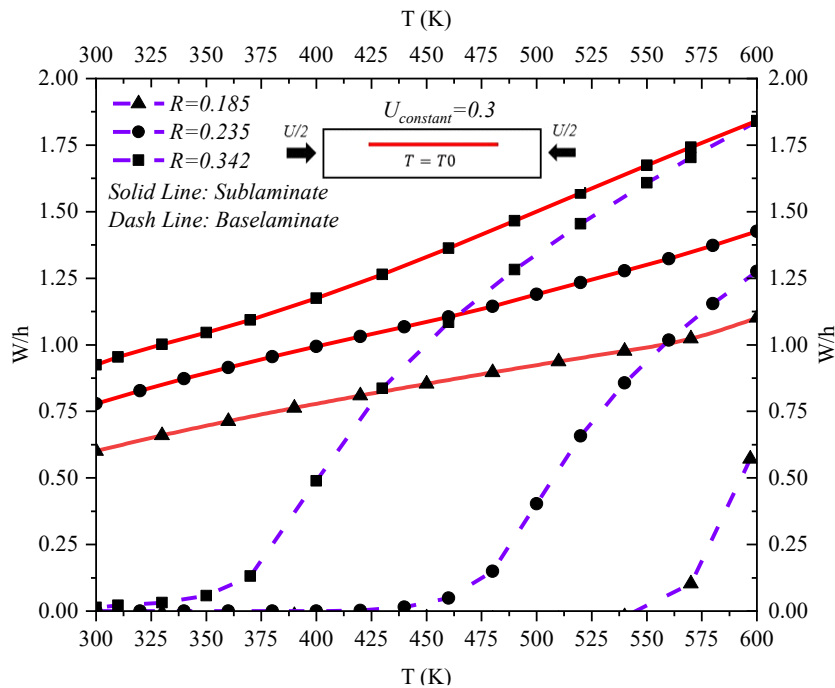


Figure 2-19 The influence of the delamination area on the thermomechanical equilibrium path of the delaminated plate with FG-X graphene distribution patterns, $R=AD/A$, $h_s/h = 0.2$

Fig 2.20 illustrates the load-temperature variation for the same FG-X delaminated plates reported in Fig 2.19. It has been discovered that the delamination area has a significant impact on

the load-carrying capacity of the FG-X plates, leading to a substantial decline in their load carrying capacity. For instance, increasing the ratio of the delamination area to the total area of the plate from 0.18 to 0.34 reduces the load carrying capacity of the FG-X delaminated plate by 68%.

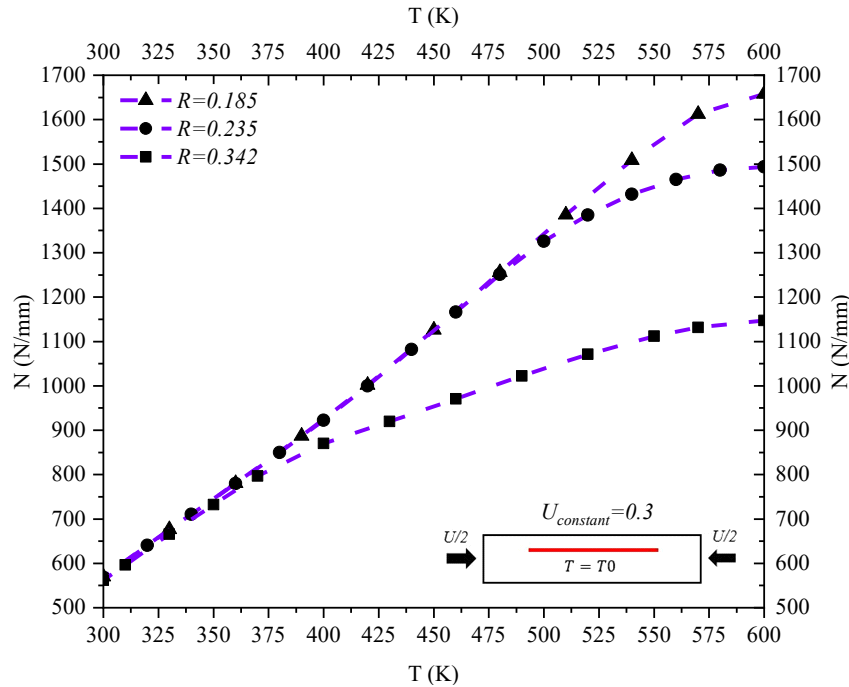


Figure 2-20 The impact of the delamination size on the load-carrying capacity of the FG-X delaminated plate subjected to both thermal and compressive loading, $R=AD/A$

Fig 2.21 compares the buckling configurations of the FG-X delaminated plates with three different delamination areas. These curves represent the deflection variations of the plate through the Y direction at $X = 0$, where $T=600$ K. It is discovered that increasing the delamination area enhances the deflections of both sublaminates and baselaminates. Furthermore, variation in the delamination area affects the deflection of the baselaminate more significantly than the sublaminates; for instance, when the ratio of the delamination area to the total plate area increases from 0.18 to 0.34, the deflection of the sublaminates increases by approximately 68%, while the deflection of the baselaminates increases three times. As a result of this influence, the distance

between the sublaminates and baselaminates at the free edge of the FG-X delaminated plate is reduced.

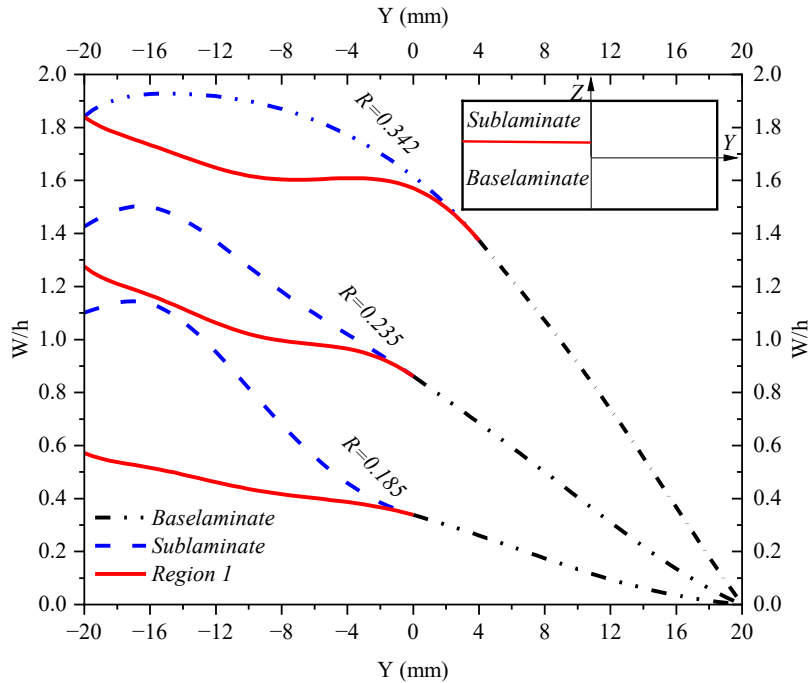
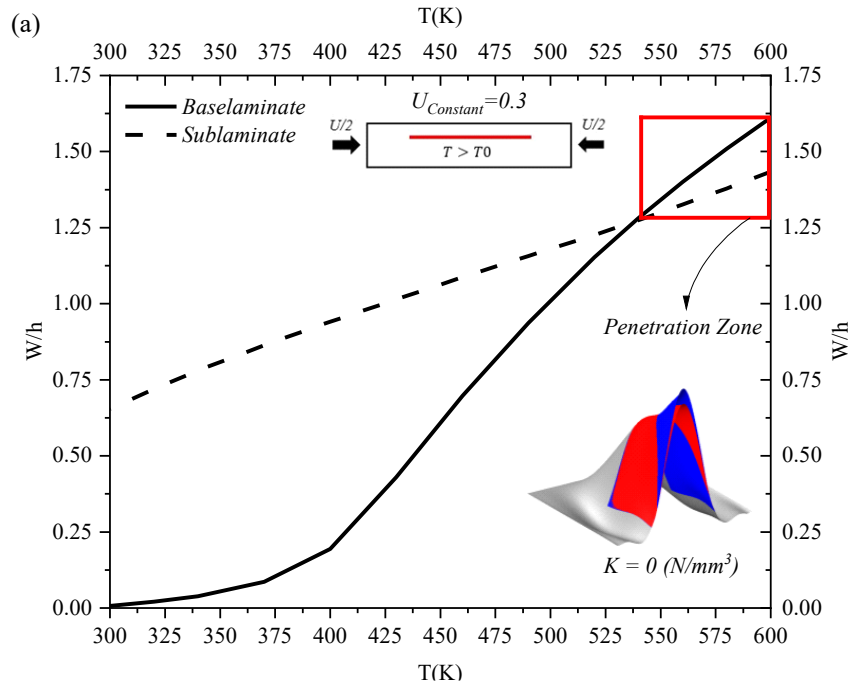


Figure 2-21 Influence of the delamination area on the out-of-plane displacement of the FG-X delaminated plate through the Y direction at $X=0$, $R=AD/A$

Fig 2.22 demonstrates the effect of the FG-X graphene sheet distribution and contact constraint on the nonlinear thermomechanical postbuckling responses of the plates with edge delamination. The ratio of the sublamine thickness (h_s) to the plate thickness (h) is equal to 0.3 ($H = \frac{h_s}{h} = 0.3$) and the lay-ups sequence of the sublamine and baselamine are $[0,90,0]$ and $[90,0,0,90,0,90,0]$, respectively. As shown in Fig 2.22(a), when a uniform temperature rise and a constant, preloaded end-shortening strain ($U=0.3$) are simultaneously applied, the local buckling of the sublamine occurs first. As the temperature increases, the baselamine also deflects substantially and the top sublamine and bottom baselamine buckle together in the same direction in the global mode of buckling. The lateral displacement of the baselamine is higher than that of the sublamine between $T=535$ K and $T=600$ K. By ignoring the contact constraint modeling in this situation,

penetration of the baselaminate and sublaminates occurs during the thermomechanical postbuckling phase, as discussed is unacceptable from the physical point of view. Therefore, the incorporation of the contact between the baselaminate and sublaminates seems necessary. As illustrated in Fig 2.22(b), when the constant stiffness of the springs is equal to $K = 700 \left(\frac{N}{mm^3} \right)$, the unacceptable penetration completely vanishes and both sublaminates and baselaminates act as a unique FG-X plate. At $T=600$ K, the global buckling mode shapes of this plate without and with contact constraint are shown in Fig 2.23. These mode shapes are related to the deflection of the sublaminates and baselaminates at the free edge of the FG-X delaminated plate.



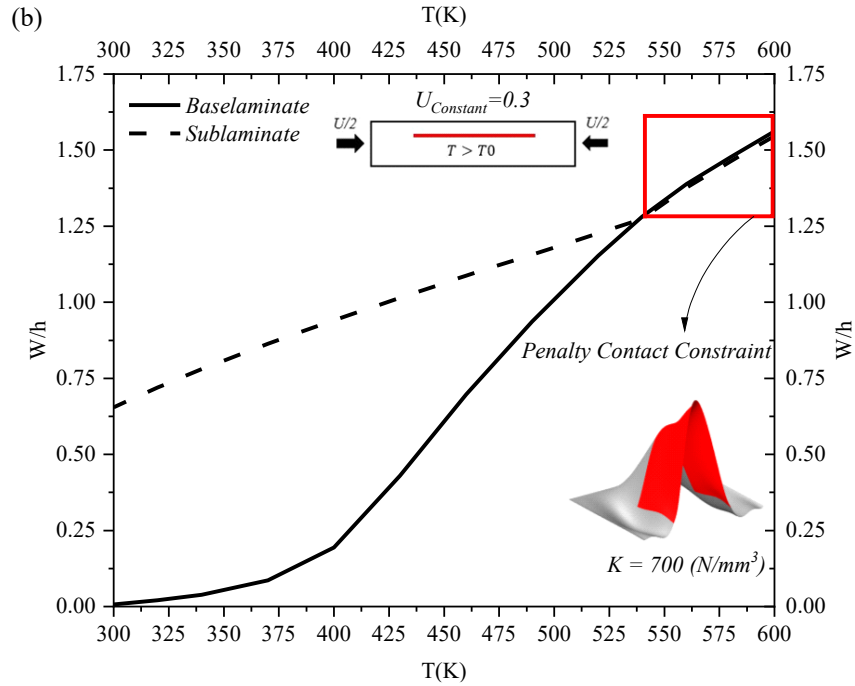
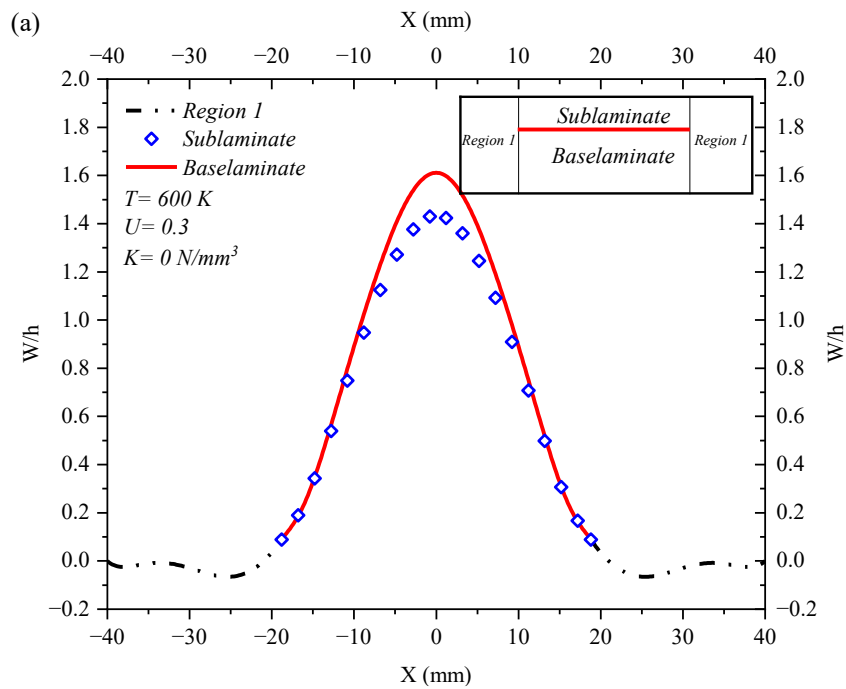


Figure 2-22 Thermomechanical equilibrium paths of the FG-X delaminated plate $R=AD/A=0.23$, SSSF. (a) without contact constraint. (b) with contact



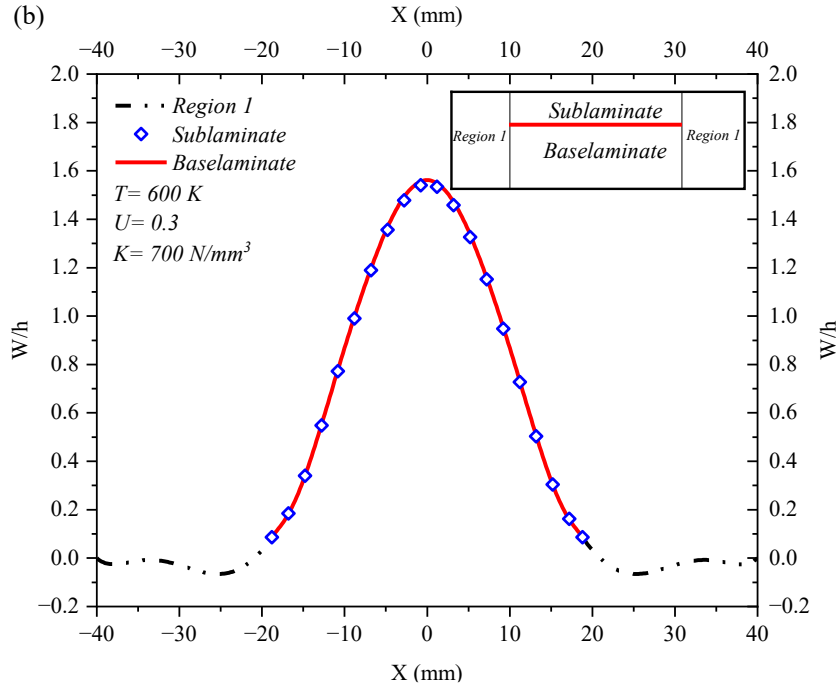
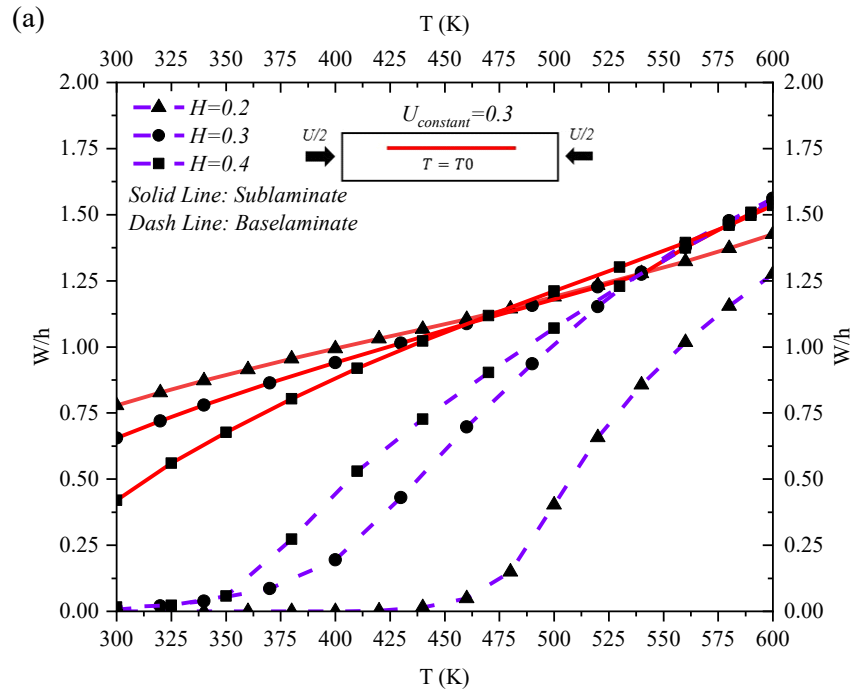


Figure 2-23 Effect of contact constraint on the free-edge's buckling mode shape of the FG-X delaminated plate

Fig 2.24(a) depicts the effect of delamination location on the thermomechanical responses of the FG-X delaminated plates subjected to the identical loading and boundary conditions as stated in Fig 2.22. As the position of the delamination gets closer to the midplane of the FG-X delaminated plate, the thickness of the sublaminates and the number of the graphene reinforced layers included in this area increase, which results in enhanced stiffness of the sublaminates. As shown in Fig 2.24, when the sublaminates thickness (h_s) to the total plate thickness (h) ratio increases from 0.2 to 0.4, its out-of-plane displacement decreases from 1.55 to 0.84 at the reference temperature, $T_0=300$ K. However, when the temperature increases, the deflection of the thicker sublaminates gradually exceeds that of the thinner sublaminates, as induced by the baselaminates deflection and taking the contact constraint into account. In contrast to the sublaminates, the thickness and stiffness of the baselaminates reduce by locating the delamination near the midplane of the FG-X plate. As a result, when the thickness ratio of the sublaminates rises from 0.2 to 0.4, the critical buckling temperature of the baselaminates is reduced from $T=460$ K to $T=350$ K.

Furthermore, Fig 2.24(b) also demonstrates that increasing the temperature affects the load-carrying capacity of the FG-X delaminated plate with thicker sublaminates more negatively than those with thinner sublaminates. These findings confirm that locating the delamination near the midplane of the plate with FG-X graphene distribution pattern makes it more vulnerable.



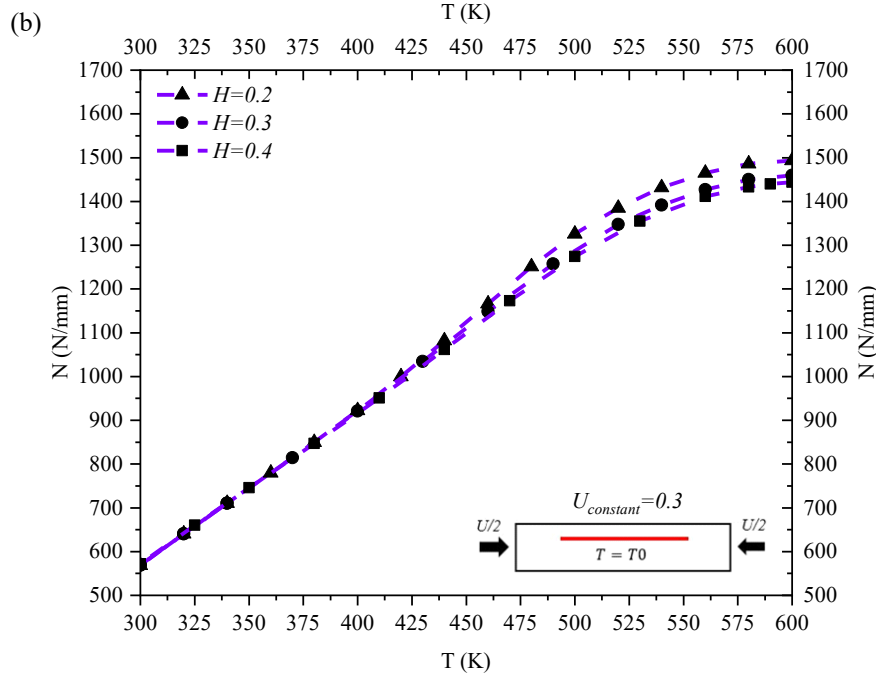


Figure 2-24 Influence of sublaminate thickness on the (a) thermomechanical instability behavior of FG-X delaminated plate. (b) Load-carrying capacity. $H=h_s/h$, SSSF

The influence of the graphene sheets' length to thickness ratio $g = \frac{a^G}{h^G}$ on the thermomechanical postbuckling behavior of the composite plate with a single edge delamination reinforced by the FG-X type of graphene distribution is shown in Fig 2.25. The delaminated plate is subjected to both end-shortening strain and thermal loading at the same time, as in the prior cases. It can be concluded that increasing the length to thickness ratio of the graphene sheets from $g=100$ to $g=1000$ while keeping their width constant enhances the postbuckling strength of the delaminated FG-X composite plate, with sublaminate and baselaminate deflections decreasing by 28% and 30%, respectively, at $T=600$ K. Furthermore, the baselaminate's critical buckling temperature rises from 420 K to 490 K. Another important point to note is that when $g=100$, the sublaminate's deflection increases continuously from $T=300$ to $T=600$, which is owing to the combined effects of the end-shortening strain and uniform temperature rise. However, From $T=300$ K to $T=480$ K, the out-of-plane displacement of the sublaminate remains relatively constant at $g=500$ and $g=1000$,

showing that the reason for the deflection is only end-shortening strain throughout this interval. This is because the delaminated plates reinforced by graphene sheets with $g=500$ and $g=1000$ has a higher postbuckling strength than those with $g=100$.

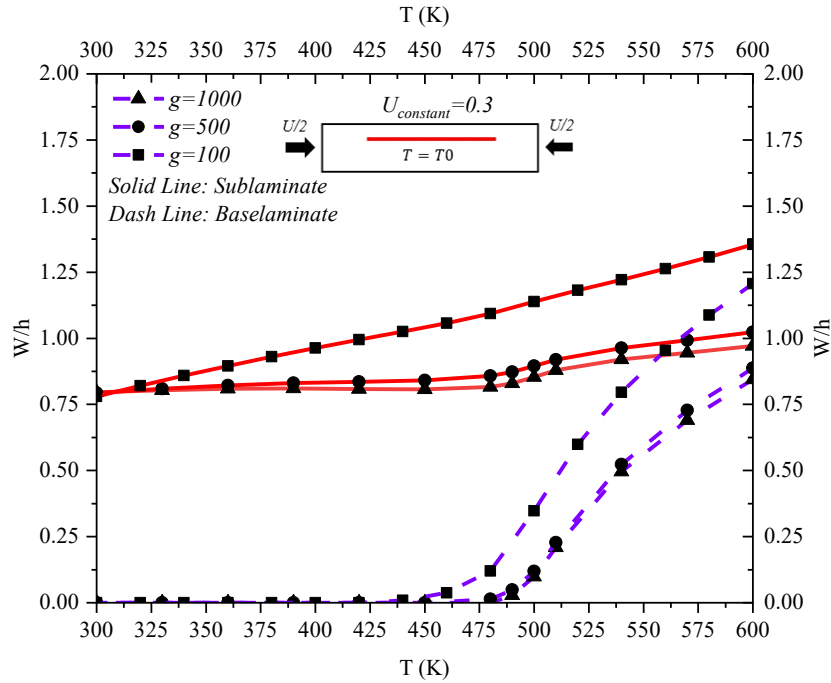


Figure 2-25 Impact of the length to thickness ratio of the graphene sheets on the postbuckling responses of the FG-X delaminated plate. $g = a^G/h_G$, SSSF

2.5. Concluding remarks

The current study analyzes the influence of the various graphene sheet distribution patterns and several types of delamination zones including embedde and edge on the non-linear thermal and thermomechanical stability responses of the FG-GRC laminated plates. A formulation is developed based on the higher order shear deformation theory and von-Karman strain–displacement relation. The governing equations are solved through the application of the minimum potential energy and the Ritz method in conjunction with the Newton–Raphson iterative procedure. The thermomechanical properties of matrix and graphene reinforcements are assumed to be temperature dependent obtained using the extended Halpin-Tsai micromechanical model.

Numerical results provide an insight into the influence of the boundary conditions, geometry of the delamination zone, size and location of the edge delamination, different graphene distribution patterns, and size of the graphene sheets on the nonlinear stability behavior of the FG-GRC delaminated plates. The numerical results elaborate on the fact that FG-GRC laminated plate designers need to carefully consider the following points in their computational simulation:

- The equilibrium path of the FG-A laminated plate as an asymmetric distribution pattern with clamped edge supports is of the bifurcation type. The behavior of this plate with simply-supported boundary conditions, on the other hand, is a unique stable equilibrium path. The inability of simply-supported edges to apply an extra moment to attenuate thermally generated moments is the reason behind this.
- Comparison of the thermal equilibrium paths of the GRC laminated plate with two different types of embedded delamination zones, circular and elliptical, reveals that under the same loading and boundary conditions, the circular embedded delamination tends to cause mixed-mode buckling, whereas the elliptical embedded delamination causes global buckling mode shape in the postbuckling regime.
- The FG-X graphene distribution pattern is the best case for increasing the postbuckling strength of the baselaminate and sublaminates.
- Although the FG-X graphene distribution pattern increases the critical buckling temperature and decreases the nonlinear thermomechanical postbuckling deflection, it generates a substantial increase in the level of stress at the top surface of the delaminated plates as compared to the FG-O, potentially increasing the risk of damage.

- The position and size of the edge delamination have an effect on the critical buckling temperature and load carrying capacity of the FG-GRC plates. Increasing the delamination area and the thickness of the sublamine deteriorate noticeably the compressive instability response of the FG-GRC plates.
- Depending on the location of the delamination zone, delaminated segments (sublamine and baselamine) may come into contact in the postbuckling regime. To acquire correct findings, a contact model must be used.
- By increasing the length-to-thickness ratio of the graphene sheets, the postbuckling strength of the FG-X delaminated plate can be improved.

3. Effect of graphene reinforcement distribution on energy release rate and vibration of thermally pre/post-buckled delaminated composite plates²

The nonlinear thermal instability responses of functionally graded graphene-reinforced composite (FG-GRC) laminated plates with single or multiple through-the-width delaminations, are investigated in the article. The possibility of delamination growth is evaluated using the three-dimensional crack tip element (3D-CTE) method, which determines the energy release rate (ERR) at the delamination edge. Furthermore, the influence of delamination configurations and the types of graphene reinforcement distribution patterns, on the free vibration of FG-GRC delaminated plates in thermally pre/post-buckled regimes is evaluated. The von Karman geometrical nonlinearity is adopted in a solution based on the layerwise third-order shear deformation theory (TSDT). The nonlinear equilibrium equations derived by the minimum total potential energy principle are solved using the Ritz method in conjunction with the Newton–Raphson iterative procedure. A three-dimensional finite element model is also developed using ABAQUS to corroborate the accuracy of the theoretical results. Parametric studies reveal that while the FGX graphene distribution pattern improves the bending stiffness of delaminated composite plates more than FGA, the ERR at the near surface delamination edge in FGX pattern is twice as high as that in FGA. This implies that the possibility of delamination propagation in FGX plates can be higher than FGA. Additionally, while the fundamental frequency of the FGX plate with and without delamination exceeds the frequency of other graphene distribution patterns at the reference temperature, its natural frequency is the lowest among all patterns in the post-buckled regime.

² A version of this chapter is published in the journal of Thin-Walled Structures, 189 (2023) 110876,

3.1. Introduction

Over the last few decades, composite laminates have been widely used in a variety of applications requiring a relatively high stiffness/strength-to-weight ratio such as aerospace and automotive structures [64]. However, these materials are susceptible to a wide variety of interlaminar flaws named delamination, which can result in severe stiffness and strength loss especially under compressive loads. Delamination may arise between any two composite plies due to several reasons such as fabrication issues, stress concentration near geometrical/ material discontinuity, and local or global buckling of plies [63]. Due to the instability of delaminated composite structures in the postbuckling phase, the probability of delamination propagation, which finally leads to the structural failure is extremely high; therefore, it is essential for the reliable design to investigate the effect of this interlaminar flaw on the postbuckling behavior and load-bearing capacity of such structures.

Many experimental, analytical, and numerical analysis have been conducted by researchers to assess the static and dynamic responses of delaminated and perfect composite structures. Herein, a comprehensive literature review is given on this topic [23,60,61,65,66,73–87]. To evaluate the critical buckling load and postbuckling load-bearing capacity of a graphite/epoxy composite plate with a single delamination zone, a compressive experimental test was conducted [23]. The primary objective of that study was to investigate the effect of geometrical parameters such as lay-up, size, and delamination location on the critical buckling load. Moreover, using finite element analysis (FEA), the nonlinear buckling and postbuckling behavior of composite laminates with two central delamination zones subjected to a uniaxial compressive load was studied by Hwang and Huang [81]. The most interesting outcome of their work was that when the shorter delamination is close to the midplane and the longer one is near to the surface, the buckling behavior of the laminate is

almost identical to that of a single long delamination; in other words, in this configuration the shorter delamination has no significant effect on the instability response of the structure.

Several semi-analytical studies have been also performed to examine the nonlinear buckling and postbuckling responses of fiber-reinforced composite laminates with various types of single and multiple delamination zones using different equivalent single layer plate theories, including the classical laminate plate theory (CLPT) [66] and the first-order shear deformation theory (FSDT) [65], additionally the layerwise theory based on the FSDT was implemented for relative thick plates [63,64]. In all of these articles the minimum total potential energy principle was applied to generate the instability equations solved based on the Ritz method. The most important conclusion derived from all these studies was that the mode of post-buckling and the related load-bearing capacity rely strongly on the size and depth location of the delaminations. This semi-analytical approach was also utilized to analyze the thermal postbuckling behavior of fiber-reinforced composite laminates with a single through-the-width [60] and embedded [61] delamination zone. It was concluded that when a composite laminate with asymmetric lay-up configurations is subjected to thermal loading, non-zero thermal moments are generated through the plate due to the asymmetric stretching-bending coupling. A simply-supported edge does not have the potential to apply an extra moment to keep the plate flat, as opposed to the clamped boundary condition, which can. For this reason, the thermal equilibrium path of the asymmetric composite laminates with simply supported edges is of the unique, whereas the response of it with clamped boundary conditions is of the primary-secondary path.

Recently a new laminate partitioning scheme was proposed to analyze the postbuckling behavior of the composite laminate with a single through-the-width delamination. The advantage of this approach is offering a better displacement consistency at the edge of the delamination zone

and providing access to the interlaminar traction [52]. Static and dynamic response of a laminated composite plate reinforced with curvilinear fibers with an embedded delamination zone were studied by Sharma [53] based on the finite element method (FEM). The most important conclusion that can be drawn from their findings was that the postbuckling deflection path is extremely sensitive to curvature, layups, and delamination features.

Notably, none of the aforementioned papers predict the delamination propagation while investigating the influence of this interlaminar flaw on the nonlinear thermal or mechanical instability behavior of laminated composite structures. However, due to the devastating effect of this phenomenon which most likely happens in the postbuckling regime, it is a great necessity to precisely estimate the possibility of delamination growth under different loading conditions, which most commonly is done by calculating the energy release rate (ERR) at the delamination edge. A brief literature review on this topic provided hereinafter [25,88–96].

The most commonly method used in papers on the postbuckling analysis of delaminated composite structures with consideration and prediction of delamination propagation was developing a two-dimensional (2D) or three-dimensional (3D) finite element models along with the virtual crack closure technique (VCCT). VCCT involves modeling a crack in the material and then applying a small virtual load to the edges of the crack. The load is gradually increased, and at each step, the energy required to close the crack is calculated. This energy is then used to determine the ERR through the delamination edge. The ERR is a crucial material property that determines the energy released when a crack propagates in a material. It is expressed as the rate at which strain energy is released per unit area of newly formed crack surface as the crack extends, and mathematically calculated as the derivative of potential energy with respect to crack length. In fracture mechanics, the ERR plays a fundamental role in governing the rate and direction of crack

propagation and is widely used to calculate the critical stress intensity factor, a measure of a material's resistance to crack propagation.

Although developing an accurate and perfect finite element model finally results in conclusive outcomes, it is computationally demanding to develop a large finite element model for most practical applications because of the need to consider and process a large number of elements and nodes. To overcome the numerical and computational limitations of the finite element models and accurately calculate the total ERR at the delamination edge, an analytical solution based on the 2D or 3D crack tip element (CTE) was presented [92,93], which operates on the basis of the near-tip forces and moments extracted from the various plate theories.

Upon conducting an extensive review of the literature, it has become evident that a significant research gap exists concerning the impact of varying distribution patterns of graphene sheet reinforcement on the thermal postbuckling response of laminated composite plates with single or multiple interlaminar flaws, delamination. While incorporating graphene reinforcements into polymeric composite laminates has been proven to enhance their stiffness and strength, the presence of delamination can significantly reduce these desirable properties. Therefore, it is crucial to evaluate which types of graphene distribution patterns can effectively mitigate the detrimental effects of delamination. In addition, the presence of one or multiple through-the-width delaminations between the arbitrary layers of a laminated composite plate can cause the plate to be segmented into multiple sublaminates across its thickness, such as top, middle, and bottom sublaminates. The number and location of delamination zones determine the number of graphene reinforced composite plies in each segment, and the volume percentage of graphene reinforcement may vary irregularly through these divided regions. This means that the distribution patterns of graphene in each sublaminate can be either symmetric or asymmetric, depending on the number

and location of delamination zones, regardless of how graphene is distributed throughout the entire thickness of the plate. As an illustration, FG-X is recognized as a symmetric distribution pattern of graphene that enhances the bending stiffness of laminated composite structures. Nonetheless, in the case of a delamination in an FG-X composite laminate, the delamination configuration may lead to asymmetric dispersion of graphene in the divided regions. Consequently, such irregularity can have substantial influence on the thermal equilibrium paths, load-bearing capacity, and types of the buckling mode shapes under different loading and boundary conditions, emphasizing the need for further investigation of these issues.

Another objective of this article is to conduct a comprehensive investigation on the distribution of ERR along the delamination edges of FG-GRC laminated plates to examine how graphene distribution can affect the delamination propagation. We identify parts of the damaged area within the composite laminate that are more susceptible to propagation under varying graphene distribution patterns and boundary conditions. An additional objective of this study is to assess the impact of various symmetric and asymmetric graphene distribution patterns in combination with distinct delamination configurations on the fundamental frequencies of thermally pre- and post-buckled FG-GRC plates.

To attain the research objectives, a layerwise theory on the basis of the third-order shear deformation theory (TSDT) is employed. The proposed method can evaluate both sublaminates local buckling and baselaminates global buckling; additionally, there are no restrictions on the type of boundary conditions that can be handled by the introduced procedure. The effect of different graphene reinforcement distributions, number and position of the delamination zones, and mechanical boundary conditions on the thermal equilibrium paths, load-bearing capacity, ERR distributions, and fundamental frequencies of the FG-GRC delaminated plates are explored.

3.2. Theoretical formulations

3.2.1. Basic parameters of the FG-GRC laminated plates

The current research considers a multilayer laminated composite plate comprised of N_L layers having a total thickness h , length L_1 , and width b_1 and between any two arbitrary layers, different kinds of delamination zones may occur. A Cartesian coordinate is defined where X and Y are in the midplane and Z defines along the upward normal direction. The origin of the reference coordinate system is in the center of the midplane as shown in Fig 2.1, in previous chapter.

The thickness of all plies is assumed to be the same. Each ply is formed from a polymeric matrix reinforced by the graphene sheets and may contain a distinct volume fraction of graphene. When the graphene volume fraction in layers varies, a piece-wise functionally graded graphene reinforced composite (FG-GRC) laminated plate is formed. In the present study, two types of graphene reinforcement layers: zigzag (referred to as 0° -ply) or armchair (referred to as 90° -ply) are considered. This article investigates eight distinct patterns of non-uniform graphene distribution, comprising of four symmetric distributions (FGX, FGX-FGX, FGO, and FGO-FGO) and four asymmetric distributions (FGA, FGA-FGA, FGV, and FGV). Table. (3.1) illustrates different lay-up configurations of the FG-GRC laminated plates, which incorporate varied graded graphene volume fractions.

Table 3-1 Lay-up arrangements of the FG-GRC laminated plates with different graded graphene distributions.

Distribution patterns	Lay-up arrangements of graphene volume fraction	Schematic distribution patterns
FGX	$[0.11,0.09,0.07,0.05,0.03]_S$	
FGX-FGX	$[0.09,0.07,0.03,0.07,0.09]_S$	
FGO	$[0.03,0.05,0.07,0.09,0.11]_S$	
FGO-FGO	$[0.05,0.07,0.11,0.07,0.05]_S$	
FGA	$[(0.03)_2, (0.05)_2, (0.07)_2, (0.09)_2, (0.11)_2]$	
FGA-FGA	$[0.03,0.05,0.07,0.09,0.11,0.03,0.05,0.07,0.09,0.11]$	
FGV	$[(0.11)_2, (0.09)_2, (0.07)_2, (0.05)_2, (0.03)_2]$	
FGV-FGV	$[0.11,0.09,0.07,0.05,0.03,0.11,0.09,0.07,0.05,0.03]$	

In Table. (3.1) the color-coded layers denote the volume fraction of graphene sheets. The darker shade of blue represents the layers with the highest graphene volume fraction (0.11), while the lighter shade of blue indicates the layers with the lowest volume percentage of graphene sheets (0.03). Furthermore, the subscripts "2" and "s" indicate two distinct characteristics. Specifically, "2" refers to the number of layers that possess an identical volume fraction of graphene, extending from the uppermost layer to the lowermost layer. On the other hand, "s" signifies the symmetric distribution of graphene reinforcement throughout the plate's thickness.

It's important to note that the equations required to calculate the thermomechanical properties of GRCs, using the modified Halpin-Tsai mathematical model, are identical to the ones detailed in section 2.2.2.

3.3. Structural model

The general higher order shear deformation theory (GHSDT) is a theoretical model used to analyze the behavior of thin-walled structures under bending, buckling, and vibration. In GHSDT, the shear strains are assumed to vary linearly through the thickness of the plate, and the displacement field includes higher-order terms than those in conventional classical plate theories. The third order shear deformation theory (TSDT) is a simplified version of the GHSDT. In TSDT, the displacement field includes only third-order terms, and the shear strains are assumed to vary linearly through the thickness of the plate. The TSDT can accurately predict the behavior of thin-walled structures under various types of loading and boundary conditions, and it is widely used in engineering applications [67].

As stated earlier, the primary objective of this study is to determine the ERR using the 3D-CTE method, which utilizes the resultant forces and moments in the vicinity of the crack tip or delamination edge. In order to accomplish this objective, the current investigation employs an

approach by integrating the layerwise theory with the TSDT methodology. This combination provides a novel framework for analyzing laminated composite plates with single and multiple through-the-width delaminations, and accurately evaluating the forces and moments at the delamination edges. Given the layerwise theory's capacity to divide composite plates into several numerical layers along their thickness direction, it represents a valuable modeling approach for capturing interlaminar defects, including delamination and debonding [64].

The TSDT-based expression for the displacement fields of each numerical layer, as defined under the layerwise theory, in the FG-GRC laminated composite plate can be stated as follows:

$$\begin{aligned}
 u^{ij}(x, y, z, t) &= u_0^{ij}(x, y, t) + \theta_1^{ij}(z)\varphi_x^{ij}(x, y, t) + \theta_2^{ij}(z)\psi_x^{ij}(x, y, t) \\
 v^{ij}(x, y, z, t) &= v_0^{ij}(x, y, t) + \theta_1^{ij}(z)\varphi_y^{ij}(x, y, t) + \theta_2^{ij}(z)\psi_y^{ij}(x, y, t) \\
 w^{ij}(x, y, z, t) &= w_0^{ij}(x, y, t)
 \end{aligned} \tag{3-1}$$

As illustrated in Figs 3.1 and 3.2, u_0^{ij} , v_0^{ij} , and w_0^{ij} represent the displacement components defined at the midplane of the i^{th} numerical layer located at the j^{th} region; φ_x^{ij} and φ_y^{ij} are also the middle surface rotations of those regions around the Y and X axes, respectively. Additionally, ψ_x^{ij} and ψ_y^{ij} denote the higher-order terms related with Taylor series. These parameters can be written as:

$$\psi_x^{ij} = \frac{\partial w^{ij}}{\partial x}, \quad \psi_y^{ij} = \frac{\partial w^{ij}}{\partial y}, \quad \theta_1^{ij}(z) = z - \frac{4z^3}{3h^{ij^2}}, \quad \theta_2^{ij}(z) = -\frac{4z^3}{3h^{ij^2}}, \quad \varphi_x^{ij} = \frac{\partial u^{ij}}{\partial z}, \quad \varphi_y^{ij} = \frac{\partial v^{ij}}{\partial z} \tag{3-2}$$

For the sake of brevity, the von-Karman nonlinear strain–displacement and linear stress-strain relations, as well as stiffness matrix equations are given in Appendix A.

3.3.1. FG-GRC laminated plate with a single through-the-width delamination

When analyzing composite laminates with Equivalent Single Layer (ESL) theories, the discontinuous shear stress distribution at the layer interface causes a noticeable inaccuracy in

determining the critical buckling load for especially thick plates. However, in the layerwise theories, displacement fields as shown in Eq. (3.1) are defined for each individual numerical layer, incorporating discrete material and shear effects into the assumed displacement fields, resulting in a higher degree of accuracy at the expense of increased computational cost compared to the ESL.

As shown in Fig 3.1, we assume that the plate is initially divided into four separate regions due to the presence of a single through-the-width delamination situated between any two arbitrary composite layers. Regions 2 and 3 denote the top and bottom sublaminates within the delamination area, respectively. As per the layerwise theory, the next step involves dividing each region into multiple numerical layers along its thickness direction, as illustrated in Fig 3.2. The figure indicates that both regions 1 and 4 have been discretized into five numerical layers. Moreover, the top sublaminate comprises a single numerical layer, while the bottom sublaminates have been discretized into four numerical layers. Consequently, the laminated FG-GRC plate with a single delamination includes a total of fifteen numerical layers.

The number of layers required may vary based on the desired level of accuracy, and this count may either exceed or fall below the number of graphene-reinforced composite plies. It is essential to define the displacement and rotation functions at the midplane of each numerical layer, based on the TSDT. The most crucial aspect is that the displacement and rotation functions must fulfill the plate's boundary conditions and continuity conditions between any separated regions and numerical layers defined through the X and Z axis, respectively.

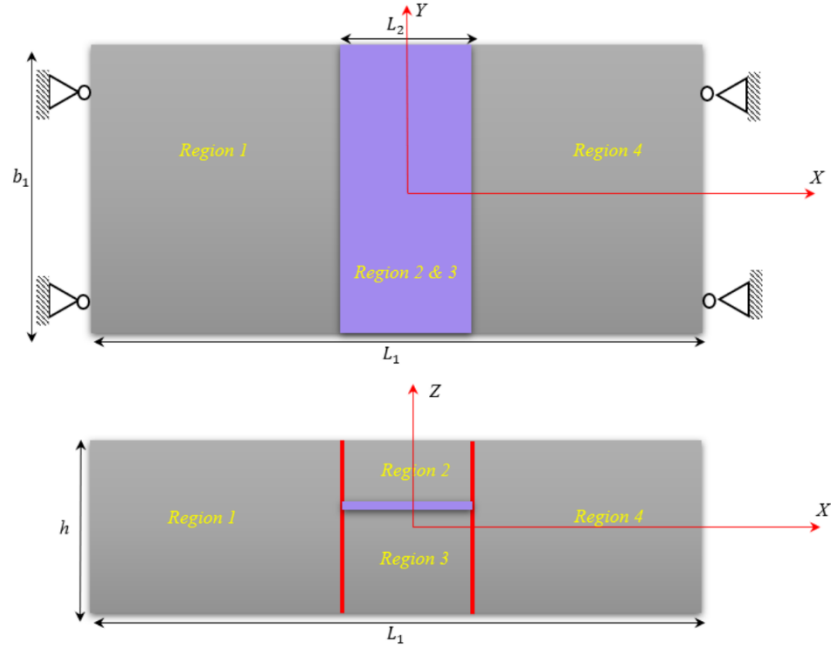


Figure 3-1 Division of the FG-GRC laminated plate with a single through-the-width delamination into four regions along the X and Z axis

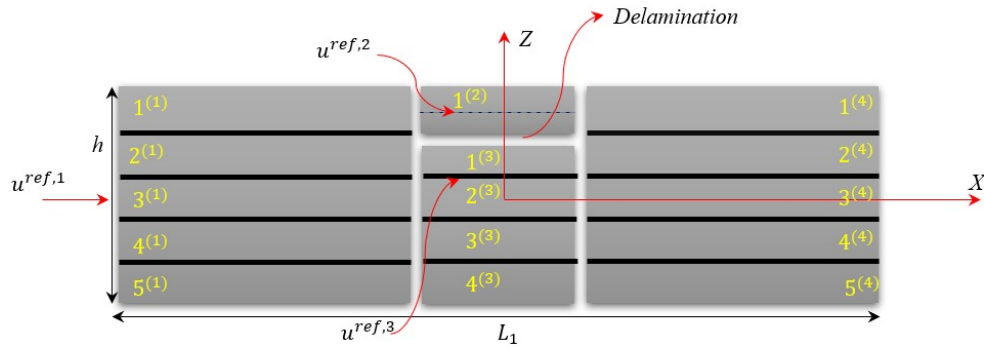


Figure 3-2 Segmentation of the FG-GRC laminated plate with a single through-the-width delamination into fifteen numerical layers along the Z axis

For the FG-GRC laminated plate with a single through-the-width delamination, the essential continuity conditions for displacement and rotation at the boundaries of several regions are expressed as:

$$(w^{i2}, u^{i2}, v^{i2})|_{x=-\frac{L_2}{2}} = (w^{i1}, u^{i1}, v^{i1})|_{x=-\frac{L_2}{2}}, \quad \{i = 1\}$$

$$(w^{i3}, u^{i3}, v^{i3})|_{x=-\frac{L_2}{2}} = (w^{(i+1)1}, u^{(i+1)1}, v^{(i+1)1})|_{x=-\frac{L_2}{2}}, \quad \{i = 1..4\}$$

$$\begin{aligned}
(w^{i2}, u^{i2}, v^{i2})|_{x=\frac{L_2}{2}} &= (w^{i4}, u^{i4}, v^{i4})|_{x=\frac{L_2}{2}}, \quad \{i = 1\} \\
(w^{i3}, u^{i3}, v^{i3})|_{x=\frac{L_2}{2}} &= (w^{(i+1)4}, u^{(i+1)4}, v^{(i+1)4})|_{x=\frac{L_2}{2}}, \quad \{i = 1..4\} \\
(\varphi_x^{i2}, \varphi_y^{i2})|_{x=-\frac{L_2}{2}} &= (\varphi_x^{i1}, \varphi_y^{i1})|_{x=-\frac{L_2}{2}}, \quad \{i = 1\} \\
(\varphi_x^{i3}, \varphi_y^{i3})|_{x=-\frac{L_2}{2}} &= (\varphi_x^{(i+1)1}, \varphi_y^{(i+1)1})|_{x=-\frac{L_2}{2}}, \quad \{i = 1..4\} \\
(\varphi_x^{i2}, \varphi_y^{i2})|_{x=\frac{L_2}{2}} &= (\varphi_x^{i4}, \varphi_y^{i4})|_{x=\frac{L_2}{2}}, \quad \{i = 1\} \\
(\varphi_x^{i3}, \varphi_y^{i3})|_{x=\frac{L_2}{2}} &= (\varphi_x^{(i+1)4}, \varphi_y^{(i+1)4})|_{x=\frac{L_2}{2}}, \quad \{i = 1..4\}
\end{aligned} \tag{3-3}$$

In Eq. (3.3), u^{ij} , v^{ij} , and w^{ij} represent the displacement fields of the i^{th} numerical layer located at the j^{th} region alongside the X, Y, and Z directions, respectively; φ_x^{ij} and φ_y^{ij} also indicate the midplane rotation of the i^{th} numerical layer around the Y and X axes.

This paper investigates two distinct types of boundary conditions for FG-GRC delaminated plates: immovable simply supported or clamped on the longitudinal ends and assumed free transverse ends (SFSF or CFCF). Table. (3.2) presents the mathematical formulas for different boundary conditions applied to the FG-GRC laminated plate with a single central through-the-width delamination. The table also shows that the only distinction between the shape functions utilized for modelling the FG-GRC delaminated plates with SFSF and CFCF boundary conditions is related to the rotational functions. In the case of CFCF, it's necessary to constrain the rotations of the midplanes of the numerical layers located at both end regions (Regions 1 and 4). The allowable polynomial displacement and rotation functions for the FG-GRC laminated plate with a single through-the-width delamination and SFSF boundary conditions are also presented below.

Table 3-2 Mathematical expressions of the boundary conditions at longitudinal ends of the FG-GRC plate with single delamination

Type of B.C	Out-of-plane displacement	In-plane displacement	Rotation
Simply Supported	$w_{ x=-\frac{L_1}{2}}^{i1} = w_{ x=-\frac{L_1}{2}}^{i4} = 0$ $i = 1..5$	$u_{ x=-\frac{L_1}{2}}^{i1} = u_{ x=-\frac{L_1}{2}}^{i4} = 0$ $i = 1..5$	-
Clamped	$w_{ x=-\frac{L_1}{2}}^{i1} = w_{ x=-\frac{L_1}{2}}^{i4} = 0$ $i = 1..5$	$u_{ x=-\frac{L_1}{2}}^{i1} = u_{ x=-\frac{L_1}{2}}^{i4} = 0$ $i = 1..5$	$\phi_{x _{x=-\frac{L_1}{2}}}^{i1} = \phi_{x _{x=-\frac{L_1}{2}}}^{i4} = 0$ $i = 1..5$

The out-of-plane displacement functions for various regions of the delaminated FG-GRC plate are mentioned below:

$$w^{11} = \sum_{m=0}^M \sum_{n=0}^N \left(x - \frac{L_1}{2}\right) \left(x + \frac{L_1}{2}\right) w_{mn}^{11} x^m y^n, \quad w^{11} = w^{i1} \quad i = 2..5$$

$$w^{12} = w^{11} + \sum_{m=0}^M \sum_{n=0}^N \left(x - \frac{L_2}{2}\right) \left(x + \frac{L_2}{2}\right) w_{mn}^{12} x^m y^n$$

$$w^{13} = w^{12} + \sum_{m=0}^M \sum_{n=0}^N \left(x - \frac{L_2}{2}\right) \left(x + \frac{L_2}{2}\right) w_{mn}^{13} x^m y^n, \quad w^{13} = w^{i3} \quad i = 2..4$$

$$w^{i1} = w^{i4}, \quad i = 1..5 \quad (3-4)$$

Eq. (3.4) stipulates that the out-of-plane displacement functions of different numerical layers placed in the same region must be identical to satisfy the out-of-plane continuity condition at their interfaces. Additionally, owing to the in-plane symmetric loading and boundary conditions, regions 1 and 4 exhibit analogous responses. As a result, their displacement and rotation functions must be identical. Given these conditions, it follows that the total quantity of unknown coefficients associated with the out-of-plane displacement of the FG-GRC laminated plate with a single delamination can be determined as $3(M + 1)(N + 1)$.

Also, in-plane displacement functions of different divided regions through the X and Y directions are mentioned in Eq. (3.5).

$$u^{ref,1} = \sum_{p=0}^P \sum_{q=0}^Q \left(x - \frac{L_1}{2}\right) \left(x + \frac{L_1}{2}\right) u_{pq}^{ref,1} x^p y^q$$

$$u_0^{11} = u^{ref,1} + \theta_1^{31} \left(\frac{h^{31}}{2}\right) \varphi_x^{31} + \theta_2^{31} \left(\frac{h^{31}}{2}\right) \psi_x^{31} + \theta_1^{21} (h^{21}) \varphi_x^{21} + \theta_2^{21} (h^{21}) \psi_x^{21} + \theta_1^{11} \left(\frac{h^{11}}{2}\right) \varphi_x^{11} + \theta_2^{11} \left(\frac{h^{11}}{2}\right) \psi_x^{11}$$

$$u_0^{21} = u^{ref,1} + \theta_1^{31} \left(\frac{h^{31}}{2}\right) \varphi_x^{31} + \theta_2^{31} \left(\frac{h^{31}}{2}\right) \psi_x^{31} + \theta_1^{21} \left(\frac{h^{21}}{2}\right) \varphi_x^{21} + \theta_2^{21} \left(\frac{h^{21}}{2}\right) \psi_x^{21}$$

$$u_0^{31} = u^{ref,1}$$

$$u_0^{41} = u^{ref,1} + \theta_1^{31} \left(-\frac{h^{31}}{2}\right) \varphi_x^{31} + \theta_2^{31} \left(-\frac{h^{31}}{2}\right) \psi_x^{31} + \theta_1^{41} \left(-\frac{h^{41}}{2}\right) \varphi_x^{41} + \theta_2^{41} \left(-\frac{h^{41}}{2}\right) \psi_x^{41}$$

$$u_0^{51} = u^{ref,1} + \theta_1^{31} \left(-\frac{h^{31}}{2}\right) \varphi_x^{31} + \theta_2^{31} \left(-\frac{h^{31}}{2}\right) \psi_x^{31} + \theta_1^{41} (-h^{41}) \varphi_x^{41} + \theta_2^{41} (-h^{41}) \psi_x^{41} + \theta_1^{51} \left(-\frac{h^{51}}{2}\right) \varphi_x^{51} \\ + \theta_2^{51} \left(-\frac{h^{51}}{2}\right) \psi_x^{51}$$

$$u^{ref,2} = u_0^{12} = u_0^{11} + \sum_{p=0}^P \sum_{q=0}^Q \left(x - \frac{L_2}{2}\right) \left(x + \frac{L_2}{2}\right) u_{pq}^{ref,2} x^p y^q$$

$$u^{ref,3} = u^{ref,1} + \theta_1^{31} \left(\frac{h^{31}}{2}\right) \varphi_x^{31} + \theta_2^{31} \left(\frac{h^{31}}{2}\right) \psi_x^{31} + \sum_{p=0}^P \sum_{q=0}^Q \left(x - \frac{L_2}{2}\right) \left(x + \frac{L_2}{2}\right) u_{pq}^{ref,3} x^p y^q$$

$$u_0^{13} = u^{ref,3} + \theta_1^{13} \left(\frac{h^{13}}{2}\right) \varphi_x^{13} + \theta_2^{13} \left(\frac{h^{13}}{2}\right) \psi_x^{13}$$

$$u_0^{23} = u^{ref,3} + \theta_1^{23} \left(-\frac{h^{23}}{2}\right) \varphi_x^{23} + \theta_2^{23} \left(-\frac{h^{23}}{2}\right) \psi_x^{23}$$

$$u_0^{33} = u^{ref,3} + \theta_1^{23} (-h^{23}) \varphi_x^{23} + \theta_2^{23} (-h^{23}) \psi_x^{23} + \theta_1^{33} \left(-\frac{h^{33}}{2}\right) \varphi_x^{33} + \theta_2^{33} \left(-\frac{h^{33}}{2}\right) \psi_x^{33}$$

$$u_0^{43} = u^{ref,3} + \theta_1^{23} (-h^{23}) \varphi_x^{23} + \theta_2^{23} (-h^{23}) \psi_x^{23} + \theta_1^{33} (-h^{33}) \varphi_x^{33} + \theta_2^{33} (-h^{33}) \psi_x^{33} + \theta_1^{43} \left(-\frac{h^{43}}{2}\right) \varphi_x^{43} \\ + \theta_2^{43} \left(-\frac{h^{43}}{2}\right) \psi_x^{43}$$

$$u_0^{i4} = u_0^{i1} \quad , \quad i = 1.5$$

$$v^{ref,1} = \sum_{r=0}^R \sum_{s=0}^S v_{rs}^{ref,1} x^r y^s$$

$$v_0^{11} = v^{ref,1} + \theta_1^{31} \left(\frac{h^{31}}{2} \right) \varphi_y^{31} + \theta_2^{31} \left(\frac{h^{31}}{2} \right) \psi_y^{31} + \theta_1^{21} (h^{21}) \varphi_y^{21} + \theta_2^{21} (h^{21}) \psi_y^{21} + \theta_1^{11} \left(\frac{h^{11}}{2} \right) \varphi_y^{11} + \theta_2^{11} \left(\frac{h^{11}}{2} \right) \psi_y^{11}$$

$$v_0^{21} = v^{ref,1} + \theta_1^{31} \left(\frac{h^{31}}{2} \right) \varphi_y^{31} + \theta_2^{31} \left(\frac{h^{31}}{2} \right) \psi_y^{31} + \theta_1^{21} \left(\frac{h^{21}}{2} \right) \varphi_y^{21} + \theta_2^{21} \left(\frac{h^{21}}{2} \right) \psi_y^{21}$$

$$v_0^{31} = v^{ref,1}$$

$$v_0^{41} = v^{ref,1} + \theta_1^{31} \left(-\frac{h^{31}}{2} \right) \varphi_y^{31} + \theta_2^{31} \left(-\frac{h^{31}}{2} \right) \psi_y^{31} + \theta_1^{41} \left(-\frac{h^{41}}{2} \right) \varphi_y^{41} + \theta_2^{41} \left(-\frac{h^{41}}{2} \right) \psi_y^{41}$$

$$v_0^{51} = v^{ref,1} + \theta_1^{31} \left(-\frac{h^{31}}{2} \right) \varphi_y^{31} + \theta_2^{31} \left(-\frac{h^{31}}{2} \right) \psi_y^{31} + \theta_1^{41} (-h^{41}) \varphi_y^{41} + \theta_2^{41} (-h^{41}) \psi_y^{41} + \theta_1^{51} \left(-\frac{h^{51}}{2} \right) \varphi_y^{51} + \theta_2^{51} \left(-\frac{h^{51}}{2} \right) \psi_y^{51}$$

$$v^{ref,2} = v_0^{12} = v_0^{11} + \sum_{r=0}^R \sum_{s=0}^S \left(x - \frac{L_2}{2} \right) \left(x + \frac{L_2}{2} \right) v_{pq}^{ref,2} x^r y^s$$

$$v^{ref,3} = v^{ref,1} + \theta_1^{31} \left(\frac{h^{31}}{2} \right) \varphi_y^{31} + \theta_2^{31} \left(\frac{h^{31}}{2} \right) \psi_y^{31} + \sum_{r=0}^R \sum_{s=0}^S \left(x - \frac{L_2}{2} \right) \left(x + \frac{L_2}{2} \right) v_{pq}^{ref,3} x^r y^s$$

$$v_0^{13} = v^{ref,3} + \theta_1^{13} \left(\frac{h^{13}}{2} \right) \varphi_y^{13} + \theta_2^{13} \left(\frac{h^{13}}{2} \right) \psi_y^{13}$$

$$v_0^{23} = v^{ref,3} + \theta_1^{23} \left(-\frac{h^{23}}{2} \right) \varphi_y^{23} + \theta_2^{23} \left(-\frac{h^{23}}{2} \right) \psi_y^{23}$$

$$v_0^{33} = v^{ref,3} + \theta_1^{23} (-h^{23}) \varphi_y^{23} + \theta_2^{23} (-h^{23}) \psi_y^{23} + \theta_1^{33} \left(-\frac{h^{33}}{2} \right) \varphi_y^{33} + \theta_2^{33} \left(-\frac{h^{33}}{2} \right) \psi_y^{33}$$

$$v_0^{43} = v^{ref,3} + \theta_1^{23} (-h^{23}) \varphi_y^{23} + \theta_2^{23} (-h^{23}) \psi_y^{23} + \theta_1^{33} (-h^{33}) \varphi_y^{33} + \theta_2^{33} (-h^{33}) \psi_y^{33} + \theta_1^{43} \left(-\frac{h^{43}}{2} \right) \varphi_y^{43} + \theta_2^{43} \left(-\frac{h^{43}}{2} \right) \psi_y^{43}$$

$$v_0^{i4} = v_0^{i1} \quad , \quad i = 1.5 \tag{3-5}$$

In Eq. (3.5), h^{ij} indicates the thickness of the i^{th} numerical layer placed at the j^{th} region. As per Eq. (3.5), to meet the in-plane continuity conditions between different numerical layer interfaces, it is necessary to consider several reference values along the X and Y directions for each separated region that can be considered at any arbitrary thickness coordinate of the FG-GRC

delaminated plate without compromising the accuracy of the results. As depicted in Eq. (3.5), the in-plane displacement functions pertaining to the middle of each numerical layer should be defined based on these reference values. Therefore, the total number of unknown coefficients of the in-plane displacements are equal to $3((P + 1)(Q + 1) + (R + 1)(S + 1))$.

In addition, the midplane rotation of each numerical layers FG-GRC delaminated plates with SFSF and CFCF boundary conditions can be expressed as Eqs. (3.6) and (3.7), respectively, with considering the continuity conditions at the boundaries of different regions.

Rotational functions SFSF:

$$\varphi_x^{i1} = \sum_{j=0}^J \sum_{k=0}^K \varphi_{x_{jk}}^{i1} x^j y^k \quad , \quad i = 1..5$$

$$\varphi_x^{12} = \varphi_x^{11} + \sum_{j=0}^J \sum_{k=0}^K \left(x - \frac{L_2}{2}\right) \left(x + \frac{L_2}{2}\right) \varphi_{x_{jk}}^{12} x^j y^k$$

$$\varphi_x^{i3} = \varphi_x^{(i+1)1} + \sum_{j=0}^J \sum_{k=0}^K \left(x - \frac{L_2}{2}\right) \left(x + \frac{L_2}{2}\right) \varphi_{x_{jk}}^{i3} x^j y^k \quad , \quad i = 1..4$$

$$\varphi_x^{i4} = \varphi_x^{i1} \quad , \quad i = 1..5$$

$$\varphi_y^{i1} = \sum_{d=0}^D \sum_{t=0}^T \varphi_{y_{dt}}^{i1} x^d y^t \quad , \quad i = 1..5$$

$$\varphi_y^{12} = \varphi_y^{11} + \sum_{d=0}^D \sum_{t=0}^T \left(x - \frac{L_2}{2}\right) \left(x + \frac{L_2}{2}\right) \varphi_{y_{dt}}^{12} x^d y^t$$

$$\varphi_y^{i3} = \varphi_y^{(i+1)1} + \sum_{d=0}^D \sum_{t=0}^T \left(x - \frac{L_2}{2}\right) \left(x + \frac{L_2}{2}\right) \varphi_{y_{dt}}^{i3} x^d y^t \quad , \quad i = 1..4$$

$$\varphi_y^{i4} = \varphi_y^{i1} \quad , \quad i = 1..5 \tag{3-6}$$

Rotational functions CFCF:

$$\varphi_x^{i1} = \sum_{j=0}^J \sum_{k=0}^K \left(x - \frac{L_1}{2}\right) \left(x + \frac{L_1}{2}\right) \varphi_{xjk}^{i1} x^j y^k \quad , \quad i = 1..5$$

$$\varphi_x^{12} = \varphi_x^{11} + \sum_{j=0}^J \sum_{k=0}^K \left(x - \frac{L_2}{2}\right) \left(x + \frac{L_2}{2}\right) \varphi_{xjk}^{12} x^j y^k$$

$$\varphi_x^{i3} = \varphi_x^{(i+1)1} + \sum_{j=0}^J \sum_{k=0}^K \left(x - \frac{L_2}{2}\right) \left(x + \frac{L_2}{2}\right) \varphi_{xjk}^{i3} x^j y^k \quad , \quad i = 1..4$$

$$\varphi_x^{i4} = \varphi_x^{i1} \quad , \quad i = 1..5$$

$$\varphi_y^{i1} = \sum_{d=0}^D \sum_{t=0}^T \varphi_{ydt}^{i1} x^d y^t \quad , \quad i = 1..5$$

$$\varphi_y^{12} = \varphi_y^{11} + \sum_{d=0}^D \sum_{t=0}^T \left(x - \frac{L_2}{2}\right) \left(x + \frac{L_2}{2}\right) \varphi_{ydt}^{12} x^d y^t$$

$$\varphi_y^{i3} = \varphi_y^{(i+1)1} + \sum_{d=0}^D \sum_{t=0}^T \left(x - \frac{L_2}{2}\right) \left(x + \frac{L_2}{2}\right) \varphi_{ydt}^{i3} x^d y^t \quad , \quad i = 1..4$$

$$\varphi_y^{i4} = \varphi_y^{i1} \quad , \quad i = 1..5 \tag{3-7}$$

In the layerwise theory, independent rotation functions should be taken into account for each of the numerical layers to precisely evaluate their stress and strain distribution. According to Fig 3.2, the FG-GRC delaminated plate with a single through-the-width delamination is discretized into fifteen numerical layers. The study noted that the mechanical response of the numerical layers placed in regions 1 and 4 are equivalent as a result of the symmetric loading and boundary conditions. Consequently, it can be inferred that there exist ten layers that necessitate the consideration of independent rotations. Therefore, the total number of unknown coefficients relating to the rotational functions amounts to $10((J + 1)(K + 1) + (D + 1)(T + 1))$. In Eqs. (3.4), (3.5), (3.6), and (3.7) the second series are defined to satisfy the continuity conditions at the boundaries of several regions those arise due to the existence of delamination.

3.3.2. FG-GRC laminated plate with double through-the-width delaminations

Similar to the plate with a single delamination, the graded graphene reinforced laminated plate with two central through-the-width delaminations whose length are the same and located in different thickness coordinates has been divided into a number of layers by two different steps. Due to the presence of these interlaminar flaws, the FG-GRC laminated plate has initially been divided into five distinct regions through the X and Z directions, as depicted in Fig 3.3. It should be noted that the regions 2, 3, and 4 refer to the top, middle, and bottom sublaminates. In the second step, in order to modelling the zigzag behavior of the in-plane displacements along the thickness direction, the specified FG-GRC laminated plate should be discretized into a number of layers along the thickness direction, as shown in Fig 3.4. The figure demonstrates that both regions 1 and 5 have been discretized into five numerical layers. It is noteworthy that these regions display analogous characteristics as a result of in-plane symmetric loading and boundary conditions. Furthermore, the top sublaminate comprises a single numerical layer, while both the middle and bottom sublaminates have been partitioned into two numerical layers. Consequently, the laminated FG-GRC plate featuring two central delaminations encompasses a total of fifteen numerical layers in the through-thickness direction.

As mentioned in the preceding section, it's crucial to take into account the continuity conditions between the different regions established along the longitudinal direction of the delaminated plate.

The necessary displacement and rotation continuity conditions that must be fulfilled at the boundaries of the FG-GRC laminated plate with double delaminations are expressed in Eq. (3.8).

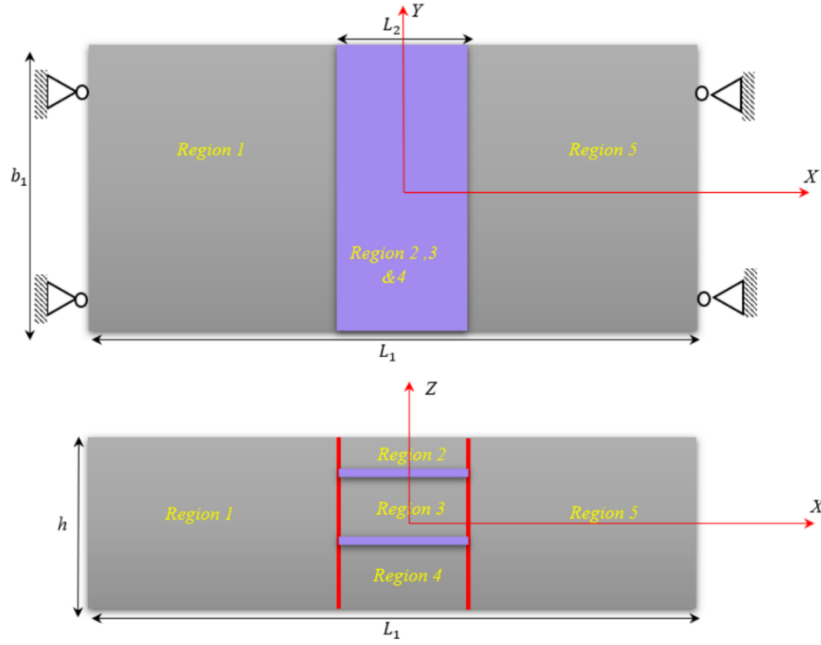


Figure 3-3 Segmentation of the FG-GRC laminated plate with two equal length through-the-width delaminations into five regions along the X axes

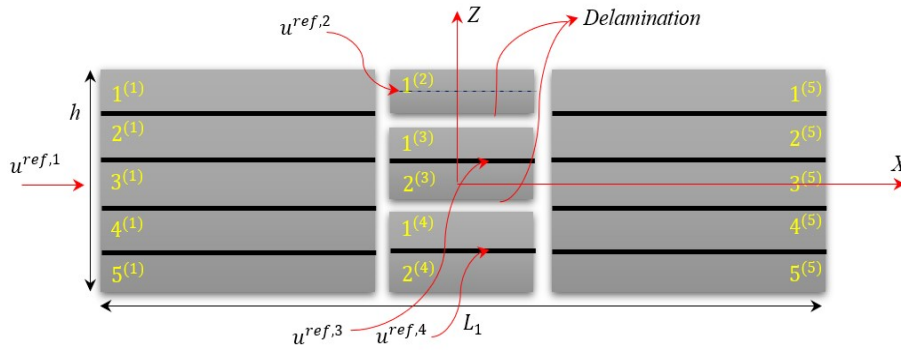


Figure 3-4 Segmentation of the FG-GRC laminated plate with multiple through-the-width delaminations into fifteen numerical layers along the Z axis

$$(w^{i2}, u^{i2}, v^{i2})|_{x=-\frac{L_2}{2}} = (w^{i1}, u^{i1}, v^{i1})|_{x=-\frac{L_2}{2}}, \quad \{i = 1\}$$

$$(w^{i3}, u^{i3}, v^{i3})|_{x=-\frac{L_2}{2}} = (w^{(i+1)1}, u^{(i+1)1}, v^{(i+1)1})|_{x=-\frac{L_2}{2}}, \quad \{i = 1..2\}$$

$$(w^{i4}, u^{i4}, v^{i4})|_{x=-\frac{L_2}{2}} = (w^{(i+3)1}, u^{(i+3)1}, v^{(i+3)1})|_{x=-\frac{L_2}{2}}, \quad \{i = 1..2\}$$

$$\begin{aligned}
(w^{i2}, u^{i2}, v^{i2})|_{x=\frac{L_2}{2}} &= (w^{i5}, u^{i5}, v^{i5})|_{x=\frac{L_2}{2}}, \quad \{i = 1 \\
(w^{i3}, u^{i3}, v^{i3})|_{x=\frac{L_2}{2}} &= (w^{(i+1)5}, u^{(i+1)5}, v^{(i+1)5})|_{x=\frac{L_2}{2}}, \quad \{i = 1..2 \\
(w^{i4}, u^{i4}, v^{i4})|_{x=\frac{L_2}{2}} &= (w^{(i+3)5}, u^{(i+3)5}, v^{(i+3)5})|_{x=\frac{L_2}{2}}, \quad \{i = 1..2 \\
(\varphi_x^{i2}, \varphi_y^{i2})|_{x=-\frac{L_2}{2}} &= (\varphi_x^{i1}, \varphi_y^{i1})|_{x=-\frac{L_2}{2}}, \quad \{i = 1 \\
(\varphi_x^{i3}, \varphi_y^{i3})|_{x=-\frac{L_2}{2}} &= (\varphi_x^{(i+1)1}, \varphi_y^{(i+1)1})|_{x=-\frac{L_2}{2}}, \quad \{i = 1..2 \\
(\varphi_x^{i4}, \varphi_y^{i4})|_{x=-\frac{L_2}{2}} &= (\varphi_x^{(i+3)1}, \varphi_y^{(i+3)1})|_{x=-\frac{L_2}{2}}, \quad \{i = 1..2 \\
(\varphi_x^{i2}, \varphi_y^{i2})|_{x=\frac{L_2}{2}} &= (\varphi_x^{i5}, \varphi_y^{i5})|_{x=\frac{L_2}{2}}, \quad \{i = 1 \\
(\varphi_x^{i3}, \varphi_y^{i3})|_{x=\frac{L_2}{2}} &= (\varphi_x^{(i+1)5}, \varphi_y^{(i+1)5})|_{x=\frac{L_2}{2}}, \quad \{i = 1..2 \\
(\varphi_x^{i4}, \varphi_y^{i4})|_{x=\frac{L_2}{2}} &= (\varphi_x^{(i+3)5}, \varphi_y^{(i+3)5})|_{x=\frac{L_2}{2}}, \quad \{i = 1..2
\end{aligned} \tag{3-8}$$

The out-of-plane displacement functions for various regions of the FG-GRC laminated plate with two central delaminations and CFCF boundary condition are mentioned below:

$$\begin{aligned}
w^{11} &= \sum_{m=0}^M \sum_{n=0}^N \left(x - \frac{L_1}{2}\right) \left(x + \frac{L_1}{2}\right) w_{mn}^{11} x^m y^n, \quad w^{11} = w^{i1} \quad i = 2..5 \\
w^{12} &= w^{11} + \sum_{m=0}^M \sum_{n=0}^N \left(x - \frac{L_2}{2}\right) \left(x + \frac{L_2}{2}\right) w_{mn}^{12} x^m y^n \\
w^{13} &= w^{21} + \sum_{m=0}^M \sum_{n=0}^N \left(x - \frac{L_2}{2}\right) \left(x + \frac{L_2}{2}\right) w_{mn}^{13} x^m y^n, \quad w^{13} = w^{23} \\
w^{14} &= w^{41} + \sum_{m=0}^M \sum_{n=0}^N \left(x - \frac{L_2}{2}\right) \left(x + \frac{L_2}{2}\right) w_{mn}^{14} x^m y^n, \quad w^{14} = w^{24} \\
w^{i1} &= w^{i5}, \quad i = 1..5
\end{aligned} \tag{3-9}$$

In this case, the total number of unknown coefficients pertaining to the out-of-plane displacement of the FG-GRC laminated plate with two central through-the-width delaminations can be calculated as $4(M + 1)(N + 1)$.

Additionally, Eq. (3.10) presents the in-plane displacement functions at the midplanes of various numerical layers, while considering the continuity conditions across interfaces.

$$u^{ref,1} = \sum_{p=0}^P \sum_{q=0}^Q \left(x - \frac{L_1}{2}\right) \left(x + \frac{L_1}{2}\right) u_{pq}^{ref,1} x^p y^q$$

$$u_0^{11} = u^{ref,1} + \theta_1^{31} \left(\frac{h^{31}}{2}\right) \varphi_x^{31} + \theta_2^{31} \left(\frac{h^{31}}{2}\right) \psi_x^{31} + \theta_1^{21}(h^{21}) \varphi_x^{21} + \theta_2^{21}(h^{21}) \psi_x^{21} + \theta_1^{11} \left(\frac{h^{11}}{2}\right) \varphi_x^{11} + \theta_2^{11} \left(\frac{h^{11}}{2}\right) \psi_x^{11}$$

$$u_0^{21} = u^{ref,1} + \theta_1^{31} \left(\frac{h^{31}}{2}\right) \varphi_x^{31} + \theta_2^{31} \left(\frac{h^{31}}{2}\right) \psi_x^{31} + \theta_1^{21} \left(\frac{h^{21}}{2}\right) \varphi_x^{21} + \theta_2^{21} \left(\frac{h^{21}}{2}\right) \psi_x^{21}$$

$$u_0^{31} = u^{ref,1}$$

$$u_0^{41} = u^{ref,1} + \theta_1^{31} \left(-\frac{h^{31}}{2}\right) \varphi_x^{31} + \theta_2^{31} \left(-\frac{h^{31}}{2}\right) \psi_x^{31} + \theta_1^{41} \left(-\frac{h^{41}}{2}\right) \varphi_x^{41} + \theta_2^{41} \left(-\frac{h^{41}}{2}\right) \psi_x^{41}$$

$$u_0^{51} = u^{ref,1} + \theta_1^{31} \left(-\frac{h^{31}}{2}\right) \varphi_x^{31} + \theta_2^{31} \left(-\frac{h^{31}}{2}\right) \psi_x^{31} + \theta_1^{41}(-h^{41}) \varphi_x^{41} + \theta_2^{41}(-h^{41}) \psi_x^{41} + \theta_1^{51} \left(-\frac{h^{51}}{2}\right) \varphi_x^{51} + \theta_2^{51} \left(-\frac{h^{51}}{2}\right) \psi_x^{51}$$

$$u^{ref,2} = u_0^{12} = u_0^{11} + \sum_{p=0}^P \sum_{q=0}^Q \left(x - \frac{L_2}{2}\right) \left(x + \frac{L_2}{2}\right) u_{pq}^{ref,2} x^p y^q$$

$$u^{ref,3} = u^{ref,1} + \theta_1^{31} \left(\frac{h^{31}}{2}\right) \varphi_x^{31} + \theta_2^{31} \left(\frac{h^{31}}{2}\right) \psi_x^{31} + \sum_{p=0}^P \sum_{q=0}^Q \left(x - \frac{L_2}{2}\right) \left(x + \frac{L_2}{2}\right) u_{pq}^{ref,3} x^p y^q$$

$$u_0^{13} = u^{ref,3} + \theta_1^{13} \left(\frac{h^{13}}{2}\right) \varphi_x^{13} + \theta_2^{13} \left(\frac{h^{13}}{2}\right) \psi_x^{13}$$

$$u_0^{23} = u^{ref,3} + \theta_1^{23} \left(-\frac{h^{23}}{2}\right) \varphi_x^{23} + \theta_2^{23} \left(-\frac{h^{23}}{2}\right) \psi_x^{23}$$

$$u^{ref,4} = u^{ref,1} + \theta_1^{31} \left(-\frac{h^{31}}{2}\right) \varphi_x^{31} + \theta_2^{31} \left(-\frac{h^{31}}{2}\right) \psi_x^{31} + \theta_1^{41}(-h^{41}) \varphi_x^{41} + \theta_2^{41}(-h^{41}) \psi_x^{41} + \sum_{p=0}^P \sum_{q=0}^Q \left(x - \frac{L_2}{2}\right) \left(x + \frac{L_2}{2}\right) u_{pq}^{ref,4} x^p y^q$$

$$u_0^{14} = u^{ref,4} + \theta_1^{14} \left(\frac{h^{14}}{2}\right) \varphi_x^{14} + \theta_2^{14} \left(\frac{h^{14}}{2}\right) \psi_x^{14}$$

$$u_0^{24} = u^{ref,4} + \theta_1^{24} \left(-\frac{h^{24}}{2} \right) \varphi_x^{24} + \theta_2^{24} \left(-\frac{h^{24}}{2} \right) \psi_x^{24}$$

$$u_0^{i5} = u_0^{i1} \quad , \quad i = 1.5$$

$$v^{ref,1} = \sum_{r=0}^R \sum_{s=0}^S v_{rs}^{ref,1} x^r y^s$$

$$v_0^{11} = v^{ref,1} + \theta_1^{31} \left(\frac{h^{31}}{2} \right) \varphi_y^{31} + \theta_2^{31} \left(\frac{h^{31}}{2} \right) \psi_y^{31} + \theta_1^{21}(h^{21}) \varphi_y^{21} + \theta_2^{21}(h^{21}) \psi_y^{21} + \theta_1^{11} \left(\frac{h^{11}}{2} \right) \varphi_y^{11} + \theta_2^{11} \left(\frac{h^{11}}{2} \right) \psi_y^{11}$$

$$v_0^{21} = v^{ref,1} + \theta_1^{31} \left(\frac{h^{31}}{2} \right) \varphi_y^{31} + \theta_2^{31} \left(\frac{h^{31}}{2} \right) \psi_y^{31} + \theta_1^{21} \left(\frac{h^{21}}{2} \right) \varphi_y^{21} + \theta_2^{21} \left(\frac{h^{21}}{2} \right) \psi_y^{21}$$

$$v_0^{31} = v^{ref,1}$$

$$v_0^{41} = v^{ref,1} + \theta_1^{31} \left(-\frac{h^{31}}{2} \right) \varphi_y^{31} + \theta_2^{31} \left(-\frac{h^{31}}{2} \right) \psi_y^{31} + \theta_1^{41} \left(-\frac{h^{41}}{2} \right) \varphi_y^{41} + \theta_2^{41} \left(-\frac{h^{41}}{2} \right) \psi_y^{41}$$

$$v_0^{51} = v^{ref,1} + \theta_1^{31} \left(-\frac{h^{31}}{2} \right) \varphi_y^{31} + \theta_2^{31} \left(-\frac{h^{31}}{2} \right) \psi_y^{31} + \theta_1^{41}(-h^{41}) \varphi_y^{41} + \theta_2^{41}(-h^{41}) \psi_y^{41} + \theta_1^{51} \left(-\frac{h^{51}}{2} \right) \varphi_y^{51} \\ + \theta_2^{51} \left(-\frac{h^{51}}{2} \right) \psi_y^{51}$$

$$v^{ref,2} = v_0^{12} = v_0^{11} + \sum_{r=0}^R \sum_{s=0}^S \left(x - \frac{L_2}{2} \right) \left(x + \frac{L_2}{2} \right) v_{pq}^{ref,2} x^p y^q$$

$$v^{ref,3} = v^{ref,1} + \theta_1^{31} \left(\frac{h^{31}}{2} \right) \varphi_y^{31} + \theta_2^{31} \left(\frac{h^{31}}{2} \right) \psi_y^{31} + \sum_{r=0}^R \sum_{s=0}^S \left(x - \frac{L_2}{2} \right) \left(x + \frac{L_2}{2} \right) v_{pq}^{ref,3} x^p y^q$$

$$v_0^{13} = v^{ref,3} + \theta_1^{13} \left(\frac{h^{13}}{2} \right) \varphi_y^{13} + \theta_2^{13} \left(\frac{h^{13}}{2} \right) \psi_y^{13}$$

$$v_0^{23} = u^{ref,3} + \theta_1^{23} \left(-\frac{h^{23}}{2} \right) \varphi_y^{23} + \theta_2^{23} \left(-\frac{h^{23}}{2} \right) \psi_y^{23}$$

$$v^{ref,4} = v^{ref,1} + \theta_1^{31} \left(-\frac{h^{31}}{2} \right) \varphi_y^{31} + \theta_2^{31} \left(-\frac{h^{31}}{2} \right) \psi_y^{31} + \theta_1^{41}(-h^{41}) \varphi_y^{41} + \theta_2^{41}(-h^{41}) \psi_y^{41} \\ + \sum_{r=0}^R \sum_{s=0}^S \left(x - \frac{L_2}{2} \right) \left(x + \frac{L_2}{2} \right) v_{pq}^{ref,4} x^p y^q$$

$$v_0^{14} = v^{ref,4} + \theta_1^{14} \left(\frac{h^{14}}{2} \right) \varphi_y^{14} + \theta_2^{14} \left(\frac{h^{14}}{2} \right) \psi_y^{14}$$

$$v_0^{24} = v^{ref,4} + \theta_1^{24} \left(-\frac{h^{24}}{2} \right) \varphi_y^{24} + \theta_2^{24} \left(-\frac{h^{24}}{2} \right) \psi_y^{24}$$

$$v_0^{i5} = v_0^{i1} \quad , \quad i = 1..5 \quad (3-10)$$

The total number of unknown coefficients associated with the in-plane displacements are equal to $4((P + 1)(Q + 1) + R + 1)(S + 1)$. In addition, the rotational functions of the midplane of each numerical regions with considering CFCF boundary condition can be found in Eq. (3.11).

$$\varphi_x^{i1} = \sum_{j=0}^J \sum_{k=0}^K \left(x - \frac{L_1}{2} \right) \left(x + \frac{L_1}{2} \right) \varphi_{xjk}^{i1} x^j y^k \quad , \quad i = 1..5$$

$$\varphi_x^{12} = \varphi_x^{11} + \sum_{j=0}^J \sum_{k=0}^K \left(x - \frac{L_2}{2} \right) \left(x + \frac{L_2}{2} \right) \varphi_{xjk}^{12} x^j y^k$$

$$\varphi_x^{13} = \varphi_x^{(i+1)1} + \sum_{j=0}^J \sum_{k=0}^K \left(x - \frac{L_2}{2} \right) \left(x + \frac{L_2}{2} \right) \varphi_{xjk}^{i3} x^j y^k \quad , \quad i = 1..2$$

$$\varphi_x^{i4} = \varphi_x^{(i+3)1} + \sum_{j=0}^J \sum_{k=0}^K \left(x - \frac{L_2}{2} \right) \left(x + \frac{L_2}{2} \right) \varphi_{xjk}^{i4} x^j y^k \quad , \quad i = 1..2$$

$$\varphi_x^{i5} = \varphi_x^{i1} \quad , \quad i = 1..5$$

$$\varphi_y^{i1} = \sum_{d=0}^D \sum_{t=0}^T \varphi_{ydt}^{i1} x^d y^t \quad , \quad i = 1..5$$

$$\varphi_y^{12} = \varphi_y^{11} + \sum_{d=0}^D \sum_{t=0}^T \left(x - \frac{L_2}{2} \right) \left(x + \frac{L_2}{2} \right) \varphi_{ydt}^{12} x^d y^t$$

$$\varphi_y^{i3} = \varphi_y^{(i+1)1} + \sum_{d=0}^D \sum_{t=0}^T \left(x - \frac{L_2}{2} \right) \left(x + \frac{L_2}{2} \right) \varphi_{ydt}^{i3} x^d y^t \quad , \quad i = 1..2$$

$$\varphi_y^{i4} = \varphi_y^{(i+3)1} + \sum_{d=0}^D \sum_{t=0}^T \left(x - \frac{L_2}{2} \right) \left(x + \frac{L_2}{2} \right) \varphi_{ydt}^{i4} x^d y^t \quad , \quad i = 1..2$$

$$\varphi_y^{i5} = \varphi_y^{i1} \quad , \quad i = 1..5 \quad (3-11)$$

The total number of unknown coefficients relating to the rotational functions amounts to $10((J + 1)(K + 1) + (D + 1)(T + 1))$.

As discussed, the total number of numerical layers established along the thickness direction of FG-GRC laminated plates with single and double through-the-width delaminations remains the same, at fifteen. Consequently, the number of required rotational functions taken into account for both types of plates is identical. However, in the latter case, owing to the presence of double delaminations, the plate has been partitioned into five distinct regions alongside the X axes, one more than the former case. This implies that the number of out-of-plane and in-plane displacement functions for the FG-GRC laminated plate with double delaminations is greater than that of the single delamination case, resulting in a higher computational cost.

3.3.3. Energy expressions for FG-GRC laminated plates with delamination

The minimal total potential energy principle is used to analyze the thermal instability response and thermally pre- and post-buckled vibration of the FG-GRC laminated plates with several delamination configurations. Using the layerwise theory, the FG-GRC delaminated plates have been discretized into multiple numerical layers, as previously mentioned. The following equation illustrates the total strain energy per unit volume (U^{Total}) of the FG-GRC laminated plate with a single through-the-width delamination obtained by summing the strain energy of each numerical layer.

$$\begin{aligned}
 U^{Total} &= \sum_{i=1}^5 U^{i1} + \sum_{i=1}^1 U^{i2} + \sum_{i=1}^4 U^{i3} + \sum_{i=1}^5 U^{i4} \\
 U^{Total} &= \left(\frac{1}{2}\right) \left[\sum_{i=1}^5 \int (\sigma_i^{(1)})^T \varepsilon_i^{(1)} dV + \sum_{i=1}^1 \int (\sigma_i^{(2)})^T \varepsilon_i^{(2)} dV + \sum_{i=1}^4 \int (\sigma_i^{(3)})^T \varepsilon_i^{(3)} dV + \sum_{i=1}^5 \int (\sigma_i^{(4)})^T \varepsilon_i^{(4)} dV \right]
 \end{aligned}
 \tag{3-12}$$

To maintain brevity, the strain energy of the first numerical layer positioned in the first region (U^{11}), illustrated in Fig 3.2, is just extended based on the mechanical and thermal strains as well as the stiffness matrixes in Eq. (3.13).

$$\begin{aligned}
U^{11} &= \int \frac{1}{2} \bar{\sigma}^T \bar{\varepsilon} dV \\
&= \frac{1}{2} \int_{-\frac{b_1}{2}}^{\frac{b_1}{2}} \int_{-\frac{L_1}{2}}^{\frac{-L_2}{2}} \left(\{\varepsilon^0\}^{11} [A]^{11} \{\varepsilon^0\}^{11T} + 2\{\varepsilon^0\}^{11} [B]^{11} \{\varepsilon^1\}^{11T} + \{\varepsilon^1\}^{11} [D]^{11} \{\varepsilon^1\}^{11T} + 2\{\varepsilon^0\}^{11} [E]^{11} \{\varepsilon^3\}^{11T} + \right. \\
&\quad \{\varepsilon^1\}^{11} [F]^{11} \{\varepsilon^3\}^{11T} + \left. \left\{ \varepsilon_{31}^{(1)} \right\} \left[H_1^{(1)} \right] \left\{ \varepsilon_{31}^{(1)} \right\}^T + \{\gamma^0\}^{11} [As]^{11} \{\gamma^0\}^{11T} + 2\{\gamma^0\}^{11} [Ds]^{11} \{\gamma^2\}^{11T} + \right. \\
&\quad \{\gamma^2\}^{11} [Fs]^{11} \{\gamma^2\}^{11T} - 2\{\varepsilon^{Th}\}^{11} [A]^{11} \{\varepsilon^0\}^{11T} - 2\{\varepsilon^{Th}\}^{11} [B]^{11} \{\varepsilon^1\}^{11T} - 2\{\varepsilon^{Th}\}^{11} [E]^{11} \{\varepsilon^3\}^{11T} + \\
&\quad \left. \{\varepsilon^{Th}\}^{11} [A]^{11} \{\varepsilon^{Th}\}^{11T} \right) \quad (3-13)
\end{aligned}$$

Similarly, the total kinetic energy (T^{total}) of the plate with a single through-the-width delamination can be expressed as follows:

$$\begin{aligned}
T^{Total} &= \sum_{i=1}^5 T^{i1} + \sum_{i=1}^1 T^{i2} + \sum_{i=1}^4 T^{i3} + \sum_{i=1}^5 T^{i4} \\
T^{Total} &= \left(\frac{1}{2} \right) \left[\sum_{i=1}^5 \int_{-\frac{b_1}{2}}^{\frac{b_1}{2}} \int_{-\frac{L_1}{2}}^{\frac{-L_2}{2}} I^{i1} \left[\left(\frac{\partial u^{i1}}{\partial t} \right)^2 + \left(\frac{\partial v^{i1}}{\partial t} \right)^2 + \left(\frac{\partial w^{i1}}{\partial t} \right)^2 \right] dx dy \right. \\
&\quad + \sum_{i=1}^1 \int_{-\frac{b_1}{2}}^{\frac{b_1}{2}} \int_{-\frac{L_2}{2}}^{\frac{L_2}{2}} I^{i2} \left[\left(\frac{\partial u^{i2}}{\partial t} \right)^2 + \left(\frac{\partial v^{i2}}{\partial t} \right)^2 + \left(\frac{\partial w^{i2}}{\partial t} \right)^2 \right] dx dy \\
&\quad + \sum_{i=1}^4 \int_{-\frac{b_1}{2}}^{\frac{b_1}{2}} \int_{-\frac{L_2}{2}}^{\frac{L_2}{2}} I^{i3} \left[\left(\frac{\partial u^{i3}}{\partial t} \right)^2 + \left(\frac{\partial v^{i3}}{\partial t} \right)^2 + \left(\frac{\partial w^{i3}}{\partial t} \right)^2 \right] dx dy \\
&\quad \left. + \sum_{i=1}^5 \int_{-\frac{b_1}{2}}^{\frac{b_1}{2}} \int_{\frac{L_2}{2}}^{\frac{L_1}{2}} I^{i4} \left[\left(\frac{\partial u^{i4}}{\partial t} \right)^2 + \left(\frac{\partial v^{i4}}{\partial t} \right)^2 + \left(\frac{\partial w^{i4}}{\partial t} \right)^2 \right] dx dy \right] \quad (3-14)
\end{aligned}$$

As an illustration, the extended format of the kinetic energy associated with the first numerical layer situated in the first region (T^{11}), shown in Fig 3.2, are written as follows:

$$\begin{aligned}
T^{11} &= \left(\frac{1}{2} \right) \int_{-\frac{b_1}{2}}^{\frac{b_1}{2}} \int_{-\frac{L_1}{2}}^{\frac{-L_2}{2}} I^{11} \left[\left(\frac{\partial u^{11}}{\partial t} \right)^2 + \left(\frac{\partial v^{11}}{\partial t} \right)^2 + \left(\frac{\partial w^{11}}{\partial t} \right)^2 \right] dx dy = \left(\frac{1}{2} \right) \int_{-\frac{b_1}{2}}^{\frac{b_1}{2}} \int_{-\frac{L_1}{2}}^{\frac{-L_2}{2}} \left[I_0^{11} \left(\frac{\partial u_0^{11}}{\partial t} \right)^2 + 2I_1^{11} \left(\frac{\partial u_0^{11}}{\partial t} \frac{\partial \varphi_x^{11}}{\partial t} \right) + \right. \\
&\quad I_2^{11} \left(\frac{\partial \varphi_x^{11}}{\partial t} \right)^2 + 2I_3^{11} \left(\frac{\partial u_0^{11}}{\partial t} \frac{\partial \psi_x^{11}}{\partial t} \right) + 2I_4^{11} \left(\frac{\partial \varphi_x^{11}}{\partial t} \frac{\partial \psi_x^{11}}{\partial t} \right) + I_5^{11} \left(\frac{\partial \psi_x^{11}}{\partial t} \right)^2 + I_0^{11} \left(\frac{\partial v_0^{11}}{\partial t} \right)^2 + 2I_1^{11} \left(\frac{\partial v_0^{11}}{\partial t} \frac{\partial \varphi_y^{11}}{\partial t} \right) + I_2^{11} \left(\frac{\partial \varphi_y^{11}}{\partial t} \right)^2 + \\
&\quad \left. 2I_3^{11} \left(\frac{\partial v_0^{11}}{\partial t} \frac{\partial \psi_y^{11}}{\partial t} \right) + 2I_4^{11} \left(\frac{\partial \varphi_y^{11}}{\partial t} \frac{\partial \psi_y^{11}}{\partial t} \right) + I_5^{11} \left(\frac{\partial \psi_y^{11}}{\partial t} \right)^2 + I_0^{11} \left(\frac{\partial w_0^{11}}{\partial t} \right)^2 \right] dx dy \quad (3-15)
\end{aligned}$$

The inertial terms are obtained through the integration of the density.

$$\{I_0^{ij} \quad I_1^{ij} \quad I_2^{ij} \quad I_3^{ij} \quad I_4^{ij} \quad I_5^{ij}\} = \int_{-\frac{h^{ij}}{2}}^{\frac{h^{ij}}{2}} \rho(z) \{1 \quad \theta_1(z) \quad \theta_1^2(z) \quad \theta_2(z) \quad \theta_1(z)\theta_2(z) \quad \theta_2^2(z)\} dz \quad (3-16)$$

A notable concern with delaminated composite structures that undergo compressive loads is the potential occurrence of a detrimental physical phenomenon known as penetration, where the sublaminates can intrude into each other. The likelihood of this phenomenon is dependent on various factors, such as the size and location of the delamination zone, the distribution pattern of graphene reinforcement, and the applied boundary conditions. In this study, the penalty constraint (61) has been used to prevent penetration violation. By establishing a restriction on the equations, this strategy results in equal displacements in the overlapped areas. To do this, various virtual linear springs are assumed throughout the contact regions, and the contact stiffness of the corresponding springs (i.e., K_f) is changed to assure the consistency of the contact region's displacements. Thus, the estimated strain energy of the assumed virtual springs might be calculated as [64]:

$$U_{contact} = \int \frac{1}{2} K_f (W^j - W^{j+1})^2 \quad (3-17)$$

In conclusion, it can be inferred that the total potential energy of the FG-GRC laminated plate with a single delamination can be expressed as follows:

$$\Pi = \left[\sum_{i=1}^5 (U^{i1} + T^{i1}) + \sum_{i=1}^1 (U^{i2} + T^{i2}) + \sum_{i=1}^4 (U^{i3} + T^{i3}) + \sum_{i=1}^5 (U^{i4} + T^{i4}) \right] + U_{contact} \quad (3-18)$$

Following this stage, the total potential energy should be minimized using the unknown displacement and rotation coefficients as shown in Eqs. (3.19) and (3.20). [60]

$$\frac{\partial \Pi}{\partial \chi} = 0 \quad (3-19)$$

where χ is the vector of unknowns.

$$\chi = \{ \sum_{j=1}^3 \sum_{p=0}^P \sum_{q=0}^Q u_{pq}^{ref,j}, \sum_{j=1}^3 \sum_{r=0}^R \sum_{s=0}^S v_{rs}^{ref,j}, \sum_{j=1}^3 \sum_{m=0}^M \sum_{n=0}^N w_{mn}^{ref,j}, (\sum_{j=1}^5 \sum_{i=0}^I \sum_{k=0}^K \varphi_{xik}^{j1} + \sum_{j=1}^1 \sum_{i=0}^I \sum_{k=0}^K \varphi_{xik}^{j2} + \sum_{j=1}^4 \sum_{i=0}^I \sum_{k=0}^K \varphi_{xik}^{j3}), (\sum_{j=1}^5 \sum_{i=0}^I \sum_{k=0}^K \varphi_{yik}^{j1} + \sum_{j=1}^1 \sum_{i=0}^I \sum_{k=0}^K \varphi_{yik}^{j2} + \sum_{j=1}^4 \sum_{i=0}^I \sum_{k=0}^K \varphi_{yik}^{j3}) \}$$

(3-20)

The Eq. (3.19) leads to the general dynamic matrix equation of the FG-GRC delaminated plate:

$$[M]\{\ddot{\chi}\} + [K(T, \chi)]\{\chi\} = \{F(T)\} \quad (3-21)$$

where $[M]$ is the mass matrix, $[K(T, \chi)]$ is the stiffness matrix; $\{\ddot{\chi}\}$ and $\{\chi\}$ are the Jacobi expanded coefficients, and $\{F(T)\}$ is the force matrices.

It is important to note that, similar to the plate with a single delamination, in the case of an FG-GRC laminated plate with two central through-the-width delaminations, the total strain energy can be determined by summing the strain energy contributions of all the numerical layers defined in accordance with the layerwise theory.

To solve Eq. (3.21), it can be assumed that the

$$\chi = \chi_s + \chi_t \quad (3-22)$$

where χ_s is the time-independent particular solution which means the incremental thermal large deflection, and χ_t is the time-dependent. Therefore, by substituting Eq. (3.22) into Eq. (3.21), two sets of system of equations can be obtained as:

$$[K(T, \chi)]\{\chi_s\} = \{F(T)\} \quad (3-23)$$

$$[M]\{\ddot{\chi}_t\} + [K(T, \chi)]\{\chi_t\} = 0 \quad (3-24)$$

Eqs. (3.23) and (3.24) relate to the investigation of thermal postbuckling and vibration in a plate that has undergone buckling because of temperature-induced changes. In addition, the subscripts 's' and 't' denote the static and dynamic displacement of the plate, respectively. The Newton-Raphson iterative procedure method is a commonly used technique to solve nonlinear system of equations in the analysis of thermal postbuckling, as described by Eq. (3.23). Once the equation has been solved and the displacement at the specified temperature load is obtained, the tangent stiffness matrix $[K(T, \chi)]$ should be updated and inserted into Eq. (3.24). This enables the

eigenvalue equation to be solved, which in turn allows for the calculation of the linear fundamental frequencies.

3.4. Determination of energy release rate (ERR) using crack tip element (CTE) method

The three-dimensional, 3D-CTE method was initially presented by Davidson [92] to analytically calculate the total energy release rate (ERR) and mode mix in terms of the plate theory force and moment resultants. In comparison to other numerical approaches, such as three-dimensional finite element analysis, one of the most noticeable advantages of the CTE methodology is its low computational cost while maintaining a high level of accuracy. In addition, this method permits the definition of a mix mode based on the assumption of linear elastic fracture mechanics in order to eliminate the oscillatory nature of the singularity. Fig 3.5 illustrates a three-dimensional section of the crack tip region. The origin of the coordinate system is assumed to be at the crack tip with respect to X and the center of the thickness with respect to Z for all plate theory investigations. The crack or delamination area is assumed lies in the $X - Y$ plane at constant Z . In CTE methodology, the most significant assumption to consider is that the length of the cracked and uncracked regions of the element should be greater than their thickness, so that various plate theories can be used to predict the deformations and strain energy.

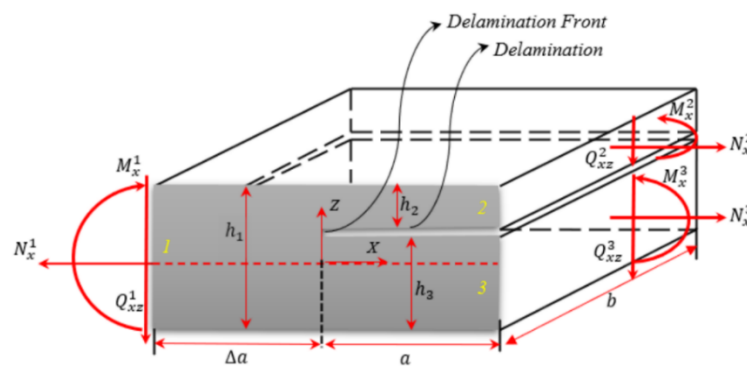


Figure 3-5 three-dimensional crack tip element

As depicted in Fig 3.5, the 3D CTE consists of three principal parts: the section located at the front of the uncracked region ($\Delta a * h_1$), referred to as 1, and two other regions located at the top and bottom of the cracked area, referred to as 2 and 3, respectively. The subsequent 3D-CTE analysis is based on the loading close to the crack tip. A double-plate model is employed to determine this loading. In other words, the problem depicted in Fig 3.5 is represented by two plates, one of which is placed at the top of the crack plane and the other at the bottom as shown in Fig 3.6.

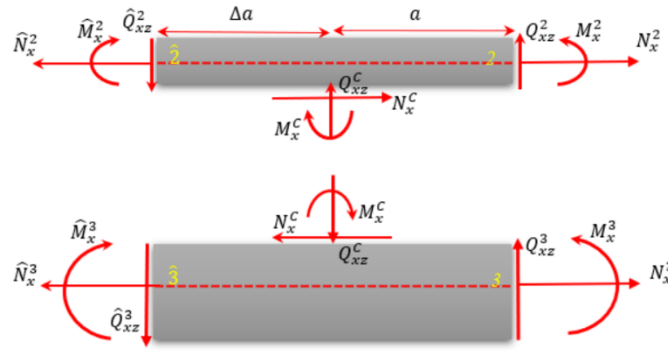


Figure 3-6 Free-body diagram for a delaminated plate above and below the crack plane

We have from the overall static equilibrium equation of the geometry shown in Fig 3.5 that

$$\begin{aligned}
 N_x^1 &= N_x^2 + N_x^3 \\
 M_x^1 &= M_x^2 + M_x^3 + N_x^2 \frac{h_2}{2} - N_x^3 \frac{h_3}{2} \\
 Q_{xz}^1 &= Q_{xz}^2 + Q_{xz}^3
 \end{aligned} \tag{3-25}$$

Based on the 3D-CTE, the ERR can be expressed in terms of the crack tip normal force Q_{xz}^C , shear force N_x^C , and bending moment M_x^C derived from the static equilibrium equations of one of the segments above or below the crack plane illustrated in Fig 3.6. Therefore, we have:

$$\begin{aligned}
 N_x^C &= N_x^2 - \hat{N}_x^2 \\
 M_x^C &= M_x^2 - \hat{M}_x^2 + N_x^C \frac{h_2}{2} \\
 Q_{xz}^C &= Q_{xz}^2 - \hat{Q}_{xz}^2
 \end{aligned} \tag{3-26}$$

As stated previously, according to the layerwise theory, a laminated plate can be subdivided along its thickness into several numerical layers. The primary purpose of using this method in this paper is to simplify evaluating the normal and shear forces as well as bending moments at regions 2 and $\hat{2}$, shown in Fig 3.6, which are equivalent to the numerical layers 1⁽¹⁾ and 1⁽²⁾ in Fig 3.2 for which independent and appropriate displacement and rotation shape functions were defined and whose unknown coefficients can be obtained at each temperature load step using the minimum total potential energy principle in conjunction with the Newton-Raphson method. Then by evaluating the stiffness matrix and strain at the mid-plane of the specified numerical layers, 1⁽¹⁾ and 1⁽²⁾, and substituting in Eq. (A-4) all the required forces and bending moments can be calculated.

Normal and shear forces as well as bending moments are all zero at the delamination front section (crack tip) before its propagation initiates. The applied load, uniform temperature rise, gradually increases until a crack extends by a small amount Δa ; in this situation, all the forces and moments have the values required to close the crack to its original length. These values are derived from the Eq. (3.25). The energy release rate G of the elements at the crack tip can be calculated using a modified virtual crack closure technique (VCCT), as shown below [93].

$$G = \frac{1}{2} (C_N (N_x^C)^2 + C_M (M_x^C)^2 + C_Q (Q_{xz}^C)^2 + 2C_{NM} N_x^C M_x^C) \quad (3-27)$$

where constants C_i are given in Eq. (3.28):

$$C_N = A_{11}^{(2)} + A_{11}^{(3)} + B_{11}^{(2)} h_2 - B_{11}^{(3)} h_3 + D_{11}^{(2)} \frac{h_2^2}{4} + D_{11}^{(3)} \frac{h_3^2}{4}$$

$$C_M = D_{11}^{(2)} + D_{11}^{(3)}$$

$$C_Q = A S_{11}^{(2)} + A S_{11}^{(3)}$$

$$C_{NM} = D_{11}^{(3)} \frac{h_3}{2} - D_{11}^{(2)} \frac{h_2}{2} - B_{11}^{(2)} - B_{11}^{(3)}$$

Where:

$$\begin{bmatrix} A'_{11} & B'_{11} \\ B'_{11} & D'_{11} \end{bmatrix} = \begin{bmatrix} A_{11} & B_{11} \\ B_{11} & D_{11} \end{bmatrix}^{-1} \quad (3-28)$$

The mode I (opening mode) and mode II (shearing mode) energy release rates could be determined by [93]:

$$G_I = \frac{1}{2} (-N_x^c \sqrt{C_N} \sin \Omega + M_x^c \sqrt{C_M} \cos (\Omega + \Gamma))^2 + \frac{1}{2} C_Q (Q_{xz}^c)^2$$

$$G_{II} = \frac{1}{2} (N_x^c \sqrt{C_N} \cos \Omega + M_x^c \sqrt{C_M} \sin (\Omega + \Gamma))^2 \quad (3-29)$$

where:

$$\Omega = \begin{cases} -24 & \zeta < -0.468 \\ 60.409\zeta + 41.738\zeta^3 & -0.468 < \zeta < 0.468 \\ 24 & \zeta > 0.468 \end{cases}, \quad \zeta = \log \left(\frac{h_3}{h_2} \right) \quad (3-30)$$

$$\text{and } \sin \Gamma = \frac{C_{NM}}{\sqrt{C_N C_M}}.$$

In contrast to the total energy release rate, as represented mathematically in Eq. (3.27), the mix mode energy release rate is determined as a function of the mode mix parameter, Ω . This parameter depends on the elastic and geometrical properties of the regions above and below the crack or delamination plane, but not on the type of loading.

3.5. Results and discussion

3.5.1. FG-GRC laminated plate with a single through-the-width delamination

The thermal equilibrium paths of FG-GRC delaminated composite square plates reinforced with four distinct, symmetric graphene distribution patterns (FGX, FGX-FGX, FGO, and FGO-FGO) are compared under SFSF and CFCF boundary conditions in Fig. (3.7). Additionally, the ratio of the top sublaminates thickness (h_t) to the thickness of the bottom segment (h_b) is assumed to be 0.25. It is worth noting that the buckling mode shapes of all four cases are identical.

At the first glance, it is clear that there is an excellent agreement between the results obtained using the layerwise TSDT (shown with LW in figures) and those evaluated by the commercial finite element software (ABAQUS) (shown with FEM in figures). Notably, the total freedom

degrees considered for the analysis of the FG-GRC laminated composite plate with a single delamination in the layerwise TSDT is 126, which means that the order of the tangent stiffness matrix of this case is 126×126 . However, In the finite element model that has been developed, the hexahedral 3D 8-node linear isoperimetric element (C3D8) has been employed, resulting in a total of 16,000 elements and 21,853 nodes. This discernible difference in the degrees of freedom handled by these two semi-analytical and numerical approaches demonstrates that the layerwise TSDT is significantly more computationally efficient than the developed finite element model.

As illustrated in Fig 3.7, for both boundary conditions, at the onset of thermal loading, the thinner top sublaminates (includes two graphene reinforced composite plies) exhibit positive out-of-plane displacements, whereas the thicker bottom sublaminates (consists of eight graphene reinforced plies) experience negative out-of-plane displacements. Additionally, for both boundary conditions and regardless of the type of graphene distribution, the negative out-of-plane displacement of the bottom sublaminates grow as the temperature rises, and in SFSF cases this thicker segment pulls the top sublaminate towards the negative direction of Z during its deflection. For instance, by increasing the temperature up to $T = 330$ K, the deflection of both top and bottom sublaminates of the FGX plate with SFSF boundary condition increases along the positive and negative directions of Z, respectively, which is referred as the mixed-mode buckling. After $T = 330$ K, the deflection of the thicker segment of the FGX laminated plate further increases in the negative direction and pulls down the top sublaminate.

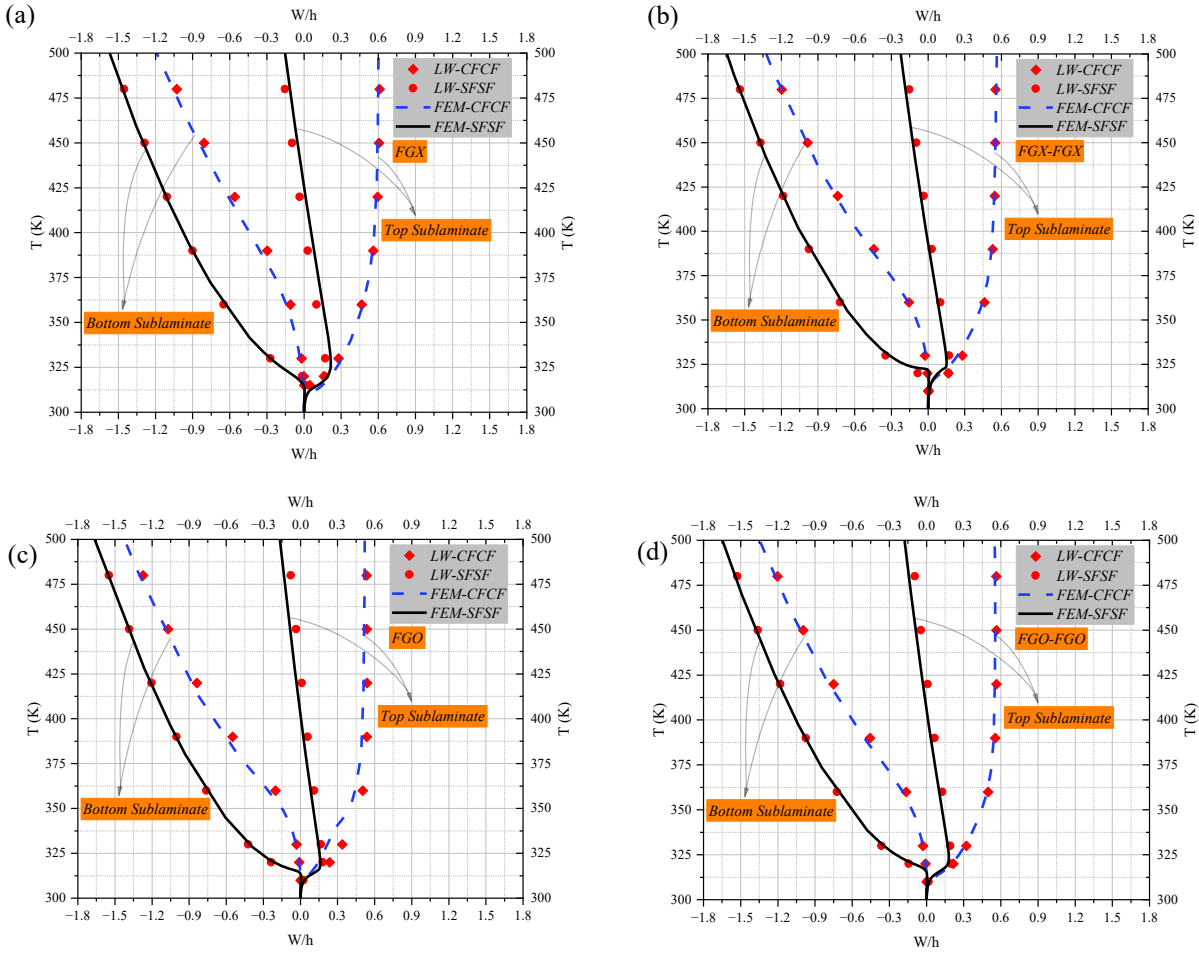


Figure 3-7 Influence of boundary conditions and several symmetric graphene distribution patterns on the thermal postbuckling deflection of the composite laminated plates with single through-the-width delamination (a) FGX, (b) FGX-FGX, (c) FGO, (d) FGO-FGO ($\frac{h_t}{h_b} = \frac{1}{4}$, $\frac{L_2}{L_1} = \frac{1}{2}$, $\frac{L_1}{b_1} = 1$).

In Fig 3.8, the impact of different asymmetric graphene distribution patterns (FGA, FGA-FGA, FGV, and FGV-FGV) and two different boundary conditions (CFCF and SFSF) on the nonlinear thermal postbuckling deflection curves of delaminated composite plates is examined. The geometry parameters and thickness coordinate of the delamination is same with those analyzed in Fig 3.7.

Regardless of graphene distribution patterns, all four cases with CFCF boundary conditions exhibit mixed-mode buckling mode shapes, in which the top and bottom segments within the delamination area deflect in opposite directions. However, for plates with SFSF boundary

conditions, the types of buckling mode shapes strongly depend on the graphene distributions. For example, for FGA, FGV, and FGV-FGV graphene distribution patterns, the top and bottom sublaminates deflect simultaneously in the same direction, which is known as the global buckling mode shape, where the top and bottom sublaminates stick together during their deflection and act as a perfect plate (without any interlaminar defect). It's important to note that there is a difference in the deflection direction among the three cases that exhibit global buckling mode shapes. Specifically, the delaminated plate with FGA graphene distribution pattern deflects downward, while the plates with FGV and FGV-FGV graphene dispersions experience upward out-of-plane displacement. This phenomenon can be attributed to the plates' different bending stiffness, which arises from their varying functionally graded patterns.

For the simply supported delaminated composite plate with FGA-FGA graphene distribution pattern, however, the top and bottom sublaminates deflect in different directions, indicating mixed-mode buckling.

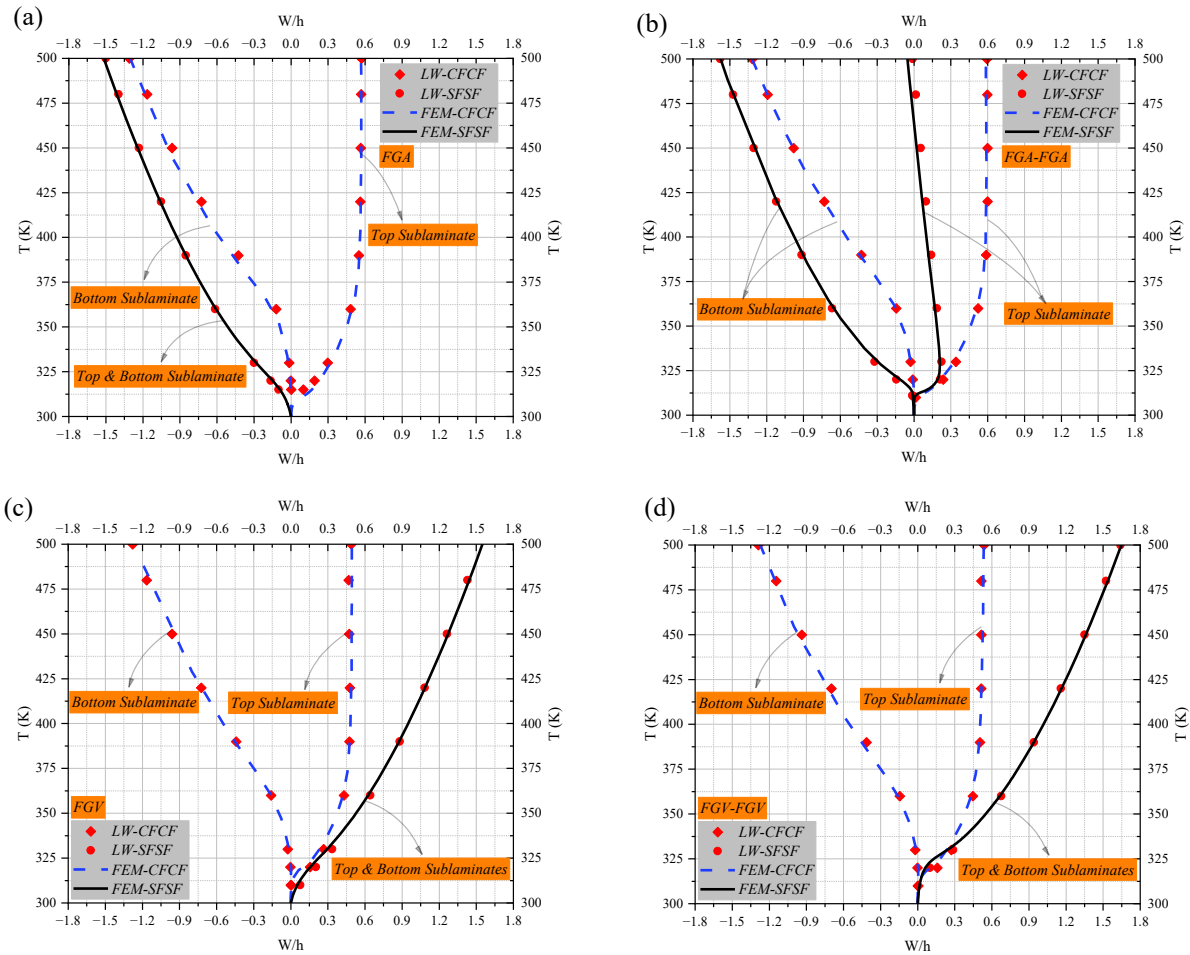


Figure 3-8 Influence of boundary conditions and several asymmetric graphene distribution patterns on the thermal postbuckling deflection of the composite laminated plates with single through-the-width delamination(a) FGA, (b)FGA-FGA, (c) FGV, (d) FGV-FGV, ($\frac{h_t}{h_b} = \frac{1}{4}$, $\frac{L_2}{L_1} = \frac{1}{2}$, $\frac{L_1}{b_1} = 1$).

In Fig. (3.9), an examination is conducted on the influence of various symmetric and asymmetric graphene distribution patterns and boundary conditions on the variation of in-plane displacements across the thickness direction of delaminated composite plates. This analysis illustrates the coherence of these factors at the numerical interfaces established according to the layerwise theory.

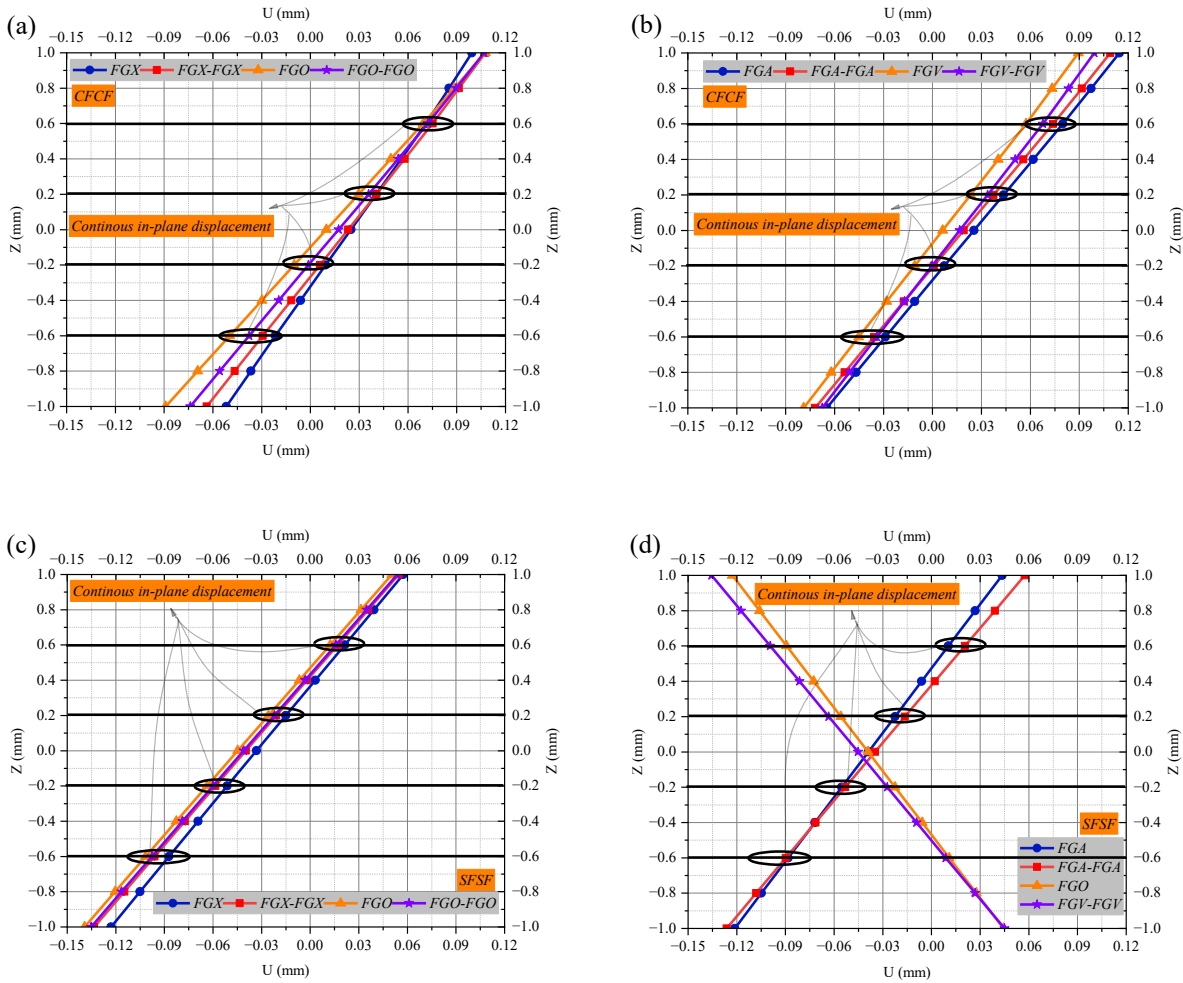


Figure 3-9 Distribution of the in-plane displacements through the thickness direction of the FG-GRC laminated composite plates at the center of the delamination front $U(-\frac{L_2}{2}, 0, z)$ (a)symmetric, CFCF (b)asymmetric, CFCF (c) symmetric, SFSF (d) asymmetric, SFSF

Table. (3.3) illustrates the schematic buckling mode shapes of graphene-reinforced laminated composite plates with a single through-the-width delamination for all eight symmetric and asymmetric graphene distribution patterns at $T=500$ K for two different boundary conditions (CFCF and SFSF).

Table 3-3 The buckled configurations of clamped and simply-supported FG-GRC laminated composite plates with single through-the-width delamination zone and several graphene graded patterns.

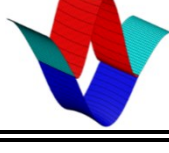
Distribution patterns	Lay-up arrangements of graphene volume fraction and delamination location	CFCF (T= 500 K)	SFSF (T=500 K)
FGX	$[0.11,0.09,0.07,0.05,0.03]_s$ [2 // d // 8]		
FGX-FGX	$[0.09,0.07,0.03,0.07,0.09]_s$ [2 // d // 8]		
FGO	$[0.03,0.05,0.07,0.09,0.11]_s$ [2 // d // 8]		
FGO-FGO	$[0.05,0.07,0.11,0.07,0.05]_s$ [2 // d // 8]		
FGA	$[(0.03)_2, (0.05)_2, (0.07)_2, (0.09)_2, (0.11)_2]$ [2 // d // 8]		
FGA-FGA	$[0.03,0.05,0.07,0.09,0.11,0.03,0.05,0.07,0.09,0.11]$ [2 // d // 8]		
FGV	$[(0.11)_2, (0.09)_2, (0.07)_2, (0.05)_2, (0.03)_2]$ [2 // d // 8]		
FGV-FGV	$[0.11,0.09,0.07,0.05,0.03,0.11,0.09,0.07,0.05,0.03]$ [2 // d // 8]		

Fig 3.10 confirms that the type of boundary condition, play a significant role in the load-bearing capacity of the FG-GRC delaminated plates. For instance, Changing the boundary conditions at the longitudinal ends of the FGX delaminated composite plate from clamped to simply supported reduces dramatically the plate's load-bearing capacity by 87% at $T=500$ K.

The load-bearing capacity and stiffness of graphene-reinforced plates are also significantly influenced by the distribution patterns of the reinforcement. For instance, under the CFCF boundary condition, a delaminated plate with FGX graphene dispersion shows the highest load-bearing capacity compared to all other symmetric and asymmetric patterns at $T=500$ K. This pattern offers approximately 1.5 times more load-bearing capacity than that of the delaminated plate with FGO graphene distribution, which represents the worst-case scenario. Furthermore, it can be deduced that in the context of the SFSF boundary condition, the load-bearing capacity of three asymmetric graphene distribution patterns, FGA, FGV, and FGV-FGV, which undergo global buckling mode shapes, surpasses that of patterns exhibiting mixed-mode buckling.

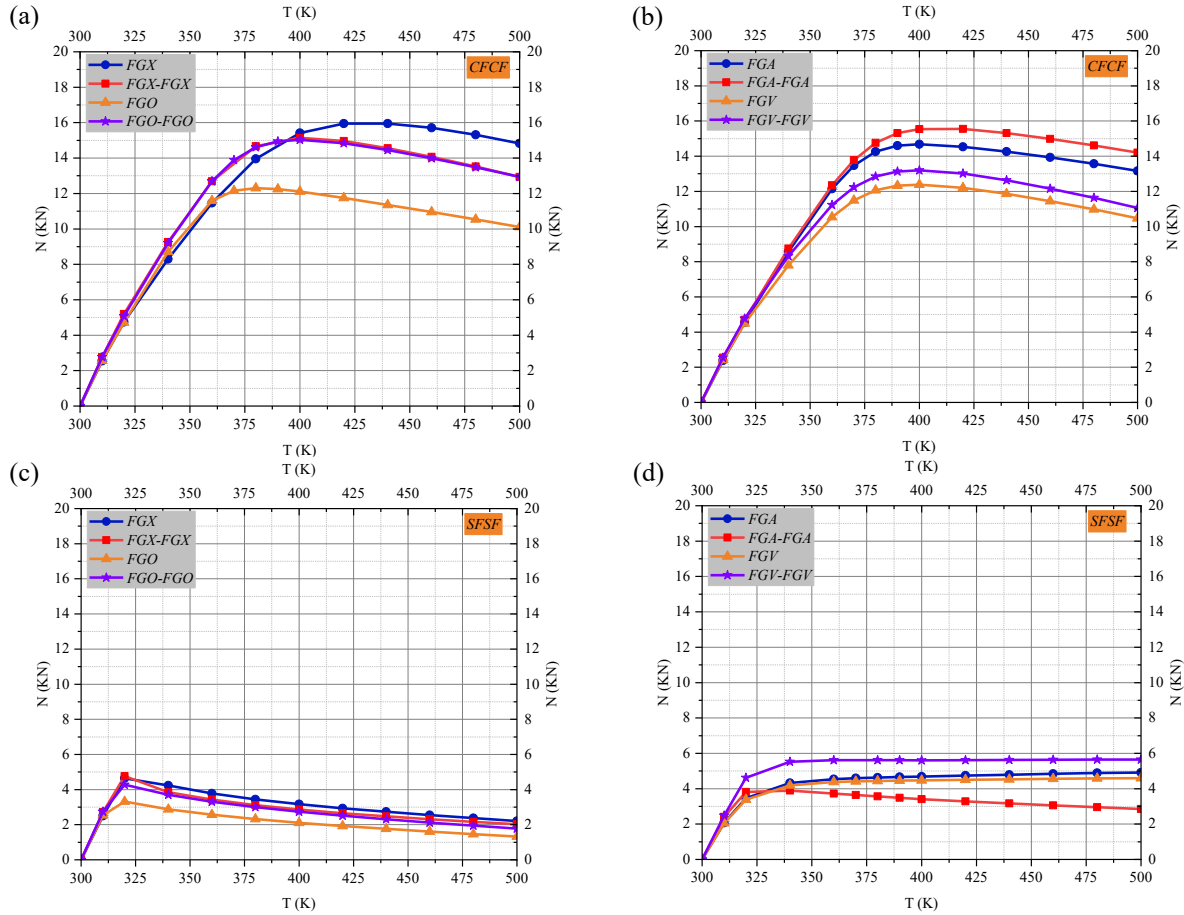


Figure 3-10 Influence of the boundary conditions and several graphene distributions on the load-bearing capacity of the FG-GRC laminated composite plates with a single through-the-width delamination (a)symmetric CFCF,

(b)asymmetric CFCF, (c)symmetric SFSE, (d)asymmetric SFSE, ($\frac{h_t}{h_b} = \frac{1}{4}$, $\frac{L_2}{L_1} = \frac{1}{2}$, $\frac{L_1}{b_1} = 1$).

The comparison of the impact of two distinct boundary conditions and symmetric distribution patterns of graphene on the variation of the energy release rate (ERR) for fracture modes I and II (opening and shearing) at the delamination edge is presented in Fig 3.11. It is worth mentioning that the delaminated composite plates' geometrical and layup sequences are the same as those analyzed in Figs 3.7 and 3.8.

As shown in Eqs. (3.26) and (3.27), according to the 3D-CTE method, the ERR strongly depends on the stiffness matrix and material properties defined for the numerical layers located

above and below the delamination or crack plane; thus, functionally graded distribution of the graphene reinforcements plays a crucial role in ERR variation, as shown in Fig 3.11.

The presence of mixed-mode shapes in delaminated composite materials can have a significant impact on the ERR at the delamination edge. This is due to the fact that mixed-mode shapes can cause a redistribution of stresses and strains in the material, resulting in changes in the mode of delamination growth and ultimately affecting the mode II ERR, therefore it is great of importance to evaluate the variation of ERR.

As shown in Table. (3.3), the delaminated composite plates with symmetric graphene distribution patterns (FGX, FGX-FGX, FGO, FGO-FGO) with both CFCF and SFSF boundary conditions exhibit mixed buckling mode shape and Fig 3.11 confirms that the ERR of mode II exceeds that of mode I for all aforementioned patterns. This indicates that in mixed-mode buckling, the sliding fracture mode exhibits greater activity than the opening fracture mode. Furthermore, the analysis reveals that the ERR is higher for nodes located near the center of the delamination edge, for both the opening and shearing modes, when compared to the regions closer to the free-edges of the plate.

Additional results about the influence of asymmetric graphene distribution patterns on the variation of ERR of Modes I and II of the delaminated plates are also illustrated in Fig. (3.12).

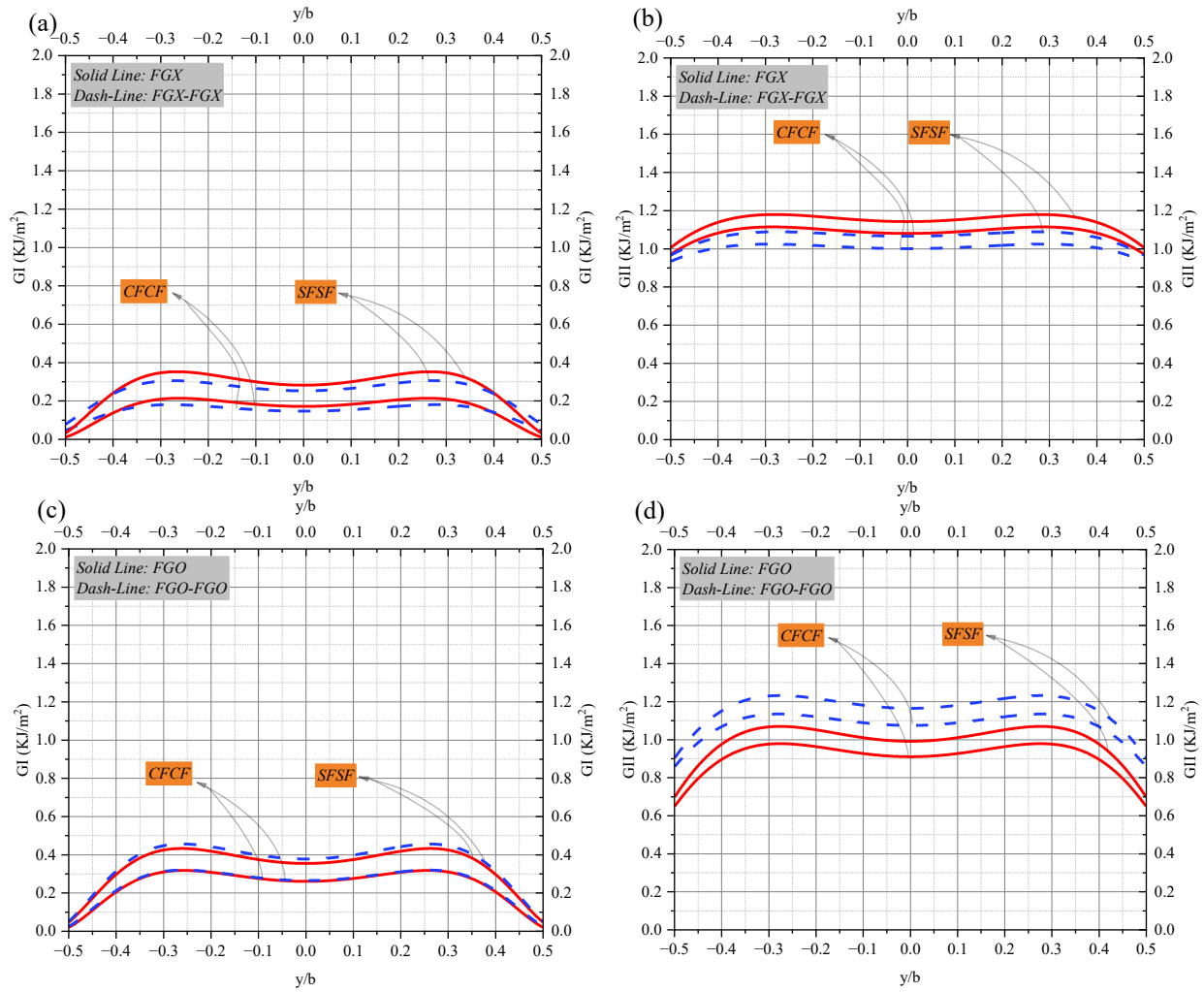


Figure 3-11 Variation of the ERR (Modes I and II) along the delamination edge of the FG-GRC laminated composite plates with different symmetric graphene distribution pattern(a)FGX, FGX-FGX, GI, (b)FGX, FGX-FGX, GII, (c)FGO,FGO-FGO, GI, (d)FGO, FGO-FGO,GII, ($\frac{h_t}{h_b} = \frac{1}{4}$, $\frac{L_2}{L_1} = \frac{1}{2}$, $\frac{L_1}{b_1} = 1$, $T=500$ K).

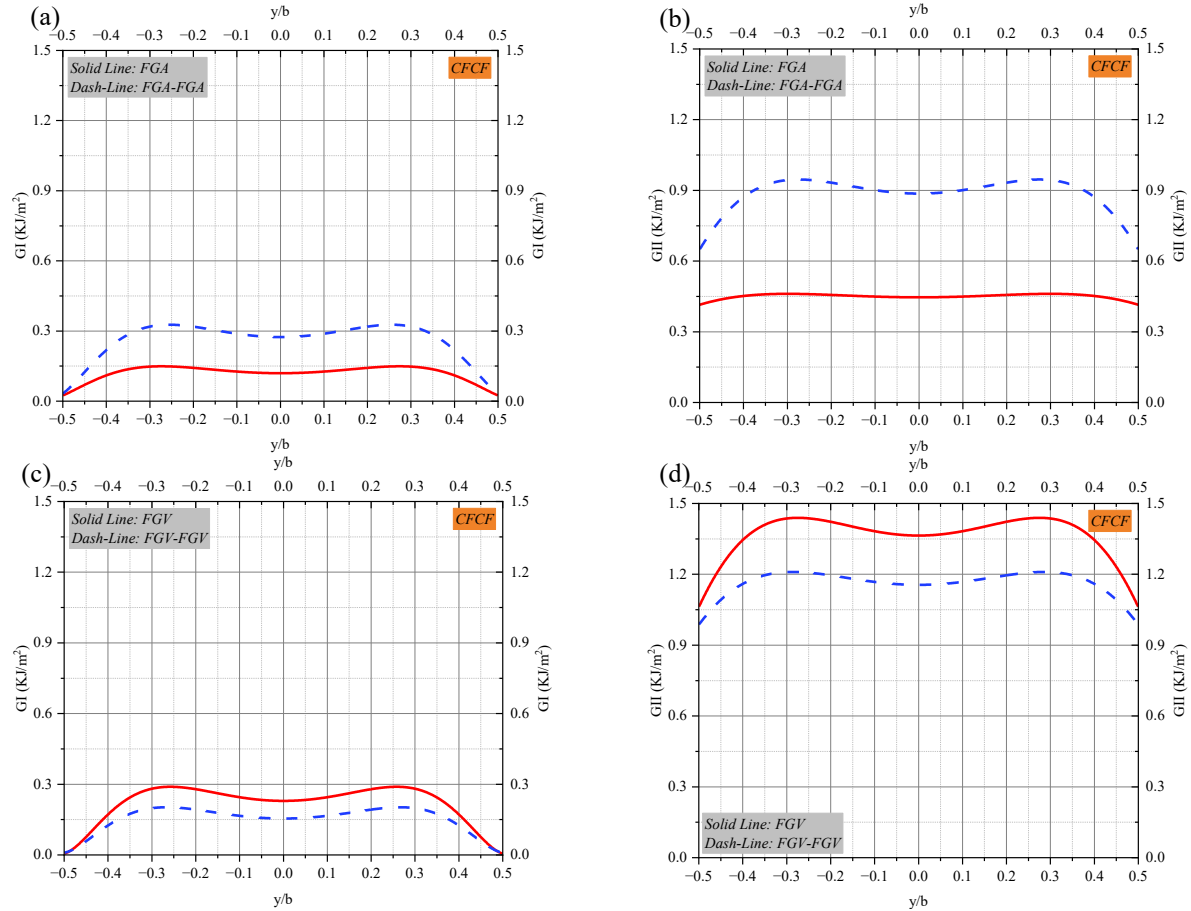


Figure 3-12 Variation of the ERRS (Modes I and II) along the delamination front of the FG-GRC laminated composite plates with different asymmetric graphene distribution patterns(a)FGA, FGA-FGA, GI, (b) FGA, FGA-FGA, GII, (c)FGV,FGV-FGV, GI, (d) FGV,FGV-FGV,GII, ($\frac{h_t}{h_b} = \frac{1}{4}$, $\frac{LD}{L} = \frac{1}{2}$, $T=500$ K).

To gain a better understanding and enable comparison of the propagation possibility of different portions of a single near-surface through-the-width delamination in FG-GRC composite plates, the total ERR is assessed for various graphene distribution patterns under two distinct boundary conditions CFCF and SFSF. The results of this analysis are depicted in Fig 3.13 and indicate that under the CFCF boundary condition, the total ERR tendency among symmetric and asymmetric graphene reinforcement patterns is consistent. The cause for this lies in the similar buckling mode shapes (mixed-mode) observed in all plates with different graphene distributions and CFCF boundary condition. Across these cases, regions near the center of the delamination edge are more susceptible to propagation than the other areas.

Of particular significance is that their level of total ERR are different, because of the functionally graded distribution of graphene along the thickness direction of the plate, which effects on the bending stiffness of different numerical layers including top and bottom sublaminates and results in various thermal postbuckling deflection. An increase in stress concentration at the delamination edge due to deflection can cause a rise in ERR, accelerating the propagation of delamination. On the other hand, if deflection leads to a redistribution of stress away from the delamination edge, it can decrease the ERR, inhibiting delamination propagation.

Additionally, when subject to the SFSF boundary condition, the ERR distribution at the delamination front section of plates with FGA, FGV, and FGV-FGV graphene patterns significantly differs from that of other graphene dispersions. In particular, points located near the transverse edges of these three plates ($\frac{y}{b} < -0.4$, $\frac{y}{b} > 0.4$) experience a higher ERR than those near the center of the delamination edge. This finding supports the notion that the graphene distribution patterns, which can influence the buckling mode shapes of delaminated plates, have a noticeable impact on the total ERR and probability of delamination propagation.

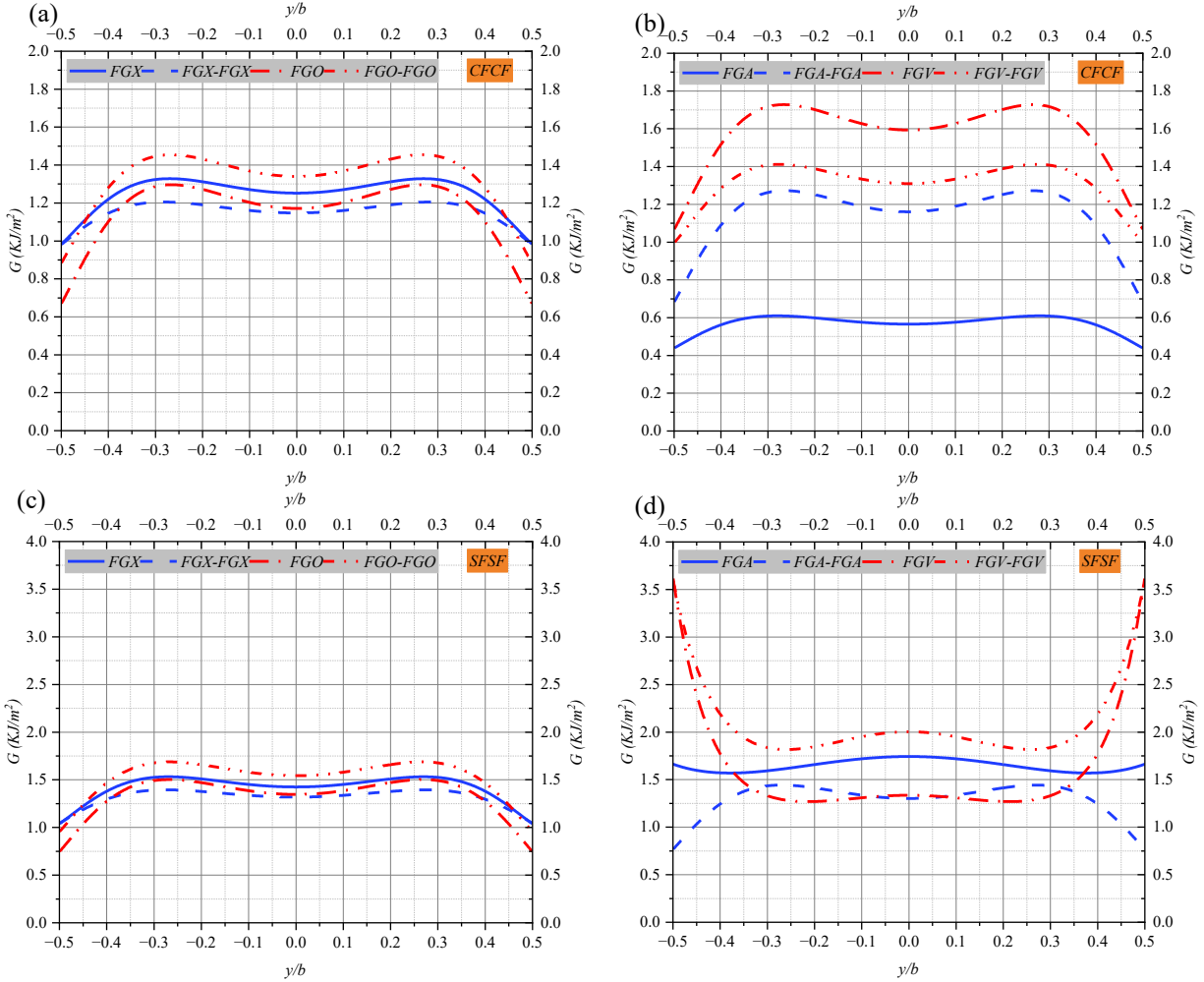


Figure 3-13 Effect of different kinds of graphene graded patterns and boundary conditions on the variation of total ERR along the delamination edge of FG-GRC laminated composite plates (a) symmetric, CFCF, (b) asymmetric, CFCF, (c) symmetric, SFSF, (d) asymmetric SFSF, ($\frac{h_t}{h_b} = \frac{1}{4}$, $\frac{L_2}{L_1} = \frac{1}{2}$, $\frac{L_1}{b_1} = 1$, $T=500$ K).

The variation of the fundamental frequencies versus temperature change for delaminated and perfect (without delamination) plates reinforced with FGX as a symmetric graphene distribution pattern and FGA as asymmetric are illustrated in Fig 3.14. The thermally induced pre- and post-buckled non-dimensional fundamental frequencies of delaminated plates with CFCF boundary conditions demonstrate notable distinctions from those of perfect plates with the same boundary conditions, irrespective of the type of graphene distribution pattern. The present study has demonstrated that the pre- and post-buckled frequency-temperature relationship of a FG-GRC

perfect plate is characterized by a single concave point associated with the critical buckling temperature. In contrast, the frequency-temperature curve of a FG-GRC plate with a near-surface through-the-width delamination exhibits three distinct concave points, corresponding to the critical buckling temperatures of the top and bottom segments within the delamination zone.

In the case of delamination, the non-dimensional fundamental frequencies of the plate are affected by temperature within the pre- and post-buckling domains. Specifically, an increase in temperature during the pre-buckling stage results in a decrease in the fundamental frequency due to the corresponding reduction in stiffness. Once the temperature reaches the critical buckling temperature, the top sublaminates deflects upward while the bottom sublaminates remain flat, which is known as local buckling mode shape. This behavior is illustrated in Figs 3.7 and 3.8. During the post-buckling regime, the thermal large deformation of the top sublaminates increases the nonlinear stiffness of the plate, leading to an increase in the fundamental frequency up to the second concave point. At this point, the thicker bottom sublaminates start to deflect, resulting in a reduction in the bending stiffness of the plate and a subsequent decrease in the non-dimensional fundamental frequency up to the third concave point, where a mixed-buckling mode shape occurs. It is important to note that the frequency increases again following the thermally induced deflection of both the top and bottom sublaminates.

Another notable aspect of the CFCF boundary condition is that, unlike the reference temperature ($T = 300\text{ K}$) where the non-dimensional fundamental frequency of the FG-GRC delaminated plate is lower than that of the perfect plate without considering the graphene distribution pattern, during the post-buckling domain, the fundamental frequencies of the specified delaminated plate, ($\frac{h_t}{h_b} = \frac{1}{4}, \frac{L_2}{L_1} = \frac{1}{2}, \frac{L_1}{b_1} = 1$), are higher than those of the perfect plate.

Observing the FGX and FGA graphene distribution patterns under the SFSF boundary condition in Fig 3.14, it can be inferred that FG-GRC plates with a single through-the-width delamination exhibit thermally induced pre- and post-buckled fundamental frequency variations similar to those of perfect plates. This means that across these curves just one concave point can be seen associated with the critical buckling temperature. According to Fig 3.7, the delaminated FGX plate with SFSF boundary condition exhibits mixed-mode buckling mode shapes from the initial loading stages and both the top and bottom segments deflect at the same temperature. As a result, there is only one critical buckling temperature for this type of scenario. Furthermore, as depicted in Fig 3.8, the thermal postbuckling equilibrium path of the delaminated plate with SFSF boundary condition and FGA graphene dispersion, is identical to that of a plate without any delamination. This implies that during the postbuckling regime, both the top and bottom segments within the delamination area remain attached and deflect in unison. Therefore, this scenario also exhibits only one critical buckling temperature.

Fig 3.15 compares the influence of different symmetric and asymmetric graphene distribution patterns on the pre- and post-buckled fundamental frequencies of GRC delaminated and perfect plates with CFCF boundary conditions. The geometrical parameters of the single delamination are similar to those discussed above. In both perfect and delaminated FG-GRC plates, a more significant difference exists between fundamental frequencies when symmetric graphene distribution patterns (FGX, FGX-FGX, FGO, and FGO-FGO) are implemented, compared to when asymmetric dispersions (FGA, FGA-FGA, FGV, and FGV-FGV) are utilized.

During the pre-buckling phase, it has been observed that the FGX graphene distribution pattern exhibits the highest fundamental frequencies in both perfect and delaminated plates. Additionally, the critical buckling temperature of the FGX perfect plate is greater than that of other graded

distributions, and the FGX delaminated plate experiences higher critical buckling temperature loads for both the thin top sublaminates and thick bottom baselaminates, owing to its higher plate stiffness. These findings provide evidence that the FGX perfect and delaminated plates enter their post-buckling phase at a later stage than the other graphene distributions, which implies that natural frequencies of the FGX plates are at the lowest during this phase.

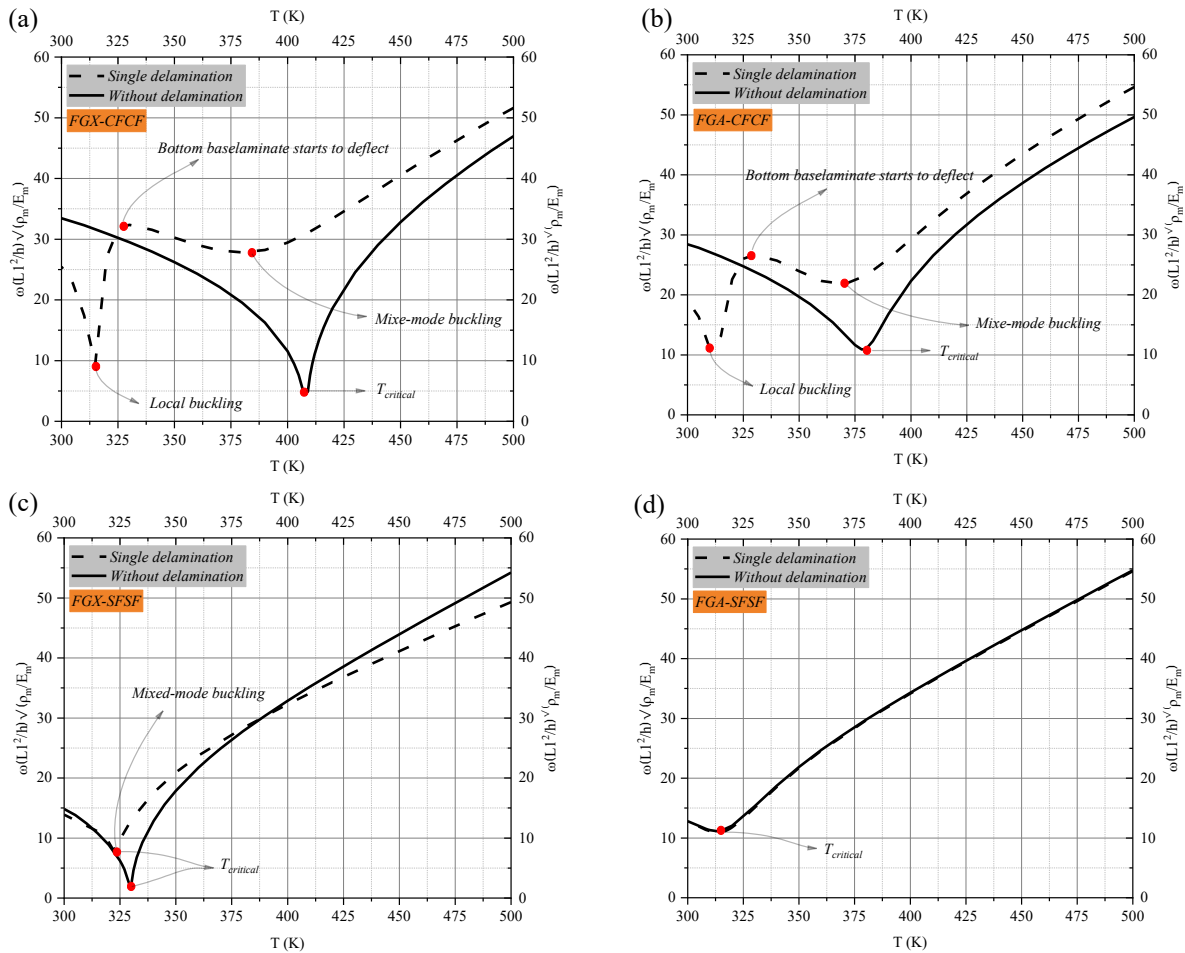


Figure 3-14 Effect of FGX and FGA graded patterns and boundary conditions on thermally pre- and post-buckled vibration of delaminated and perfect GRC plates (a)FGX, CFCF (b)FGA, CFCF(c)FGX, SFSF(d) FGA, SFSF, $(\frac{h_t}{h_b} =$

$$\frac{1}{4} \cdot \frac{L_2}{L_1} = \frac{1}{2} \cdot \frac{L_1}{b_1} = 1).$$

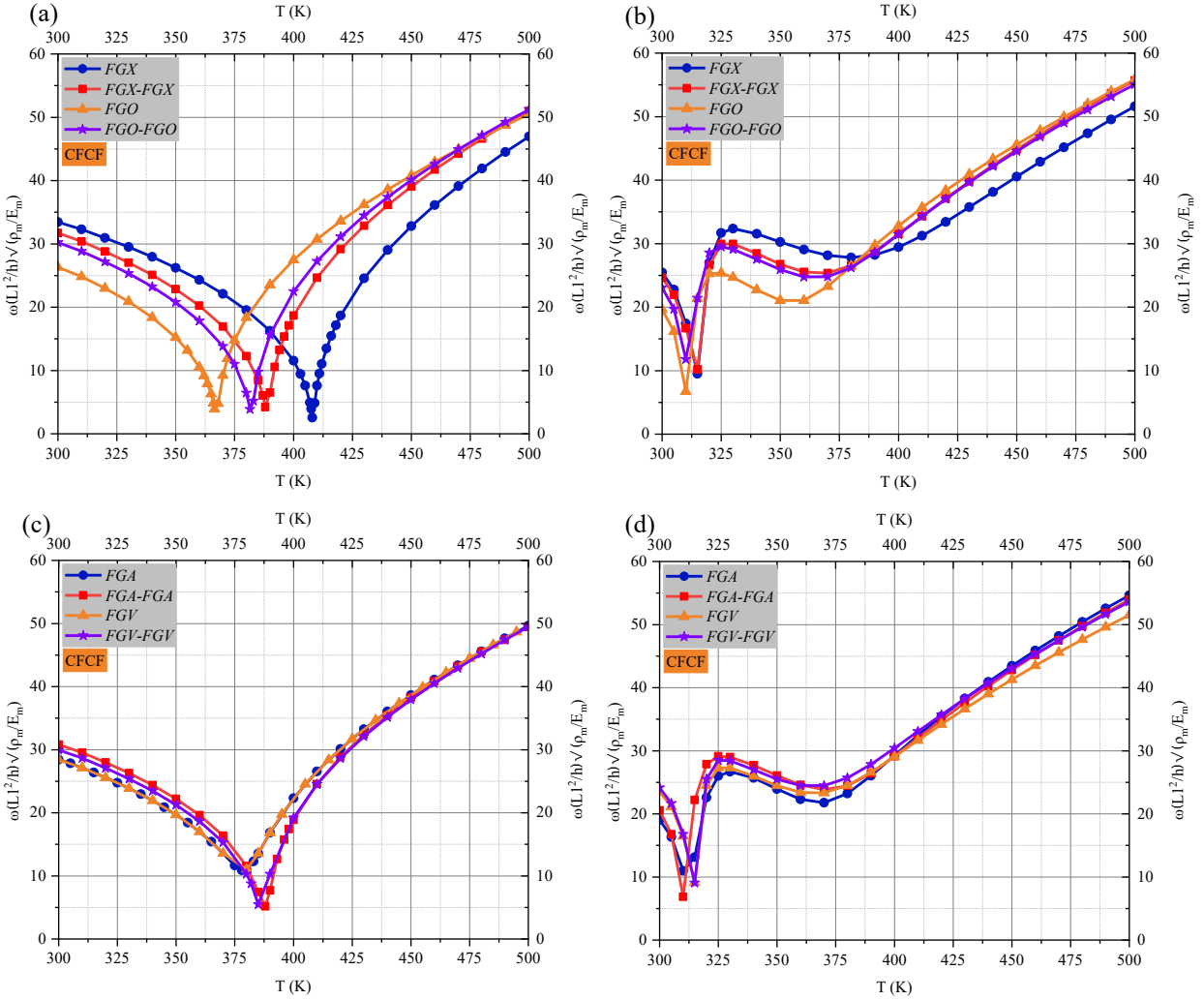


Figure 3-15 Effect of several symmetric and asymmetric functionally graded patterns on thermally pre- and post-buckled vibration of perfect and delaminated GRC plates (a) perfect plate, symmetric (b) delaminated plate, symmetric (c) perfect plate, asymmetric, (d) delaminated plate, asymmetric, ($\frac{h_t}{h_b} = \frac{1}{4}$, $\frac{L_2}{L_1} = \frac{1}{2}$, $\frac{L_1}{2^2 b_1} = 1$).

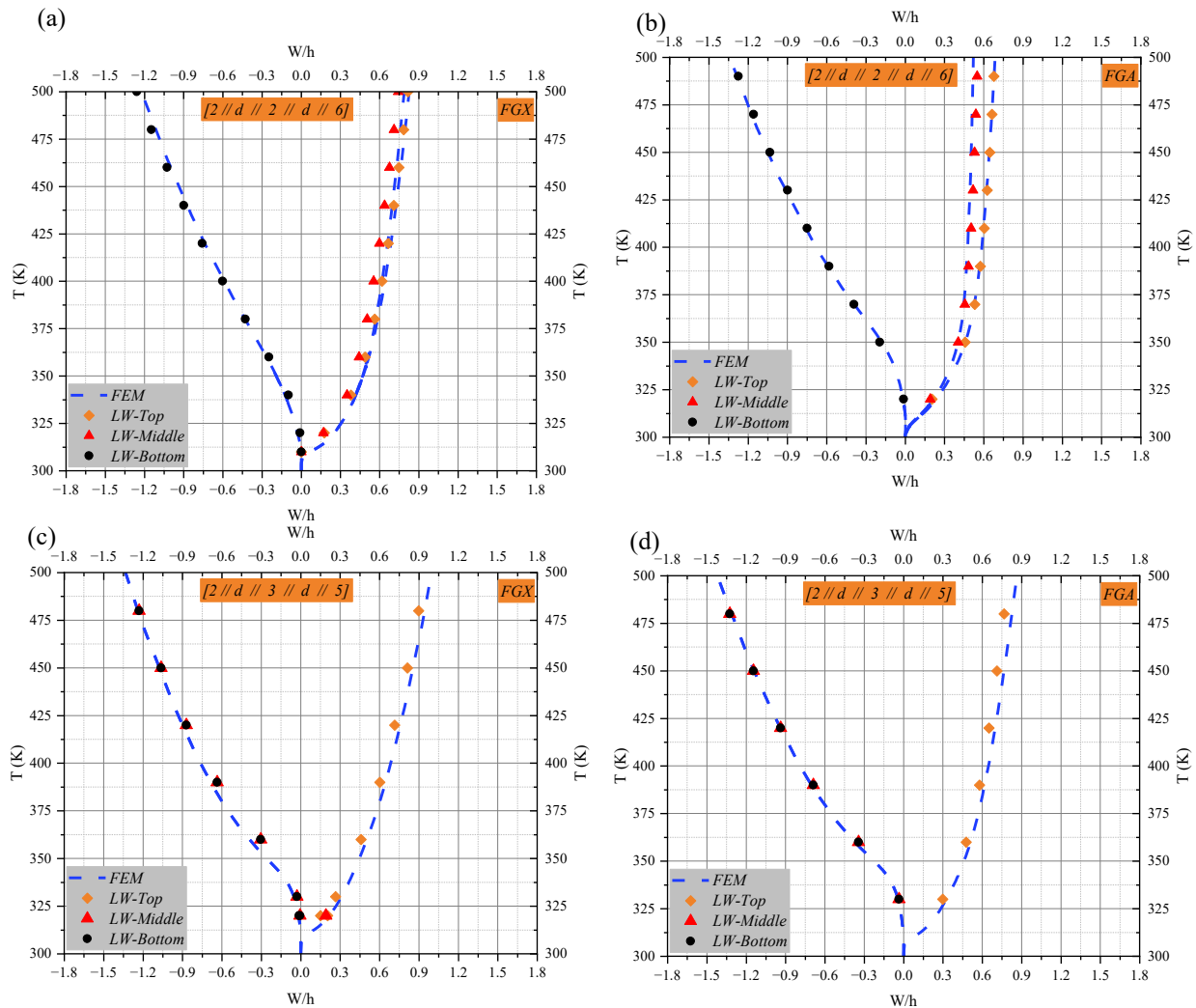
3.5.2. FG-GRC laminated plate with multiple through-the-width delaminations

To have a better understanding about the influence of interlaminar defects on the thermal compressive instability behavior of the FG-GRC plates, it is assumed that double central through-the-width delaminations with the same size ($\frac{L_2}{L_1} = \frac{1}{2}$) as illustrated in Fig 3.4 take place at different thickness coordinates of the plates. In this section, for the sake of brevity, only two types of graphene distribution patterns are considered: FGX as a symmetric and FGA as an asymmetric dispersion, with the CFCF boundary condition. Fig 3.16 compares the thermal equilibrium paths

of the FGX and FGA composite plates with consideration four different delamination configurations, including $[2 / d / 2 / d / 6]$ as the first case, in which the top sublaminates consists of two graphene-reinforced composite plies, the first delamination occurs, the middle sublaminates also consists of two graphene-reinforced composite plies, another delamination zone occurs, and the bottom sublaminates includes six composite plies. By maintaining the thickness of the top sublaminates constant (consists of two composite plies) while adjusting the location of the second delamination through the thickness of the plates, which changes the thickness of the middle and bottom sublaminates, the influence of the delamination location is studied as well. As can be seen, changing the location of the delamination causes some unexpected thermal postbuckling behaviors in the top, middle, and bottom sublaminates of the FGX and FGA plates. In the first case, where the delamination configuration is $[2 / d / 2 / d / 6]$, for both FGX and FGA graphene distribution patterns, increasing the temperature causes the top and middle sublaminates to deflect upward, while the bottom sublaminates experience a negative out-of-plane displacement. However, In the second and third cases, when the delamination configurations are $[2 / d / 3 / d / 5]$ and $[2 / d / 5 / 3]$, respectively, the middle sublaminates responds in an entirely different way and buckles through the negative Z direction. It should be highlighted that between the middle and bottom sublaminates in the second and third configurations a penalty contact constraint is implemented to prevent the penetration, a physically unacceptable phenomenon.

The buckling mode shapes of the FGX and FGA laminated composite plates differ in the final case, $[2 / d / 6 / d / 2]$, when both delamination zones are symmetrically located close to the top and bottom plate surfaces. When the temperature increases uniformly from 300 K to 500 K, the middle sublaminates of the FGX delaminated composite plate remains flat, but the top and bottom sublaminates deflect in opposite directions. The middle and top sublaminates of the FGA

delaminated plate, however, deflect in positive direction, whereas the bottom sublaminates buckle downward. It should be noted that at the beginning of the temperature loading, the top and middle sublaminates of the plate with FGA graphene distribution deflect independently. As the temperature rises, the middle sublaminates' deflection increases until it reaches the top sublaminates around $T=420$ K, where they connect to each other and deflect simultaneously. To evaluate the accuracy of the results obtained using the layerwise TSDT, a finite element model was developed for the multiple through-the-width delamination as well. An excellent agreement between these results can be seen.



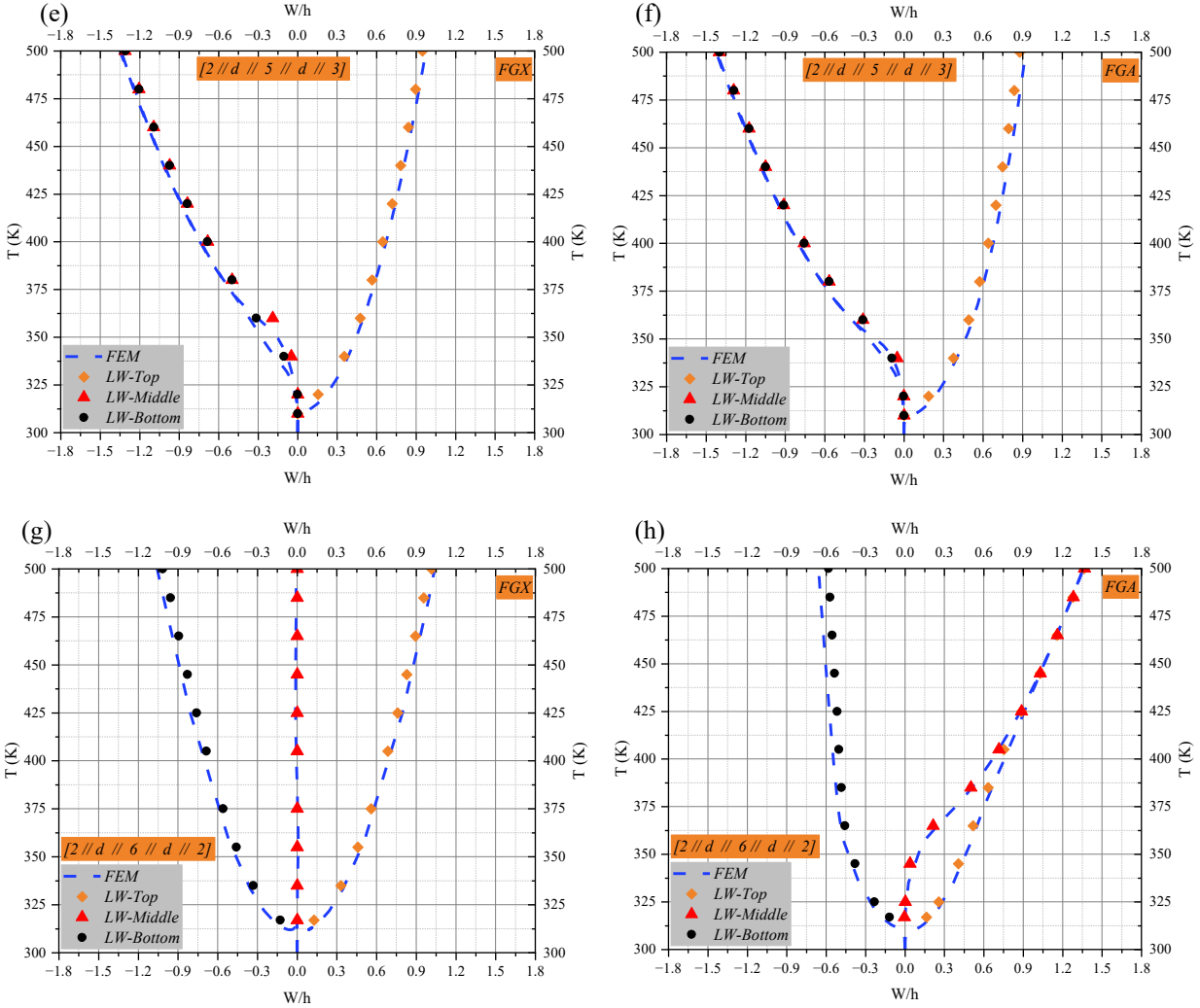


Figure 3-16 Influence of the double same size through-the-width delaminations with different configurations on the thermal potbuckling deflection paths of the FGX and FGA laminated composite plates with CFCF boundary condition (a)FGX, [2/d/2/d/6] (b)FGA, [2/d/2/d/6](c)FGX, [2/d/3/d/5](d)FGA, [2/d/3/d/5](e)FGX, [2/d/5/d/3](f)FGA, [2/d/5/d/3](g) FGX, [2/d/6/d/2](h) FGA, [2/d/6/d/2], ($\frac{L_2}{L_1} = \frac{1}{2}, \frac{L_1}{b_1} = 1$)

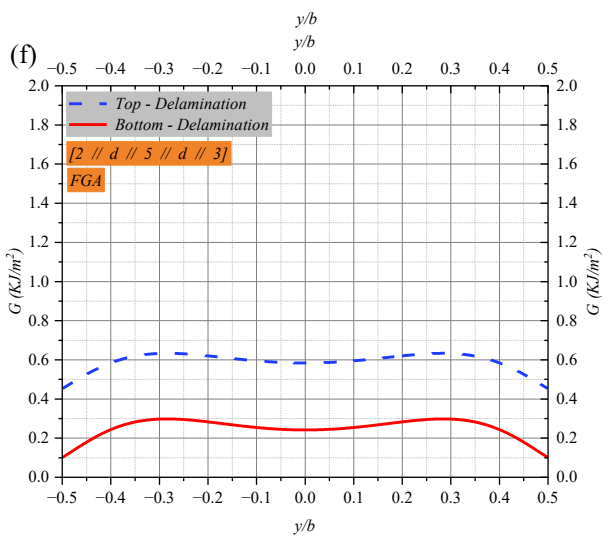
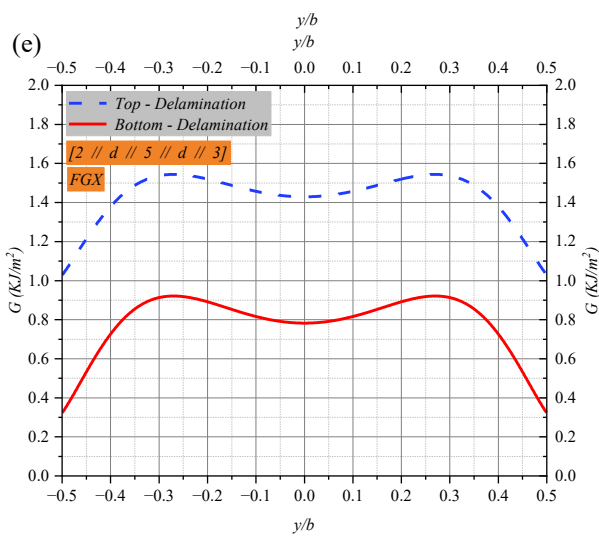
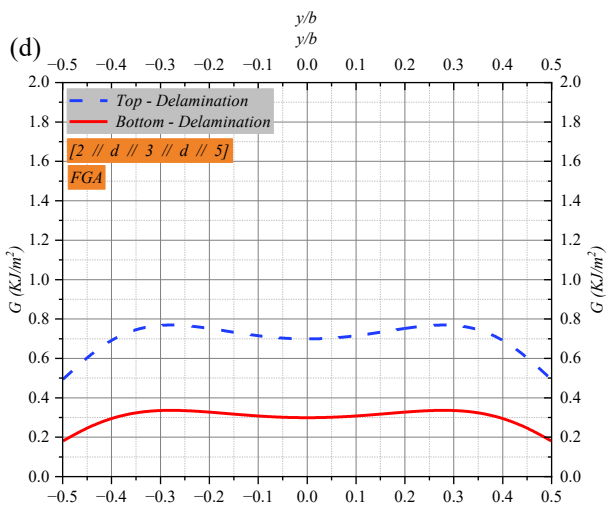
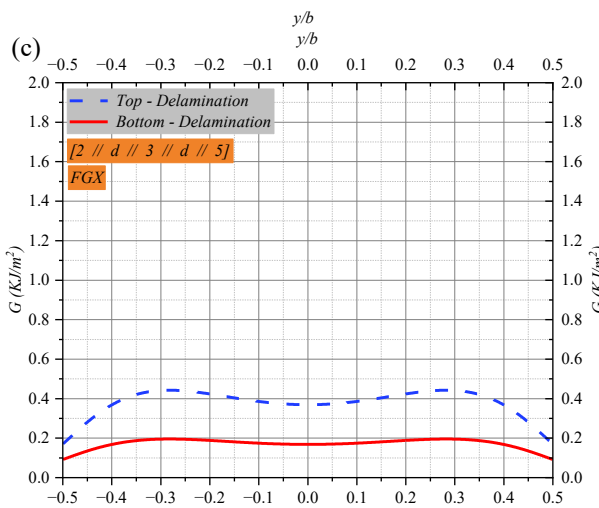
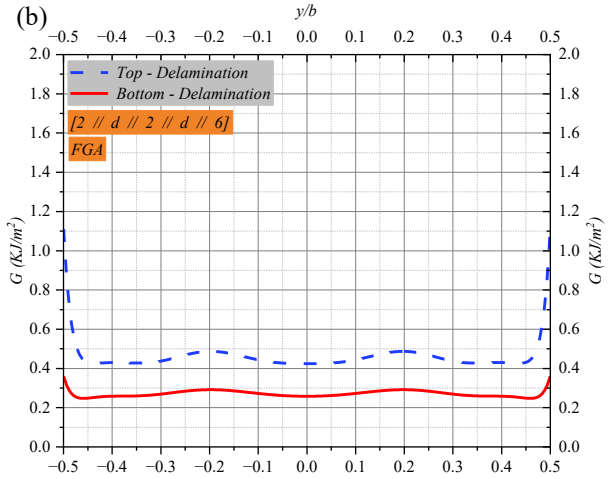
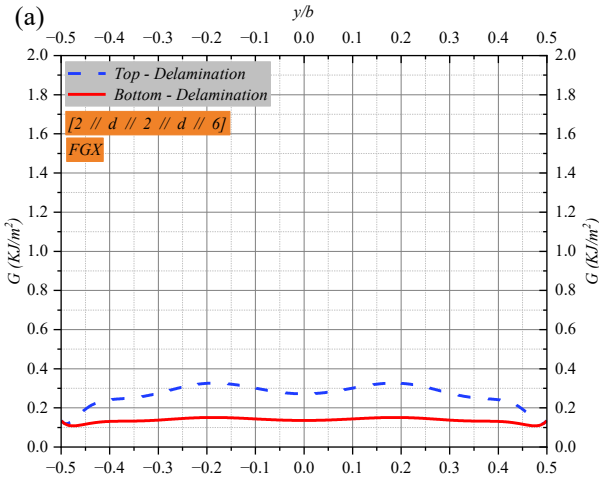
Table. (3.4) presents the buckling mode shapes of FGX and FGA graphene reinforced composite plates with CFCF boundary condition that contain double through-the-width delaminations. It is worth noting that the top, middle, and bottom sublaminates are depicted with the colors yellow, red, and dark blue, respectively. Moreover, when the middle sublaminates's deflection is equivalent to either the top or middle ones, it was removed to provide a clearer representation of the mode

shapes. Consequently, in some instances, only the yellow and dark blue sublaminates are presented.

Table 3-4 Buckled configurations of the FGX and FGA laminated composite plates with double through-the-width delaminations at T=350 K and T=500 K.

Distribution patterns	Lay-up arrangements of the graphene volume fraction and delamination locations	CFCF (T= 350 K)	CFCF (T=500 K)
FGX	$[0.11,0.09,0.07,0.05,0.03]_S$ $[2 // d // 2 // d // 6]$		
FGX	$[0.11,0.09,0.07,0.05,0.03]_S$ $[2 // d // 3 // d // 5]$		
FGX	$[0.11,0.09,0.07,0.05,0.03]_S$ $[2 // d // 5 // d // 3]$		
FGX	$[0.11,0.09,0.07,0.05,0.03]_S$ $[2 // d // 6 // d // 2]$		
FGA	$[(0.03)_2, (0.05)_2, (0.07)_2, (0.09)_2, (0.11)_2]$ $[2 // d // 2 // d // 6]$		
FGA	$[(0.03)_2, (0.05)_2, (0.07)_2, (0.09)_2, (0.11)_2]$ $[2 // d // 3 // d // 5]$		
FGA	$[(0.03)_2, (0.05)_2, (0.07)_2, (0.09)_2, (0.11)_2]$ $[2 // d // 5 // d // 3]$		
FGA	$[(0.03)_2, (0.05)_2, (0.07)_2, (0.09)_2, (0.11)_2]$ $[2 // d // 6 // d // 2]$		

According to Fig 3.16, it was assumed that double central through-width delaminations with the same size occurred at distinct thickness coordinates on the FG-GRC laminated plates. In order to determine which is more susceptible to propagation, it is necessary to examine the variation of total ERR at their front sections for both FGX and FGA graphene reinforcement distributions. As illustrated in Fig 3.17, the thickness of the top sublaminates remains constant (consists of two graphene reinforced composite plies), and several delamination configurations are investigated through changing the thickness coordinate of the bottom delamination. This illustration emphasizes that if the delamination zones are present in the top half plate, the total ERR at the delamination edges is almost equivalent for both FGX and FGA graphene reinforced composite plates. However, if the second delamination occurs in the bottom half plate, there is a significant disparity between the total ERR at the delamination edges of FGX and FGA plates, which is due to different buckling mode shapes. Moreover, apart from the last configuration of FGX delaminated plate, the total ERR at the edges of the upper delamination is higher than that of the bottom delamination, implying that the propagation possibility of the upper near-surface delamination is more than the bottom delamination in the thermal postbuckling regime. However, in the final case, FGX delaminated plate with two delamination zones placed symmetrically near the top and bottom surfaces of the plate ($[2 / d / 6 / d / 2]$), the lower delamination is more prone to propagation than the upper one.



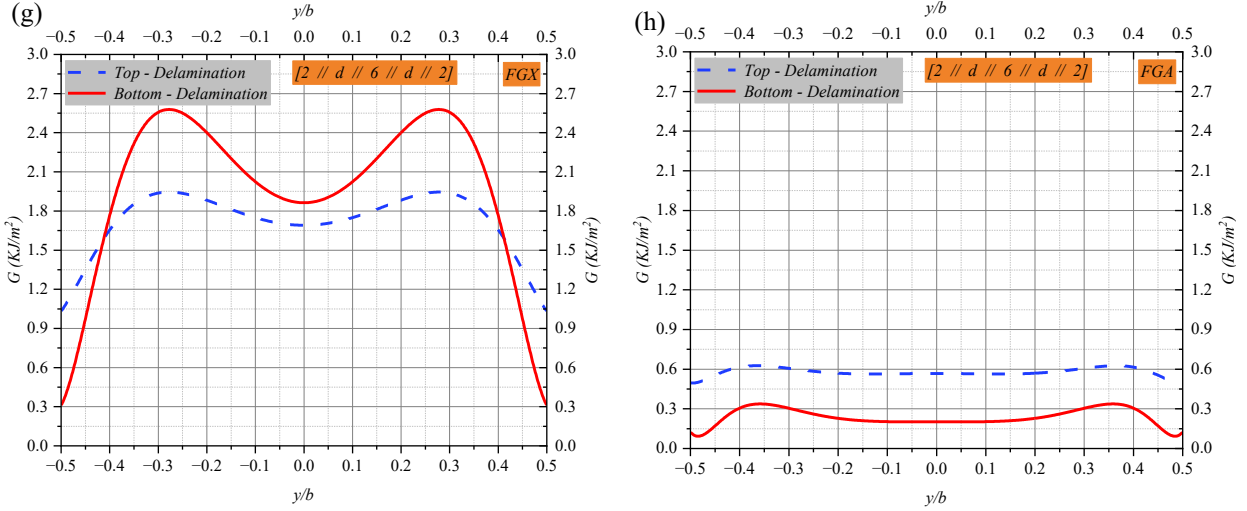


Figure 3-17 Influence of several delamination configurations on the distribution of total ERR along their edges for the FGX and FGA graphene reinforced composite plates(a)FGX, [2/d/2/d/6] (b)FGA, [2/d/2/d/6](c)FGX, [2/d/3/d/5](d)FGA, [2/d/3/d/5](e)FGX, [2/d/5/d/3](f)FGA, [2/d/5/d/3](g) FGX, [2/d/6/d/2](h) FGA, [2/d/6/d/2], $(\frac{L_2}{L_1} = \frac{1}{2}, \frac{L_1}{b_1} = 1, T=500 \text{ K})$.

In Fig 3.18, we can see the fundamental frequency-temperature curves of FGX and FGA graphene-reinforced plates with double central delamination zones. Notably, there is a significant difference between the pre- and post-buckling vibration response of the double delaminated plates compared to the perfect plates shown in Fig 3.15.

This difference is due to the presence of double delaminations, which affects the buckling mode shapes of different segments within the delamination area. These segments include the top, middle, and bottom sublaminates, each exhibiting a different postbuckling response. The fundamental frequency-temperature curves display fluctuations and concave points that correspond to different postbuckling responses. The location of delamination zones plays a crucial role in determining the behavior of these curves. In particular, when the delamination zones are symmetrically placed near the upper and lower surfaces of an FGX graphene reinforced plate with CFCF boundary condition, the post-buckling fundamental frequency-temperature curve shows a noticeable jump and is higher than other delamination configurations. This phenomenon occurs because of a special

postbuckling deflection mode shape illustrated in Fig 3.16, where the middle sublaminates remains flat while both top and bottom sublaminates deflect in opposite directions. The unique buckling mode shapes enhance the nonlinear stiffness of the plates, resulting in an improvement in their natural frequencies.

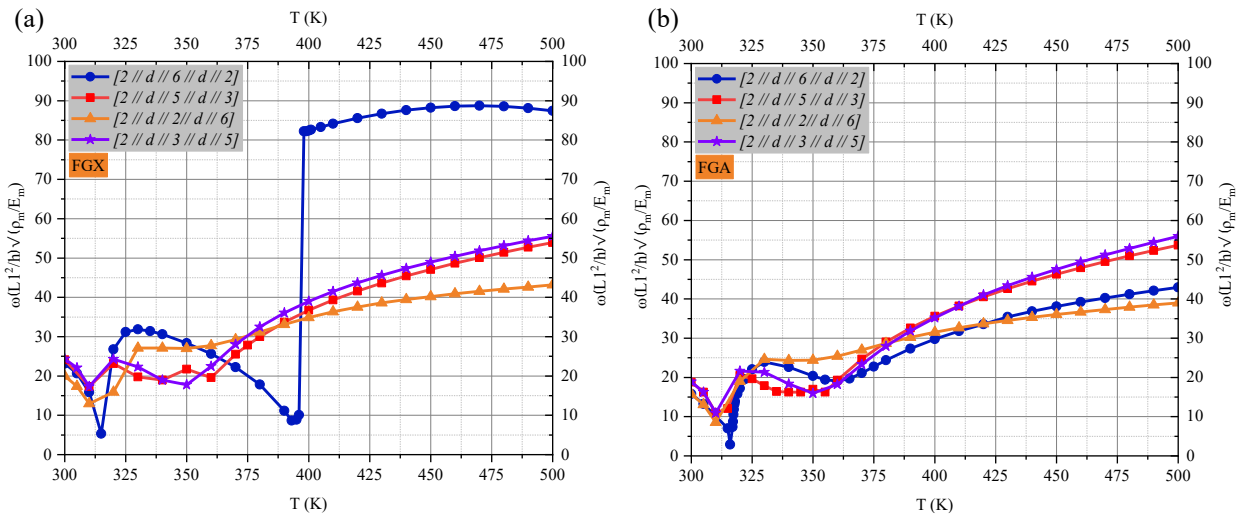


Figure 3-18 Effect of several delamination configurations on thermally pre- and post-buckled vibration of delaminated FGX and FGA graphene reinforced plate with CFC (a) FGX, (b)FGA, ($\frac{L_2}{L_1} = \frac{1}{2}$, $\frac{L_1}{b_1} = 1$).

3.6. Concluding remarks

The present research investigates the impact of graphene distribution patterns and delamination configurations on the nonlinear thermal stability responses of FG-GRC laminated plates. The study aims to assess and predict the likelihood of delamination propagation in such plates. Furthermore, the study elucidates the influence of various delamination configurations and graphene distribution patterns on the pre- and post-buckling vibrations induced by thermal loading and compare them with those in perfect FG-GRC plates. A formulation was developed based on the layerwise TSdT and von-Karman strain–displacement relation. The governing equations are solved through the application of the minimum total potential energy principle and the Ritz method in conjunction with the Newton–Raphson iterative procedure. The thermo-mechanical properties of matrix and

graphene reinforcements were assumed to be temperature-dependent obtained using the extended Halpin-Tsai micromechanical model. The numerical results elaborate on the fact that FG-GRC laminated plate designers need to carefully consider the following points in their computational simulation:

- The equilibrium paths of composite plates with a single through-the-width delamination reinforced with asymmetric graphene distribution patterns (FGA, FGA-FGA, FGV, FGV-FGV) with clamped edge supports are bifurcation types. The behavior of these plates with simply supported boundary conditions is a unique stable equilibrium path. This is due to the inability of simply supported edges to apply an extra moment to neutralize thermally induced moments.
- For the FG-GRC plates with a single central near-surface through-the-width delamination and CFCF boundary condition, the mixed mode buckling is the moderate one, regardless of the type of graphene distribution patterns, in contrast to the SFSF boundary condition, where the global buckling mode shape is most likely to occur for plates with asymmetric graphene distribution patterns.
- FGX as a symmetric graphene distribution pattern reduces the thermal postbuckling deflection of the composite plate with a single delamination, whereas FGA as an asymmetric graphene distribution pattern is not suitable for enhancing the bending stiffness of the delaminated composite plates. However, ERR at the delamination front of the FGX plate is greater than that of the plate reinforced with FGA graphene dispersion; consequently, the near-surface delamination zone in the FGX laminated composite plate can be more prone to propagation than in the FGA composite plates.

- For the FG-GRC laminated plates with a single near-surface delamination and CFCF boundary condition, it is discovered that the variations of the buckling mode shapes and tendency of ERR variation are independent to the functionally graded graphene patterns. For plates with multiple through-width delaminations and CFCF boundary condition, however, the graphene reinforcement distribution may have noticeable influence on both the buckling mode shapes and ERR distributions.
- The presence of delamination between the layers of FG-GRC laminated plates results in distinct differences in the pre- and post-buckling vibration responses compared to perfect plates (i.e., those without delamination).
- The findings of this study suggest that in some cases, specifically for FG-GRC plates with CFCF boundary conditions, the presence of delamination can lead to an enhancement in the post-buckling thermally induced fundamental frequencies, as compared to perfect plates without any delamination.

4. Effects of functionally graded graphene reinforcements on nonlinear post-local buckling and axial stiffness of laminated channel section struts³

The role of local buckling on the behavior of slender members under compression has received considerable attention in the field. For thin-walled sections, in particular, there is a noticeable decrease in the axial compressive stiffness, resulting in a substantial reduction in their load-bearing capacity due to the occurrence of local buckling. The principal purpose of this article is to explore the potential improvements in the postbuckling characteristics of polymeric composite laminated channel section struts subjected to a progressive end-shortening by employing multi-layer graphene sheets reinforcements. The solution methodology incorporates the von Karman geometrical nonlinearity and is based on the layerwise third-order shear deformation theory (LW-TSDT). To verify the accuracy of the results obtained based on the LW-TSDT and to evaluate its computational efficiency, a three-dimensional (3D) finite element model is also developed using ABAQUS for comparative analysis. A thorough examination of nonlinear stability is conducted on composite laminated channel section struts, featuring distinctive graphene distribution patterns through the thickness directions of the flanges and webs to identify the most effective material distribution with the objective of a significant increase in critical buckling end-shortening and axial compressive stiffness. The influence of the geometrical parameters on the critical buckling end-shortening, postbuckling equilibrium paths, and load-bearing capacity of functionally graded graphene reinforced composite (FG-GRC) laminated channel section struts are also elicited. The conducted parametric analyses emphasize that altering the distribution patterns of graphene reinforcement across the flanges and web, while keeping the geometrical parameters constant, can

³ A version of this chapter is published in the journal of Thin-Walled Structures, 195 (2024) 111517,

enhance the critical buckling end-shortening and load-bearing capacity by approximately 80% and 25%, respectively.

4.1. Introduction

In recent years, composite laminates have experienced substantial growth in various industries, owing to their capacity to provide a beneficial balance between stiffness, strength, and weight. Moreover, significant progress has been witnessed in manufacturing techniques like 3D printing, which has revolutionized the production of composite laminates, presenting numerous benefits in terms of design adaptability, customization, and manufacturing efficiency. By combining the advantages of both 3D printing and composite materials, this groundbreaking approach has unlocked fresh opportunities for fabricating complex and functional engineering structures with intriguing material properties, including thin-walled composite laminated struts [26,27]. These structures are commonly utilized in scenarios that involve in-plane compressive loading, particularly in the aerospace industry. The industry's focus on developing efficient and lightweight structures requires considering the potential occurrence of local buckling/post buckling at designated load levels. The precise analysis of compressive stability is crucial for these structures, considering the substantial reduction in compressive stiffness and load-bearing capacity during the post-local-buckling phase [28]. As a result, extensive research involving numerical simulations, analytical methods, and experimental investigations has been conducted on thin-walled open and close section struts for varied sectional geometries composed of diverse isotropic and anisotropic materials [28,29,97–115].

A novel P-version technique was introduced to construct a 3D finite element model (FEM) for the assessment of local, overall, and interactive buckling behavior in thin-walled components. The considered sectional geometries encompassed channel sections, boxes, and I section. One of the

key findings from this study highlights the significant influence of the length-to-web width ratio (L/B_w) on the types of buckling. Specifically, for short struts with an L/B_w ratio close to 1, a moderate mode of local buckling was observed. In contrast, the transition between local and overall buckling modes occurred at low L/B_w ratios, leading to an interactive buckling mode shape [97].

The local buckling analysis of fiber reinforced composite laminated beams subjected to a uniformly compressive load with diverse sectional geometries, including I, C, Z, T, and L shapes, was conducted analytically using two distinctive methods [101,102,108]. In the initial approach, the beam's sub-elements, such as flanges and webs, were examined individually according to the energy based semi-analytical approach, applying elastic rotational conditions at the junction where the flange and web are connected. Alternatively, another study introduced a comprehensive technique based on the Ritz method. This method involved the simultaneous analysis of individual webs and flanges in one system, incorporating appropriate continuity conditions at the junctions of the webs and flanges. Both approaches provided closed-form formulas to determine key quantities, such as the critical buckling load. This characteristic renders these two approaches highly valuable and practical from an engineering standpoint.

The impact of geometrical imperfections and the elastoplastic material behavior on the post-local-buckling response, compressive stiffness, and failure of thin-walled I and box section struts was assessed using finite element analysis [104]. The objective was to accurately compare the variation in axial compressive stiffness under elastic conditions to scenarios where material nonlinearity was taken into account. A series of experimental tests were also carried out on thin-walled sectional structures with intricate cross-sectional profiles, incorporating multiple

intermediate stiffeners. The obtained strength test results were compared with numerical simulations, validating the finding that the presence of intermediate stiffeners increases the local buckling stress level [106]. The exact finite strip method (FSM) was employed to assess the local buckling and initial postbuckling behavior of thin-walled I section struts [105]. Furthermore, the postbuckling stiffness and geometrically nonlinear response of channel section struts were evaluated using two distinctive analytical methods: the semi-energy and the full-energy FSM [28], [116]. In the initial approach, only the out-of-plane displacement is stipulated, whereas in the subsequent approach, both in-plane and out-of-plane displacement functions are encompassed in the computation right from the outset of the solution process. It is worth noting that in a compelling previous study, the impact of interlaminar flaws, specifically delamination, on the post-local buckling behavior of fiber-reinforced composite laminated angle section and T-section struts was examined according to the layerwise theory. The investigation revealed that the presence of delamination between the layers of the flanges significantly diminished the load-bearing capacity of composite laminated thin-walled structures [104].

In summary, based on an extensive literature review, it is evident that local buckling should be regarded as a critical design consideration for thin-walled struts, irrespective of their cross-sectional profile. Local buckling significantly impacts the axial compressive stiffness and, subsequently, the load-bearing capacity in an adverse manner. Consequently, it is imperative to prioritize the resolution of this pivotal concern in this type of practical and extensively utilized engineering structures by diligently exploring diverse avenues to identify effective solutions.

Given the proven enhancements in stiffness and strength achieved by incorporating graphene reinforcements in polymeric composite laminates, this paper represents an initial exploration into utilizing this two-dimensional nanomaterial as a reinforcement in composite laminated channel

section struts to assess how the incorporation of graphene with several symmetric and asymmetric distributions can improve the performance of channel section struts under compressive loads (uniform end-shortening), while avoiding the addition of intermediate stiffeners.

This study aims to compare different configurations of functionally graded graphene sheets distributed along the thickness directions of the flanges and web plates in channel section struts to determine the combination of patterns that has the greatest influence on enhancing the critical buckling end-shortening and the compressive axial stiffness. In addition to the material configuration study and comprehensive comparison of the post-local buckling characteristics between the most and least influential cases with the uniform distribution (UD) graphene pattern, the effect of geometrical parameters on critical buckling ends-shortening, post-local buckling equilibrium paths, and load-bearing capacity is also examined for various graphene distribution patterns in this research.

To achieve the research objectives, a layerwise theory based on the third-order shear deformation theory (TSDT) is developed for the first attempt on the channel section struts. Additionally, a detailed 3D finite element study is conducted by using the commercial software ABAQUS to incorporate the results obtained from the LW-TSDT. Furthermore, this paper includes a comparative analysis of the central processing unit (CPU) time between the two methods. These methods necessitate distinct total numbers of displacement and rotational degrees of freedom (DOFs) for an accurate assessment of the nonlinear response in channel section struts.

4.2. Theoretical formulation

This study specifically investigates multilayer laminated composite channel section struts, which consist of several subelements including two vertical plates referred to as flange1&2 and a horizontal plate known as the web, as illustrated in Fig. (4.1). The dimensions of the flanges and

web, represented by t_f , b_f , t_w , and b_w , respectively, are defined in terms of their thickness and width.

The overall length of the channel section strut is also denoted as L . Fig. (4.1) also visually represents the establishment of a local Cartesian coordinate system, with its origin positioned at the center of the mid-plane for each subelement within the structure. These coordinate systems serve as the basis for defining appropriate displacement and rotational shape functions.

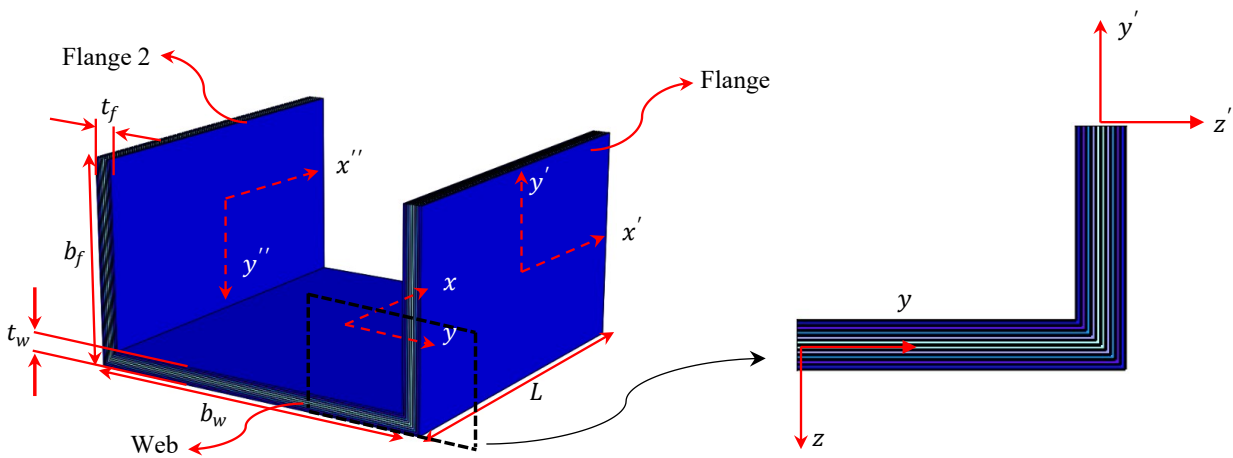


Figure 4-1 (a) A schematic FG-GRC laminated channel section struts with their local coordinate systems (b) detailed view half of the piecewise functionally graded graphene reinforced cross-section

As previously noted, every subcomponent (flanges and web) comprises N composite layers, with each layer composed of a polymeric matrix reinforced by graphene sheets, wherein the volume percentage of graphene varies. This variation leads to the formation of a laminated structure called a piecewise functionally graded graphene reinforced composite. In this study, two types of graphene reinforcement layers are considered: zigzag (referred to as 0° -ply) and armchair (referred to as 90° -ply). This article concentrates on analyzing and assessing six distinct non-uniform distribution patterns of graphene, comparing their reinforcing influence on that of the UD graphene dispersion. These non-uniform patterns include four symmetric distributions (FG-X,

FGX-FGX, FG-O, and FGO-FGO) and two asymmetric distributions (FG-V and FGV-FGV) presented in Table. (3.1), chapter 3.

Various combinations of the graphene distribution patterns outlined in Table. (3.1) can be chosen independently for both the flanges and the web. In order to enhance clarity, Fig. (4.2) presents schematic depictions of channel section struts where the flanges and web incorporate the same FG-X graphene distribution pattern.

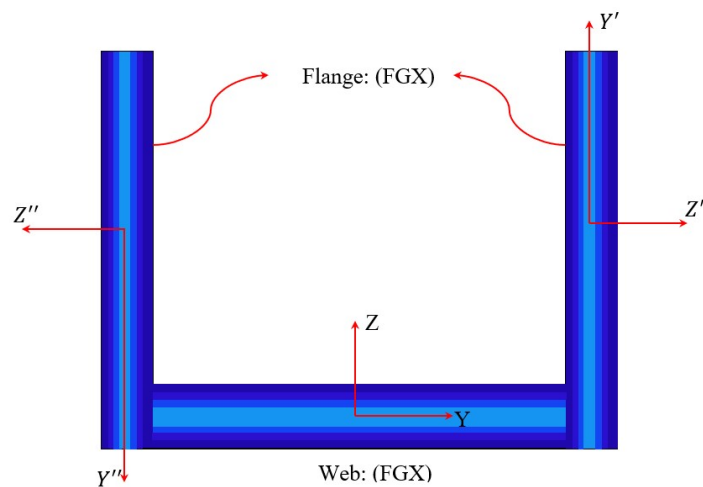


Figure 4-2 Schematic depiction of the cross-section with an FG-X graphene distribution pattern within both the flanges and the web.

It is imperative to acknowledge that the equations necessary for determining the thermomechanical properties of GRCs through the modified Halpin-Tsai mathematical model are congruent with those elaborated in section 2.2.2. Furthermore, the examination of the nonlinear instability behavior of the channel section struts employs the TSDT in conjunction with the Layerwise Theory. The comprehensive displacement equations derived from the TSDT were discussed in section 3.3.

4.3. Structural modelling of channel section struts

4.3.1. Modelling based on the LW-TSDT

According to the layerwise theory, the flanges and web plates need to be discretized into multiple numerical layers along their thickness directions. The number of numerical layers can vary, either being equal to, lower than, or higher than the number of graphene reinforced polymeric composite plies from the flanges and web. Increasing the number of numerical layers promises more accurate results. However, it is important to bear in mind that this advantage comes with a trade-off: an increase in the computational cost and CPU usage. In the context of the layerwise theory, it is necessary to assume independent rotational functions around the X and Y axes for each of the discretized layers. In this paper, the in-plane and out-of-plane displacement functions at the midplane of each numerical layer are defined by employing the TSDT.

Figure (4.3) depicts in detail the sequential procedures involved in accurately implementing the LW-TSDT. Initially, the FG-GRC channel section strut is divided into three distinct plates: two flanges and a web, each having its own local coordinate system positioned at the midplane center. Subsequently, each of these individual plates is discretized into arbitrary number of numerical layers along the thickness direction. During this stage, each of the divided numerical layers is treated as a plate. Accordingly, rotational and displacement shape functions can be established for their respective midplanes, in accordance with the principles of the TSDT. A critical aspect to be mindful of is ensuring that the shape functions meet the continuity conditions at the interface between any two adjacent, divided numerical layers. Additionally, they have to address the boundary conditions at both longitudinal ends of the channel section struts. The proposed theoretical advancements do not impose any limitations regarding the use of various types of edge supports. However, for the sake of conciseness, the present analysis focuses exclusively on the

FG-GRC channel section struts with clamped boundary conditions at both longitudinal ends, shown mathematically in Table. (4.1).

Table 4-1 Mathematical expressions of the boundary conditions at longitudinal ends of the FG-GRC channel section struts

Boundary condition		Out-of-plane displacement	Rotation
Clamped-Clamped	Flange	$w_f^{(i)} \Big _{x=-\frac{L_1}{2}} = w_f^{(i)} \Big _{x=\frac{L_1}{2}} = 0$ $i = 1..n$	$\varphi_{xf}^{(i)} \Big _{x=-\frac{L_1}{2}} = \varphi_{xf}^{(i)} \Big _{x=\frac{L_1}{2}} = 0$ $i = 1..n$
	Web	$w_w^{(i)} \Big _{x=-\frac{L_1}{2}} = w_w^{(i)} \Big _{x=\frac{L_1}{2}} = 0$ $i = 1..n$	$\varphi_{xw}^{(i)} \Big _{x=-\frac{L_1}{2}} = \varphi_{xw}^{(i)} \Big _{x=\frac{L_1}{2}} = 0$ $i = 1..n$

In the final step, the three plates (two flanges and a web) are assembled together to form a unique system for analysis. An essential consideration in this assembly process is ensuring that the rotational and displacement functions defined in the previous step satisfy the continuity conditions at the junction of the flange and web, where these plates are interconnected.

In-plane stress-free edge has been extensively adopted as a continuity condition at the junction of flange and web in different open section struts to bring the analytical and numerical approaches closer to reality when investigating their nonlinear post-local-buckling response. According to this condition considered in this paper, the nodes of the flanges and web plates located at the junction are allowed to move in-plane freely and their out-of-plane displacements are restricted. In details there are two coincidental nodes at any particular length location along the junction. One of which correspond to the flange, while the second node is associated with the web plate. This specific continuity condition limits the in-plane displacement of those nodes in the X-direction with the same value and have the same rotation around X and Y-axis. The physical meaning of the in-plane

stress-free edge condition is that after local buckling of the wall sections the junctions remain flat without any out-of-plane displacements, the mathematical formula is expressed as follows:

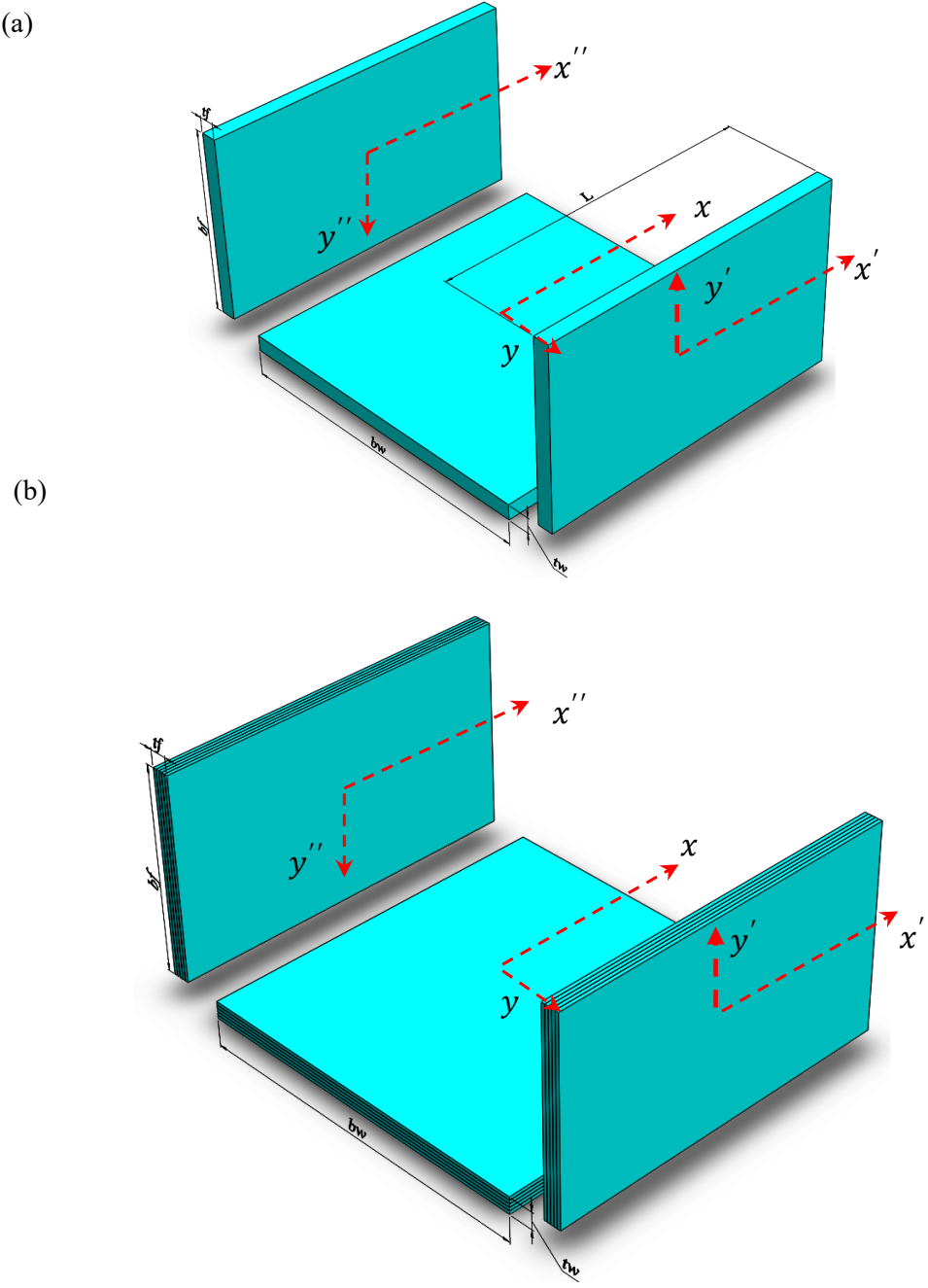


Figure 4-3 A typical channel section strut and segmentation of the flanges and web (a) Separation of flanges and web, (b) Discretization of flanges and web through their thickness based on the layerwise theory

$$(u_f^{(i)}, \varphi_{xf}^{(i)}, \varphi_{yf}^{(i)})|_{y' = \frac{-b_f}{2}} = (u_w^{(i)}, \varphi_{xw}^{(i)}, \varphi_{yw}^{(i)})|_{y = \frac{b_w}{2}}, \quad \{i = 1..n\}$$

$$(u_f^{(i)}, \varphi_{xf}^{(i)}, \varphi_{yf}^{(i)})|_{y'' = \frac{b_f}{2}} = (u_w^{(i)}, \varphi_{xw}^{(i)}, \varphi_{yw}^{(i)})|_{y = \frac{-b_w}{2}}, \quad \{i = 1..n\}$$

$$w_w^{(i)}|_{x = \frac{-L_1}{2}} = w_w^{(i)}|_{x = \frac{L_1}{2}} = w_w^{(i)}|_{y = \frac{-b_w}{2}} = w_w^{(i)}|_{y = \frac{b_w}{2}} = 0, \quad \{i = 1..n\} \quad (4-1)$$

These factors contribute to the increased complexity involved in designing the rotational and displacement functions for FG-GRC channel section struts. In Eq. (4.1), indexes "f" and "w" associated with the flange and web, respectively. For instance, $(u_f^{(i)}, w_f^{(i)})$ and $(u_w^{(i)}, w_w^{(i)})$ represent the in-plane and out-of-plane displacements of the i^{th} numerical layer located through the thickness of the flange and web, respectively. Additionally, $(\varphi_{xf}^{(i)}, \varphi_{yf}^{(i)})$ and $(\varphi_{xw}^{(i)}, \varphi_{yw}^{(i)})$ correspond to the midplane rotation of the i^{th} numerical layer of the flange and web, respectively.

As expressed in Eq. (4.1), all these rotational and displacement shape functions are defined according to the local coordinate systems established at the mid-plane center of the flanges and web plates.

Based on the boundary and continuity conditions described in Table. (4.1) and Eq. (4.1), the displacement fields for the assumed regions are modeled using polynomial expressions. The permissible functions for out-of-plane displacements are then determined according to Eq. (4.2):

$$w_w^{(1)} = \sum_{m=0}^M \sum_{n=0}^N \left(x - \frac{L}{2}\right) \left(x + \frac{L}{2}\right) \left(y + \frac{b_w}{2}\right) \left(y - \frac{b_w}{2}\right) w_{w,mn}^{(1)} x^m y^n, \quad w_w^{(1)} = w_w^{(i)} \quad i = 2..n$$

$$w_{f1}^{(1)} = \sum_{m=0}^M \sum_{n=0}^N \left(x - \frac{L}{2}\right) \left(x + \frac{L}{2}\right) \left(y' + \frac{b_f}{2}\right) w_{f1,mn}^{(1)} x^m y^n, \quad w_{f1}^{(1)} = w_{f1}^{(i)} \quad i = 2..n$$

$$w_{f2}^{(1)} = \sum_{m=0}^M \sum_{n=0}^N \left(x - \frac{L}{2}\right) \left(x + \frac{L}{2}\right) \left(y'' - \frac{b_f}{2}\right) w_{f2,mn}^{(1)} x^m y^n, \quad w_{f2}^{(1)} = w_{f2}^{(i)} \quad i = 2..n \quad (4-2)$$

As shown in Eq. (4.2), the out-of-plane displacement of the web (w_w) is restricted at its four longitudinal and transverse edges to meet both the boundary and continuity conditions. As discussed, these conditions involve the web being clamped at both longitudinal ends and maintaining straight at the junctions. This ensures proper alignment and structural integrity of the system. Furthermore, as a result of satisfying the continuity condition at the junctions, the deflection of the flanges is also restricted at those points. Given the absence of any interlaminar flaws, such as delamination, between the graphene reinforced composite plies in the flanges and web, all the plies included at each of these regions (flanges/web) experience the same out-of-plane displacement during deflection. Consequently, it is assumed that the out-of-plane displacements of all the discretized numerical layers within each flange or web are identical. This assumption ensures the continuity condition is met at the interface of numerical layers along the out-of-plane direction. With these explanations, it can be established that the total number of degrees of freedom considered for the out-of-plane displacements of channel section struts amounts to $3(M + 1)(N + 1)$.

The presumed polynomial displacement functions within the X and Y directions for both the flanges and web are expressed in Eqs. (4.3) and (4.4), respectively:

$$U_w^{ref} = -\varepsilon \times x + \sum_{p=0}^P \sum_{q=0}^Q \left(x - \frac{L}{2}\right) \left(x + \frac{L}{2}\right) U_{w,pq}^{ref} x^p y^q$$

$$U_w^{(1)} = U_w^{ref} + \theta_w^{(1)} \left(\frac{h_w^{(1)}}{2}\right) \varphi_{w,x}^{(1)} + \gamma_w^{(1)} \left(\frac{h_w^{(1)}}{2}\right) \psi_{w,x}^{(1)}$$

$$U_w^{(2)} = U_w^{ref} - \theta_w^{(2)} \left(\frac{h_w^{(2)}}{2}\right) \varphi_{w,x}^{(2)} - \gamma_w^{(2)} \left(\frac{h_w^{(2)}}{2}\right) \psi_{w,x}^{(2)}$$

⋮

$$U_w^{(n)} = U_w^{(n-1)} - \theta_w^{(n-1)} \left(\frac{h_w^{(n-1)}}{2} \right) \varphi_{w,x}^{(n-1)} - \gamma_w^{(n-1)} \left(\frac{h_w^{(n-1)}}{2} \right) \psi_{w,x}^{(n-1)} - \theta_w^{(n)} \left(\frac{h_w^{(n)}}{2} \right) \varphi_{w,x}^{(n)} - \gamma_w^{(n)} \left(\frac{h_w^{(n)}}{2} \right) \psi_{w,x}^{(n)}$$

$$U_{f_1}^{ref} = \left[\sum_{p=0}^P \sum_{q=0}^Q \left(x - \frac{L}{2} \right) \left(x + \frac{L}{2} \right) \left(y' + \frac{b_{f_1}}{2} \right) U_{f_1,pq}^{ref} x^p y^q \right] + U_w^{ref} \left(x, \frac{b_w}{2} \right)$$

$$U_{f_1}^{(1)} = U_{f_1}^{ref} + \theta_{f_1}^{(1)} \left(\frac{h_{f_1}^{(1)}}{2} \right) \varphi_{f_1,x}^{(1)} + \gamma_{f_1}^{(1)} \left(\frac{h_{f_1}^{(1)}}{2} \right) \psi_{f_1,x}^{(1)}$$

$$U_{f_1}^{(2)} = U_{f_1}^{ref} - \theta_{f_1}^{(2)} \left(\frac{h_{f_1}^{(2)}}{2} \right) \varphi_{f_1,x}^{(2)} - \gamma_{f_1}^{(2)} \left(\frac{h_{f_1}^{(2)}}{2} \right) \psi_{f_1,x}^{(2)}$$

⋮

$$U_{f_1}^{(n)} = U_{f_1}^{(n-1)} - \theta_{f_1}^{(n-1)} \left(\frac{h_{f_1}^{(n-1)}}{2} \right) \varphi_{f_1,x}^{(n-1)} - \gamma_{f_1}^{(n-1)} \left(\frac{h_{f_1}^{(n-1)}}{2} \right) \psi_{f_1,x}^{(n-1)} - \theta_{f_1}^{(n)} \left(\frac{h_{f_1}^{(n)}}{2} \right) \varphi_{f_1,x}^{(n)} - \gamma_{f_1}^{(n)} \left(\frac{h_{f_1}^{(n)}}{2} \right) \psi_{f_1,x}^{(n)}$$

$$U_{f_2}^{ref} = \left[\sum_{p=0}^P \sum_{q=0}^Q \left(x - \frac{L}{2} \right) \left(x + \frac{L}{2} \right) \left(y'' - \frac{b_{f_2}}{2} \right) U_{f_2,pq}^{ref} x^p y^q \right] + U_w^{ref} \left(x, \frac{-b_w}{2} \right)$$

$$U_{f_2}^{(1)} = U_{f_2}^{ref} + \theta_{f_2}^{(1)} \left(\frac{h_{f_2}^{(1)}}{2} \right) \varphi_{f_2,x}^{(1)} + \gamma_{f_2}^{(1)} \left(\frac{h_{f_2}^{(1)}}{2} \right) \psi_{f_2,x}^{(1)}$$

$$U_{f_2}^{(2)} = U_{f_2}^{ref} - \theta_{f_2}^{(2)} \left(\frac{h_{f_2}^{(2)}}{2} \right) \varphi_{f_2,x}^{(2)} - \gamma_{f_2}^{(2)} \left(\frac{h_{f_2}^{(2)}}{2} \right) \psi_{f_2,x}^{(2)}$$

⋮

$$U_{f_2}^{(n)} = U_{f_2}^{(n-1)} - \theta_{f_2}^{(n-1)} \left(\frac{h_{f_2}^{(n-1)}}{2} \right) \varphi_{f_2,x}^{(n-1)} - \gamma_{f_2}^{(n-1)} \left(\frac{h_{f_2}^{(n-1)}}{2} \right) \psi_{f_2,x}^{(n-1)} - \theta_{f_2}^{(n)} \left(\frac{h_{f_2}^{(n)}}{2} \right) \varphi_{f_2,x}^{(n)} - \gamma_{f_2}^{(n)} \left(\frac{h_{f_2}^{(n)}}{2} \right) \psi_{f_2,x}^{(n)} \quad (4-3)$$

$$V_w^{ref} = \sum_{r=0}^R \sum_{s=0}^S V_{w,rs}^{ref} x^r y^s$$

$$V_w^{(1)} = V_w^{ref} + \theta_w^{(1)} \left(\frac{h_w^{(1)}}{2} \right) \varphi_{w,y}^{(1)} + \gamma_w^{(1)} \left(\frac{h_w^{(1)}}{2} \right) \psi_{w,y}^{(1)}$$

$$V_w^{(2)} = V_w^{ref} - \theta_w^{(2)} \left(\frac{h_w^{(2)}}{2} \right) \varphi_{w,y}^{(2)} - \gamma_w^{(2)} \left(\frac{h_w^{(2)}}{2} \right) \psi_{w,y}^{(2)}$$

⋮

$$V_w^{(n)} = V_w^{(n-1)} - \theta_w^{(n-1)} \left(\frac{h_w^{(n-1)}}{2} \right) \varphi_{w,y}^{(n-1)} - \gamma_w^{(n-1)} \left(\frac{h_w^{(n-1)}}{2} \right) \psi_{w,y}^{(n-1)} - \theta_w^{(n)} \left(\frac{h_w^{(n)}}{2} \right) \varphi_{w,y}^{(n)} - \gamma_w^{(n)} \left(\frac{h_w^{(n)}}{2} \right) \psi_{w,y}^{(n)}$$

$$V_{f1}^{ref} = \sum_{r=0}^R \sum_{s=0}^S V_{f1,pq}^{ref} x^p y^q$$

$$V_{f1}^{(1)} = V_{f1}^{ref} + \theta_{f1}^{(1)} \left(\frac{h_{f1}^{(1)}}{2} \right) \varphi_{f1,y}^{(1)} + \gamma_{f1}^{(1)} \left(\frac{h_{f1}^{(1)}}{2} \right) \psi_{f1,y}^{(1)}$$

$$V_{f1}^{(2)} = V_{f1}^{ref} - \theta_{f1}^{(2)} \left(\frac{h_{f1}^{(2)}}{2} \right) \varphi_{f1,y}^{(2)} - \gamma_{f1}^{(2)} \left(\frac{h_{f1}^{(2)}}{2} \right) \psi_{f1,y}^{(2)}$$

⋮

$$V_{f1}^{(n)} = V_{f1}^{(n-1)} - \theta_{f1}^{(n-1)} \left(\frac{h_{f1}^{(n-1)}}{2} \right) \varphi_{f1,y}^{(n-1)} - \gamma_{f1}^{(n-1)} \left(\frac{h_{f1}^{(n-1)}}{2} \right) \psi_{f1,y}^{(n-1)} - \theta_{f1}^{(n)} \left(\frac{h_{f1}^{(n)}}{2} \right) \varphi_{f1,y}^{(n)} - \gamma_{f1}^{(n)} \left(\frac{h_{f1}^{(n)}}{2} \right) \psi_{f1,y}^{(n)}$$

$$V_{f2}^{ref} = \sum_{r=0}^R \sum_{s=0}^S V_{f2,pq}^{ref} x^p y^q$$

$$V_{f2}^{(1)} = V_{f2}^{ref} + \theta_{f2}^{(1)} \left(\frac{h_{f2}^{(1)}}{2} \right) \varphi_{f2,y}^{(1)} + \gamma_{f2}^{(1)} \left(\frac{h_{f2}^{(1)}}{2} \right) \psi_{f2,y}^{(1)}$$

$$V_{f2}^{(2)} = V_{f2}^{ref} - \theta_{f2}^{(2)} \left(\frac{h_{f2}^{(2)}}{2} \right) \varphi_{f2,y}^{(2)} - \gamma_{f2}^{(2)} \left(\frac{h_{f2}^{(2)}}{2} \right) \psi_{f2,y}^{(2)}$$

⋮

$$V_{f2}^{(n)} = V_{f2}^{(n-1)} - \theta_{f2}^{(n-1)} \left(\frac{h_{f2}^{(n-1)}}{2} \right) \varphi_{f2,y}^{(n-1)} - \gamma_{f2}^{(n-1)} \left(\frac{h_{f2}^{(n-1)}}{2} \right) \psi_{f2,y}^{(n-1)} - \theta_{f2}^{(n)} \left(\frac{h_{f2}^{(n)}}{2} \right) \varphi_{f2,y}^{(n)} - \gamma_{f2}^{(n)} \left(\frac{h_{f2}^{(n)}}{2} \right) \psi_{f2,y}^{(n)} \quad (4-4)$$

One crucial aspect that requires attention is the inclusion of reference values, U^{ref} and V^{ref} , for in-plane displacements of the flanges and web through the X and Y directions. These reference values are essential to maintain in-plane continuity condition at the interface of the numerical layers discretized throughout the thickness of each different subelements (flanges and web).

Moreover, in order to fulfill the continuity condition at the junction, the reference in-plane displacements of the flange (U_f^{ref}, V_f^{ref}) must be equivalent to the reference values of the web (U_w^{ref}, V_w^{ref}) through the junction at any specific length coordinate. In Eq. (4.3), the expression $\varepsilon \times x$ represents the longitudinal compression-induced end-shortening applied to the channel section strut. Additionally, $h_f^{(i)}$ and $h_w^{(i)}$ indicate the thickness of the i^{th} numerical layer within the flanges and web, respectively. Drawing from the outlined requirements concerning continuity and boundary conditions necessary for in-plane displacement functions in both X and Y directions, it can be deduced that the overall number of degrees of freedom pertaining to these functions is given by $3[(P + 1)(Q + 1) + (R + 1)(S + 1)]$.

In addition, the midplane rotation of each numerical layers defined through the flanges and web can be expressed as follows with considering the continuity conditions at the boundaries of different regions,

$$\varphi_{w,x}^{(1)} = \sum_{j=0}^J \sum_{k=0}^K \left(x + \frac{L}{2}\right) \left(x + \frac{L}{2}\right) \phi_{wx,jk}^{(1)} x^j y^k$$

⋮

$$\varphi_{w,x}^{(n)} = \sum_{j=0}^J \sum_{k=0}^K \left(x + \frac{L}{2}\right) \left(x + \frac{L}{2}\right) \phi_{wx,jk}^{(n)} x^j y^k$$

$$\varphi_{f1,x}^{(1)} = \left[\sum_{j=0}^J \sum_{k=0}^K \left(x + \frac{L}{2}\right) \left(x + \frac{L}{2}\right) \left(y' + \frac{b_{f1}}{2}\right) \phi_{f1x,jk}^{(1)} x^j y^k \right] + \varphi_{w,x}^{(1)} \left(x, \frac{b_w}{2}\right)$$

⋮

$$\varphi_{f1,x}^{(n)} = \left[\sum_{j=0}^J \sum_{k=0}^K \left(x + \frac{L}{2}\right) \left(x + \frac{L}{2}\right) \left(y' + \frac{b_{f1}}{2}\right) \phi_{f1x,jk}^{(n)} x^j y^k \right] + \varphi_{w,x}^{(n)} \left(x, \frac{b_w}{2}\right)$$

$$\varphi_{f2,x}^{(1)} = \left[\sum_{j=0}^J \sum_{k=0}^K \left(x + \frac{L}{2}\right) \left(x + \frac{L}{2}\right) \left(y'' - \frac{b_f}{2}\right) \phi_{f2x,jk}^{(1)} x^j y^k \right] + \varphi_{w,x}^{(1)} \left(x, \frac{-b_w}{2}\right)$$

⋮

$$\varphi_{f2,x}^{(n)} = \left[\sum_{j=0}^J \sum_{k=0}^K \left(x + \frac{L}{2}\right) \left(x + \frac{L}{2}\right) \left(y'' - \frac{b_f}{2}\right) \phi_{f2x,jk}^{(n)} x^j y^k \right] + \varphi_{w,x}^{(n)} \left(x, \frac{-b_w}{2}\right) \quad (4-5)$$

$$\varphi_{w,y}^{(1)} = \sum_{d=0}^D \sum_{t=0}^T \phi_{wy,dt}^{(1)} x^d y^t$$

⋮

$$\varphi_{w,y}^{(n)} = \sum_{d=0}^D \sum_{t=0}^T \phi_{wy,dt}^{(n)} x^d y^t$$

$$\varphi_{f1,y}^{(1)} = \left[\sum_{d=0}^D \sum_{t=0}^T \left(y' + \frac{b_{f1}}{2}\right) \phi_{f1y,dt}^{(1)} x^d y^t \right] + \varphi_{w,y}^{(1)} \left(x, \frac{b_w}{2}\right)$$

⋮

$$\varphi_{f1,y}^{(n)} = \left[\sum_{d=0}^D \sum_{t=0}^T \left(y' + \frac{b_{f1}}{2}\right) \phi_{f1y,dt}^{(n)} x^d y^t \right] + \varphi_{w,y}^{(n)} \left(x, \frac{b_w}{2}\right)$$

$$\varphi_{f2,y}^{(1)} = \left[\sum_{d=0}^D \sum_{t=0}^T \left(y'' - \frac{b_f}{2}\right) \phi_{f2y,dt}^{(1)} x^d y^t \right] + \varphi_{w,y}^{(1)} \left(x, \frac{-b_w}{2}\right)$$

⋮

$$\varphi_{f2,y}^{(n)} = \left[\sum_{d=0}^D \sum_{t=0}^T \left(y'' - \frac{b_f}{2}\right) \phi_{f2y,dt}^{(n)} x^d y^t \right] + \varphi_{w,y}^{(n)} \left(x, \frac{-b_w}{2}\right) \quad (4-6)$$

As depicted in Eq. (4.5), the midplane rotation of various numerical layers around the Y-axes, $(\varphi_{w,x}^{(i)}, \varphi_{f,x}^{(i)})$ is constrained at the longitudinal ends of the channel section strut. This constraint arises due to the presence of fixed boundary conditions at those edges. In the layerwise theory, it is essential to consider individual rotation functions for each numerical layer to accurately assess their stress and strain distribution. Referring to Fig. (4.3), the FG-GRC channel section strut is

discretized into $3n$ numerical layers. Thus, we can conclude that there are $3n$ layers requiring independent rotation considerations. Therefore, the total number of unknown coefficients relating to the rotational functions amounts to $3n((J + 1)(K + 1) + (D + 1)(T + 1))$.

In the evaluation of the nonlinear compressive behavior in FG-GRC laminated channel section struts, the analysis employs the minimum total potential energy principle. The total potential energy involves the summation of two components: the potential energy of external loads, which accounts for the work done by external forces on the structure, and the total strain energy, which considers the internal stresses and deformations within the material of the structure [67]. Regarding the fact that the channel section strut experiences uniform end-shortening, it follows that the potential energy associated with external forces is negligible, resulting in the total potential energy of the structure being equivalent to the total strain energy. As previously discussed, the laminated structure is discretized into multiple numerical layers along the thickness direction of the flanges and web. To account for deformation effects, rotational and displacement shape functions are applied to each of these layers, based on the TSDT, consequently, it can be inferred that the total potential energy which is equal to the total internal strain energy of the structure can be derived by summing the individual strain energy contributions from each of the numerical layers, as illustrated in the following equations:

$$\begin{aligned} \Pi^{Total} &= \sum_{i=1}^n U_w^{(i)} + \sum_{i=1}^n U_{f1}^{(i)} + \sum_{i=1}^n U_{f2}^{(i)} \\ \Pi^{Total} &= \left(\frac{1}{2}\right) \left[\sum_{i=1}^n \int (\sigma_w^{(i)})^T \varepsilon_w^{(i)} dV + \sum_{i=1}^n \int (\sigma_{f1}^{(i)})^T \varepsilon_{f1}^{(i)} dV + \sum_{i=1}^n \int (\sigma_{f2}^{(i)})^T \varepsilon_{f2}^{(i)} dV \right] \end{aligned} \quad (4-7)$$

To maintain brevity, the strain energy of the first numerical layer positioned in the web ($U_w^{(1)}$), illustrated in Fig. (4.3), is just extended based on the mechanical strains as well as the stiffness matrixes as follows

$$\begin{aligned}
U_w^{(1)} &= \int \frac{1}{2} \bar{\sigma}^T \bar{\varepsilon} dV \\
&= \frac{1}{2} \int_{-\frac{b_w}{2}}^{\frac{b_w}{2}} \int_{-\frac{L}{2}}^{\frac{L}{2}} \left(\{\varepsilon^0\}_w^{(1)} [A]_w^{(1)} \{\varepsilon^0\}_w^{(1)T} + 2\{\varepsilon^0\}_w^{(1)} [B]_w^{(1)} \{\varepsilon^1\}_w^{(1)T} + \{\varepsilon^1\}_w^{(1)} [D]_w^{(1)} \{\varepsilon^1\}_w^{(1)T} + 2\{\varepsilon^0\}_w^{(1)} [E]_w^{(1)} \{\varepsilon^3\}_w^{(1)T} + \right. \\
&\quad \left. \{\varepsilon^1\}_w^{(1)} [F]_w^{(1)} \{\varepsilon^3\}_w^{(1)T} + \{\varepsilon^3\}_w^{(1)} [H]_w^{(1)} \{\varepsilon^3\}_w^{(1)T} + \{\gamma^0\}_w^{(1)} [As]_w^{(1)} \{\gamma^0\}_w^{(1)T} + 2\{\gamma^0\}_w^{(1)} [Ds]_w^{(1)} \{\gamma^2\}_w^{(1)T} + \right. \\
&\quad \left. \{\gamma^2\}_w^{(1)} [Fs]_w^{(1)} \{\gamma^2\}_w^{(1)T} \right) \quad (4-8)
\end{aligned}$$

Following this stage, the total potential energy should be minimized by using the unknown displacement and rotation coefficients as shown in Eqs. (4.9) and (4.10) [60]

$$\frac{\partial \Pi}{\partial \chi} = 0 \quad (4-9)$$

where χ is the vector of unknowns, expressed by

$$\begin{aligned}
\chi = & \left\{ \sum_{p=0}^P \sum_{q=0}^Q (u_{w,pq}^{ref} + u_{f1,pq}^{ref} + u_{f2,pq}^{ref}), \sum_{r=0}^R \sum_{s=0}^S (v_{w,rs}^{ref} + v_{f1,rs}^{ref} + v_{f2,rs}^{ref}), \sum_{m=0}^M \sum_{n=0}^N (w_{w,mn}^{ref} + w_{f1,mn}^{ref} + \right. \\
& w_{f2,mn}^{ref}), (\sum_{i=1}^n \sum_{j=0}^J \sum_{k=0}^K \phi_{wx,jk}^{(i)} + \sum_{i=1}^n \sum_{j=0}^J \sum_{k=0}^K \phi_{f1x,jk}^{(i)} + \sum_{i=1}^n \sum_{j=0}^J \sum_{k=0}^K \phi_{f2x,jk}^{(i)}), (\sum_{i=1}^n \sum_{d=0}^D \sum_{t=0}^T \phi_{wy,dt}^{(i)} + \\
& \left. \sum_{i=1}^n \sum_{d=0}^D \sum_{t=0}^T \phi_{f1y,dt}^{(i)} + \sum_{i=1}^n \sum_{d=0}^D \sum_{t=0}^T \phi_{f2y,dt}^{(i)}) \right\} \quad (4-10)
\end{aligned}$$

Eq. (4.10) leads to the nonlinear matrix equation of the FG-GRC channel section strut:

$$[K(T, \chi)]\{\chi\} = \{F\} \quad (4-11)$$

where $[K(T, \chi)]$ is the stiffness matrix; and $\{\chi\}$ is the Jacobi expanded coefficients, and $\{F\}$ is the force matrices.

The Newton-Raphson iterative procedure is a commonly used technique to solve nonlinear system of equations in the analysis of nonlinear postbuckling, as described by Eq. (4.11).

4.3.2. Modelling based on the finite element simulation

As part of the verification process to ensure the accuracy of the results obtained from the LW-TSDT approach, a 3D FEM is developed using ABAQUS nonlinear finite element code. Notably, conducting a nonlinear postbuckling analysis with ABAQUS requires two crucial steps. First, after

creating the 3D model and incorporating appropriate material properties, loading, and boundary conditions, a linear perturbation buckling analysis is performed to determine various buckling mode shapes of the channel section struts. Once this step is completed, the linear buckling analysis is replaced by the static Riks method in the next step. The Riks method accounts for nonlinear geometric effects, and the first buckling mode shape obtained in the first step is introduced into the Riks method as an imperfection. It is essential to emphasize that the amplitude of this imperfection significantly influences the convergence of the nonlinear postbuckling problem. In this paper, the amplitude assigned to the channel section struts is set at 0.001 times the magnitude of the first buckling mode shape.

The clamped boundary condition adopted as edge support in this study, as depicted in Fig. (4.4) (a), is implemented in the finite element simulation to confine the local out-of-plane displacement of the flanges and web. Additionally, a displacement load, functioning as an end-shortening, is uniformly applied to both ends of the channel section strut.

In the finite element simulation, the 3D, 8-node, linear isoperimetric element (C3D8) is utilized. The C3D8 element in ABAQUS represents a brick-shaped volume with eight nodes situated at specific coordinates in the 3D space, defining its geometry. It is capable of deformation and shape alteration when subjected to applied loads or constraints. With each node having three DOFs, translation displacement along the X, Y, and Z axes, the element possesses a total of 24 DOFs (8 nodes * 3 DOFs per node).

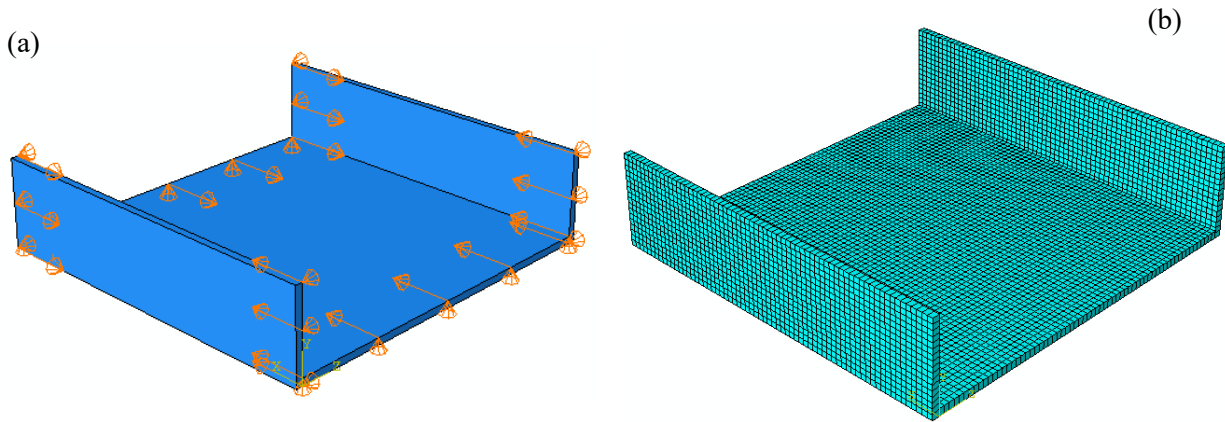


Figure 4-4 A typical channel section strut modelled based on the finite element simulation (a) Implementing loading and boundary conditions, (b) Diagrammatic representation of the mesh for the channel section strut

4.4. Results and discussion

4.4.1. GRC laminated channel section strut with UD graphene pattern

As elucidated in this paper, the main objective is to perform a comparative analysis focused on the distribution patterns of graphene. This analysis involves evaluating how these patterns impact both the post-local-buckling behavior and the axial compressive stiffness of composite channel section struts. To accomplish this, a comparison is necessary between various distribution patterns and a reference case, where the UD pattern is considered as the benchmark for the analysis.

The initial assumption dictates that all distinct regions of the channel section struts, encompassing two vertical plates (flanges) and a horizontal one (web), are composed of ten graphene-reinforced composite plies exhibiting the UD distribution pattern. Consequently, all outcomes pertaining to the analysis of nonlinear compressive stability are obtained based on this configuration. Subsequently, the analysis proceeds with an assumption that the UD graphene reinforcement distribution pattern for the web remains unaltered. Meanwhile, the graphene distribution patterns across the thickness directions of both flanges undergo modification, transitioning to non-uniform distributions including FG-X, FGX-FGX, FG-O, FGO-FGO, FG-V, and FGV-FGV. The purpose is to assess the influence of different non-uniform graphene

distribution patterns applied to the flanges on the post-local-buckling response of channel section struts, while keeping the web's graphene distribution constant (UD) to identify the most and least effective non-uniform distributions can be chosen for the flanges of channel section struts.

Finally, the optimal non-uniform graphene distribution pattern is chosen for the flanges, remaining unchanged. In contrast, various non-uniform graphene distribution patterns are examined for the web, replacing the UD pattern, to compare their effects with the reference case (flanges and web with UD graphene distribution pattern). This comparative analysis is performed to identify the most advantageous graphene distribution patterns to be adopted for this open-section strut. Furthermore, this process will be reiterated using the least favorable non-uniform graphene distribution patterns obtained for the flanges to ultimately determine the weakest graphene distribution patterns that can be chosen for the entire channel section strut.

There are two essential points to emphasize: first, this paper considers the same graphene distribution for both flanges in all cases under evaluation to maintain the symmetric condition. Second, the total graphene volume percentage remains constant across all case studies; the only variation lies in the graphene distribution patterns.

As illustrated in Fig. (4.5), the influence of the geometrical parameter, specifically the ratio of the flange width to the web width, on the critical buckling end-shortening of the UD channel section struts (Web: UD, both flanges: UD) is evaluated through conducting a nonlinear buckling analysis. The purpose is to identify the ratio at which the structure exhibits the maximum value of critical buckling end-shortening. The results demonstrate a strong concurrence between the outcomes obtained through the LW-TSDT and those assessed using the FEM. Clearly, an optimal shape factor (the ratio of flange width to web width) exists ($\frac{b_f}{b_w} = 0.25$), where channel section

struts with a UD graphene distribution experience the highest level of critical buckling end-shortening which is approximately $u_{cr0} = 0.225$. Conversely, an increase in the shape factor adversely impacts the critical buckling end-shortening of the structure, leading to a weakening of the channel section strut. Notably, the highest critical buckling end-shortening is around 1.5 times the minimum value, $u_{cr0} \approx 0.15$, associated with a shape factor of 1.

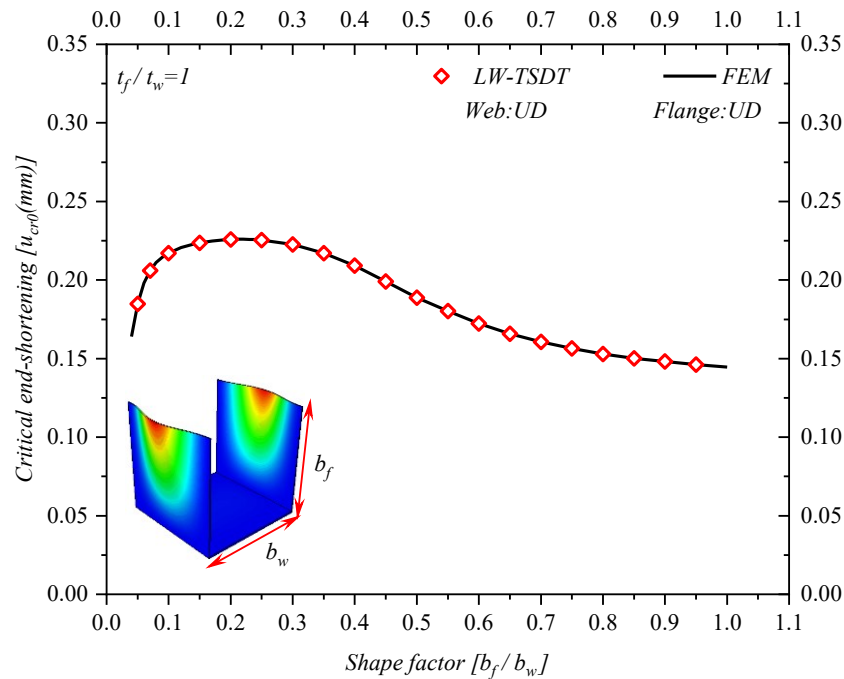


Figure 4-5 Variation of the critical buckling end-shortening with the shape factor

Based on the conclusions drawn from Fig. (4.5), the best shape factor ratio of $\frac{b_f}{b_w} = 0.25$ is chosen for the subsequent comparative analysis, where the flange thickness is equal to that of the web ($\frac{t_f}{t_w} = 1$).

It is noteworthy that the LW-TSDT analysis considers a total of 6615 DOFs for the buckling analysis of the UD laminated composite channel section strut, resulting in a tangent stiffness matrix order of 6615*6615. In contrast, the finite element model employs hexahedral 3D 8-node linear isoperimetric elements (C3D8), leading to 16272 independent DOFs. This significant difference

in number of DOF handled by the two approaches (semi-analytical and numerical) illustrates the LW-TSDT's superior computational efficiency over the developed finite element model. Table. (4.2) provides a comprehensive overview of the analysis's runtime and CPU usage. Upon a brief examination of the table, it is evident that the proposed method (LW-TSDT) exhibits a relative running time approximately 31% quicker than the FEM.

Table 4-2 Comparison of computing time and CPU usage in performed simulations and computational performance of proposed methodology (UD, $\frac{b_f}{b_w} = 0.25, \frac{t_f}{t_w} = 1$)

Solution method		
	DOF	6615
Present Method (LW-TSDT)	Running time (s)	758
	CPU usage (%)	21
	U_{cr}	0.22541
	DOF	16272
Finite Element Method (ABAQUS)	Running time (s)	993
	CPU usage (%)	37
	U_{cr}	0.22541
Discrepancy performance time (%)		
$\frac{(ABAQUS - LWTSDT)}{LWTSDT} \times 100$		31 %

Fig. (4.6) depicts the postbuckling equilibrium paths of the flanges and web in a channel section strut with UD graphene distribution patterns by considering the straightness of the junctions (post-local-buckling). The out-of-plane displacement of the flange is related to the center of the flange's free-edge, while the deflection of the web is connected to its center. Like Fig. (4.5), there is a remarkable agreement between the results obtained through the LW-TSDT and those evaluated using the finite element analysis.

Another noteworthy observation from this figure is that in this particular geometry, both the flange and web deflect simultaneously.

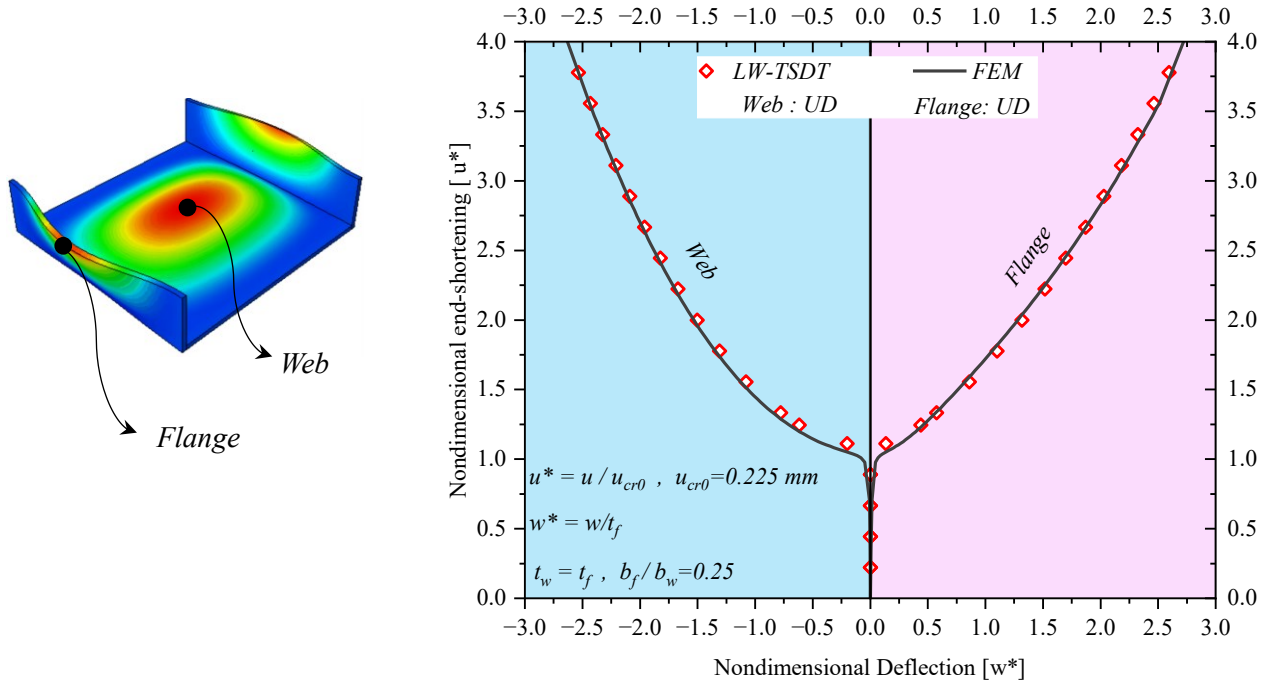


Figure 4-6 Nonlinear postbuckling equilibrium paths of flange and web in a channel section strut with UD graphene distribution pattern

4.4.2. Comparison analysis on the nonuniform graphene distribution patterns

In this phase, the substitution of various non-uniform graphene distribution patterns is necessitated. Specifically, four symmetric patterns (FG-X, FGX-FGX, FG-O, and FGO-FGO) and two asymmetric patterns (FG-V and FGV-FGV) are introduced in place of UD along the thickness direction of the flanges. Meanwhile, the web maintains a constant UD graphene pattern. The objective is to compare the impact of these symmetric and asymmetric substitutions on the nonlinear stability of the channel section struts as depicted in Figs. (4.7) and (4.8), respectively.

Firstly, it is important to emphasize that in Figs. (4.7) and (4.8) as well as subsequent figures in this section and section 4.3, the UD graphene distribution pattern serves as the reference case.

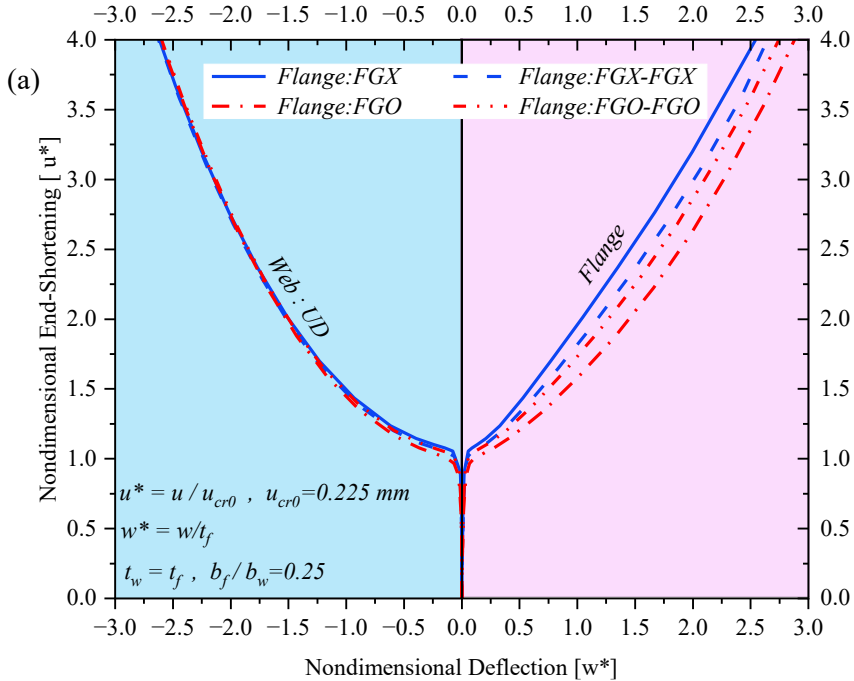
Consequently, all cases' end-shortening and compressive loads are normalized based on the critical values associated with the UD dispersion, namely $u_{cr0}^* = 0.225$ (mm) and $P_{cr0}^* = 60$ (KN).

The results shown in Figs. (4.7)(a) and (4.8)(a) imply that beyond the bifurcation point (at that point the deformation of the structure commences), at any level of loading (u^*), the nondimensional out-of-plane displacement of the flange with FG-X graphene distribution pattern is consistently lower than other symmetric and asymmetric graphene distributions. Conversely, the nondimensional out-of-plane displacement of the flange with FG-O graphene dispersion is higher than other cases.

Furthermore, Figs. (4.7)(b) and (4.8)(b) reveals that the load-bearing capacity of the channel section strut with flange of FG-X graphene distribution surpasses that of the other distributions. For example, when the nondimensional end-shortening reaches $u^* = 2$, the nondimensional compressive load (P^*) of the channel section strut with FG-X flange amounts to 1.62, whereas the weakest case, FG-O flange, has a value of 1.5. Notably, at this end-shortening, the nondimensional out-of-plane displacement of the FG-X and FG-O flanges are approximately 1 and 1.5, respectively, providing clear evidence that the flange's compressive stiffness with FG-X graphene distribution patterns is higher than the other cases, as it exhibits lower deflection under greater compressive loading.

Additionally, it is evident that at this particular value of shape factor ($\frac{b_f}{b_w} = 0.25$), the postbuckling response of the web takes precedence. On one hand, the variation of the graphene distribution pattern of the flange does not exert any discernible influence on the postbuckling equilibrium paths of the web, with all cases showing almost identical responses when the webs have UD graphene patterns. On the other hand, despite the flanges being composed of several

distinct graphene distribution patterns and displaying different postbuckling responses, the bifurcation points of all evaluated cases nearly coincide with each other.



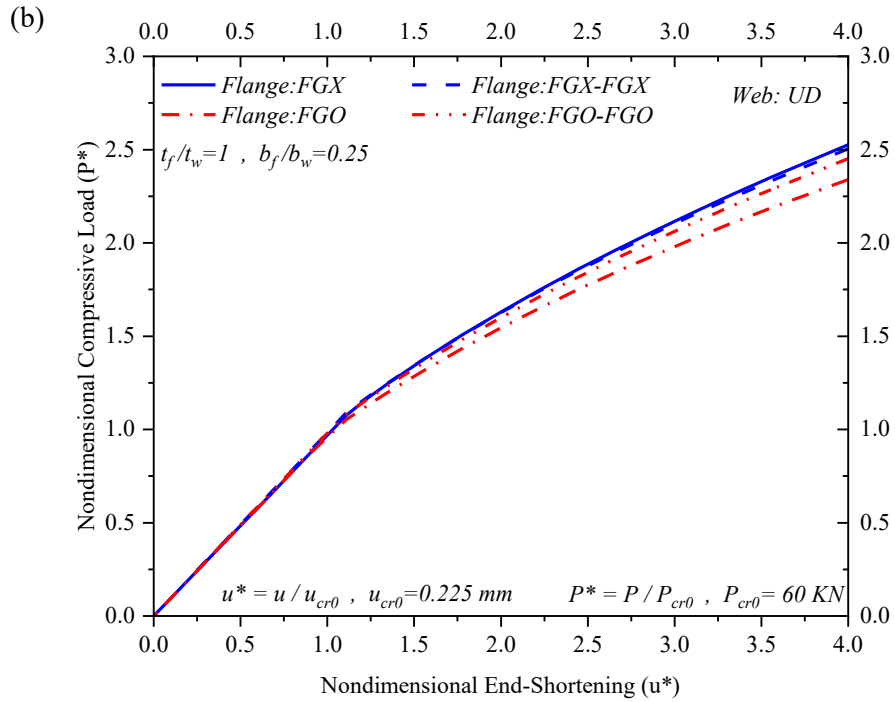
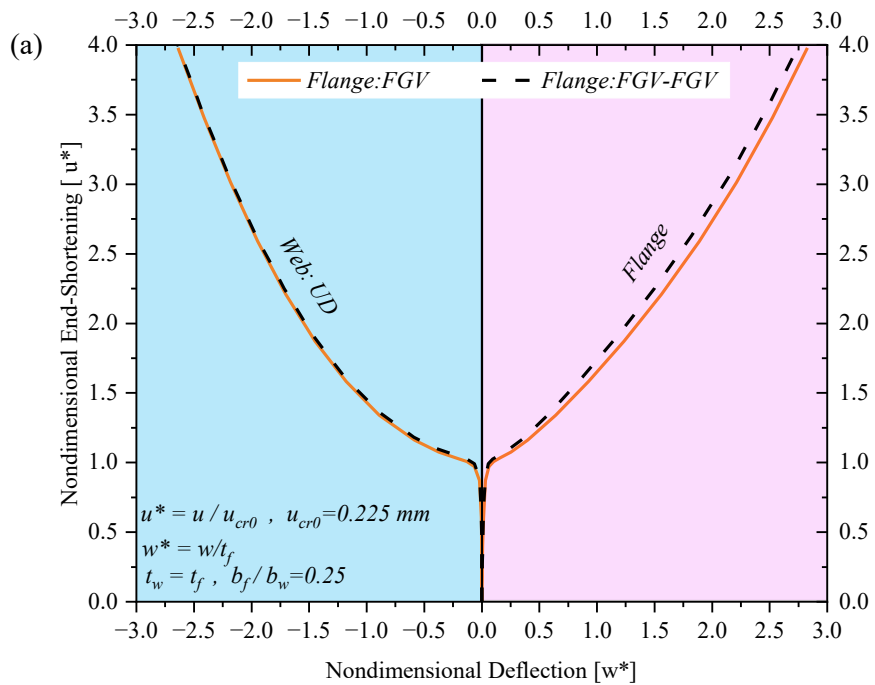


Figure 4-7 Comparison of nonuniform symmetric graphene distribution patterns of the flanges on (a) nonlinear postbuckling response and (b) load-bearing capacity of the FG-GRC channel section struts with web: UD



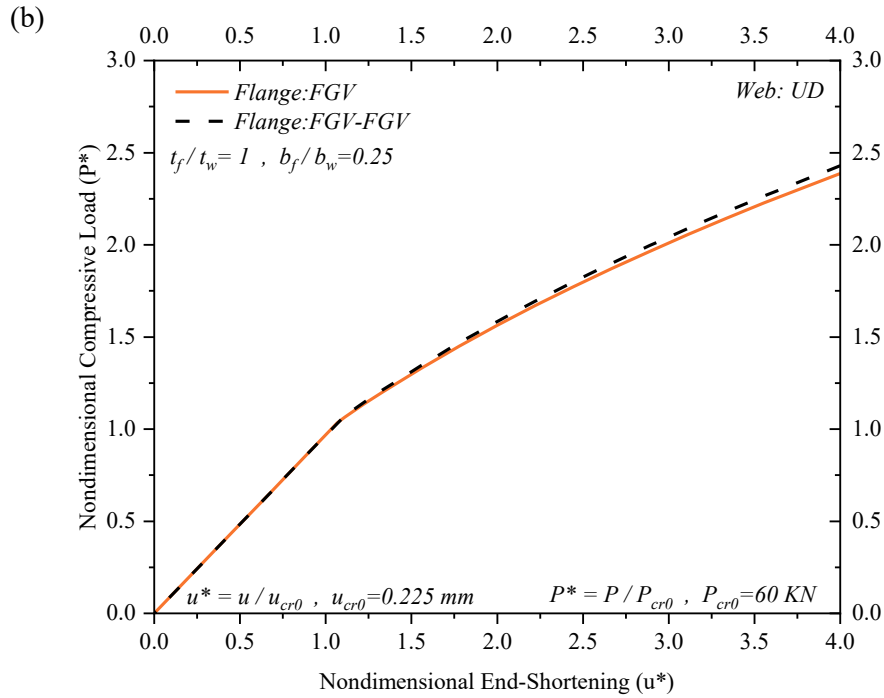


Figure 4-8 Comparison of nonuniform asymmetric graphene distribution patterns of the flanges on (a) nonlinear postbuckling response and (b) load-bearing capacity of the FG-GRC channel section struts with web: UD

In the final stage of the comparison, the foremost objective is to identify the optimal arrangements of graphene distribution patterns for the flanges and web. These arrangements are intended to yield the most favorable impact on both the critical buckling end-shortening and nonlinear compressive response of the channel section struts when compared to the UD graphene dispersion. To achieve this, it is required to consider the FG-X graphene distribution pattern as the best case for the flanges of the channel section struts, based on the above-mentioned results. Subsequently, stability analysis is conducted, where several distinct symmetric and asymmetric graphene distribution patterns are introduced along the thickness direction of the web. As a result of the comparative analysis, the optimal combination of graphene distribution patterns to be implemented for both flanges and the web is identified. As previously stated, this process needs to be repeated to investigate the worst combination. The only difference lies in employing the FG-O

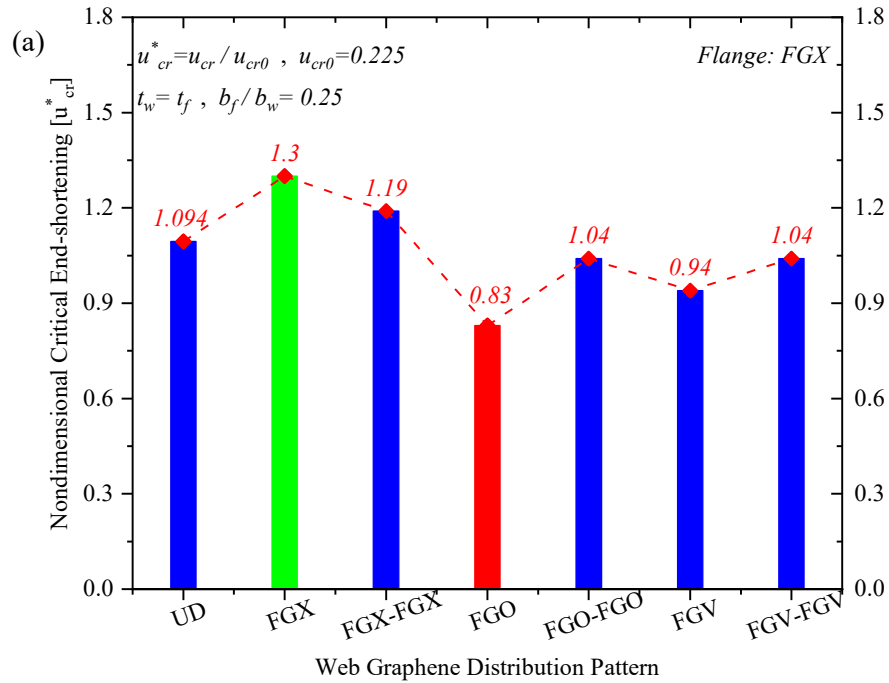
graphene distribution pattern as the weakest case for the flanges of the channel section strut, in contrast to the previous employment of FG-X.

Figure (4.9) presents bar charts that depict the correlation between the nondimensional critical buckling end-shortening of the channel section struts and the different graphene distribution patterns utilized for the web plate. It is important to note that Fig. (4.9)(a) corresponds to cases where the FG-X graphene distribution pattern is used for the flanges, while Fig. (4.9)(b) represents the results associated with the implementation of FG-O through the thickness direction of the flanges. As previously elucidated, the critical buckling end-shortening values (u_{cr}) for all nonuniform configurations are normalized with respect to the critical buckling end-shortening of the UD graphene dispersion ($u_{cr0} = 0.225$).

The analysis of this figure leads to the following key findings: when FG-X graphene distribution patterns are employed for both flanges and web, the critical buckling end-shortening of the channel section struts is 1.3 times that of the case reinforced with the UD graphene dispersion. On the other hand, when FG-O graphene distribution patterns are utilized for both flanges and web, this ratio reduces to 0.74. These results conclusively establish that FG-X and FG-O graphene distribution patterns represent the most favorable and least favorable combinations, respectively, in terms of their impact on the critical buckling end-shortening for this particular type of open section struts. Moreover, with respect to the given geometry ($\frac{t_f}{t_w} = 1$ & $\frac{b_f}{b_w} = 0.25$), the web buckling is predominant. As a result, any alterations in the graphene distribution pattern of the web significantly impact the critical buckling end-shortening of the channel section struts. This stands in contrast to the scenarios depicted in Figs (4.7) and (4.8), where changes in the graphene reinforcement distribution patterns of the flanges, while keeping the graphene distribution pattern

of the web constant (UD), do not exert substantial effects on the critical buckling end-shortening of the structure.

It is important to observe that the nonlinear postbuckling responses of all the cases assessed in Fig. (4.9) are depicted in Figs (4.10) and (4.11).



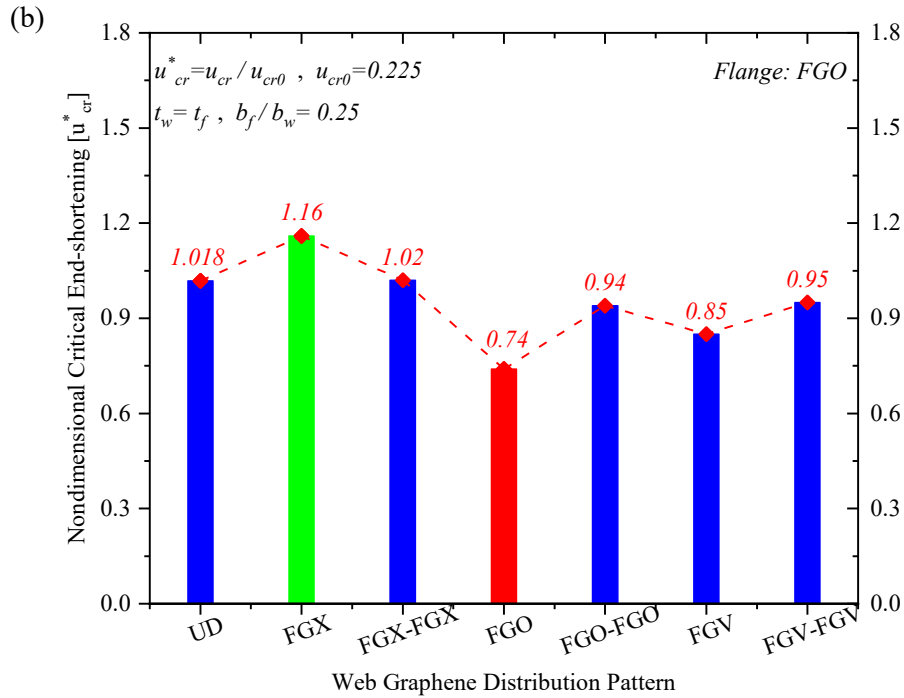
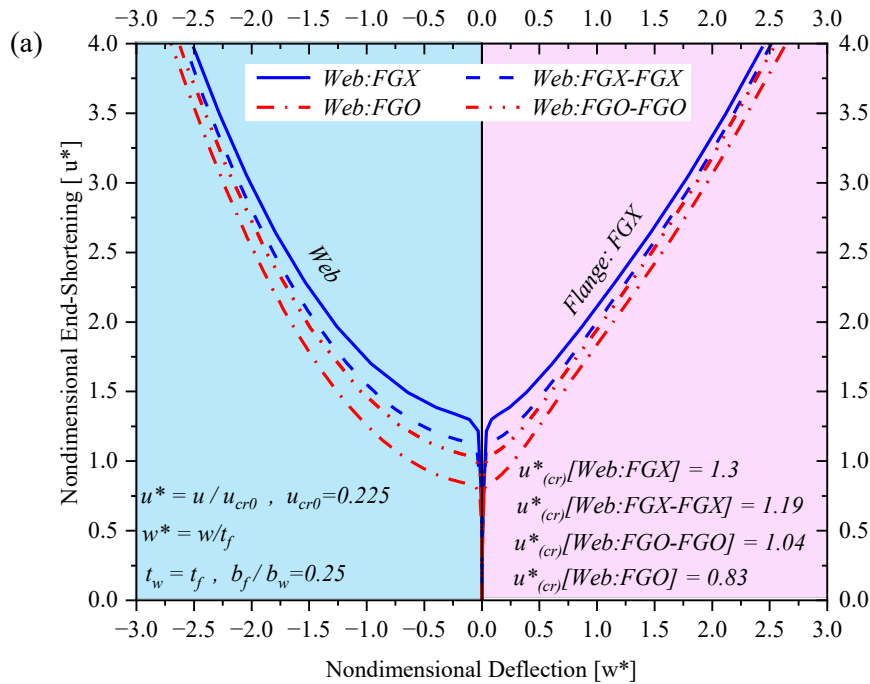


Figure 4-9 Influence of the nonuniform graphene distribution pattern of the web on the critical buckling end-shortening of the FG-GRC channel section struts (a) Flanges with FG-X, (b) Flanges with FG-O

Fig. (4.10)(a) displays the postbuckling equilibrium paths of the flanges and web, considering the use of FG-X graphene distribution pattern for the flanges and various nonuniform symmetric graphene dispersions for the web. Subsection (b) of the same figure maintains a constant flange arrangement while introducing nonuniform asymmetric graphene dispersions for the web.

A notable distinction between this figure and Figs. (4.7) and (4.8) lies in the varying bifurcation points observed in different case studies. This observation ascertains the significance of the web graphene distribution patterns on the overall structural response. A comprehensive comparison of the results clearly demonstrates that, beyond the bifurcation point and throughout the postbuckling phase, the out-of-plane displacement of the flanges and web with FG-X graphene distribution pattern is consistently lower than those of the other cases, regardless of the level of compressive loading applied as end-shortening. This behavior indicates that this particular graphene distribution pattern also exerts a favorable influence on the postbuckling behavior.

Figure (4.11) illustrates the influence of various functionally graded graphene distribution patterns along the thickness of the web plate on the nonlinear stability responses of channel section struts, while in all cases the flanges are reinforced by the FGO graphene distribution pattern. The key inference drawn from this figure is that when employing FGO graphene distribution patterns for both flanges and web, the channel section strut exhibits the most vulnerable nonlinear postbuckling response. This is evidenced by higher deflections of both flanges and web compared to other graphene dispersions under the same level of loading.



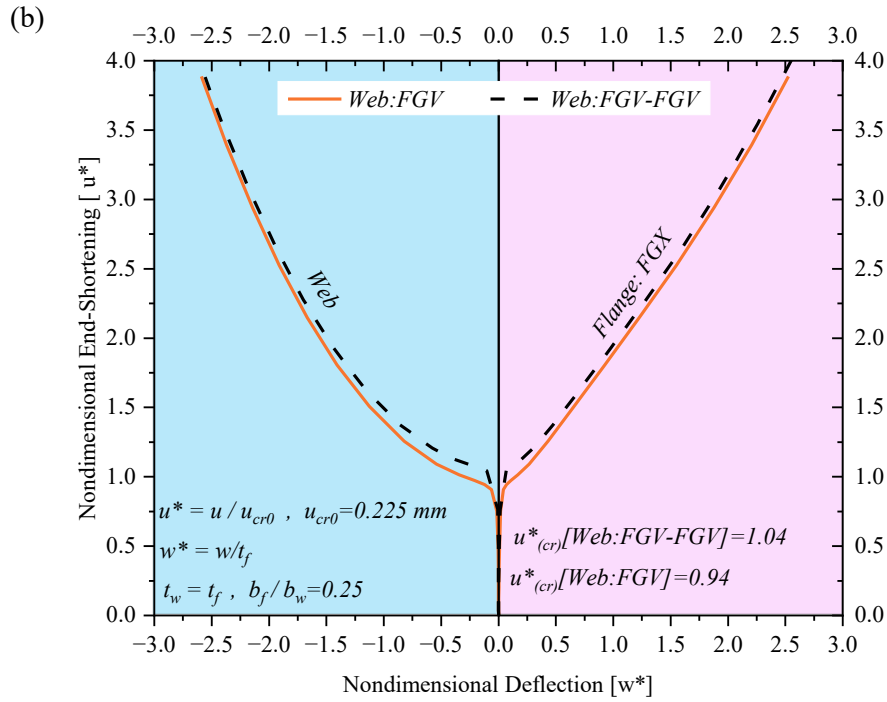
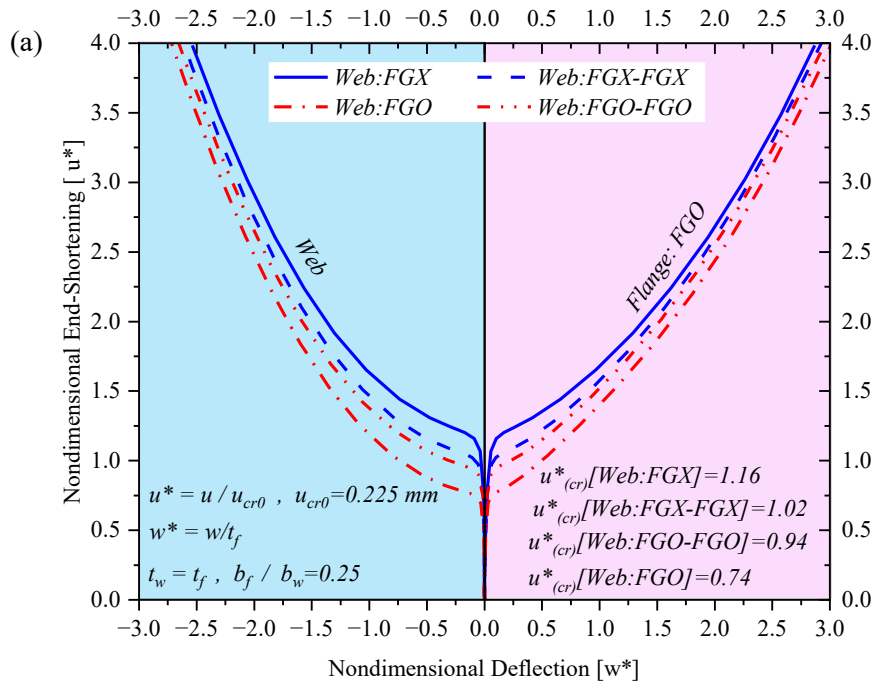


Figure 4-10 Influence of the nonuniform graphene distribution pattern of the web on the postbuckling behavior of the FG-GRC channel section struts where flanges: FGX (a) web with symmetric graphene distributions, (b) web with asymmetric graphene distributions



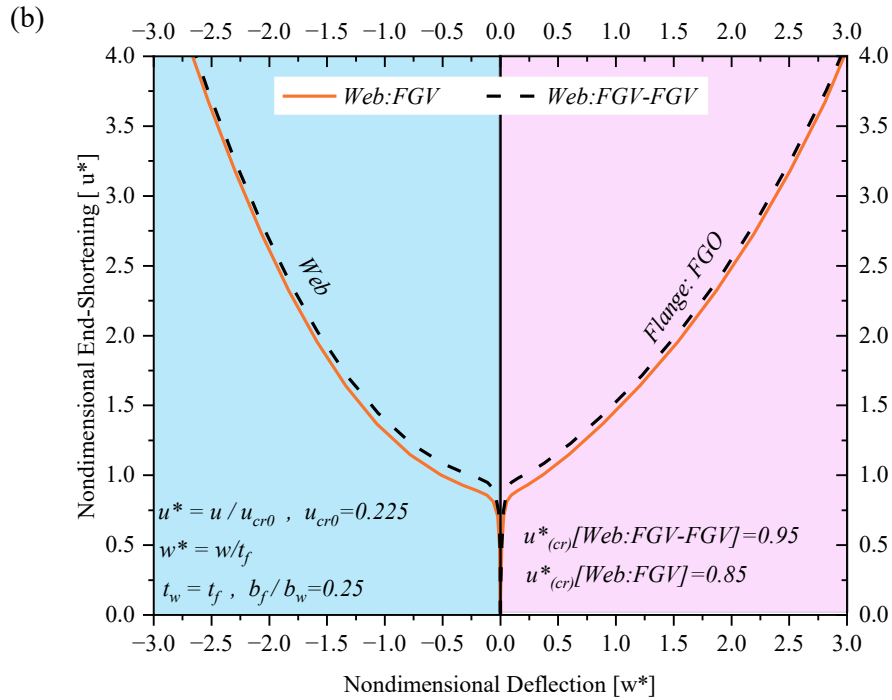
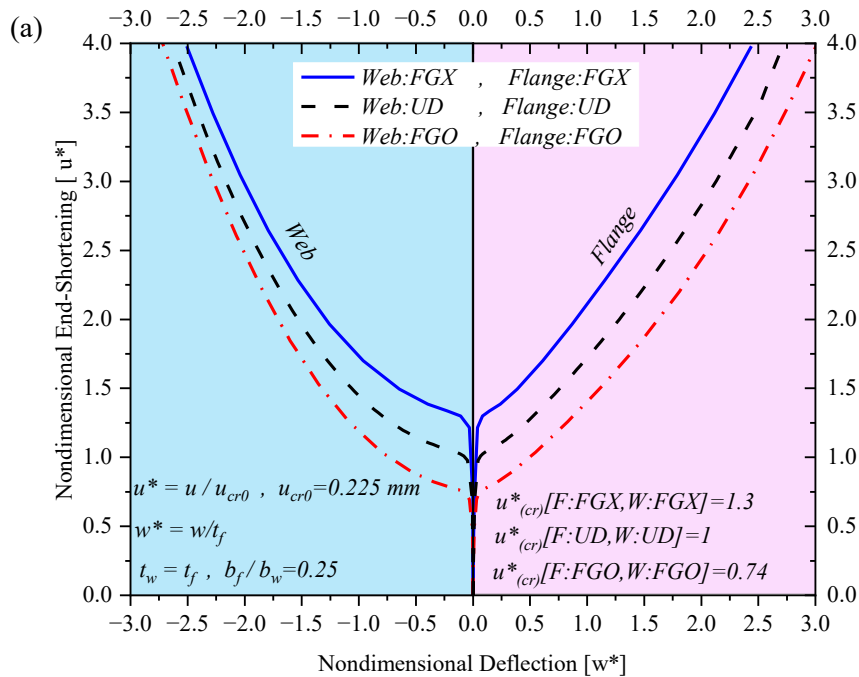


Figure 4-11 Influence of the nonuniform graphene distribution pattern of the web on the postbuckling behavior of the FG-GRC channel section struts where flanges: FGO (a) web with symmetric graphene distributions, (b) web with asymmetric graphene distributions

4.4.3. Parametric study on the channel section struts with FG-X, UD, and FG-O graphene distribution patterns

The results presented in Fig. (4.12) compare the impact of three distinct graphene distribution patterns, including FG-X, UD, and FGO, on the nonlinear postbuckling characteristics, load-bearing capacity, and nonlinear axial compressive stiffness of the channel section struts. The results substantiate that the channel section strut reinforced with the FG-X graphene distribution pattern displays notably higher compressive stiffness in comparison to the FG-O graphene dispersion. In particular, when the nondimensional uniform end-shortening is equal to $u^* = 3$, the channel section struts with FG-X, UD, and FG-O graphene distribution patterns can withstand compressive loads of 126 KN, 127.2 KN, and 102 KN, respectively. This indicates that if the FG-O graphene distribution patterns along the flanges and web's thickness direction are substituted with the FG-X graphene dispersion, the load-bearing capacity of the channel section struts can be increased by

approximately 25%, without altering the geometrical parameters such as the shape factor or flange thickness. The enhanced load-bearing capacity is accompanied by a notable reduction of approximately 30% in the maximum deflection of the FG-X flanges and around 11% in the maximum deflection of the FG-X web, as compared to the channel section struts with the FG-O graphene distribution pattern. Furthermore, under this specific level of nondimensional end-shortening, the out-of-plane displacement of the FG-X flanges and web is reduced by approximately 17% and 9%, respectively, in comparison to the channel section struts with the UD graphene dispersion.



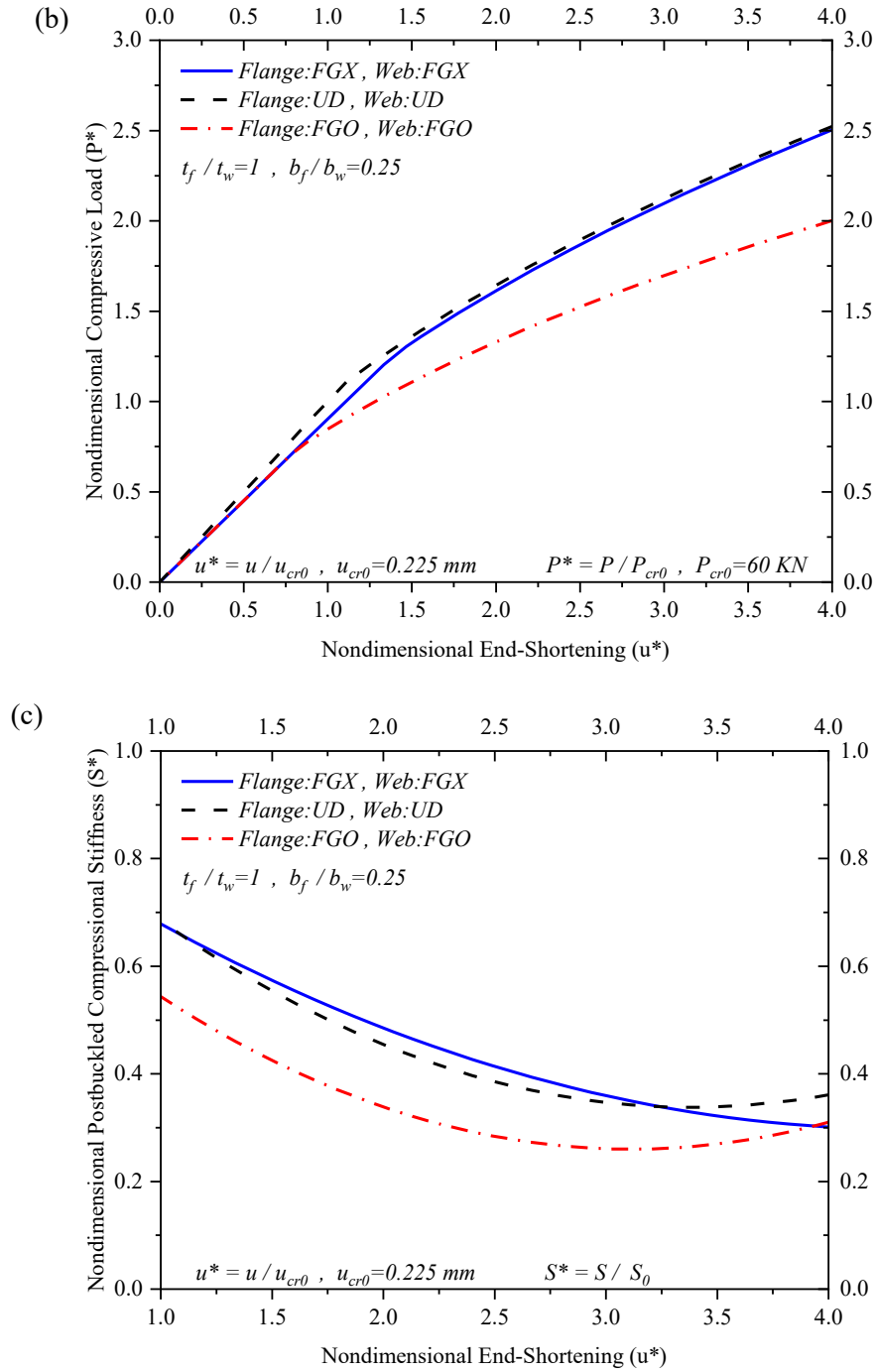


Figure 4-12 Comparison the influence of FG-X, UD, and FG-O graphene distribution patterns on (a) nonlinear postbuckling response, (b) load-bearing capacity, (c) postbuckling compressional stiffness ratio of the channel section strut

Figure (4.13) presents a comparative analysis of the influence of the three designated graphene reinforcement distributions discussed in Fig. (4.12) (FG-X, UD, and FG-O) on the local deflection

of the web and flange at the buckle crest, half length of the channel section struts. Due to the symmetry condition about the Z local axis of the web, as shown in Fig. (4.3), the deflection variations are demonstrated for only half of the cross-section. The local deflection is showcased at an end-shortening equivalent to four times the critical buckling end-shortening of the UD channel section struts, which is regarded as the reference case. The initial deduction drawn from the presented results is that the out-of-plane displacement of the channel section struts is consistently zero at the junction of the flange and web (Point B in the figure), regardless of the type of graphene distribution pattern. This is a consequence of the local-buckling assumption taken into account in this study. As depicted, the out-of-plane displacement of the channel section struts with the FG-X graphene distribution pattern is consistently lower across the the entire cross-section than those with UD and FG-O graphene dispersions.

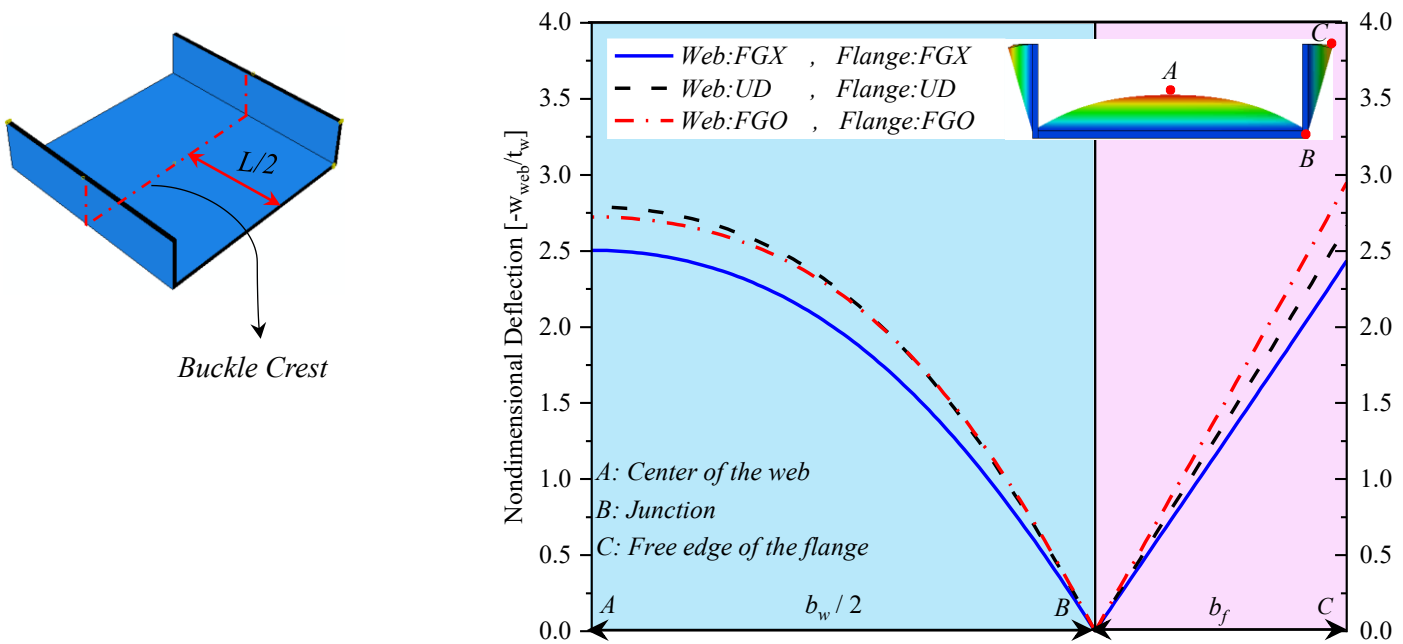


Figure 4-13 Local deflection at the crest of the buckle for channel section struts with different graphene distribution patterns

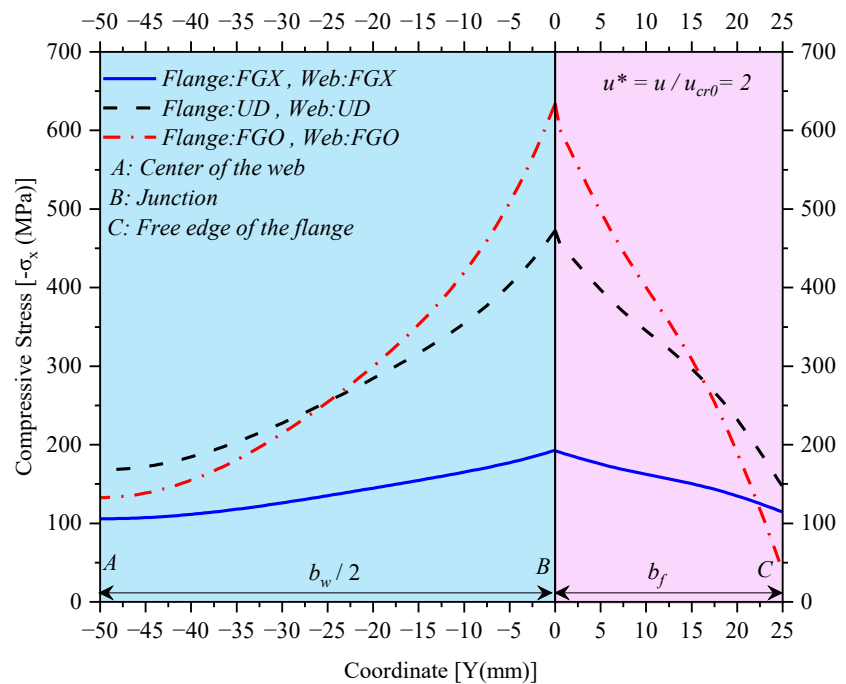
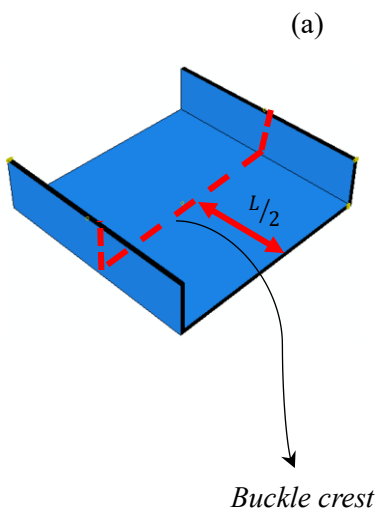
Figure (4.14) illustrates the longitudinal membrane stress distribution along the half cross-section of the channel section strut, ABC shown in Fig. (4.13), with varying types of graphene distribution patterns, namely FG-X, UD, and FG-O. It is important to note that the stress distribution is reported at the mid-plane of three cross-sections located in different longitudinal coordinates, which include the buckle crest (half length), section ends or buckle nodes, and a quarter length of the strut (mid-way between the buckle nodes and buckle crest). The stress evaluation in the figure is conducted at a load equivalent to twice the critical buckling end-shortening of the UD channel section struts.

One of the consistent responses observed across various cross-sections located in different length coordinates, is that the stress level at the midplane of the channel section strut with FG-X graphene distribution is lower than the other two cases with UD and FG-O graphene dispersions. This difference in stress distribution can be attributed to the variation in graphene volume fraction, as presented in Table. (3.1). In the FG-X graphene dispersion, the midplane contains the lowest percentage of graphene (0.03), whereas in the FG-O dispersion, the midplane contains the maximum percentage of graphene (0.11). Consequently, the midplane of the FG-O is stiffer than that of the FG-X, leading to a higher level of stress under the same applied load.

In the design process, a critical aspect involves identifying specific regions within a structure that are more vulnerable under various loading conditions. Upon a comprehensive examination of the various graphs presented in Fig. (4.14) it is evident that regardless of the graphene distribution pattern, the junction of the buckle crest cross-section experiences the highest longitudinal membrane stress. For the three different graphene distribution patterns indicated in Fig. (4.14) (a), the compressive stress levels at the center of the web (location A) range from 100 to 170 MPa, while at the flange free-edge (location C), the stress levels range from 50 to 150 MPa. Notably, the

maximum compressive stress occurs at the section-junction (location B). This phenomenon of load shedding toward the section junction is a typical characteristic observed in the post-local-buckling mechanics of thin-walled structures. This observation confirms that as the compressive load increases, this region becomes more prone to failure compared to other locations. Since the buckle crest is one of the heavily buckled regions in the channel section struts under the compressive load.

The longitudinal membrane stress depicted in Fig. (4.14) (b) and (c), pertaining to the cross sections located at the quarter length and the buckle nodes of the struts, respectively, reveal that load shedding through the FG-X web and flange exhibits a notably smoother distribution than the other graphene patterns UD and FG-O, particularly at the cross section situated at the quarter length of the strut. Consequently, the stress distribution near the junction along the FG-X flange width appears to be more uniform.



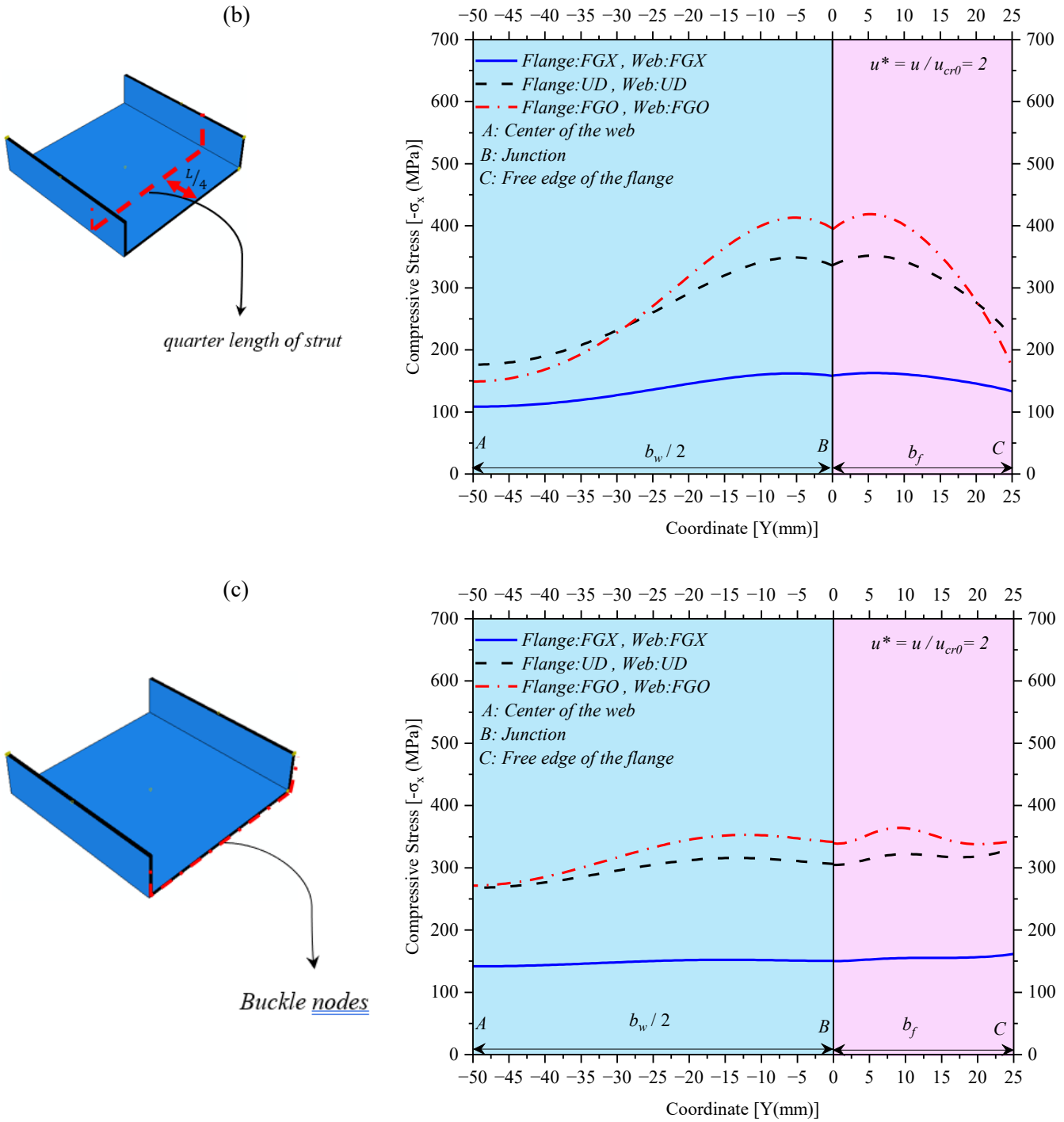


Figure 4-14 Influence of various graphene distribution patterns on the longitudinal membrane stress distribution at (a) buckle crest, (b) quarter length of the strut, (c) buckle nodes

Figure (4.15) illustrates concurrently the influence of geometrical parameters and graphene distribution patterns on the critical buckling end-shortening of channel section struts. This

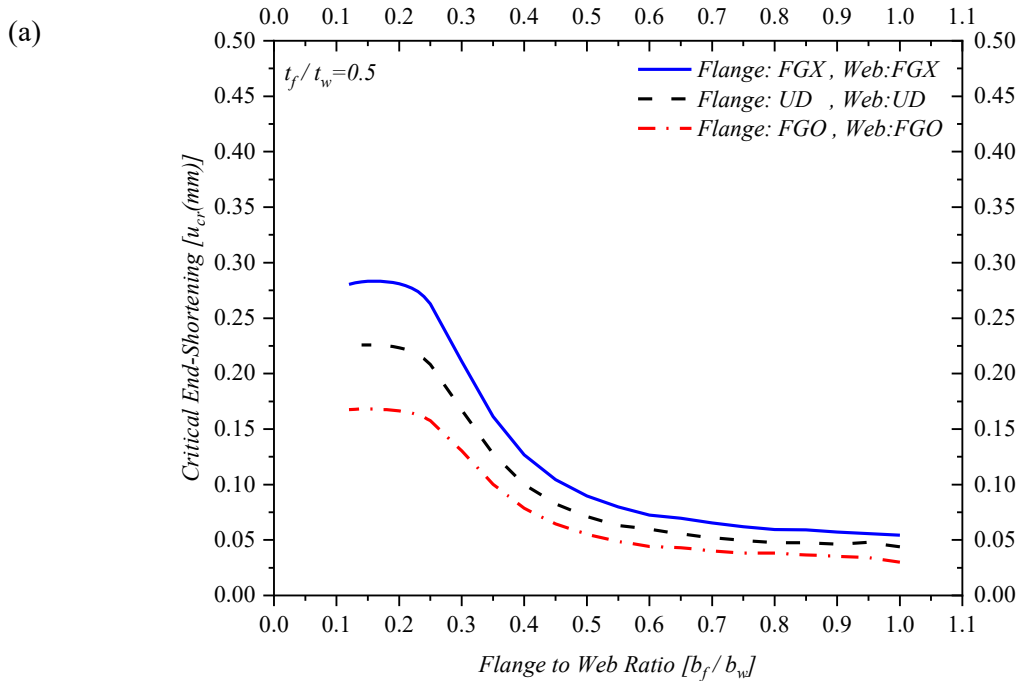
evaluation includes composite laminated channel section struts with three distinct graphene distribution patterns: FG-X, UD, and FG-O, each having varied shape factors. This study examines three distinct thickness ratios (defined as the ratio of flange thickness to web thickness). In each scenario, the web thickness remains consistent at $t_w = 2 \text{ mm}$. Consequently, the flange thickness is adjusted to achieve the specific ratio as illustrated in Fig. (4.15). Furthermore, a similar methodology is applied to varying the shape factor ratio, defined as the proportion between the width of the flange and the width of the web. Here, the web width remains constant at $b_w = 100 \text{ mm}$.

A noteworthy and mutual observation evident from these findings is that across all three different thickness ratios, irrespective of the shape factor of the channel section struts, those with FG-X graphene distribution patterns consistently exhibit a greater critical buckling end-shortening compared to struts reinforced with UD and FG-O graphene dispersions. This outcome further substantiates the superior structural stiffness imparted by FG-X graphene distributions when compared to the other patterns.

Additionally, in cases where the flange is thicker than the web ($\frac{t_f}{t_w} = 2$), regardless of the type of graphene distribution patterns, they exhibit higher critical buckling end-shortening than the other situations. In summary, it can be concluded that across the range of three different graphene distribution patterns utilized within the channel section struts, all share a uniform web thickness, and designs incorporating thicker flanges consistently exhibit higher levels of compressive stiffness than other cases.

By conducting a thorough comparison of the results depicted in Figs. (4.15)(a) ($\frac{t_f}{t_w} = 0.5$) and (4.15)(b) ($\frac{t_f}{t_w} = 1$), it becomes evident that as the shape factor increases, there is a noticeable

decrease in the critical buckling end-shortening experienced by the graphene reinforced channel section struts. This observation strongly supports the idea that, in these specific scenarios characterized by thinner or equal flange thickness compared to the web, augmenting the flange width leads to a reduction in the overall compressive stiffness. However, as shown in Fig. (4.15)(c) where the flange is thicker than the web ($\frac{t_f}{t_w} = 2$), the changes in the shape factor do not significantly affect the critical buckling end-shortening, which confirms that across all the considered shape factors, the primary mode of buckling stems from the web, which is inherently weaker than the flange.



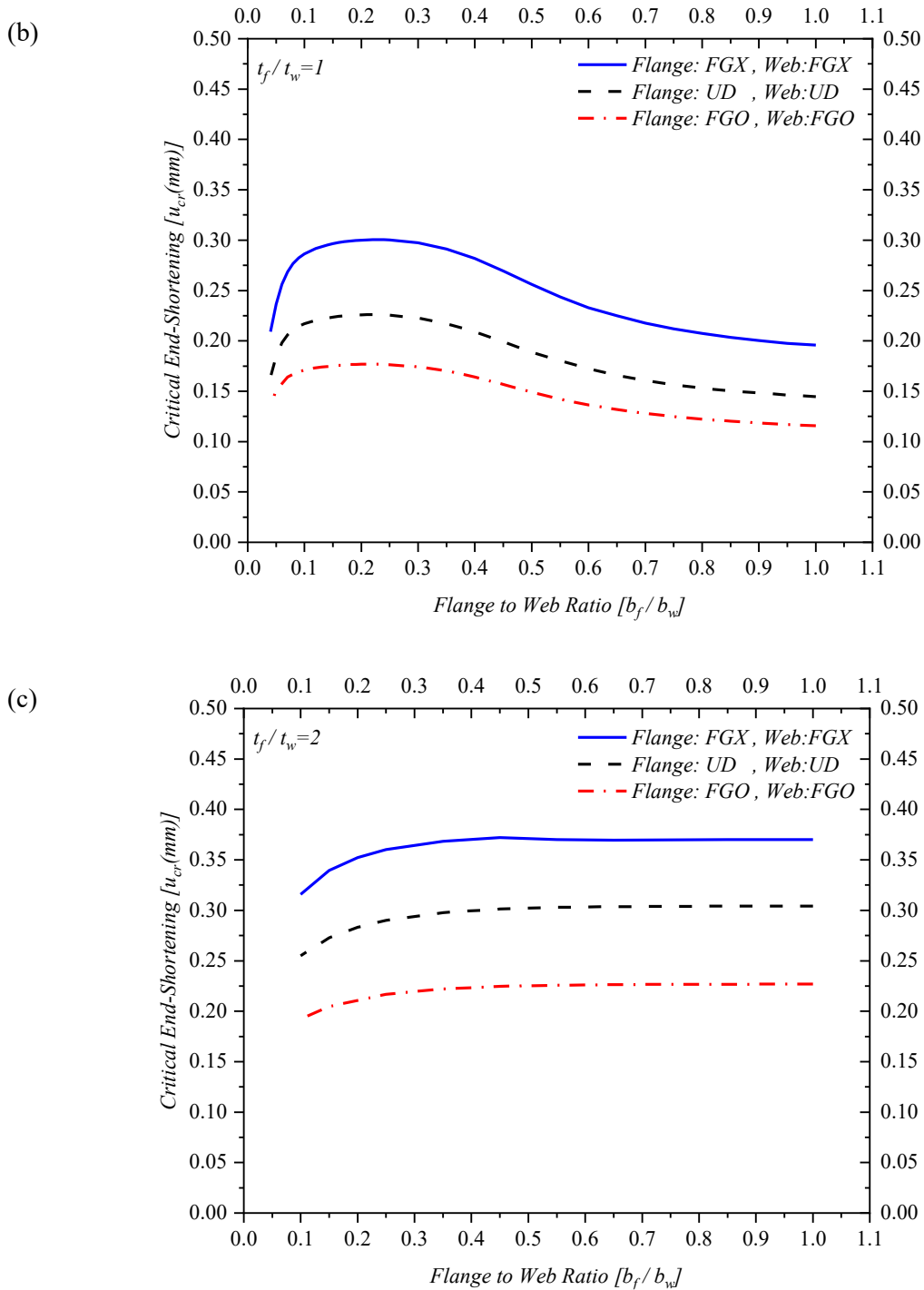
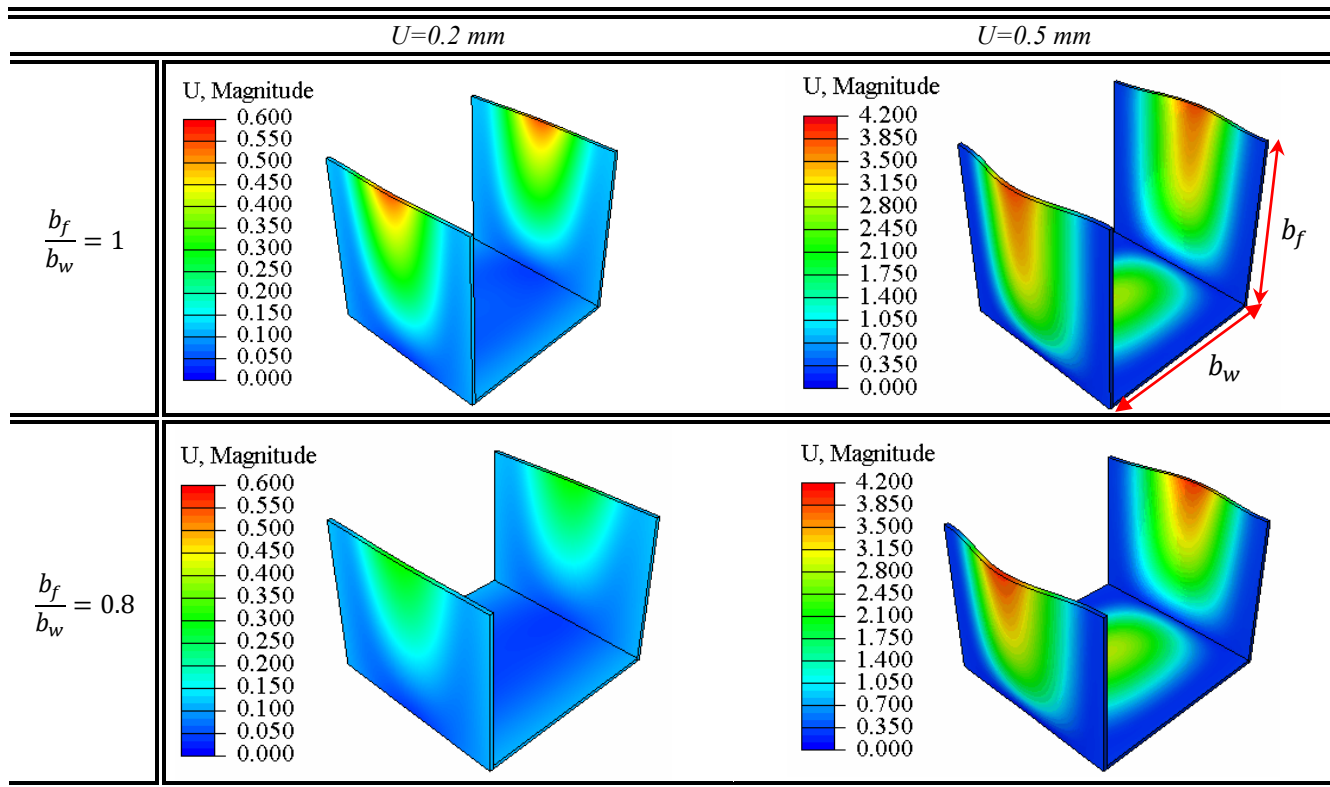


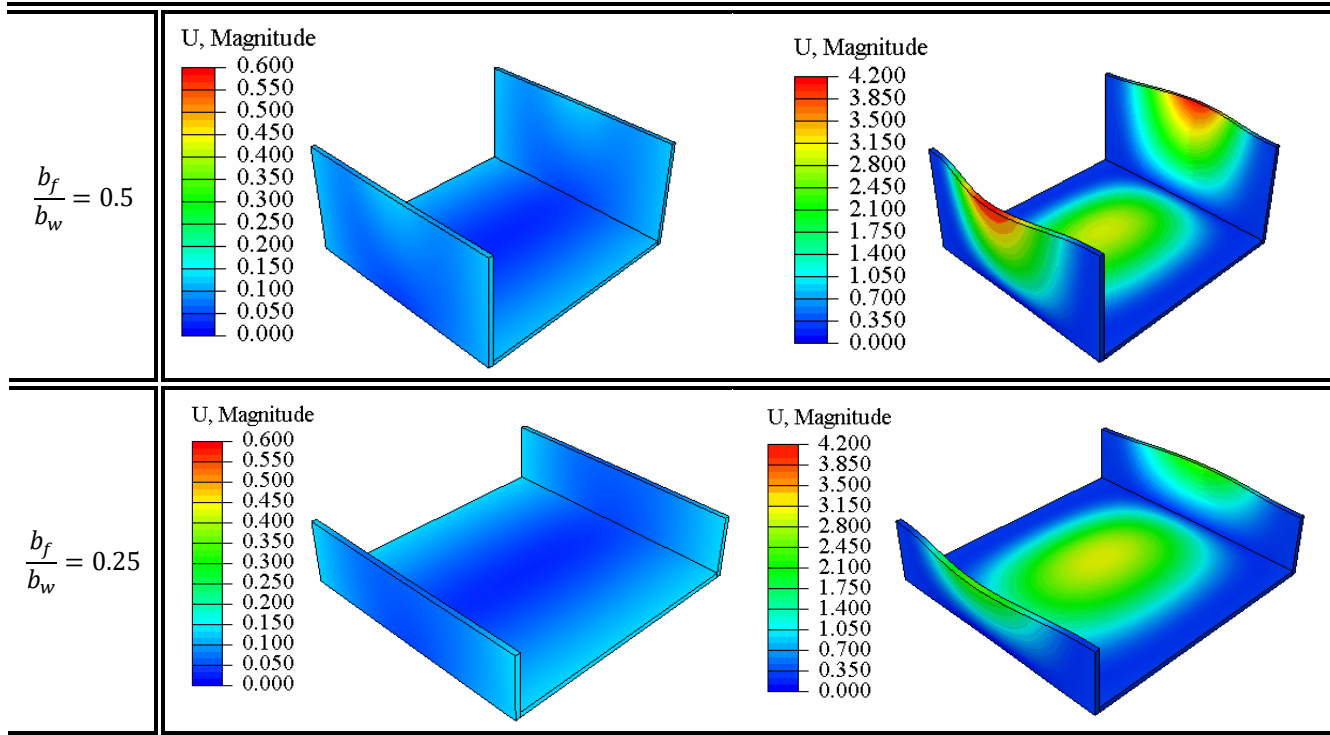
Figure 4-15 Influence of various graphene distribution patterns and geometrical parameters on the critical buckling end-shortening of FG-GRC channel section struts (a) $\frac{t_f}{t_w} = 1$, (b) $\frac{t_f}{t_w} = 0.5$, (c) $\frac{t_f}{t_w} = 2$

The conclusions drawn from the findings presented in Fig. (4.15), concerning the significance of the shape factor, are further supported by the graphical depiction of diverse contouring mode-

shapes, as shown in Table (4.3). These mode-shapes pertain to the FG-X channel section struts, where both flanges and web have identical thickness. For instance, when the applied end-shortening is $u=0.2$ mm, the FG-X channel section strut with $\frac{b_f}{b_w} = 1$ experiences a maximum out-of-plane displacement of approximately 0.6 at the free-edge of the flange. However, when reducing the shape factor to $\frac{b_f}{b_w} = 0.25$, the flange remains nearly flat under the same compressive end-shortening loading.

Table 4-3 Influence of different shape factors and compressive end-shortening loads on the buckling mode-shapes of FG-X channel section struts where $\frac{t_f}{t_w} = 1$.





Based on the preceding results, which indicate the superior compressive stiffness of the FG-X graphene distribution patterns compared to other graphene dispersions, an investigation into the impact of the flange to web thickness ratio on the nonlinear postbuckling equilibrium paths and load-bearing capacity of FG-X channel section struts is conducted and presented in Figs. (4.16) (a) and (b), respectively. The evaluation is performed under a constant shape factor of $\frac{b_f}{b_w} = 0.25$, which is considered the optimum ratio. It is important to emphasize that the end-shortening and compressive load values for all three distinct case studies have been normalized with reference to the critical buckling end-shortening and compressive load of the scenario featuring identical flange and web thickness represented as $u_{cr[R=1]} = 0.292 \text{ mm}$ and $P_{cr[R=1]} = 72 \text{ KN}$ in Fig. (4.16).

As depicted in Fig. (4.16)(a), it is evident that the critical buckling-induced end-shortening of FG-X channel section struts, wherein the flanges possess greater thickness than the web ($R = 2$), is approximately 15% and 25% higher than those with flanges of equal ($R = 1$) and reduced ($R =$

0.5) thickness, respectively. Additionally, within FG-X channel section struts characterized by uniform flange and web thickness, or in the scenario featuring thinner flanges, the points at which the flanges and web reach their respective bifurcation thresholds coincide. This indicates a simultaneous deflection of both plates (flange and web). However, in the context of thicker flanges, a noticeable difference in the bifurcation points between the flange and web becomes apparent.

An additional deduction that can be drawn is that, under the specific condition of $\frac{b_f}{b_w} = 0.25$ for the shape factor, the primary buckling behavior of the channel section strut is attributed to the web. However, when the flange thickness equals ($R = 1$) or is less ($R = 0.5$) than that of the web, there is a lack of significant impact of R on the postbuckling behavior of the web which means that the flanges are too weak to provide a great deal of constraint on the buckled web. In these two scenarios, the out-of-plane displacements of the webs are nearly equal to each other.

The influence of the flange becomes increasingly significant in shaping the postbuckling behavior of the web as its thickness increases. This augmentation subsequently leads to an enhancement in the overall compressive stiffness of the structure. It can also be supported through the results indicated in Fig. (4.16) (b), at a nondimensional end-shortening of $u^* = 3$, where the nondimensional compressive load for the FG-X channel section strut with $R = 2$ stands at $P^* = 3$. In comparison, the corresponding values for cases with $R = 1$ and $R = 0.5$ are $P^* = 2.1$ and $P^* = 1.25$, respectively, while the deflection of both flange and web are much larger than that of the case with thicker flange.

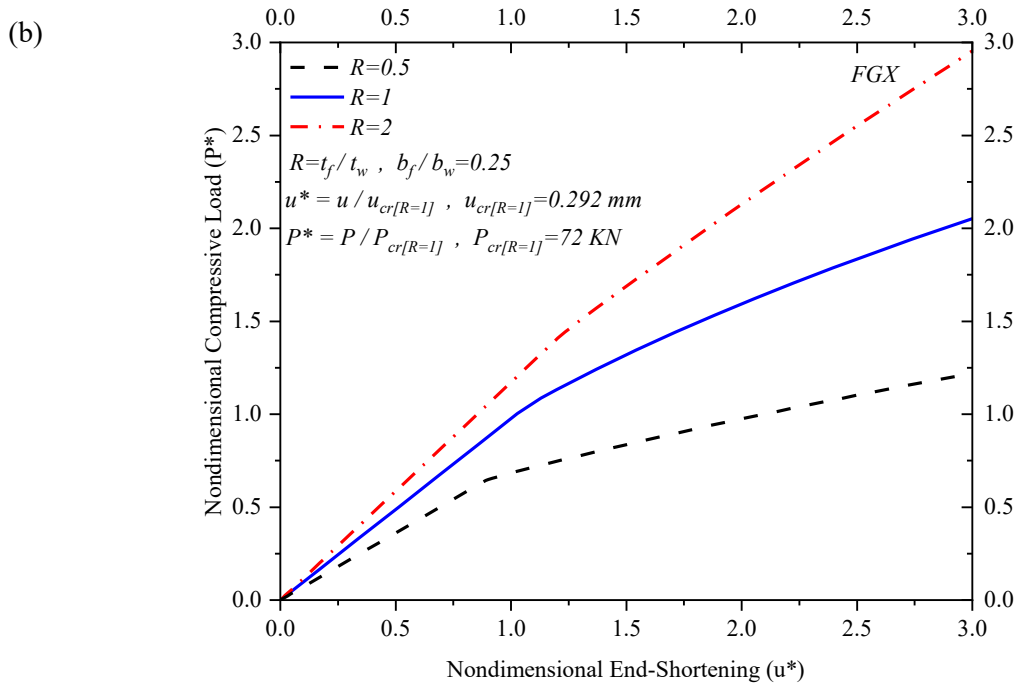
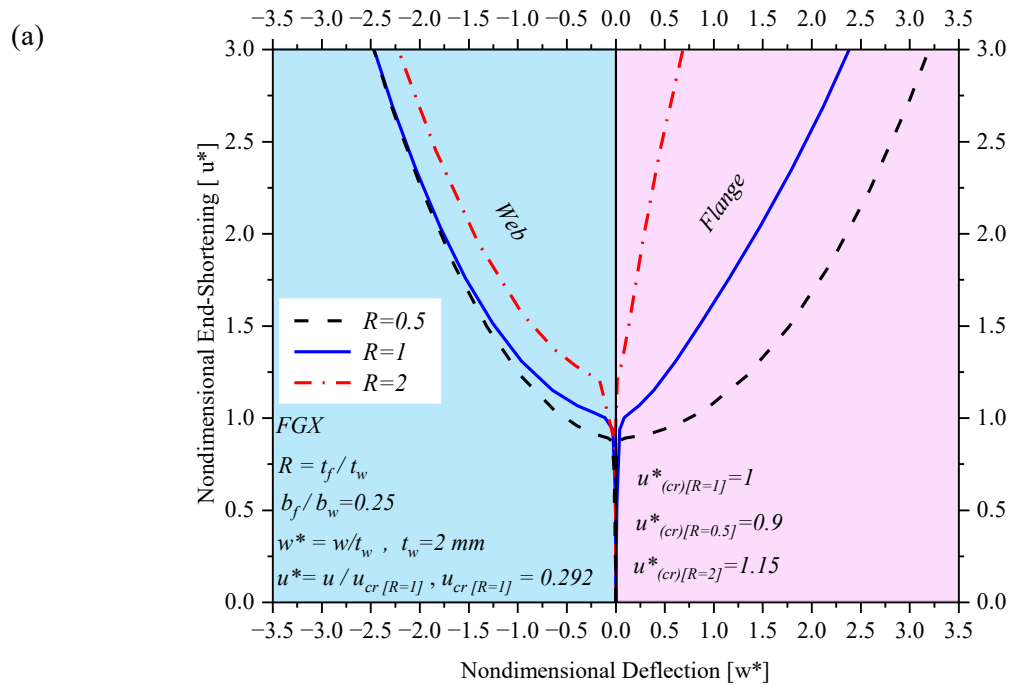


Figure 4-16 Influence of different flange to web thickness ratios on (a) nonlinear postbuckling equilibrium paths, and (b) load-bearing capacity of the FG-X channel section strut

4.5. Concluding remarks

Considering the vulnerability of laminated composite open section struts, a widely employed type of engineering structure, to local buckling when subjected to compressive loads, the present research undertakes an investigation to explore the potential solution of this susceptibility through the incorporation of graphene sheet reinforcements. The main purpose of the paper is to recognize how distinct arrangements of graphene sheet reinforcements, distributed across the thickness of the flange and web plates within channel section struts, influence their compressive stability responses. The focus has been directed towards discerning which combination of graphene distribution patterns yield the most and least advantageous impact on augmenting the critical buckling-induced end-shortening and compressive stiffness of these structures. A formulation is developed based on the LW-TSDT and von-Karman strain–displacement relation. The governing equations are solved through the application of the minimum total potential energy principle and the Ritz method in conjunction with the Newton–Raphson iterative procedure and the obtained results finally compared with those evaluated using the 3D finite element simulation. The thermo-mechanical properties of matrix and graphene reinforcements are evaluated using the extended Halpin-Tsai micromechanical model. This research not only contributes to a deeper understanding of the complex interplay between material properties and structural behavior but also provides valuable insights for designing more resilient and efficient engineering structures. Specifically:

- The application of the FG-X graphene distribution pattern along the thickness of the web and flanges in channel section struts leads to a substantial 30% improvement in the critical buckling-induced end-shortening of the structures, as compared to channel section struts with identical geometric parameters reinforced using the UD graphene dispersion.

However, the FG-O pattern brings about a noteworthy reduction of approximately 26% in the critical buckling-induced end-shortening.

- In situations where the buckling of the web is predominant, any modifications in the graphene distribution patterns across the thickness direction of the flanges exhibit an almost negligible influence on the stability response of the web with a uniform graphene dispersion. Conversely, adjustments in the graphene distribution patterns along the web's thickness, while flanges possessing constant graphene dispersion, noticeably affect the critical buckling end-shortening and post-local buckling equilibrium paths of the entire channel section struts.
- Nondimensional axial compressive stiffness of the channel section struts with FG-X graphene distribution pattern is higher than the stiffness of sections with UD or FG-O graphene dispersions.
- Disregarding the specific graphene distribution patterns, the point of highest membrane stress occurs at the junction of the flange and web, precisely positioned at the buckle crest of the channel section struts.
- In channel section struts with FG-X graphene distribution patterns, membrane stress within the central plane of the web and flange is notably lower than in sections reinforced with UD and FG-O graphene dispersions. This decline is attributed to lower graphene percentage at the midplane, resulting in decreased stiffness.
- In scenarios where the flange thickness equals or is less than that of the web, the optimal shape factor signifying the highest critical buckling-induced end-shortening remains constant at $\frac{b_f}{b_w} = 0.25$, irrespective of the varied graphene distribution patterns employed.

- When the flange thickness is equal to or less than the web thickness, it fails to provide adequate stiffness to restrict web deflection, resulting in the alignment of their bifurcation points. Conversely, if the flange surpasses the web in thickness, it effectively restrains the web from buckling, enhancing its resistance and stiffness. This leads to a noticeable disparity in bifurcation points between the flange and web.

5. Imperfection sensitivity of free vibration of FG-GRC laminated channel section struts in thermally pre- and post-buckling equilibrium states⁴

This study explores the effect of local buckling on the compressive performance of slender structural elements, particularly those with thin-walled sections. The phenomenon of local buckling significantly reduces the axial compressive stiffness, leading to a notable decrease in the load-bearing capacity of these elements. The main goal of this research is to examine how the post-buckling characteristics of polymeric composite channel section struts can be improved under thermal loading by incorporating multi-layer graphene reinforcements. The solution methodology incorporates the von Karman geometrical nonlinearity and is based on the layerwise third-order shear deformation theory (LW-TSDT). To ascertain the precision and computational performance of the results derived from LW-TSDT, a three-dimensional (3D) finite element model is created in ABAQUS for comparative evaluation. An extensive analysis of nonlinear thermal instability in perfect and geometrically imperfect FG-GRC laminated channel section struts is undertaken to discern the graphene distribution patterns that are most and least effective in elevating the critical buckling temperature and natural frequencies through pre- and post-buckling conditions. The comparative analysis indicates that employing the FG-X graphene distribution pattern across the thickness of the web and flanges in channel section struts leads to a projected increase of 12% in the critical buckling temperature for clamped channel section struts, in contrast to those that adopt the FGO graphene distribution pattern. For cases with simply-supported boundary conditions, this increase is noted to be approximately 9%. Moreover, findings confirm that incorporating an asymmetric graphene distribution pattern (FGV) or introducing geometrical imperfections in the flanges and web that generate a bending moment within the structure from the beginning of thermal

⁴ A version of this chapter is currently under review in the journal of Composite Structures

loading effectively prevents the primary natural frequencies of FG-GRC channel section struts from declining to zero close to the critical buckling temperature. This is significantly different from scenarios involving perfectly structured and symmetrically reinforced graphene distribution patterns such as FGX.

5.1. Introduction

In reference to the matter at hand, it is imperative to acknowledge that the discourse presented herein extends the investigations delineated in Chapter 4. The methodological framework and micromechanical models employed within this study remain consistent with those expounded in the preceding section. Furthermore, it should be noted that there exists a significant overlap in the reference materials cited in these concurrent papers. To maintain conciseness and avoid redundancy, these references have not been reiterated in the current chapter. This approach ensures a streamlined presentation of our findings while upholding the integrity and continuity of the research narrative.

This research conducts a comparative analysis of various arrangements of functionally graded graphene sheets, distributed along the thickness directions of the flanges and web plates in channel section struts. The aim is to identify the specific pattern combinations that most effectively enhance the critical buckling temperature, as well as the fundamental and second-order frequencies, in both pre- and post-buckling states. Alongside examining various material configurations and conducting an in-depth comparison of the thermal post-buckling characteristics between the most and least impactful cases against the uniform distribution (UD) graphene pattern, this study also assesses how boundary conditions and localized geometrical imperfections, applied either individually or collectively to each flange and web, influence the thermal instability response and variation of pre- and post-buckled frequencies.

To fulfill the research goals effectively, an advanced, layerwise theoretical model based on the third-order shear deformation theory (TSDT) is developed. This innovative approach is instrumental in analyzing the thermal and mechanical instability responses of thin-walled structures. The initial step in this methodology involves treating the constituent plates (including flanges and web) as separate, distinct elements. This is followed by a discretization process, wherein each plate is segmented into several numerical layers along its thickness. A pivotal element of this method is the establishment of displacement and rotation shape functions at the midplane of each layer. It is crucial to underscore the importance of ensuring these shape functions adhere rigorously to the continuity and boundary conditions that govern the structural entirety. Moreover, a 3D finite element model is implemented, utilizing the commercial software ABAQUS, to incorporate some of the findings derived from the LW-TSDT. Additionally, this study presents a comparative evaluation of the central processing unit (CPU) time required by both methodologies. These approaches demand differing quantities of displacement and rotational degrees of freedom (DOFs) to precisely evaluate the nonlinear behavior observed in channel section struts.

5.2. Theoretical formulation

It is crucial to recognize that the equations required to calculate the thermomechanical characteristics of GRCs using the modified Halpin-Tsai mathematical model align with those detailed in section 2.2.2. Additionally, the analysis of the nonlinear thermal instability behavior of channel section struts utilizes the TSDT alongside the Layerwise Theory. The detailed displacement equations based on the TSDT are presented in section 3.3.

5.3. Structural modelling of channel section struts

5.3.1. Modelling based on the LW-TSDT

It is imperative to recognize that the layerwise theory, in conjunction with the TSDT framework, is utilized for conducting the nonlinear thermal instability analysis of FG-GRC channel section struts. This approach aligns with the methodology employed for the nonlinear compressive analysis of analogous structures subjected to uniform end-shortening, as elaborated in Chapter 4. Consequently, the specialized formulations employed in both instances for the incorporation of the layerwise theory into the channel section strut analysis remain consistent. Due to this methodological consistency, the detailed formulations can be found in section 4.3.

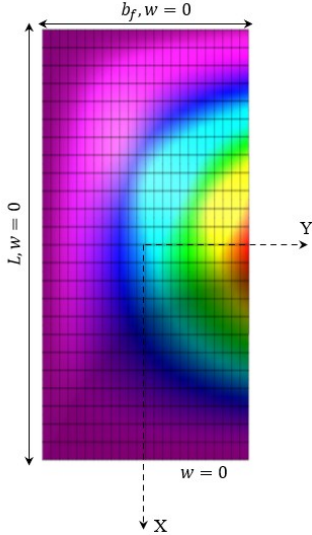
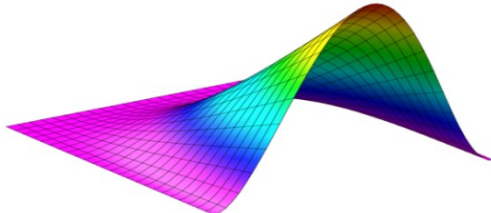
This paper focuses on examining the influence of geometrical imperfections on the nonlinear thermal compressive behavior of channel section struts. These imperfections, which happen due to several reasons including manufacturing tolerances, material defects, thermal effects, and aging, add a realistic dimension to the study. Essentially, these imperfections are deviations from the perfect flatness of FG-GRC laminated channel section struts. Given the boundary conditions and ensuring stress-free edge continuity at the junction, the formulation of the initial imperfection affecting the entire strut is detailed as follows [117]:

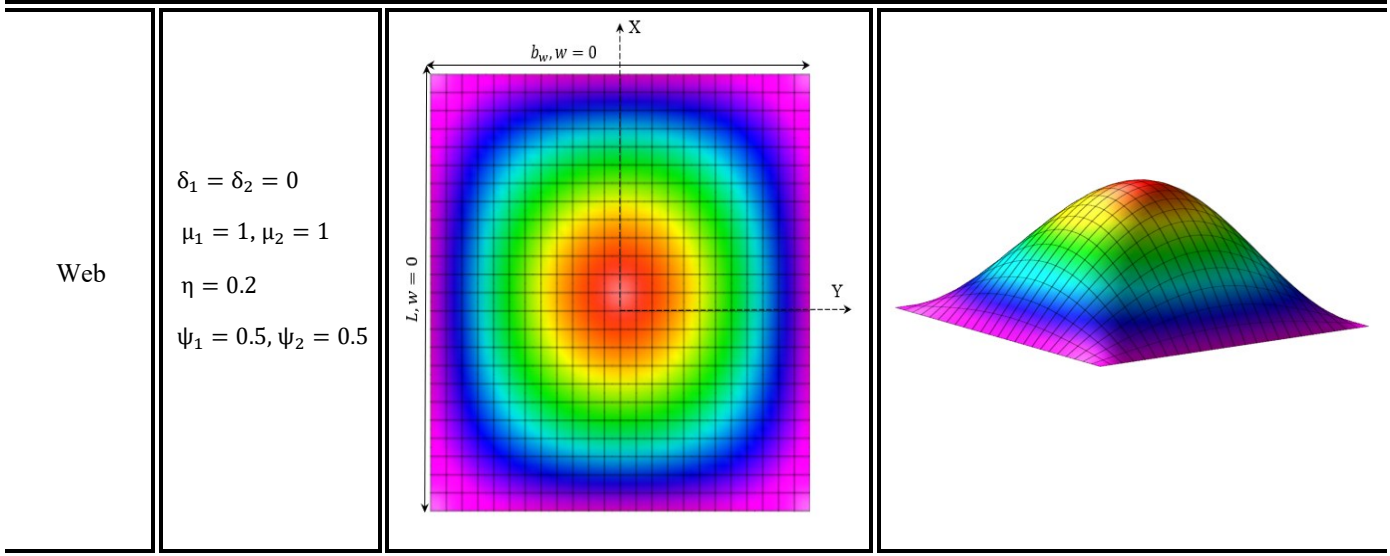
$$\bar{W}^* = \eta h \operatorname{sech}[\delta_1(x_1 - \psi_1)] \cos[\mu_1 \pi(x_1 - \psi_1)] \operatorname{sech}[\delta_2(x_2 - \psi_2)] \cos[\mu_2 \pi(x_2 - \psi_2)] \quad (5-1)$$

where $x_1 = \frac{x + (\frac{L}{2})}{L}$ and $x_2 = \frac{y + (\frac{b}{2})}{b}$, η is the maximum dimensionless amplitude of the initially deflected geometry, δ_1 and δ_2 are the constants defining the localization degree of the imperfection that is symmetric about ψ_1 and ψ_2 and μ_1 and μ_2 are the half-wave numbers of the imperfection in X and Y -axes, respectively. This equation is designed to accommodate a broad spectrum of initial imperfection patterns.

Table. (5.1) displays the specific geometrical imperfections implemented locally to the flange and web segments of FG-GRC laminated channel section struts. These imperfections are aligned with the first buckling mode of these thin-walled structures. Highlighting the importance of these imperfections, it is crucial to understand that they play a significant role in the accurate prediction of thermal instability response under various conditions. By simulating real-life scenarios where minor deviations from perfect geometry can have a profound impact on the structural integrity, this method enhances the reliability of structural analysis and design.

5-1 schematic of local imperfections applied to flange and web of channel section struts

Segment	Parameters	Imperfection mode (x-y plane)	Imperfection mode (3D)
Flange	$\delta_1 = \delta_2 = 0$ $\mu_1 = 1, \mu_2 = 0.5$ $\eta = 0.2$ $\psi_1 = 0.5, \psi_2 = 1$		



In analyzing the nonlinear thermal compressive behavior and the thermally induced pre- and post-buckling free vibration characteristics of FG-GRC laminated channel section struts, the approach is based on the principle of minimum total potential energy. The total potential energy of a structure is a comprehensive measure that encompasses several key components. It includes the potential energy due to external loads, reflecting the work exerted by external forces on the structure. Additionally, it accounts for the total strain energy, which represents the energy associated with internal stresses and deformations within the structure's material. Kinetic energy, which pertains to the motion of the structure, also forms a part of the total potential energy calculation (67). Regarding the fact that the channel section strut is uniformly subjected to thermal loading, it can be inferred that the potential energy associated with external forces is negligible. Consequently, in this context, the total potential energy of the structure primarily comprises the sum of its total strain energy and kinetic energy.

Given that the channel section strut's flanges and web are divided into several numerical layers as per layerwise theory, and each layer has specific displacement and rotational functions, the total

potential energy of the structure is obtained by summing the strain and kinetic energy of each layer as illustrated in the following equations:

$$\begin{aligned}\Pi^{Total} &= \sum_{i=1}^n (U_w^{(i)} + T_w^{(i)}) + \sum_{i=1}^n (U_{f1}^{(i)} + T_{f1}^{(i)}) + \sum_{i=1}^n (U_{f2}^{(i)} + T_{f2}^{(i)}) \\ \Pi^{Total} &= \left(\frac{1}{2}\right) \left[\sum_{i=1}^n \int \left((\sigma_w^{(i)})^T \varepsilon_w^{(i)} + \rho h (\dot{U}_w^{(i)} + \dot{V}_w^{(i)} + \dot{w}_w^{(i)}) \right) dV + \sum_{i=1}^n \int \left((\sigma_{f1}^{(i)})^T \varepsilon_{f1}^{(i)} + \rho h (\dot{U}_{f1}^{(i)} + \dot{V}_{f1}^{(i)} + \dot{w}_{f1}^{(i)}) \right) dV + \sum_{i=1}^n \int \left((\sigma_{f2}^{(i)})^T \varepsilon_{f2}^{(i)} + \rho h (\dot{U}_{f2}^{(i)} + \dot{V}_{f2}^{(i)} + \dot{w}_{f2}^{(i)}) \right) dV \right] \quad (5-2)\end{aligned}$$

To maintain brevity, the strain and kinetic energy of the first numerical layer positioned in the web ($U_w^{(1)}$ and $T_w^{(1)}$), illustrated in Fig. (4.3), are extended in Eqs. (5.3) and (5.4), respectively:

$$\begin{aligned}U_w^{(1)} &= \int \frac{1}{2} \bar{\sigma}^T \bar{\varepsilon} dV \\ &= \frac{1}{2} \int_{-\frac{b_w}{2}}^{\frac{b_w}{2}} \int_{-\frac{L}{2}}^{\frac{L}{2}} \left(\{\varepsilon^0\}_w^{(1)} [A]_w^{(1)} \{\varepsilon^0\}_w^{(1)T} + 2\{\varepsilon^0\}_w^{(1)} [B]_w^{(1)} \{\varepsilon^1\}_w^{(1)T} + \{\varepsilon^1\}_w^{(1)} [D]_w^{(1)} \{\varepsilon^1\}_w^{(1)T} + 2\{\varepsilon^0\}_w^{(1)} [E]_w^{(1)} \{\varepsilon^3\}_w^{(1)T} + \{\varepsilon^1\}_w^{(1)} [F]_w^{(1)} \{\varepsilon^3\}_w^{(1)T} + \{\varepsilon^3\}_w^{(1)} [H]_w^{(1)} \{\varepsilon^3\}_w^{(1)T} + \{\gamma^0\}_w^{(1)} [As]_w^{(1)} \{\gamma^0\}_w^{(1)T} + 2\{\gamma^0\}_w^{(1)} [Ds]_w^{(1)} \{\gamma^2\}_w^{(1)T} + \{\gamma^2\}_w^{(1)} [FS]_w^{(1)} \{\gamma^2\}_w^{(1)T} \right) dx dy \quad (5-3)\end{aligned}$$

$$\begin{aligned}T_w^{(1)} &= \left(\frac{1}{2}\right) \int_{-\frac{b_w}{2}}^{\frac{b_w}{2}} \int_{-\frac{L}{2}}^{\frac{L}{2}} I_w^{(i)} \left[\left(\frac{\partial U_w^{(1)}}{\partial t}\right)^2 + \left(\frac{\partial V_w^{(1)}}{\partial t}\right)^2 + \left(\frac{\partial w_w^{(1)}}{\partial t}\right)^2 \right] dx dy = \left(\frac{1}{2}\right) \int_{-\frac{b_1}{2}}^{\frac{b_1}{2}} \int_{-\frac{L_1}{2}}^{\frac{L_1}{2}} \left[I0_w^{(i)} \left(\frac{\partial U_w^{ref}}{\partial t}\right)^2 + 2I1_w^{(i)} \left(\frac{\partial U_w^{ref}}{\partial t} \frac{\partial \varphi_{w,x}^{(1)}}{\partial t}\right) + I2_w^{(i)} \left(\frac{\partial \varphi_{w,x}^{(1)}}{\partial t}\right)^2 + 2I3_w^{(i)} \left(\frac{\partial U_w^{ref}}{\partial t} \frac{\partial \psi_{w,x}^{(1)}}{\partial t}\right) + 2I4_w^{(i)} \left(\frac{\partial \varphi_{w,x}^{(1)}}{\partial t} \frac{\partial \psi_{w,x}^{(1)}}{\partial t}\right) + I5_w^{(i)} \left(\frac{\partial \psi_{w,x}^{(1)}}{\partial t}\right)^2 + I0_w^{(i)} \left(\frac{\partial V_w^{ref}}{\partial t}\right)^2 + 2I1_w^{(i)} \left(\frac{\partial V_w^{ref}}{\partial t} \frac{\partial \varphi_{w,y}^{(1)}}{\partial t}\right) + I2_w^{(i)} \left(\frac{\partial \varphi_{w,y}^{(1)}}{\partial t}\right)^2 + 2I3_w^{(i)} \left(\frac{\partial V_w^{ref}}{\partial t} \frac{\partial \psi_{w,y}^{(1)}}{\partial t}\right) + 2I4_w^{(i)} \left(\frac{\partial \varphi_{w,y}^{(1)}}{\partial t} \frac{\partial \psi_{w,y}^{(1)}}{\partial t}\right) + I5_w^{(i)} \left(\frac{\partial \psi_{w,y}^{(1)}}{\partial t}\right)^2 + I0_w^{(i)} \left(\frac{\partial w_w^{(1)}}{\partial t}\right)^2 \right] dx dy \quad (5-4)\end{aligned}$$

The inertial terms are obtained through the integration of the density.

$$\{I_0^{ij} \quad I_1^{ij} \quad I_2^{ij} \quad I_3^{ij} \quad I_4^{ij} \quad I_5^{ij}\} = \int_{-\frac{h^{ij}}{2}}^{\frac{h^{ij}}{2}} \rho(z) \{1 \quad \theta_1(z) \quad \theta_1^2(z) \quad \theta_2(z) \quad \theta_1(z)\theta_2(z) \quad \theta_2^2(z)\} dz \quad (5-5)$$

Following this stage, the total potential energy should be minimized by using the unknown displacement and rotation coefficients as shown in Eq. (3.19) in chapter 3. The solution procedure of the derived nonlinear system of equation was discussed in details in section 3.3.3.

5.3.2. Modelling based on the finite element simulation

To validate the accuracy of the results derived from the LW-TSDT approach, this study employs a sophisticated 3D-FEM developed using the ABAQUS, which encompasses two critical phases. Initially, a comprehensive 3D model is constructed, integrating specific material characteristics, load conditions, and boundary parameters. Subsequently, a linear perturbation buckling analysis is conducted to identify the various buckling modes of the channel section struts. Following this, the analysis transitions to the static Riks method, replacing the linear buckling approach. This method considers nonlinear geometric factors, incorporating the first buckling mode shape identified earlier as an imperfection within the Riks method. It's imperative to highlight the significant impact of the imperfection amplitude on the convergence of the nonlinear post-buckling analysis. In the nonlinear simulation conducted using ABAQUS, the imperfection amplitude for the channel section struts is set to 0.001 times the magnitude of the initial buckling mode shape.

In this research, as previously highlighted, the edge supports are modeled as either clamped or simply-supported boundary conditions. Additionally, it is crucial to consider that the in-plane displacement of the channel section struts in the X direction must be constrained, as illustrated in Fig. (5.1)(a). This constraint is particularly pertinent due to the thermal loading involved in the study. When the temperature uniformly increases, it induces expansion throughout the entire structure. The imposed restriction counteracts this expansion, thereby precipitating the buckling phenomenon.

In the finite element simulation, the 3D, 8-node, linear isoperimetric element (C3D8) is utilized. The C3D8 element in ABAQUS represents a brick-shaped volume with eight nodes situated at specific coordinates in the 3D space, defining its geometry. It is capable of deformation and shape alteration when subjected to applied loads or constraints. With each node having three DOFs, translation displacement along the X, Y, and Z axes, the element possesses a total of 24 DOFs (8 nodes * 3 DOFs per node).

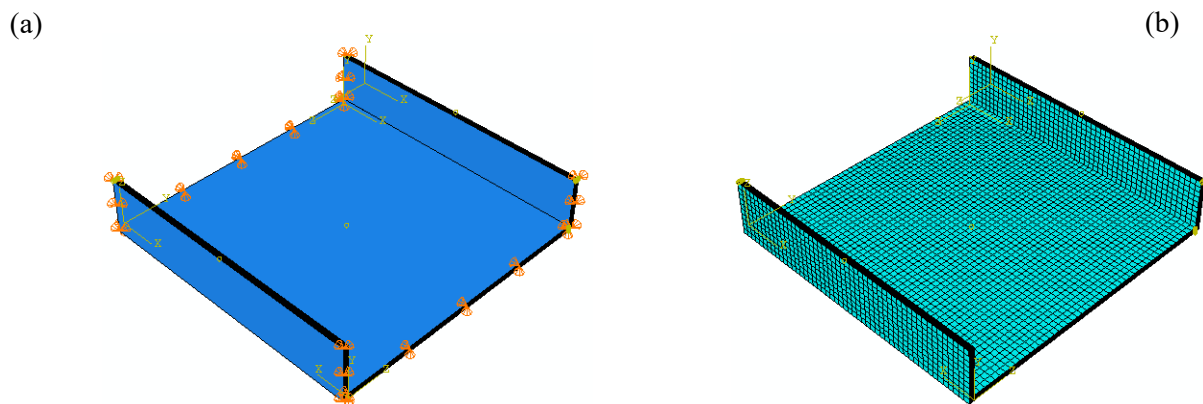


Figure 5-1 Typical channel section strut modelled based on the finite element simulation (a) implementing clamped boundary conditions, (b) diagrammatic representation of the mesh for the channel section strut

5.4. Results and discussion

5.4.1. GRC laminated channel section strut with UD graphene pattern

One of the principal targets of this study is to undertake a comprehensive comparative evaluation of how varying graphene distribution patterns impact the nonlinear thermal instability responses and the thermally induced natural frequencies variations in composite laminated channel section struts, both in pre-buckling and post-buckling states. To achieve this objective, a thorough comparison is made between several graphene distribution patterns, with the UD pattern serving as the reference case.

The comparison methodology employed in this research comprises three distinct phases. initially, the comparative analysis begins with the presumption that each distinct segment of the

channel section strut, which includes two vertical walls (flanges) and one horizontal wall (web), is constructed from ten plies of graphene reinforced composite material, all adhering to the UD distribution pattern. Following this assumption, a detailed nonlinear thermal instability analysis is performed to acquire results pertinent to the reference case. In the second step of the comparative analysis, the graphene distribution patterns through the flanges thickness are altered to include various non-uniform distribution patterns such as FG-X, FGX-FGX, FG-O, FGO-FGO, FG-V, and FGV-FGV. This analysis endeavors to ascertain which specific types of non-uniform graphene distribution patterns, applied through the flanges, exert the most and least significant impact on the critical buckling temperature and fundamental natural frequencies of the channel section struts, while maintaining a constant UD graphene distribution pattern across the web's thickness in all case studies.

The final step involves selecting and maintaining the best non-uniform graphene distribution pattern for the flanges obtained from the second step. Simultaneously, the web is subjected to a variety of non-uniform graphene distribution patterns, replacing the initial UD pattern. Consequently, it becomes feasible to identify the optimal combination of graphene distribution patterns that can be applied across the thickness of the flanges and web, with the aim of improving the critical buckling temperature and fundamental natural frequencies. Furthermore, this process is conducted again, but this time employing the least effective non-uniform graphene distribution patterns for the flanges. The purpose of this stage is to conclusively recognize the least efficient combination of graphene distribution patterns when used on the entire channel section strut.

Two key points should be highlighted for clarity: First, in all the scenarios examined in this paper, the graphene distribution pattern is kept identical for both flanges to ensure symmetry.

Second, the total volume percentage of graphene used remains the same in all case studies; the primary difference lies in the distribution patterns of the graphene.

Prior to initiating the comparative analysis of various graphene distribution patterns using the aforementioned methodology, it's crucial to establish a baseline of verification results. This is demonstrated in Fig. (5.2), which showcases the thermal equilibrium paths for channel section struts with three different shape factors, $R = b_f/b_w$, reinforced with a UD graphene distribution pattern and considering the clamped boundary conditions at both longitudinal ends of the structure.

This paper employs a specific notation to represent boundary conditions: 'CCC-CCC' for clamped and 'SSS-SSS' for simply-supported conditions. This format reflects the setup where, at each longitudinal end of the structure, there are three edges, two belonging to the flanges and one to the web's edge. The notation confirms that at both ends, all edges are subjected to the same type of boundary condition. Moreover, the various types of graphene reinforcement combinations utilized for the web and flanges of the channel section struts, represented schematically in the A-B format. In this notation, the first element (A) represents the graphene distribution pattern applied to the web, and the second element (B) corresponds to the specific type of graphene reinforcement pattern used for the flange. For example, in the UD-FGX case, UD refers to the graphene distribution for the web, and FGX indicates the graphene distribution pattern adopted for the flanges in the channel section struts.

As shown, the deflection curve for the flange corresponds to the center of its longitudinal free edge, while the deflection of the web is associated with its central point. These paths are derived using the LW-TSDT and compared with outcomes from numerical simulations conducted using the ABAQUS commercial software.

A preliminary analysis of Fig. (5.2) reveals a significant correlation between the findings acquired from the LW-TSDT and those computed using the FEM. Moreover, the results demonstrate that increasing the flange width dimension inversely affects the compressive strength of the channel section struts, leading to greater flange deflection in the post-buckling phase and a subsequent decrease in the critical buckling temperature. To clarify, with a flange-to-web width ratio $R = 0.2$, the critical buckling temperature for UD channel section struts is approximately $T = 400 K$. Increasing this ratio to $R = 0.8$ results in a reduction of the critical buckling temperature to $T = 370 K$. Another interesting observation that can be drawn from the figure is the apparent lack of noticeable influence of varying flange widths on the post-buckling equilibrium path of the web. This is evidenced by the nearly identical web post-buckling deflection across three different shape factor types.

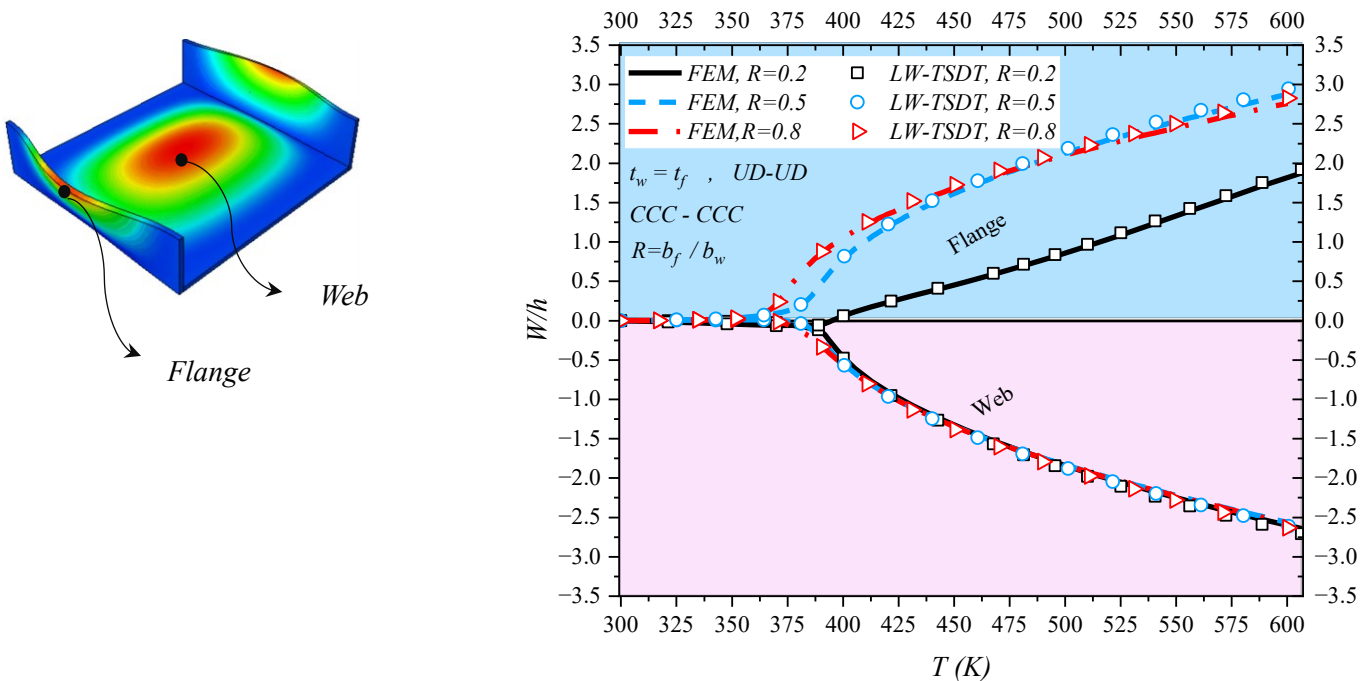


Figure 5-2 Comparison the nonlinear thermal equilibrium paths of flange and web in a channel section strut with UD graphene distribution pattern

The LW-TSDT approach accounts for 6591 degrees of freedom (DOFs) in its buckling analysis

for the UD laminated composite channel section strut, which is reflected in a stiffness matrix of the order 6591 by 6591. On the other hand, the finite element analysis utilizes 3D 8-node linear hexahedral elements (C3D8), resulting in a total of 17421 DOFs. This marked discrepancy in the DOFs between the semi-analytical LW-TSDT and the numerical finite element method underscores the enhanced computational efficiency of the LW-TSDT. Table. (5.2) offers a detailed summary of the analysis in terms of runtime and CPU usage. A cursory review of this table clearly shows that the implemented LW-TSDT method operates around 33% faster in terms of runtime compared to the numerical finite element simulation.

Table 5-2. Comparison of computing time and CPU usage in performed simulations and computational performance of proposed methodology (UD, $b_f/b_w = 0.2$, $t_f/t_w = 1$, CCC-CCC)

Solution method		
Present Method (LW-TSDT)	DOF	6591
	Running time (s)	938
	CPU usage (%)	25%
Finite Element Method (ABAQUS)	DOF	17421
	Running time (s)	1247
	CPU usage (%)	37%
Discrepancy performance time (%)		
$\frac{(ABAQUS - LWTSDT)}{LWTSDT} \times 100$		33 %

5.4.2. Influence of different graphene distribution patterns on the thermal post-buckling equilibrium paths and vibration characteristics of channel section struts

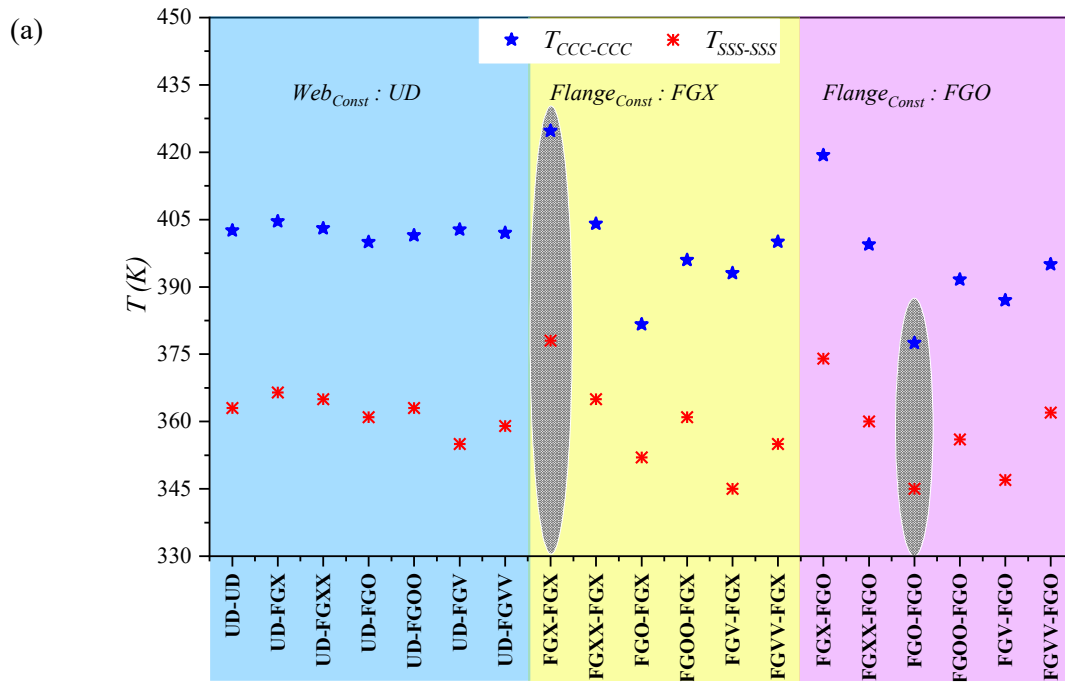
By conducting a nonlinear thermal instability analysis of polymeric laminated channel section struts, reinforced with various graphene distribution patterns, and subjected to both clamped and

simply-supported boundary conditions, Fig. (5.3) compares the outcomes pertaining to their critical buckling temperatures and fundamental natural frequencies. Following the aforementioned explanations, the initial step of the comparison involves case studies, where UD graphene distribution pattern is consistently applied across the web, while variations in graphene dispersions are examined in the thickness direction of the flanges. The outcomes of these studies are presented in Figs. (5.3)(a) and (b), distinguished by a blue background for clarity. The results demonstrate that where the web is reinforced with UD graphene distribution, the configuration employing FGX graphene distribution for flanges reinforcement yield the highest critical buckling temperatures and fundamental natural frequencies. Conversely, configuration with FGO graphene distribution in the flanges are associated with the lowest values for both critical buckling temperature and fundamental natural frequency.

In the subsequent step of the comparative analysis, the FGX graphene distribution pattern, identified as the most effective, is consistently applied for reinforcing the flanges. Concurrently, various non-uniform graphene dispersions are explored through the thickness direction of the web. The results pertaining to this specific scenario are demonstrated within the yellow regions of Figs. (5.3)(a) and (b). The findings confirm that when the FGX graphene distribution pattern is employed for both the flanges and the web, the laminated channel section struts achieve their peak performance in terms of critical buckling temperature and fundamental natural frequency.

Furthermore, this scenario is replicated with the objective of identifying the least effective graphene distribution pattern. This is illustrated in the pink area of Fig. (5.3). Here, the FGO graphene distribution, acknowledged as the least effective, is selected for reinforcing the flanges of the channel section struts. simultaneously, a range of non-uniform graphene distributions are

explored through the thickness direction of the web. The results conclusively demonstrate that the lowest critical buckling temperature and fundamental natural frequency correspond to the case in which both the flanges and the web are reinforced with the FGO graphene distribution pattern.



(b)

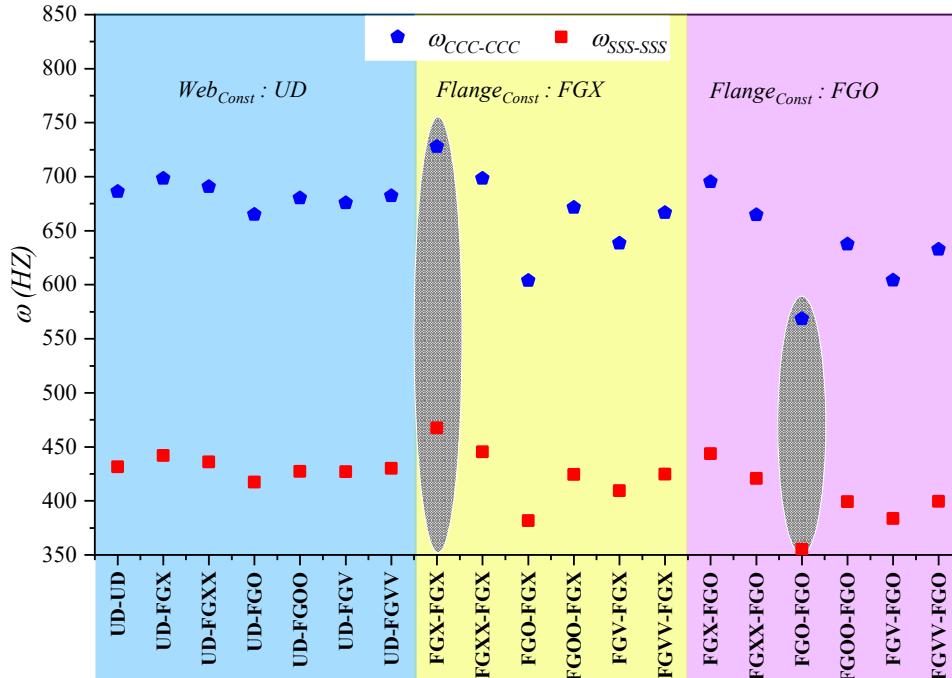


Figure 5-3 Investigation the influence of various kinds of graphene distribution patterns and boundary conditions on the critical buckling temperatures and fundamental natural frequencies of laminated channel section struts

Based on the findings presented in Fig. (5.3), the subsequent section of this paper will undertake a comparative analysis of four distinct graphene distribution patterns. These patterns will be evaluated from various analytical perspectives, including thermal post-buckling equilibrium paths, bending moment, and pre- and post-buckling thermally induced free vibration. It is important to note that the four graphene patterns under review include UD-UD, serving as the benchmark case, along with FGX-FGX and FGO-FGO, identified respectively as the most and least effective scenarios. Additionally, the analysis will also consider the FGV-FGO combination, where an asymmetric graphene distribution pattern (FGV) is utilized for reinforcing the web.

Figure 7 presents a comparison of the thermal post-buckling equilibrium paths for laminated channel section struts, reinforced with various uniform and non-uniform graphene distribution patterns. As depicted, Fig. (5.4)(a) pertains to the struts under clamped (CCC-CCC) boundary conditions, whereas Fig. (5.4)(b) displays the outcomes for struts with simply-supported (SSS-

SSS) boundary conditions. The results clearly demonstrate that, under both types of boundary conditions, laminated channel section struts reinforced with FGX graphene distribution pattern exhibit a higher critical buckling temperature compared to those with alternative graphene dispersions. Furthermore, during the post-buckling phase, the deflection observed at the flange (center of the free edge) and the web (central point) is comparatively lower in the FGX graphene reinforced cases than in other graphene distribution patterns. Conversely, independent of the boundary conditions applied, structures reinforced with FGO graphene distribution pattern experience a lower critical buckling temperature and a higher post-buckling deflection at the flange and web. For example, consider a scenario with a clamped boundary condition where the geometrical parameters of the channel section strut, and the total percentage of graphene utilized in reinforcing the laminated structure remain constant. Adjusting the graphene distribution pattern from FGO to FGX results in a relative increase of 12% in the critical buckling temperature.

From Fig. (5.4), another significant observation emerges regarding the distinctive thermal equilibrium path of the FGV-FGO laminated channel section strut under simply-supported boundary conditions. This path markedly differs from those associated with other graphene distribution patterns that preserve symmetry or those found in channel section struts subjected to clamped boundary conditions.

The results illustrate that in cases featuring symmetric graphene distribution patterns, the thermal equilibrium paths exhibit a primary-secondary characteristic. The stable primary thermal equilibrium path is defined by a direct correlation between the applied thermal load and the structural response. As illustrated in Fig. (5.4), up until the critical buckling temperature, identified as the point of instability or bifurcation, both flanges and the web retain a flat configuration with no out-of-plane displacement, signifying their alignment with the primary equilibrium path. At the

onset of the critical buckling temperature, however, there is a noticeable jump in the deflection of both the flanges and the web. Consequently, in the post-buckling state, the instability response of both the flanges and the web is characterized by their transition to the second set of equilibrium paths.

Nonetheless, the thermal equilibrium path exhibited by simply-supported channel section struts reinforced with FGV-FGO graphene distribution patterns is distinct. Initially, as thermal loading commences, the structure undergoes out-of-plane displacement, transitioning into the first buckling mode shape. However, the magnitude of this initial deflection is minimal. Notably, the rate of deflection increases near specific temperatures, $T=347$ K. The observed phenomenon is due to the generation of non-zero thermal bending moments within the web reinforced with FGV graphene distribution pattern under thermal loading. This arises from stretching-bending coupling of asymmetric graphene distribution pattern, a process clearly illustrated in Fig. (5.5).

Figure 8 demonstrates that under both clamped and simply-supported boundary conditions, the bending moment at the center of the web, reinforced with symmetric graphene distribution patterns, remains zero until the critical buckling temperature. At this point, a bending moment is induced, leading to deflection. In contrast, for the web reinforced with FGV, characterized as an asymmetric graphene distribution pattern, a bending moment is present at the center of the web from the initial stage of thermal loading. The rate of change in this bending moment intensifies around $T=387$ K for clamped boundary conditions and $T=347$ K for simply-supported conditions. It should be noted that the simply-supported edge lacks the capability to provide an additional moment necessary for maintaining the flatness of the channel section strut, in contrast to a clamped structure, where the supports are designed to exert an extra moment.

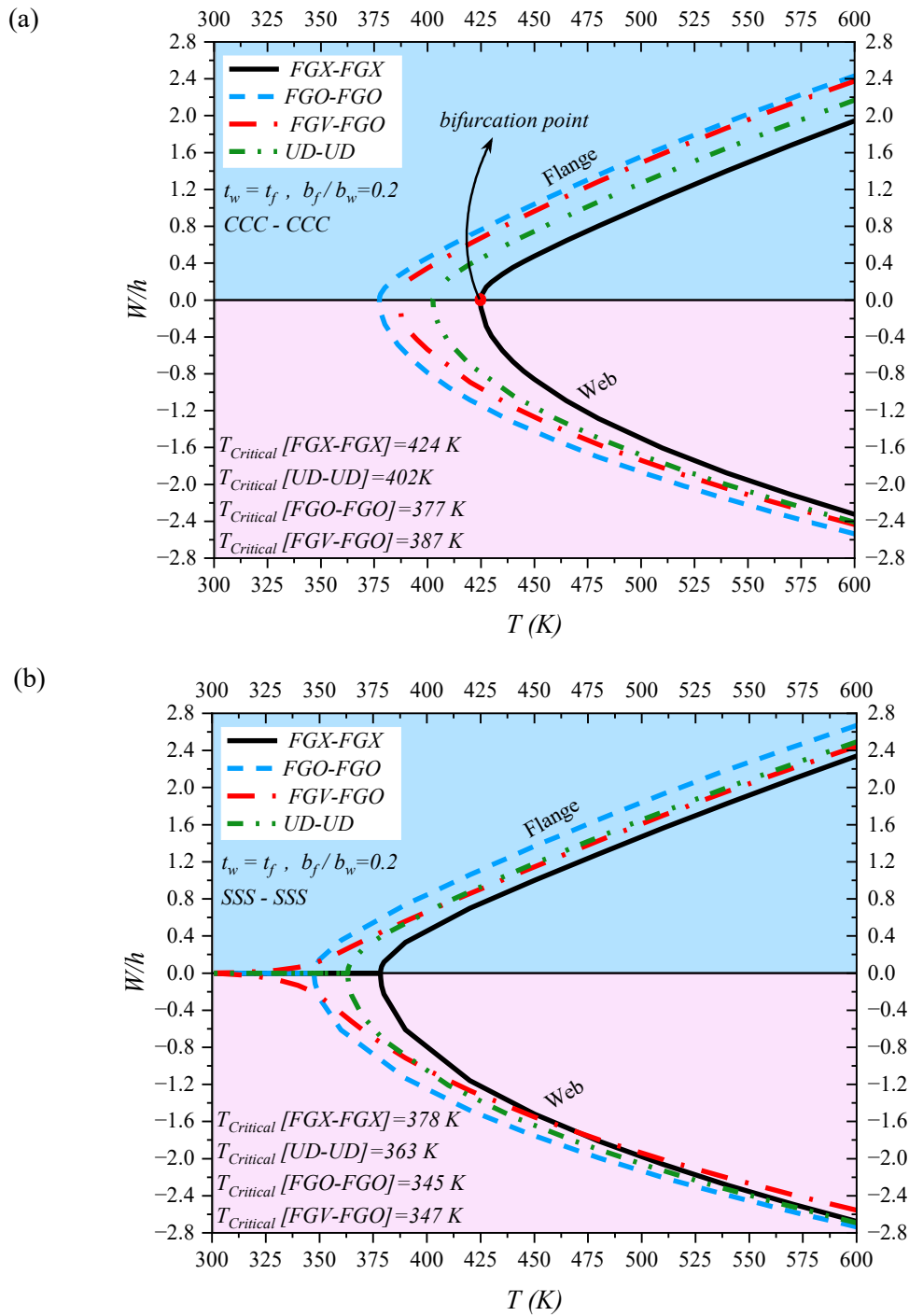


Figure 5-4 Investigation the boundary conditions and various graphene distribution patterns on the thermal equilibrium paths of laminated channel section struts subjected to uniform temperature rise (a) clamped (b) simply-supported

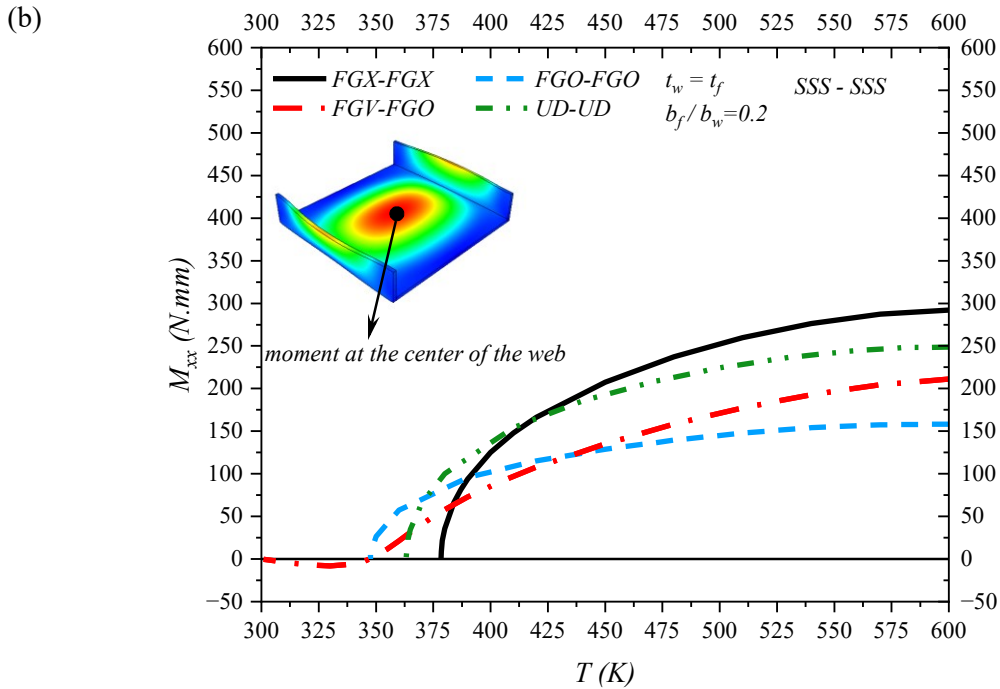
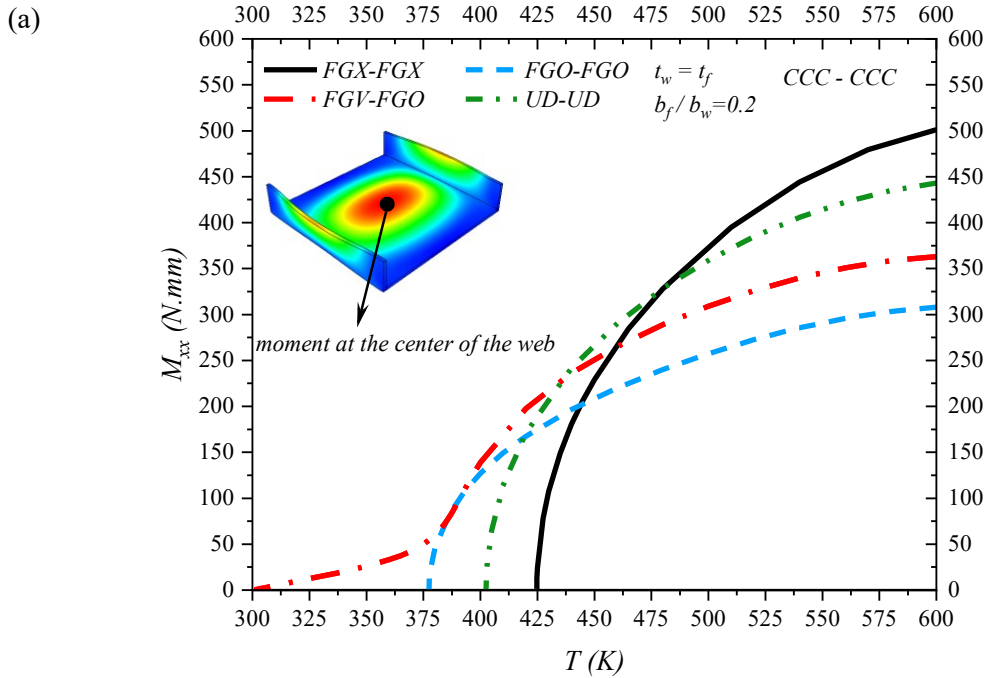


Figure 5-5 Influence of the boundary conditions and various graphene distribution patterns on the variation of bending moment at the center of the web (a) clamped (b) simply-supported

Figure 9 illustrates the variation of thermally induced pre- and post-buckling vibration of FG-GRC channel section struts. At the reference temperature, both the fundamental and second order

natural frequencies of FGX channel section struts are higher compared to those reinforced with other types of graphene distribution patterns.

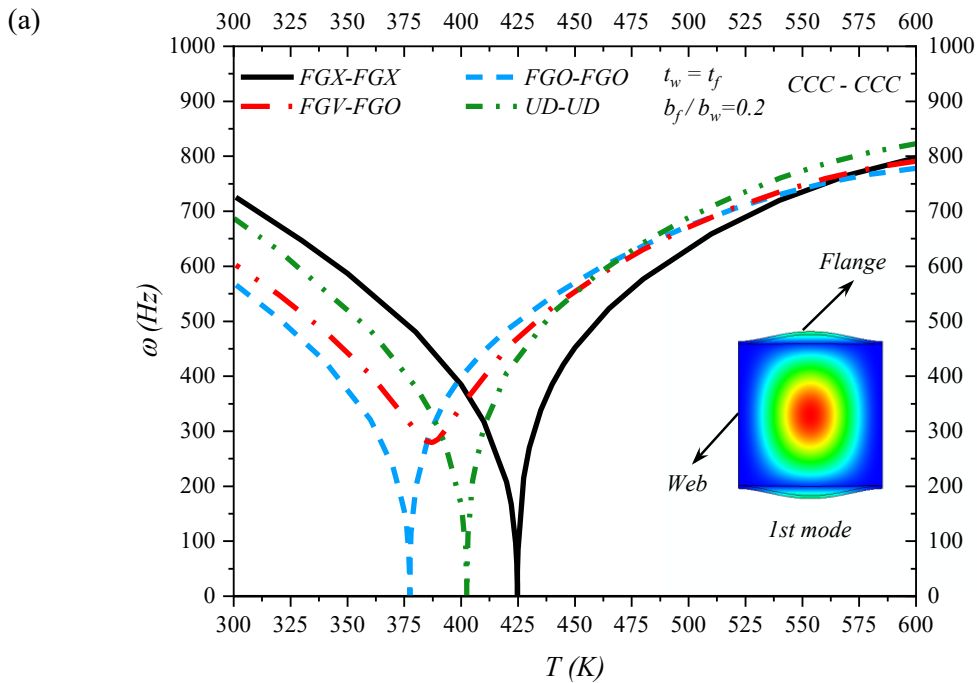
As indicated, independent of the variations in graphene distribution patterns and boundary conditions, a uniform increase in temperature leads to a continuous decrease in both the first and second-order natural frequencies during the pre-buckling phase. This decrease continues until reaching near the critical buckling temperature or instability point, primarily because of the reduction in stiffness caused by in-plane compressive thermal loading. It is essential to highlight that, across the majority of the cases examined, following the critical buckling temperature in the post-buckling phase, there is an observed increase in both first second natural frequencies. This perception emphasizes the predominance of the stiffening effect because of static buckling deformation over the softening impact induced by thermal stress.

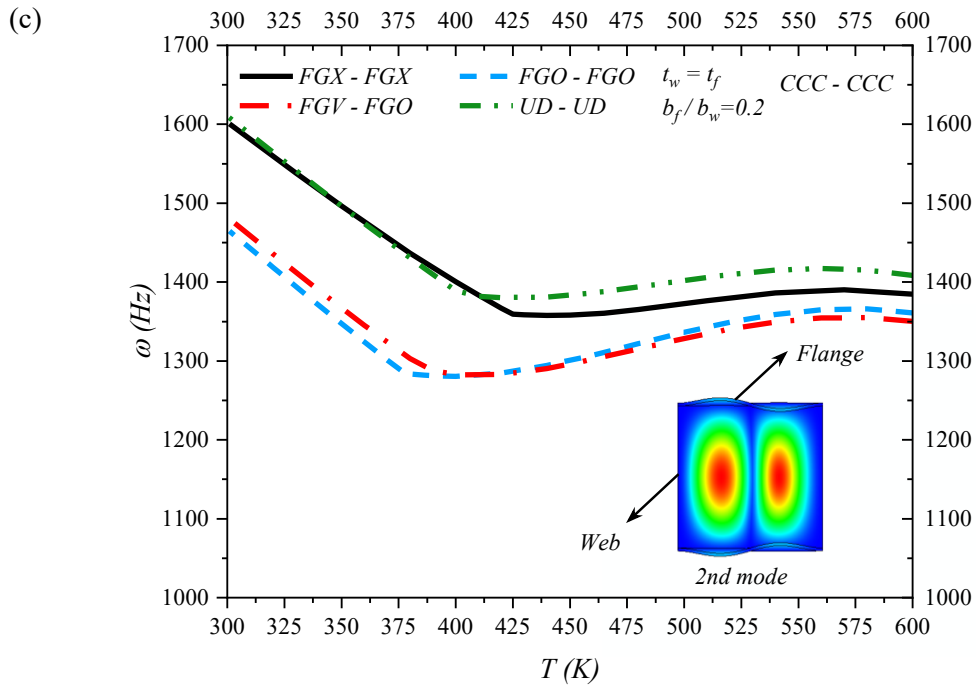
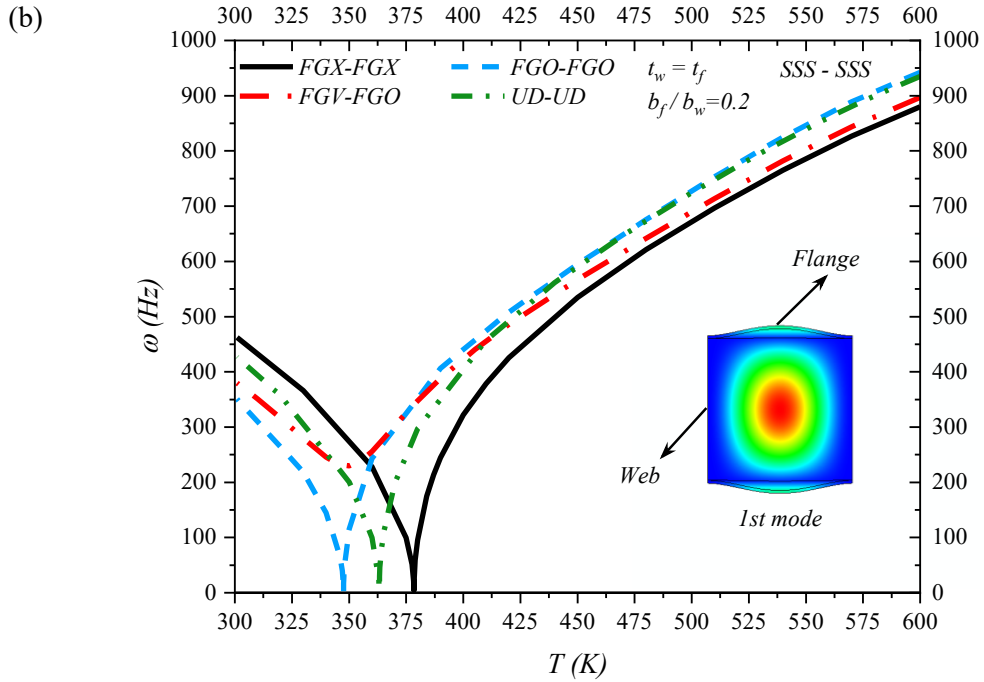
In the analysis of fundamental natural frequencies, it is observed that, in instances where symmetric graphene distribution patterns (FGX, FGO, UD) reinforce the laminated channel section strut, these fundamental frequencies diminish to zero at the critical buckling temperature, before transitioning into the post-buckling phase. Conversely, Employing an asymmetric graphene distribution pattern (FGV) results in an elevation of the fundamental frequency close to the critical buckling temperature. This approach prevents the frequency from decreasing to zero. The underlying mechanism involves the generation of thermal bending moment through the web at the beginning stage of thermal loading, as discussed in Fig. (5.5). This bending moment induces static buckling deflection, which, as noted, leads to an increase in stiffness.

As mentioned, FGX channel section struts exhibit enhanced thermal compressive strength relative to alternative configurations, causing them to transition into the post-buckling phase at a later stage compared to other cases. Consequently, the fundamental natural frequencies during the

post-buckling phase are lower for FGX struts than for structures reinforced with other types of graphene distribution patterns.

An additional insight derived from Fig. (5.6) pertains to the variance in the fundamental and second-order natural frequencies under different boundary conditions. Specifically, in the pre-buckling stage, the fundamental frequencies of channel section struts with clamped boundary conditions are substantially higher than those with simply-supported boundary conditions. Conversely, this pattern reverses in certain segments of the post-buckling phase, indicating a notable shift in frequencies behavior dependent on the boundary condition applied. For example, at the reference temperature of $T=300$ K, the fundamental frequency of FGX channel section struts under clamped boundary conditions is approximately 1.67 times greater than that of struts with simply-supported boundary conditions. However, at the maximum temperature of $T=600$ K in the post-buckling phase, this ratio decreases to 0.9.





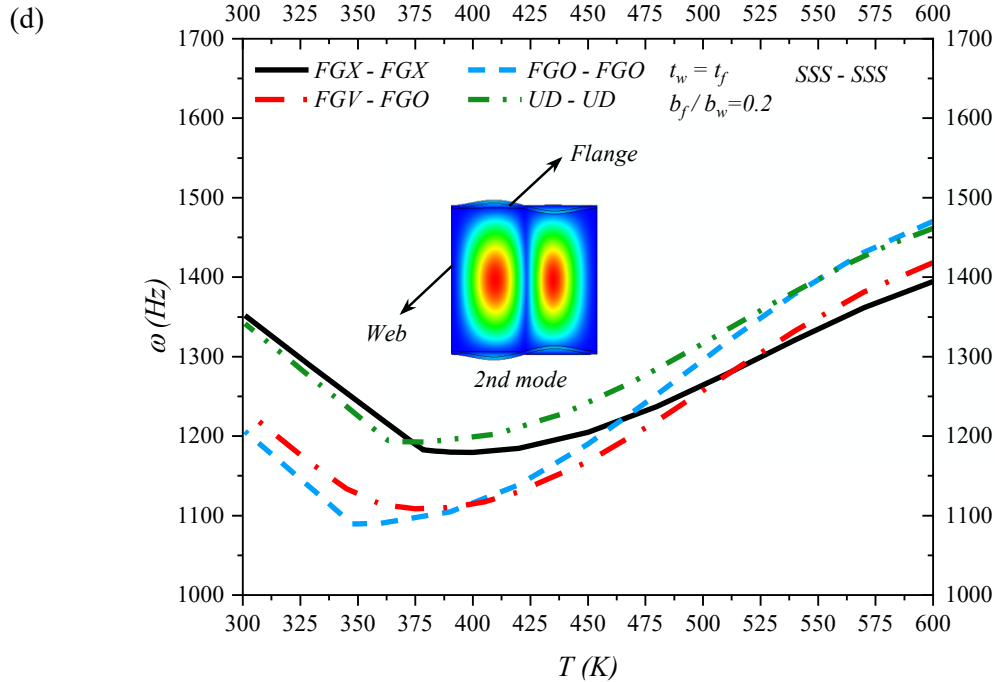
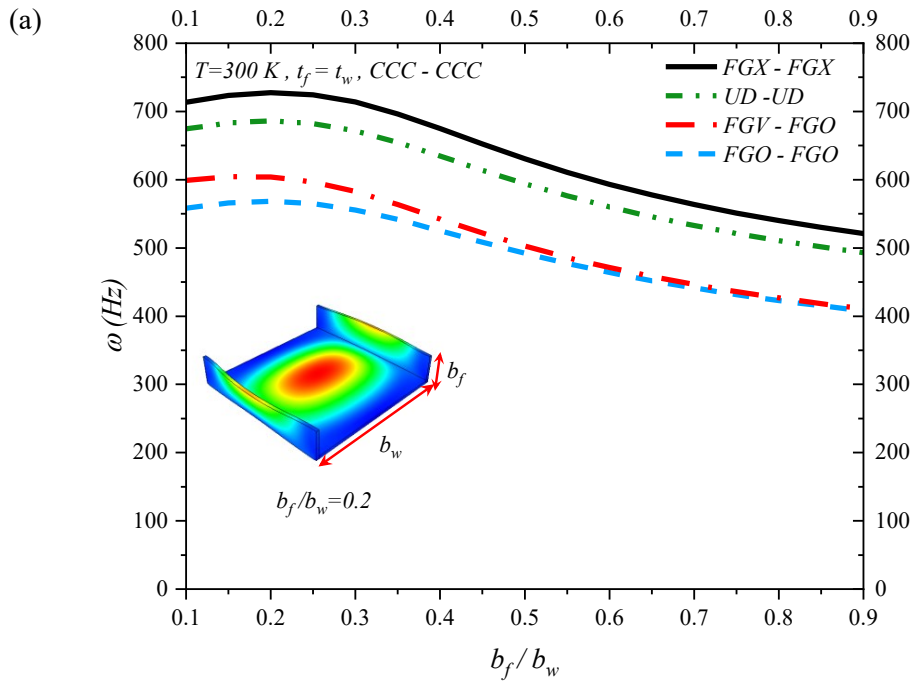


Figure 5-6 Influence of different graphene distribution patterns on variations of thermally induced pre- and post-buckling vibration of laminated channel section struts (a) fundamental frequency with clamped boundary condition (b) fundamental frequency with simply-supported boundary condition (c) second mode frequency with clamped boundary condition (d) second order with simply-supported boundary condition

Investigation the influence of the shape factor of channel section struts (b_f/b_w), which is the ratio of the flange width to the web width, on their fundamental natural frequencies at the reference temperature ($T=300$ K) is conducted in Fig. (5.7). As with the earlier results, this analysis is undertaken for both clamped and simply-supported boundary conditions. A key inference drawn from these findings is that, irrespective of the boundary condition type, an increase in the shape factor, assuming a constant web width while the flange width increases, leads to a decrease in the fundamental natural frequencies. This suggests a significant reduction in the compressive stiffness of the structure. This phenomenon can be logically attributed to the increased leverage effect of the wider flanges, which amplifies bending and reduces the overall stiffness, thereby impacting the fundamental frequency characteristics.

Furthermore, the optimal shape factor for laminated channel section struts, as suggested by the data, is approximately $b_f/b_w = 0.2$, where the structure exhibits the highest fundamental frequencies. Specifically, in the case of clamped FGX channel section struts, it is observed that increasing the flange width from 0.2 to 0.9 leads to an approximate 30% decrease in the fundamental frequency. This highlights the critical role of shape factors in determining the vibrational characteristics of these structures.



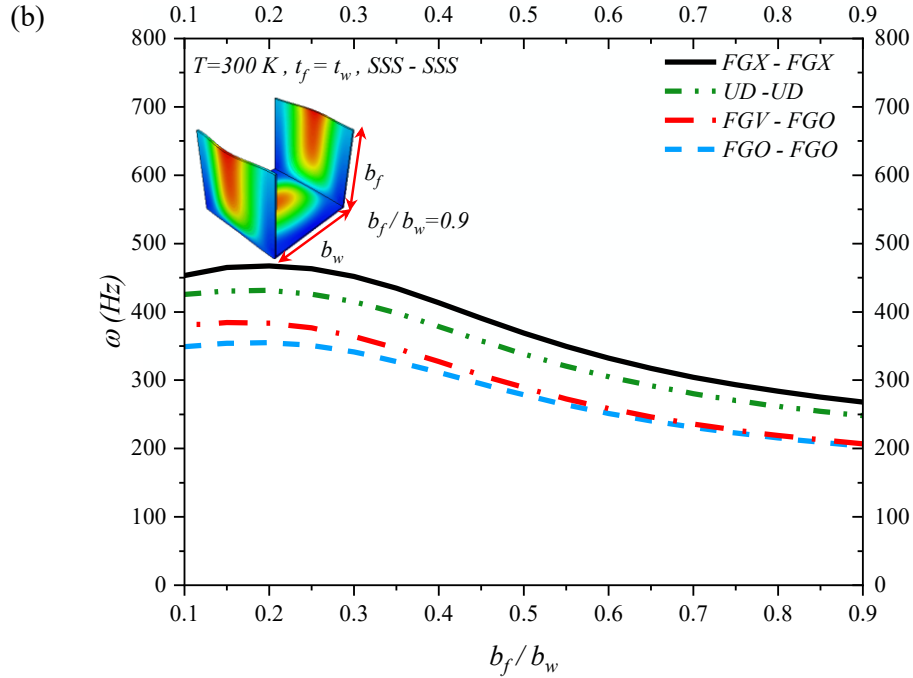


Figure 5-7 Influence of various graphene distribution patterns and geometrical parameters on the fundamental frequencies of FG-GRC channel section struts (a) clamped boundary condition (b) simply-supported boundary condition

5.4.3. Imperfection sensitivity of post-buckling equilibrium paths and free vibration of FGX channel section struts

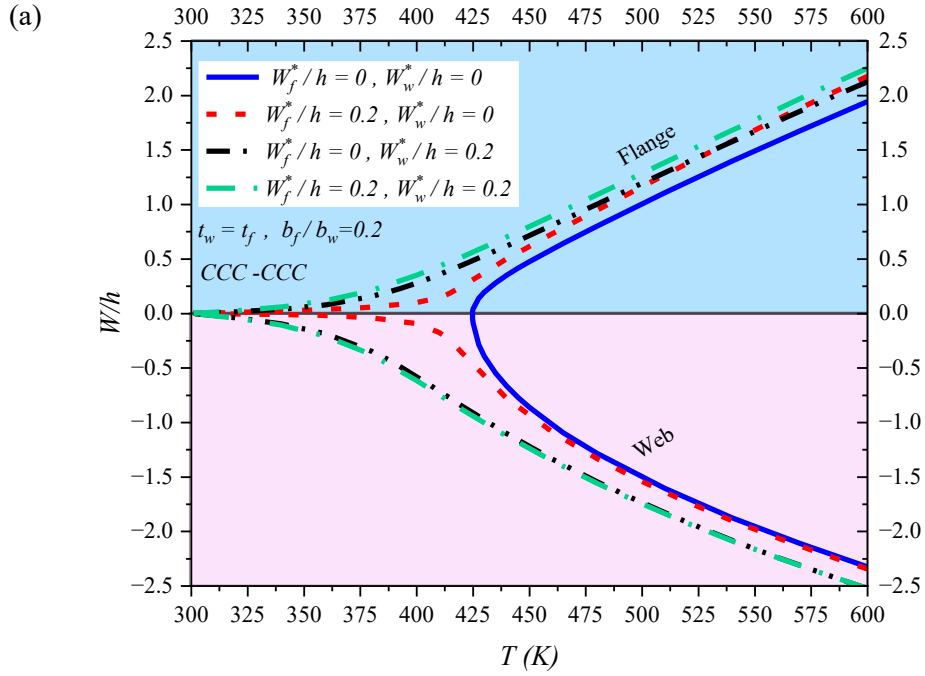
To determine the impact of geometrical imperfections on the post-buckling behavior and free vibration characteristics of channel section struts, just the FGX graphene distribution pattern is selected as the most effective in enhancing in-plane compressive stiffness. For a thorough analysis of the impact of local geometrical imperfection, three distinct methodologies are employed to apply it. In the initial method, the web of the channel section strut is presumed to be perfect, with local geometrical imperfections applied exclusively to the flanges. This induced imperfection corresponds to the first buckling mode of the flanges, as depicted in Table (5.1). Conversely, in the subsequent approach, the local geometrical imperfection is exclusively applied to the web, aligning with the first mode of buckling for this component, while the flanges are assumed to be without imperfection. In the final approach, geometrical imperfections are applied simultaneously to both

the flanges and the web of the channel section struts. It is crucial to emphasize that throughout the process of introducing geometrical imperfections to both the flanges and the web, the preservation of straightness at the junction is maintained as an assumption to meet the stress free edge criteria.

Figure (5.8) clearly shows that under any boundary condition, the perfect FGX laminated channel section strut demonstrates a bifurcation-type instability across both the web and flange. This behavior indicates that these components stay undeformed and flat until reaching the critical temperature threshold. Conversely, the presence of geometrical imperfections initiates lateral deflections in both the flange and web right from the onset of thermal loading. An additional noteworthy observation is that the instability response of channel section struts, where imperfection is solely applied to the web, more closely resembles the scenario in which imperfections are introduced simultaneously to all segments.

A comparative analysis highlighting the effects of geometrical imperfections on the local deflection of the web and flange at the buckle crest (half length) of the channel section struts is presented in Fig. (5.9). Owing to the symmetry along the Z local axis of the web, as shown in Fig. (4.1), deflection variations are illustrated for only one half of the cross-section. It is essential to emphasize that the presented results are for temperatures $T=450$ K and $T=380$ K, which are very close to the critical buckling temperatures of the FGX channel section struts, under clamped and simply-supported boundary conditions, respectively. As illustrated, the deflection observed in the perfect channel section strut at temperatures marginally exceeding the critical buckling temperature is virtually insignificant when compared to scenarios incorporating geometrical imperfections. In particular, the maximum out-of-plane displacement seen in the clamped FGX channel section strut, when it undergoes imperfections with an amplitude of $w^*/h = 0.2$ affecting both flanges and web, is approximately 2 times higher than in instance without any imperfections.

It should be highlighted that the out-of-plane displacement of the flange and web is equal to zero at the junction to satisfy the in-plane stress-free edge condition.



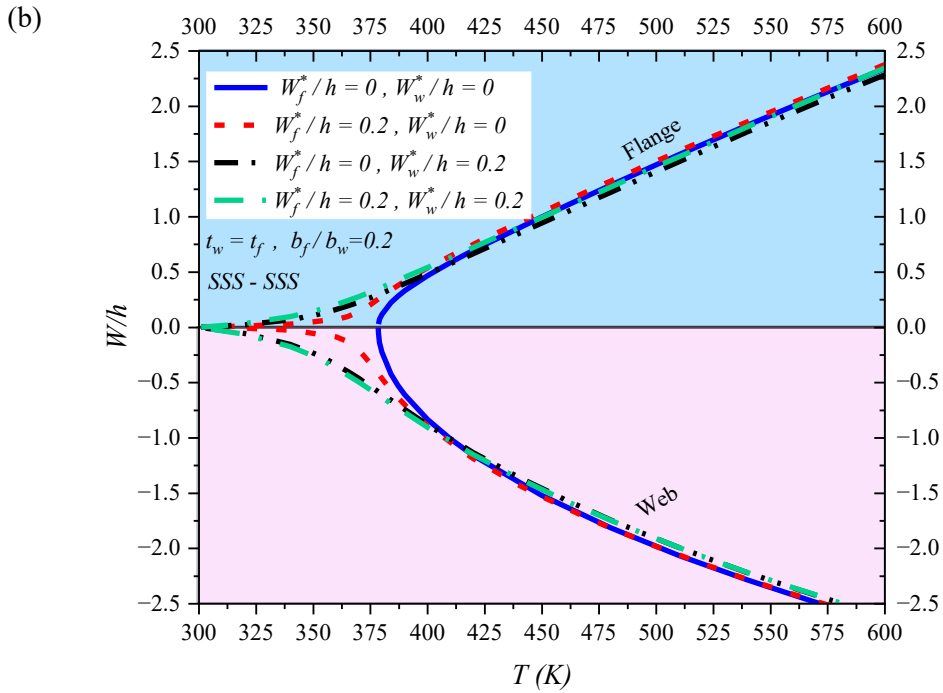
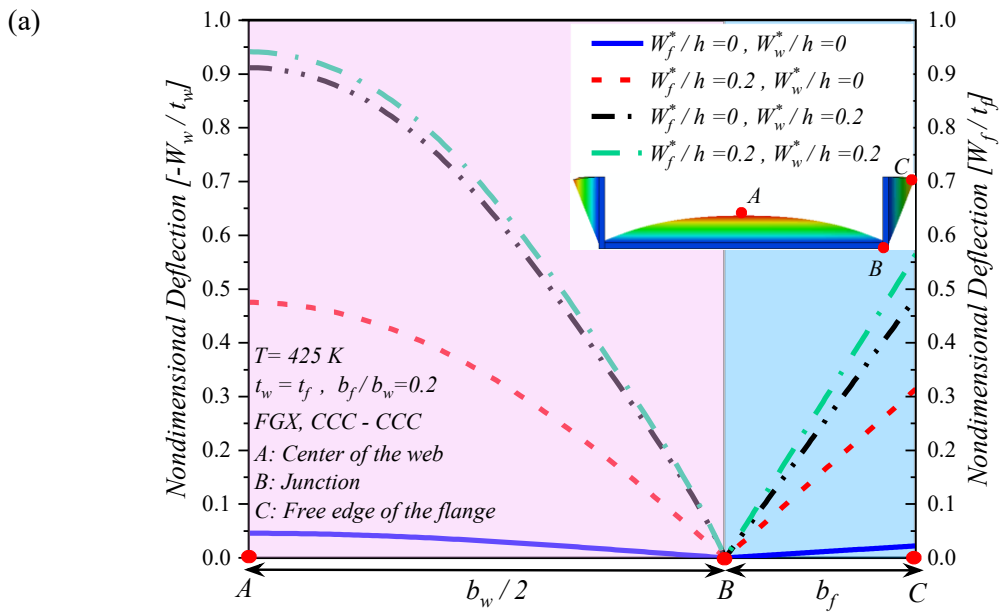


Figure 5-8 Influence of geometrical imperfection on the thermal post-buckling equilibrium paths of the FGX channel section struts (a) clamped boundary condition (b) simply-supported boundary condition



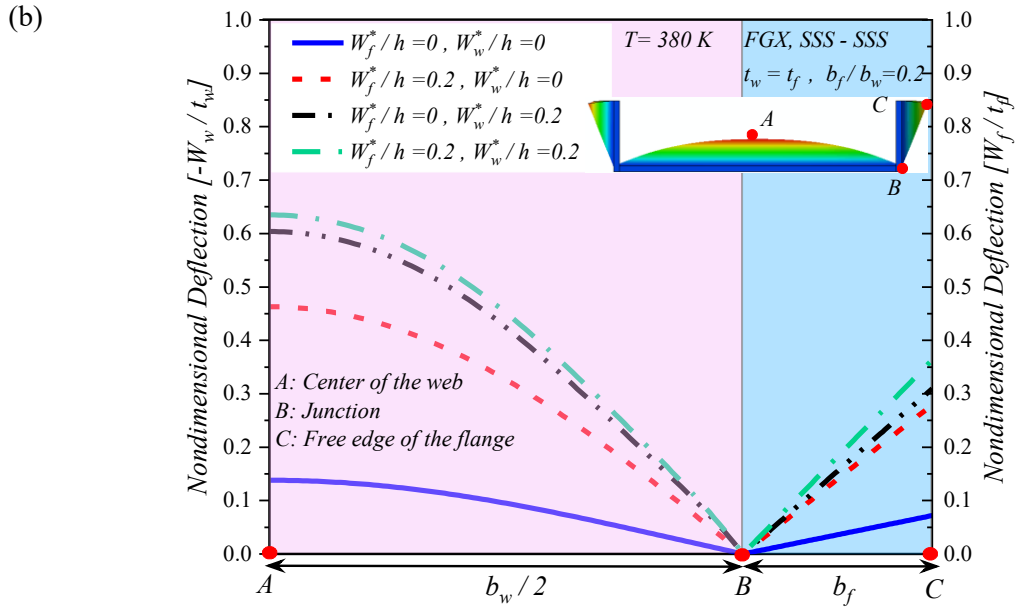
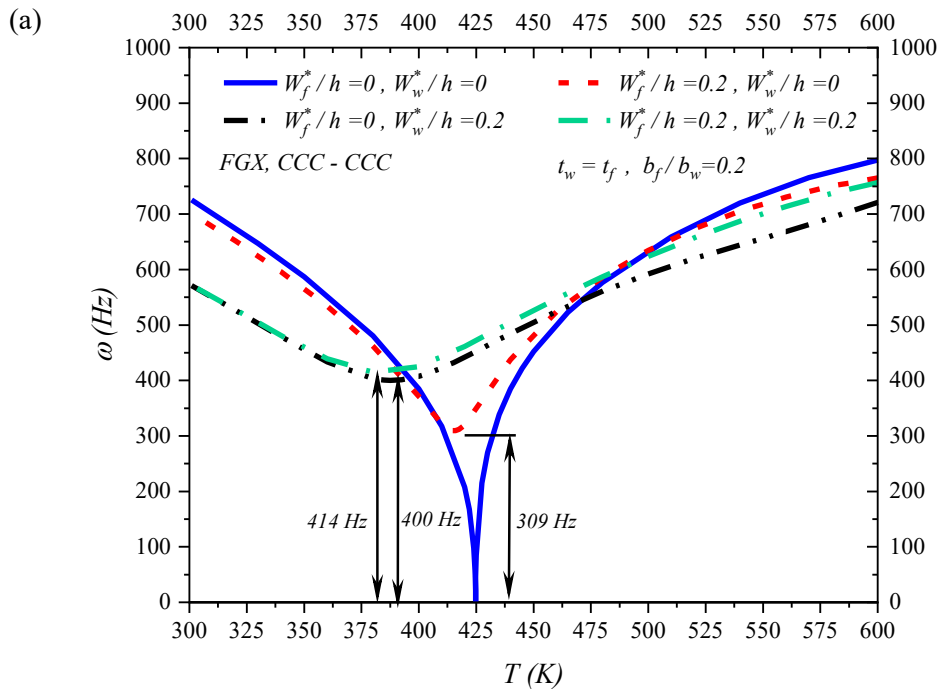


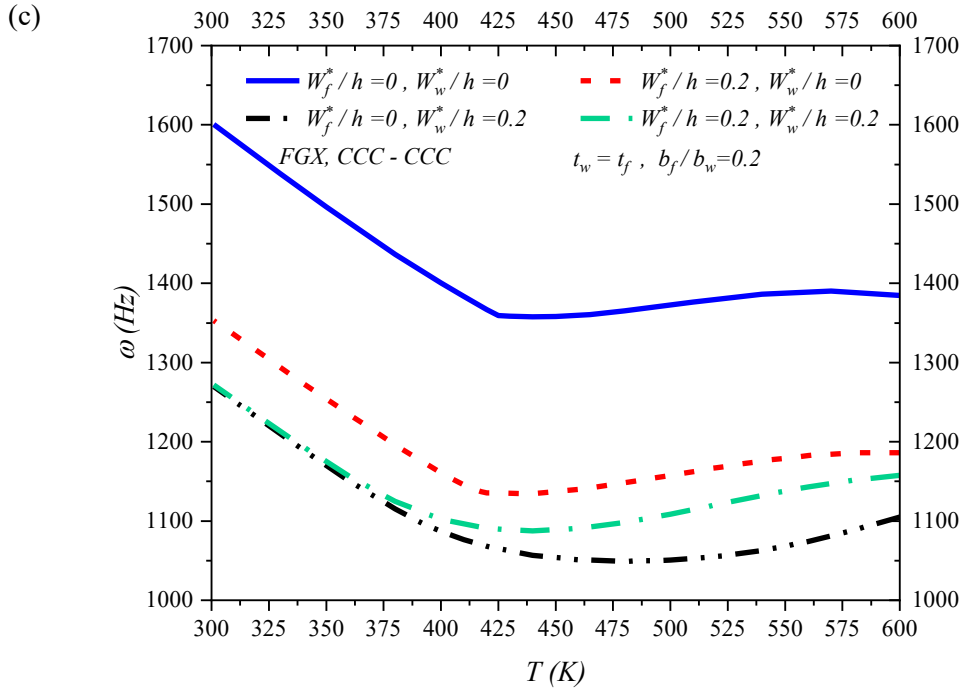
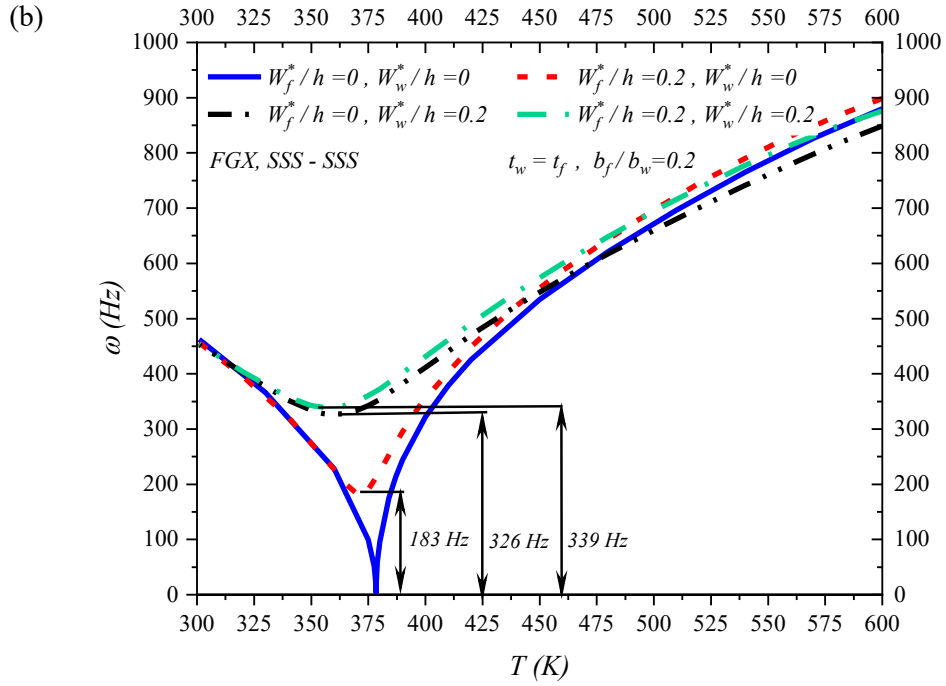
Figure 5-9 Influence of geometrical imperfection on the local deflection at the buckle crest of FGX channel section struts (a) clamped boundary condition (b) simply-supported boundary condition

Fig. (5.10) illustrates the comparison between the pre- and post-buckling free vibrations of both perfect and imperfect channel section struts. This analysis is crucial for understanding the potential effects that deviations from ideal geometrical configurations can have on the natural frequencies of FGX channel section struts with clamped and simply-supported boundary conditions.

A pivotal observation from the analysis reveals that geometrical imperfections, characterized by an amplitude of $W^*/h = 0.2$, prevent the fundamental frequencies of FGX channel section struts from diminishing to zero near the critical buckling temperature. Furthermore, introduction of these imperfections across the entire structure notably increases their fundamental frequencies in the vicinity of this critical buckling temperature. This augmentation results in enhanced frequencies, achieving up to 414 Hz for struts under clamped boundary conditions and 339 Hz for those with simply-supported boundary conditions, respectively. This phenomenon is due to the enhanced structural stiffness around the critical buckling temperature that arises from the static buckling deflection caused by the geometrical imperfection. Nevertheless, in both the pre-buckling and

post-buckling phases, particularly with the clamped boundary condition, the presence of geometrical imperfections leads to a decrease in the fundamental natural frequencies. Furthermore, as clearly demonstrated in Figs. (5.10)(c) and (5.10)(d), the geometrical imperfections substantially diminish the second-order natural frequencies across both pre- and post-buckling states. It is important to highlight that there is no occurrence of order exchange phenomena between the first two modes of natural frequencies.





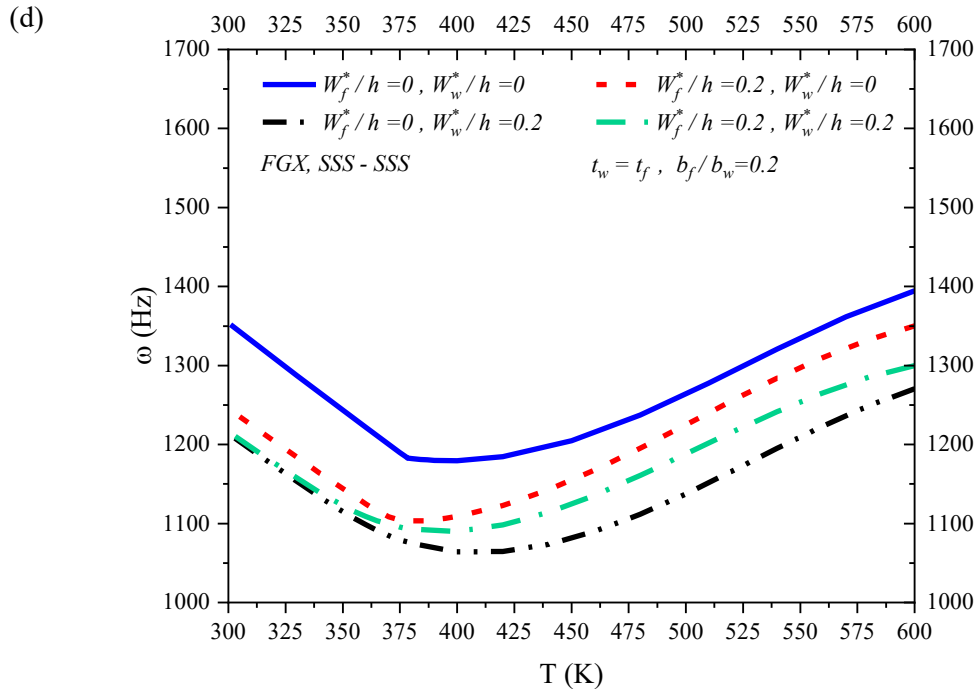


Figure 5-10 Influence of geometrical imperfections on variations of thermally induced pre- and post-buckling vibration of FGX laminated channel section struts (a) fundamental frequency with clamped boundary condition (b) fundamental frequency with simply-supported boundary condition (c) second order frequency with clamped boundary condition (d) second order with simply-supported boundary condition

5.5. Concluding remarks

This research addresses the issue of laminated composite open section struts, which are commonly used in engineering, being prone to local buckling when exposed to compressive thermal loads. The investigation seeks to discover effective solutions to this problem by employing graphene sheet reinforcements. The primary objective of this study is to assess how different distributions of graphene sheet reinforcements, through the thickness of the flange and web plates of channel section struts, affect their thermal compressive instability and their pre- and post-buckling free vibration. Attention has been given to discerning the distribution patterns of graphene that most significantly enhance the critical buckling temperature and natural frequencies. Furthermore, the effect of geometrical imperfections on the nonlinear thermal compression behavior of the FG-GRC laminated channel section struts has been assessed to obtain results that

more accurately reflect real-world conditions. A framework is constructed on the foundations of LW-TSDT and the von-Karman strain-displacement equation. To solve the governing equations, the minimum total potential energy principle and the Ritz method are applied in tandem with the Newton-Raphson iterative process; the obtained results are finally compared with those evaluated using the 3D finite element simulation. This study significantly enhances our comprehension of the relationship between material distribution and structural characteristics, offering pertinent insights for the development of more robust and effective engineering structures. In particular:

- Utilizing the FG-X graphene distribution pattern within the thickness of the web and flanges of channel section struts results in an estimated 12% increase in the critical buckling temperature for clamped channel section struts, when compared with those utilizing the FGO graphene distribution pattern. In scenarios with simply-supported boundary conditions, this increment is observed to be about 9%.
- This study reveals that within the shape factor, $b_f/b_w = 0.2$, analyzed, altering the graphene distribution patterns through the thickness of the flanges, while maintaining a constant graphene distribution in the web, does not significantly impact the critical buckling temperature of channel section struts. Conversely, modifying the graphene distribution patterns in the web, while reinforcing the flanges with a consistent type of graphene sheet, can change the critical buckling temperature by up to 12%. This indicates that, for the specific shape factor considered, the buckling behavior of the web plays a dominant role in the overall instability response of channel section struts.
- The analysis of thermally induced pre- and post-buckling free vibration in channel section struts, which are reinforced with differing graphene distribution patterns, demonstrates

that, through the pre-buckling situation, struts featuring the FGX channel section configurations achieve the highest natural frequencies. However, this pattern alters in the post-buckling stage.

- The enhancement of natural frequencies in FG-GRC laminated channel section struts through the post-buckling states, as a result of uniform temperature increase, can be attributed to the dominance of the stiffening effect, which is a consequence of static buckling deflection, over the softening effect caused by thermal stress.
- The equilibrium path of perfect FG-GRC channel section struts typically follows a primary-secondary trajectory, wherein the out-of-plane displacement remains unchanged with increasing temperature up to the instability point, at which the structure deflects. However, the introduction of geometrical imperfections initiates deformation from the onset of thermal loading, thereby leading to a unique equilibrium path.
- Incorporating an asymmetric graphene distribution pattern (FGV) or introducing geometrical imperfections that induce a bending moment throughout the structure from the initial stages of thermal loading effectively prevents the fundamental natural frequencies of FG-GRC channel section struts from reaching zero in proximity to the critical buckling temperature.

6. Conclusions and future perspectives

6.1. Conclusions

This Ph.D. thesis is meticulously organized into two principal sections. The first section, included in chapters 2 and 3, is dedicated to a comprehensive analysis of the impact of different graphene distribution patterns and varieties of interlaminar flaws, whether embedded or through-the-width, on the nonlinear thermomechanical instability and vibration characteristics of FG-GRC laminated plates. This investigation aims to elucidate the complex interactions between material composition, probability of damage propagation, and mechanical behavior, offering insights into optimizing the structural integrity and performance of advanced composite materials under various thermal and mechanical loading conditions. The research employs sophisticated analytical and numerical modeling techniques to capture the nuanced effects of graphene reinforcement on the performance of laminated, graphene composite plates.

The second section of the thesis, included in chapters 4 and 5, culminates with a comprehensive synthesis of findings derived from section 1 into the effects of graphene sheet reinforcements within laminated composite open section struts, with a particular emphasis on their vulnerability to local buckling under both compressive and thermal loading conditions. This rigorous analysis meticulously examines various graphene distribution patterns throughout the thickness of the flange and web plates in channel section struts. Through this detailed examination, the research provides an essential foundation for understanding the ways in which structural stability, buckling behavior, and vibrational properties can be enhanced through strategic design of graphene distribution. This section contributes significantly to the advancement of composite material science, offering innovative strategies for optimizing the mechanical performance and durability of graphene composite structures in engineering applications.

The study leverages sophisticated computational techniques, incorporating the LW-TSDT alongside the von-Karman nonlinear strain-displacement relations. These theoretical frameworks allows for building the solution through the application of the minimum total potential energy principle, utilizing the Ritz method. This approach is further augmented by the implementation of the Newton-Raphson iterative procedure, which enhances the accuracy and convergence of the solutions. The comprehensive, computational methodology enables a detailed and precise examination of the mechanical behaviors in the analysis.

To verify the accuracy and computational efficiency of the outcomes obtained from the LW-TSDT, a comprehensive three-dimensional (3D) finite element model has been developed using ABAQUS software for the purpose of comparative assessment.

It should be noted that the thermo-mechanical properties of both the matrix and graphene reinforcements, assumed to be temperature-dependent, were determined using the extended Halpin-Tsai micromechanical model.

Some of the key conclusions drawn from the present research include:

- The equilibrium path of FG-GRC laminated plates exhibits bifurcation or unique, stable equilibrium paths depending on the boundary conditions and graphene distribution patterns. Plates with clamped edges and asymmetric graphene distributions tend to show bifurcation-type paths, while those with simply-supported boundaries display unique equilibrium paths, attributed to the latter's inability to counteract thermally induced bending moments.
- The shape, and position of delamination significantly affect the nonlinear postbuckling response of the FG-GRC laminated plates. Specifically, circular and elliptical embedded

delaminations induce mixed-mode and global buckling modes, respectively, highlighting the importance of considering delamination characteristics in design and analysis.

- The presence of delamination alters the pre- and post-buckling vibration responses of FG-GRC plates compared to perfect plates. In some cases, delamination can enhance post-buckling, thermally induced fundamental frequencies, indicating complex interactions between delamination, graphene distribution, and vibrational behavior.
- The implementation of the FG-X graphene distribution pattern across the thickness of the web and flanges in channel section struts results in a 30% improvement in the critical buckling-induced end-shortening of the structures, in comparison to channel section struts of identical geometric configurations that are reinforced with a uniform dispersion (UD) of graphene.
- Conversely, the adoption of the FG-O pattern is associated with a considerable decrement of the critical buckling-induced end-shortening by approximately 26%. This analysis underscores the profound impact of strategic graphene distribution on the mechanical performance of composite structures, highlighting the potential for material optimization in enhancing structural resilience against buckling phenomena.
- Irrespective of the particular graphene distribution patterns employed, the location of maximum membrane stress is consistently observed at the interface between the flange and web, accurately located at the buckle crest within the channel section struts. This finding emphasizes the critical nature of this junction in terms of stress concentration.
- Integrating an asymmetric graphene distribution pattern, referred to as FGV, or the introduction of geometric imperfections that generate a bending moment across the structure from the onset of thermal loading, serves to effectively prevent the fundamental

natural frequencies of FG-GRC channel section struts from diminishing to zero near the critical buckling temperature.

- The enhancement of natural frequencies in FG-GRC laminated channel section struts through the post-buckling states, as a result of uniform temperature increase, can be attributed to the dominance of the stiffening effect, which is a consequence of static buckling deflection, over the softening effect caused by thermal expansion.

6.2. Recommendations for future work

This research has undertaken a thorough analysis on the effects of graphene reinforcement on the nonlinear thermomechanical instability and pre- and post-buckled vibration responses of laminated composite plates. Additionally, it has explored how graphene distribution patterns influence the instability behaviors of channel section struts, employing the LW-TSDT as the semi-analytical framework. Despite the comprehensive scope of this investigation, it identifies several opportunities for further scholarly exploration within this field. Some of them are suggested as following:

- Since their discovery in 2012, Perovskite Solar Cells (PSCs) have quickly become a leading third-generation photovoltaic technology, thanks to their flexibility, lightweight, high-power output, and low production costs. A PSC typically consists of a thin laminated structure with five layers: Indium Tin Oxide (ITO), PEDOT:PSS, perovskite, PCBM, and gold (Au), enabling efficient sunlight to electricity conversion. Yet, PSCs' effectiveness and durability are greatly affected by environmental factors like moisture, heat, and UV light, which can degrade the cells over time. This susceptibility underscores the imperative for conducting instability analysis of PSCs. Given their laminated structures, such analysis can be effectively performed using the LW-TSDT methodology proposed in this study.

- PSCs are envisioned for use in environments where they may be subject to various mechanical stresses, including vibrations from wind, transportation, or machinery. Vibration analysis helps ensure that these cells can withstand such conditions without structural failure. Another practical and vital recommendation for the photovoltaic sector is to apply the methodology proposed in this thesis, which pertains to the analysis of delaminated structures, to assess how such delaminations affect the dynamic instability behavior of the PSCs.
- Owing to their superior electrical properties, graphene and its derivatives are highly promising in the development of advanced smart composite materials. This thesis proposes utilizing these distinct characteristics along with the methodology to perform nonlinear vibration analysis and capture the vibration responses in FG-GRC plates with various delamination zones, which can be altered by adjusting the electrical field attributes for a broader scope of applications of graphene composites.
- It is recommended to integrate the proposed methodologies that assess the instability responses of delaminated FG-GRC plates and FG-GRC channel section struts to examine how various interlaminar defects, which may arise between the layers of the flanges and the web in channel section struts, affect their static and dynamic behaviors.
- The utilization of the proposed methodology in this thesis for the analysis of FG-GRC channel section struts is suggested, aiming at the optimization of both graphene distribution patterns and topological geometries, simultaneously, which can be considered for the cross-sections of either open or closed thin-walled structures to enhance their postbuckling strength.

- Future research could benefit from manufacturing both open and closed section struts through 3D printing technology, employing two distinct filament types: one consisting of pure polymer and the other being polymer filaments enhanced with a specific weight percentage of graphene. Subsequent compressive testing could then be conducted to compare the results with those obtained from the semi-analytical and numerical analyses presented in this thesis.

References

1. Potts JR, Dreyer DR, Bielawski CW, Ruoff RS. Graphene-based polymer nanocomposites. *Polymer (Guildf)* [Internet]. 2011;52(1):5–25. Available from: <https://www.sciencedirect.com/science/article/pii/S0032386110010372>
2. Stankovich S, Dikin DA, Dommett GHB, Kohlhaas KM, Zimney EJ, Stach EA, et al. Graphene-based composite materials. *Nature* [Internet]. 2006;442(7100):282–6. Available from: <https://doi.org/10.1038/nature04969>
3. Das TK, Prusty S. Graphene-Based Polymer Composites and Their Applications. *Polym Plast Technol Eng* [Internet]. 2013 Mar 16;52(4):319–31. Available from: <https://doi.org/10.1080/03602559.2012.751410>
4. Blees MK, Barnard AW, Rose PA, Roberts SP, McGill KL, Huang PY, et al. Graphene kirigami. *Nature*. 2015 Aug 29;524(7564):204–7.
5. Das TK, Prusty S. Graphene-Based Polymer Composites and Their Applications. *Polym Plast Technol Eng* [Internet]. 2013 Mar 16;52(4):319–31. Available from: <https://doi.org/10.1080/03602559.2012.751410>
6. Reddy CD, Rajendran S, Liew KM. Equilibrium configuration and continuum elastic properties of finite sized graphene. *Nanotechnology* [Internet]. 2006;17(3):864. Available from: <https://dx.doi.org/10.1088/0957-4484/17/3/042>
7. Balandin AA, Ghosh S, Bao W, Calizo I, Teweldebrhan D, Miao F, et al. Superior Thermal Conductivity of Single-Layer Graphene. *Nano Lett* [Internet]. 2008 Mar 1;8(3):902–7. Available from: <https://doi.org/10.1021/nl0731872>
8. Lee C, Wei X, Kysar JW, Hone J. Measurement of the Elastic Properties and Intrinsic Strength of Monolayer Graphene. *Science (1979)*. 2008 Jul 18;321(5887):385–8.
9. Scarpa F, Adhikari S, Srikantha Phani A. Effective elastic mechanical properties of single layer graphene sheets. *Nanotechnology* [Internet]. 2009;20(6):065709. Available from: <https://dx.doi.org/10.1088/0957-4484/20/6/065709>
10. Magnin Y, Förster GD, Rabilloud F, Calvo F, Zappelli A, Bichara C. Thermal expansion of free-standing graphene: benchmarking semi-empirical potentials. *Journal of Physics: Condensed Matter* [Internet]. 2014;26(18):185401. Available from: <https://dx.doi.org/10.1088/0953-8984/26/18/185401>
11. Cadelano E, Palla PL, Giordano S, Colombo L. Nonlinear Elasticity of Monolayer Graphene. *Phys Rev Lett* [Internet]. 2009 Jun 11;102(23):235502. Available from: <https://link.aps.org/doi/10.1103/PhysRevLett.102.235502>
12. Ni Z, Bu H, Zou M, Yi H, Bi K, Chen Y. Anisotropic mechanical properties of graphene sheets from molecular dynamics. *Physica B Condens Matter* [Internet]. 2010;405(5):1301–6. Available from: <https://www.sciencedirect.com/science/article/pii/S0921452609014379>
13. Chen S, Chrzan DC. Monte Carlo simulation of temperature-dependent elastic properties of graphene. *Phys Rev B* [Internet]. 2011 Nov 2;84(19):195409. Available from: <https://link.aps.org/doi/10.1103/PhysRevB.84.195409>
14. Park S, Ruoff RS. Chemical methods for the production of graphenes. *Nat Nanotechnol*. 2009 Apr 29;4(4):217–24.
15. Zhang C, Akbarzadeh A, Kang W, Wang J, Mirabolghasemi A. Nano-architected metamaterials: Carbon nanotube-based nanotrusses. *Carbon N Y* [Internet]. 2018;131:38–46. Available from: <https://www.sciencedirect.com/science/article/pii/S0008622318300915>

16. Zhao X, Zhang Q, Chen D, Lu P. Enhanced mechanical properties of graphene-based poly (vinyl alcohol) composites. *Macromolecules*. 2010;43(5):2357–63.
17. Milani MA, González D, Quijada R, Basso NRS, Cerrada ML, Azambuja DS, et al. Polypropylene/graphene nanosheet nanocomposites by in situ polymerization: synthesis, characterization and fundamental properties. *Compos Sci Technol*. 2013;84:1–7.
18. Putz KW, Compton OC, Palmeri MJ, Nguyen ST, Brinson LC. High-nanofiller-content graphene oxide–polymer nanocomposites via vacuum-assisted self-assembly. *Adv Funct Mater*. 2010;20(19):3322–9.
19. Kulkarni DD, Choi I, Singamaneni SS, Tsukruk V V. Graphene oxide– polyelectrolyte nanomembranes. *ACS Nano*. 2010;4(8):4667–76.
20. İpek G, Arman Y, Çelik A. The effect of delamination size and location to buckling behavior of composite materials. *Compos B Eng*. 2018 Dec 15;155:69–76.
21. Pekbey Y, Sayman O. A numerical and experimental investigation of critical buckling load of rectangular laminated composite plates with strip delamination. *Journal of Reinforced Plastics and Composites*. 2006 May;25(7):685–97.
22. Dabiryan H, Jesri M, Ovesy HR, Mazloomi ZS. Numerical and experimental study of buckling behavior of delaminated plate in glass woven fabric composite laminates. *J Eng Fiber Fabr*. 2022 Apr 1;17.
23. Gu H, Chattopadhyay A. An experimental investigation of delamination buckling and postbuckling of composite laminates. *Compos Sci Technol* [Internet]. 1999;59(6):903–10. Available from: <https://www.sciencedirect.com/science/article/pii/S0266353898001304>
24. Zak A_, Krawczuk M, Ostachowicz W. Numerical and experimental investigation of free vibration of multilayer delaminated composite beams and plates.
25. Gaudenzi P, Perugini P, Riccio A. Post-buckling behavior of composite panels in the presence of unstable delaminations. *Compos Struct* [Internet]. 2001;51(3):301–9. Available from: <https://www.sciencedirect.com/science/article/pii/S026382230000146X>
26. Yazdani Sarvestani H, Akbarzadeh AH, Niknam H, Hermenean K. 3D printed architected polymeric sandwich panels: Energy absorption and structural performance. *Compos Struct*. 2018 Sep 15;200:886–909.
27. Younes H, Kuang X, Lou D, DeVries B, Rahman MM, Hong H. Magnetic-field-assisted DLP stereolithography for controlled production of highly aligned 3D printed polymer-Fe₃O₄@graphene nanocomposites. *Mater Res Bull*. 2022 Oct 1;154.
28. Ovesy HR, Ghannadpour SAM. An exact finite strip for the initial postbuckling analysis of channel section struts. In: *Computers and Structures*. 2011. p. 1785–96.
29. Dawe JL, Kulak GL, Members /. LOCAL BUCKLING OF W SHAPE COLUMNS AND BEAMS.
30. Zhao S, Zhao Z, Yang Z, Ke L, Kitipornchai S, Yang J. Functionally graded graphene reinforced composite structures: A review. *Eng Struct*. 2020;210:110339.
31. Rafiee MA, Rafiee J, Yu ZZ, Koratkar N. Buckling resistant graphene nanocomposites. *Appl Phys Lett*. 2009;95(22):223103.
32. Parashar A, Mertiny P. Representative volume element to estimate buckling behavior of graphene/polymer nanocomposite. *Nanoscale Res Lett*. 2012;7(1):1–6.
33. Feng C, Kitipornchai S, Yang J. Nonlinear bending of polymer nanocomposite beams reinforced with non-uniformly distributed graphene platelets (GPLs). *Compos B Eng*. 2017;110:132–40.

34. Yang J, Wu H, Kitipornchai S. Buckling and postbuckling of functionally graded multilayer graphene platelet-reinforced composite beams. *Compos Struct*. 2017;161:111–8.
35. Wu H, Yang J, Kitipornchai S. Dynamic instability of functionally graded multilayer graphene nanocomposite beams in thermal environment. *Compos Struct*. 2017;162:244–54.
36. Song M, Kitipornchai S, Yang J. Free and forced vibrations of functionally graded polymer composite plates reinforced with graphene nanoplatelets. *Compos Struct* [Internet]. 2017;159:579–88. Available from: <https://www.sciencedirect.com/science/article/pii/S0263822316314672>
37. Shen HS, Xiang Y, Lin F, Hui D. Buckling and postbuckling of functionally graded graphene-reinforced composite laminated plates in thermal environments. *Compos B Eng*. 2017;119:67–78.
38. Shen HS, Xiang Y, Lin F. Nonlinear bending of functionally graded graphene-reinforced composite laminated plates resting on elastic foundations in thermal environments. *Compos Struct*. 2017;170:80–90.
39. Shen HS, Xiang Y, Lin F. Nonlinear vibration of functionally graded graphene-reinforced composite laminated plates in thermal environments. *Comput Methods Appl Mech Eng*. 2017;319:175–93.
40. Shen HS, Xiang Y, Fan Y, Hui D. Nonlinear vibration of functionally graded graphene-reinforced composite laminated cylindrical panels resting on elastic foundations in thermal environments. *Compos B Eng* [Internet]. 2018;136:177–86. Available from: <https://www.sciencedirect.com/science/article/pii/S1359836817333413>
41. Shen HS, Xiang Y, Lin F. Thermal buckling and postbuckling of functionally graded graphene-reinforced composite laminated plates resting on elastic foundations. *Thin-Walled Structures*. 2017;118:229–37.
42. Shen HS, Xiang Y, Fan Y. Postbuckling of functionally graded graphene-reinforced composite laminated cylindrical panels under axial compression in thermal environments. *Int J Mech Sci* [Internet]. 2018;135:398–409. Available from: <https://www.sciencedirect.com/science/article/pii/S0020740317321380>
43. Shen HS, Xiang Y, Fan Y. Nonlinear vibration of functionally graded graphene-reinforced composite laminated cylindrical shells in thermal environments. *Compos Struct* [Internet]. 2017;182:447–56. Available from: <https://www.sciencedirect.com/science/article/pii/S0263822317322262>
44. Shen HS, Xiang Y. Postbuckling behavior of functionally graded graphene-reinforced composite laminated cylindrical shells under axial compression in thermal environments. *Comput Methods Appl Mech Eng* [Internet]. 2018;330:64–82. Available from: <https://www.sciencedirect.com/science/article/pii/S0045782517306941>
45. Shen HS, Xiang Y. Postbuckling of functionally graded graphene-reinforced composite laminated cylindrical shells subjected to external pressure in thermal environments. *Thin-Walled Structures* [Internet]. 2018;124:151–60. Available from: <https://www.sciencedirect.com/science/article/pii/S0263823117309308>
46. Shen HS, Lin F, Xiang Y. Nonlinear bending and thermal postbuckling of functionally graded graphene-reinforced composite laminated beams resting on elastic foundations. *Eng Struct*. 2017;140:89–97.
47. Ma R, Jin Q. Stability of functionally graded graphene-reinforced composite laminated thick plates in thermal environment. *Acta Mech*. 2022;233(10):3977–96.
48. Phuong NT, Trung NT, Van Doan C, Thang ND, Duc VM, Nam VH. Nonlinear thermomechanical buckling of FG-GRC laminated cylindrical shells stiffened by FG-GRC stiffeners subjected to external pressure. *Acta Mech* [Internet]. 2020;231(12):5125–44. Available from: <https://doi.org/10.1007/s00707-020-02813-5>
49. Chen X, Shen HS, Huang XH. Thermo-mechanical postbuckling analysis of sandwich plates with functionally graded auxetic GRMMC core on elastic foundations. *Compos Struct*. 2022;279:114796.

50. Chen X, Shen HS, Xiang Y. Thermo-mechanical postbuckling analysis of sandwich cylindrical shells with functionally graded auxetic GRMMC core surrounded by an elastic medium. *Thin-Walled Structures* [Internet]. 2022;171:108755. Available from: <https://www.sciencedirect.com/science/article/pii/S0263823121007539>
51. Gu H, Chattopadhyay A. An experimental investigation of delamination buckling and postbuckling of composite laminates.
52. Shabanijafroudi N, Ganesan R. A new methodology for buckling, postbuckling and delamination growth behavior of composite laminates with delamination. *Compos Struct* [Internet]. 2021;268:113951. Available from: <https://www.sciencedirect.com/science/article/pii/S0263822321004116>
53. Sharma N, Swain PK, Maiti DK, Singh BN. Static and free vibration analyses and dynamic control of smart variable stiffness laminated composite plate with delamination. *Compos Struct* [Internet]. 2022;280:114793. Available from: <https://www.sciencedirect.com/science/article/pii/S026382232101240X>
54. Ameri B, Moradi M, Mohammadi B, Salimi-Majd D. Investigation of nonlinear post-buckling delamination in curved laminated composite panels via cohesive zone model. *Thin-Walled Structures* [Internet]. 2020;154:106797. Available from: <https://www.sciencedirect.com/science/article/pii/S0263823120306753>
55. Fathi F, de Borst R. Geometrically nonlinear extended isogeometric analysis for cohesive fracture with applications to delamination in composites. *Finite Elements in Analysis and Design* [Internet]. 2021;191:103527. Available from: <https://www.sciencedirect.com/science/article/pii/S0168874X21000111>
56. Nguyen VP, Kerfriden P, Bordas SPA. Two- and three-dimensional isogeometric cohesive elements for composite delamination analysis. *Compos B Eng* [Internet]. 2014;60:193–212. Available from: <https://www.sciencedirect.com/science/article/pii/S1359836813007488>
57. Nasirmanesh A, Mohammadi S. Eigenvalue buckling analysis of cracked functionally graded cylindrical shells in the framework of the extended finite element method. *Compos Struct* [Internet]. 2017;159:548–66. Available from: <https://www.sciencedirect.com/science/article/pii/S0263822316309709>
58. Afshar A, Hatefi Ardakani S, Mohammadi S. Transient analysis of stationary interface cracks in orthotropic bi-materials using oscillatory crack tip enrichments. *Compos Struct* [Internet]. 2016;142:200–14. Available from: <https://www.sciencedirect.com/science/article/pii/S0263822316001094>
59. Afshar A, Hatefi Ardakani S, Mohammadi S. Stable discontinuous space–time analysis of dynamic interface crack growth in orthotropic bi-materials using oscillatory crack tip enrichment functions. *Int J Mech Sci* [Internet]. 2018;140:557–80. Available from: <https://www.sciencedirect.com/science/article/pii/S0020740317332344>
60. Nikrad SF, Asadi H. Thermal postbuckling analysis of temperature dependent delaminated composite plates. *Thin-Walled Structures* [Internet]. 2015;97:296–307. Available from: <https://www.sciencedirect.com/science/article/pii/S0263823115301075>
61. Nikrad SF, Asadi H, Akbarzadeh AH, Chen ZT. On thermal instability of delaminated composite plates. *Compos Struct* [Internet]. 2015;132:1149–59. Available from: <https://www.sciencedirect.com/science/article/pii/S0263822315005619>
62. Nikrad SF, Keyoursangsari S, Asadi H, Akbarzadeh AH, Chen ZT. Computational study on compressive instability of composite plates with off-center delaminations. *Comput Methods Appl Mech Eng* [Internet]. 2016;310:429–59. Available from: <https://www.sciencedirect.com/science/article/pii/S0045782516307794>
63. Kharazi M, Ovesy HR, Asghari Mooneghi M. Buckling analysis of delaminated composite plates using a novel layerwise theory. *Thin-Walled Structures* [Internet]. 2014;74:246–54. Available from: <https://www.sciencedirect.com/science/article/pii/S0263823113002024>

64. Ovesy HR, Asghari Mooneghi M, Kharazi M. Post-buckling analysis of delaminated composite laminates with multiple through-the-width delaminations using a novel layerwise theory. *Thin-Walled Structures* [Internet]. 2015;94:98–106. Available from: <https://www.sciencedirect.com/science/article/pii/S0263823115001160>
65. Ovesy HR, Kharazi M. Compressional stability behavior of composite plates with through-the-width and embedded delaminations by using first order shear deformation theory. *Comput Struct* [Internet]. 2011;89(19):1829–39. Available from: <https://www.sciencedirect.com/science/article/pii/S0045794910002488>
66. Kharazi M, Ovesy HR. Postbuckling behavior of composite plates with through-the-width delaminations. *Thin-Walled Structures* [Internet]. 2008;46(7):939–46. Available from: <https://www.sciencedirect.com/science/article/pii/S0263823108000426>
67. J. N. Reddy. *Mechanics of Laminated Composite Plates and Shells*. CRC Press; 2003.
68. Affdl JCH, Kardos JL. The Halpin-Tsai equations: A review. *Polym Eng Sci* [Internet]. 1976 May 1;16(5):344–52. Available from: <https://doi.org/10.1002/pen.760160512>
69. Lin F, Xiang Y, Shen HS. Temperature dependent mechanical properties of graphene reinforced polymer nanocomposites – A molecular dynamics simulation. *Compos B Eng* [Internet]. 2017;111:261–9. Available from: <https://www.sciencedirect.com/science/article/pii/S135983681632203X>
70. Mehar K, Panda SK, Bui TQ, Mahapatra TR. Nonlinear thermoelastic frequency analysis of functionally graded CNT-reinforced single/doubly curved shallow shell panels by FEM. *Journal of Thermal Stresses* [Internet]. 2017 Jul 3;40(7):899–916. Available from: <https://doi.org/10.1080/01495739.2017.1318689>
71. Bui TQ, Do T Van, Ton LHT, Doan DH, Tanaka S, Pham DT, et al. On the high temperature mechanical behaviors analysis of heated functionally graded plates using FEM and a new third-order shear deformation plate theory. *Compos B Eng* [Internet]. 2016;92:218–41. Available from: <https://www.sciencedirect.com/science/article/pii/S1359836816001621>
72. Kiani Y. NURBS-based isogeometric thermal postbuckling analysis of temperature dependent graphene reinforced composite laminated plates. *Thin-Walled Structures*. 2018;125:211–9.
73. Davidson BD. Delamination Buckling: Theory and Experiment. *J Compos Mater* [Internet]. 1991 Oct 1;25(10):1351–78. Available from: <https://doi.org/10.1177/002199839102501007>
74. Chai H, Babcock CD, Knauss WG. One dimensional modelling of failure in laminated plates by delamination buckling. *Int J Solids Struct* [Internet]. 1981;17(11):1069–83. Available from: <https://www.sciencedirect.com/science/article/pii/0020768381900147>
75. Anastasiadis JS, Simitses GJ. Spring simulated delamination of axially-loaded flat laminates. *Compos Struct* [Internet]. 1991;17(1):67–85. Available from: <https://www.sciencedirect.com/science/article/pii/0263822391900613>
76. Suemasu H. Compressive behavior of fiber reinforced composite plates with a center delamination. *Advanced Composite Materials* [Internet]. 1991 Jan 1;1(1):23–37. Available from: <https://doi.org/10.1163/156855191X00045>
77. Suemasu H. Effects of Multiple Delaminations on Compressive Buckling Behaviors of Composite Panels. *J Compos Mater* [Internet]. 1993 Dec 1;27(12):1172–92. Available from: <https://doi.org/10.1177/002199839302701202>
78. Adan M, Sheinman I, Altus E. Buckling of Multiply Delaminated Beams. *J Compos Mater* [Internet]. 1994 Jan 1;28(1):77–90. Available from: <https://doi.org/10.1177/002199839402800106>

79. Ali Kouchakzadeh M, Sekine H. Compressive buckling analysis of rectangular composite laminates containing multiple delaminations. *Compos Struct* [Internet]. 2000;50(3):249–55. Available from: <https://www.sciencedirect.com/science/article/pii/S0263822300001008>
80. Ju-fen Z, Gang Z, Howson WP, Williams FW. Reference surface element modelling of composite plate/shell delamination buckling and postbuckling. *Compos Struct* [Internet]. 2003;61(3):255–64. Available from: <https://www.sciencedirect.com/science/article/pii/S0263822303000163>
81. Hwang SF, Huang SM. Postbuckling behavior of composite laminates with two delaminations under uniaxial compression. *Compos Struct* [Internet]. 2005;68(2):157–65. Available from: <https://www.sciencedirect.com/science/article/pii/S0263822304000662>
82. Tafreshi A. Efficient modelling of delamination buckling in composite cylindrical shells under axial compression. *Compos Struct* [Internet]. 2004;64(3):511–20. Available from: <https://www.sciencedirect.com/science/article/pii/S0263822303002903>
83. Kharazi M, Ovesy HR, Taghizadeh M. Buckling of the composite laminates containing through-the-width delaminations using different plate theories. *Compos Struct* [Internet]. 2010;92(5):1176–83. Available from: <https://www.sciencedirect.com/science/article/pii/S0263822309004395>
84. Yang WD, Zhang W, Wang X, Lu G. Nonlinear delamination buckling and expansion of functionally graded laminated piezoelectric composite shells. *Int J Solids Struct* [Internet]. 2014;51(3):894–903. Available from: <https://www.sciencedirect.com/science/article/pii/S0020768313004605>
85. Meng F, Wang H, Wang X, Li Z. Elliptically delaminated buckling near the surface of piezoelectric laminated shells under electric and thermal loads. *Compos Struct* [Internet]. 2010;92(3):684–90. Available from: <https://www.sciencedirect.com/science/article/pii/S0263822309003626>
86. Kamarian S, Shakeri M, Yas MH, Bodaghi M, Pourasghar A. Free vibration analysis of functionally graded nanocomposite sandwich beams resting on Pasternak foundation by considering the agglomeration effect of CNTs. *Journal of Sandwich Structures & Materials* [Internet]. 2015 Jun 17;17(6):632–65. Available from: <https://doi.org/10.1177/1099636215590280>
87. Guo X, Zhang Y, Luo Z, Cao D. Nonlinear dynamics analysis of a graphene laminated composite plate based on an extended Rayleigh–Ritz method. *Thin-Walled Structures* [Internet]. 2023;186:110673. Available from: <https://www.sciencedirect.com/science/article/pii/S0263823123001519>
88. Whitcomb JD, Shivakumar KN. Strain-Energy Release Rate Analysis of Plates with Postbuckled Delaminations. *J Compos Mater* [Internet]. 1989 Jul 1;23(7):714–34. Available from: <https://doi.org/10.1177/002199838902300705>
89. Wang S, Zhang Y. Buckling, post-buckling and delamination propagation in debonded composite laminates Part 2: Numerical applications. *Compos Struct* [Internet]. 2009;88(1):131–46. Available from: <https://www.sciencedirect.com/science/article/pii/S0263822308000500>
90. Tafreshi A, Oswald T. Global buckling behaviour and local damage propagation in composite plates with embedded delaminations. *International Journal of Pressure Vessels and Piping* [Internet]. 2003;80(1):9–20. Available from: <https://www.sciencedirect.com/science/article/pii/S0308016102001527>
91. Wang S, Zhang Y. Buckling, post-buckling and delamination propagation in debonded composite laminates Part 2: Numerical applications. *Compos Struct* [Internet]. 2009;88(1):131–46. Available from: <https://www.sciencedirect.com/science/article/pii/S0263822308000500>
92. Yu L, Davidson BD. A Three-Dimensional Crack Tip Element for Energy Release Rate Determination in Layered Elastic Structures. *J Compos Mater* [Internet]. 2001 Mar 1;35(6):457–88. Available from: <https://doi.org/10.1177/002199801772662118>

93. Davidson BD, Yu L, Hu H. Determination of energy release rate and mode mix in three-dimensional layered structures using plate theory. *Int J Fract* [Internet]. 2000;105(1):81–105. Available from: <https://doi.org/10.1023/A:1007672131026>
94. Whitcomb JD, Shivakumar KN. Strain-Energy Release Rate Analysis of Plates with Postbuckled Delaminations. *J Compos Mater* [Internet]. 1989 Jul 1;23(7):714–34. Available from: <https://doi.org/10.1177/002199838902300705>
95. Davidson BD, Hu H, Schapery RA. An Analytical Crack-Tip Element for Layered Elastic Structures. *J Appl Mech* [Internet]. 1995 Jun 1;62(2):294–305. Available from: <https://doi.org/10.1115/1.2895931>
96. Sheinman I, Kardomateas GA. Energy release rate and stress intensity factors for delaminated composite laminates. *Int J Solids Struct* [Internet]. 1997;34(4):451–9. Available from: <https://www.sciencedirect.com/science/article/pii/S0020768396000182>
97. Basu PK, Akhtar MN. Interactive and Local Buckling of Thin-Walled Members. Vol. 12, *Thin-Walled Structures*. 1991.
98. Loughlan J, Yidris N. The local-overall flexural interaction of fixed-ended plain channel columns and the influence on behaviour of local conditions at the constituent plate ends. *Thin-Walled Structures*. 2014;81:132–7.
99. Nikrad SF, Asadi H, Ozbakkaloglu T. Compressive instability of open section nanocomposite struts using a layerwise theory. *Comput Methods Appl Mech Eng*. 2019 Oct 1;355:820–39.
100. John DeWolf BT, Peokoz T, Members A, Winter G, Asce HM. JOURNAL OF THE STRUCTURAL DIVISION LOCAL AND OVERALL BUCKLING OF COLD-FORMED MEMBERS.
101. Schreiber P, Mittelstedt C. A holistic approach for local buckling of composite laminated beams under compressive load. *Archive of Applied Mechanics*. 2019 Jul 15;89(7):1243–57.
102. Qiao P, Asce M, Zou G. Local Buckling of Elastically Restrained Fiber-Reinforced Plastic Plates and its Application to Box Sections.
103. Szló L, Kollá P. Local Buckling of Fiber Reinforced Plastic Composite Structural Members with Open and Closed Cross Sections.
104. Nikrad SF, Asadi H, Wang Q. Postbuckling behaviors of open section composite struts with edge delamination using a layerwise theory. *Int J Non Linear Mech*. 2017 Oct 1;95:315–26.
105. Loughlan J, Yidris N, Cunningham PR. The effects of local buckling and material yielding on the axial stiffness and failure of uniformly compressed I-section and box-section struts. *Thin-Walled Structures*. 2011 Feb;49(2):264–79.
106. Chen J, He Y, Jin WL. Stub column tests of thin-walled complex section with intermediate stiffeners. *Thin-Walled Structures*. 2010 Jun;48(6):423–9.
107. Ghannadpour SAM, Ovesy HR. An exact finite strip for the calculation of relative post-buckling stiffness of I-section struts. *Int J Mech Sci*. 2008;50(9):1354–64.
108. Mittelstedt C. Local buckling of wide-flange thin-walled anisotropic composite beams. *Archive of Applied Mechanics*. 2007 Jul;77(7):439–52.
109. Rhodes J, Harvey JM. PLAIN CHANNEL SECTION STRUTS IN COMPRESSION AND BENDING BEYOND THE LOCAL BUCKLING LOAD. Vol. 8, *Int. J. mech. Sci*. Pergamon Press; 1976.

110. Ovesy HR, Loughlan J, GhannadPour SAM, Morada G. Geometric non-linear analysis of box sections under end shortening, using three different versions of the finite-strip method. *Thin-Walled Structures*. 2006 Jun;44(6):623–37.
111. Ovesy HR, Loughlan J, GhannadPour SAM. Geometric non-linear analysis of channel sections under end shortening, using different versions of the finite strip method. *Comput Struct*. 2006 May;84(13–14):855–72.
112. Rhodes J. Buckling of thin plates and members-and early work on rectangular tubes [Internet]. Vol. 40, *Thin-Walled Structures*. 2002. Available from: www.elsevier.com/locate/tws
113. Graves Smith TR. THE EFFECT OF INITIAL IMPERFECTIONS ON THE STRENGTH OF THIN-WALLED BOX COLUMNS. Vol. 13, *Int. J. mech. Sci.* Pergamon Press; 1971.
114. Wysmulski P, Debski H, Falkowicz K. Sensitivity of Compressed Composite Channel Columns to Eccentric Loading. *Materials*. 2022 Oct 1;15(19).
115. Falkowicz K, Wysmulski P, Debski H. Buckling Analysis of Laminated Plates with Asymmetric Layup by Approximation Method. *Materials*. 2023 Jul 1;16(14).
116. Falkowicz K. Experimental and numerical failure analysis of thin-walled composite plates using progressive failure analysis. *Compos Struct* [Internet]. 2023;305:116474. Available from: <https://www.sciencedirect.com/science/article/pii/S0263822322012065>
117. Kitipornchai S, Yang J, Liew KM. Semi-analytical solution for nonlinear vibration of laminated FGM plates with geometric imperfections. *Int J Solids Struct* [Internet]. 2004;41(9):2235–57. Available from: <https://www.sciencedirect.com/science/article/pii/S0020768303007194>

Appendix A

According to the TSDT, the normal and transverse shear strain tensors of the FG-GRC laminated plate can be written as [61]:

$$\begin{cases} \varepsilon_{xx} \\ \varepsilon_{yy} \\ \gamma_{xy} \end{cases} = \begin{cases} \varepsilon_{xx}^{(0)} \\ \varepsilon_{yy}^{(0)} \\ \gamma_{xy}^{(0)} \end{cases} + z \begin{cases} \varepsilon_{xx}^{(1)} \\ \varepsilon_{yy}^{(1)} \\ \gamma_{xy}^{(1)} \end{cases} + z^3 \begin{cases} \varepsilon_{xx}^{(3)} \\ \varepsilon_{yy}^{(3)} \\ \gamma_{xy}^{(3)} \end{cases}$$

$$\begin{cases} \gamma_{yz} \\ \gamma_{xz} \end{cases} = \begin{cases} \gamma_{yz}^{(0)} \\ \gamma_{xz}^{(0)} \end{cases} + z^2 \begin{cases} \gamma_{yz}^{(2)} \\ \gamma_{xz}^{(2)} \end{cases} \quad (\text{A.1})$$

where:

$$\begin{cases} \varepsilon_{xx}^{(0)} \\ \varepsilon_{yy}^{(0)} \\ \gamma_{xy}^{(0)} \end{cases} = \begin{cases} \frac{\partial u_0}{\partial x} + \left(\frac{1}{2}\right) \left(\frac{\partial w_0}{\partial x}\right)^2 \\ \frac{\partial v_0}{\partial y} + \left(\frac{1}{2}\right) \left(\frac{\partial w_0}{\partial y}\right)^2 \\ \frac{\partial u_0}{\partial y} + \frac{\partial v_0}{\partial x} + \frac{\partial w_0}{\partial x} \frac{\partial w_0}{\partial y} \end{cases}$$

$$\begin{cases} \varepsilon_{xx}^{(1)} \\ \varepsilon_{yy}^{(1)} \\ \gamma_{xy}^{(1)} \end{cases} = \begin{cases} \frac{\partial \varphi_x}{\partial x} \\ \frac{\partial \varphi_y}{\partial y} \\ \frac{\partial \varphi_x}{\partial y} + \frac{\partial \varphi_y}{\partial x} \end{cases}$$

$$\begin{cases} \varepsilon_{xx}^{(3)} \\ \varepsilon_{yy}^{(3)} \\ \gamma_{xy}^{(3)} \end{cases} = \begin{cases} \left(\frac{-4}{3h^2}\right) \left(\frac{\partial \varphi_x}{\partial x} + \frac{\partial^2 w_0}{\partial x^2}\right) \\ \left(\frac{-4}{3h^2}\right) \left(\frac{\partial \varphi_y}{\partial y} + \frac{\partial^2 w_0}{\partial y^2}\right) \\ \left(\frac{-4}{3h^2}\right) \left(\frac{\partial \varphi_x}{\partial y} + \frac{\partial \varphi_y}{\partial x} + 2 \frac{\partial^2 w_0}{\partial x \partial y}\right) \end{cases}$$

$$\begin{cases} \gamma_{yz}^{(0)} \\ \gamma_{xz}^{(0)} \end{cases} = \begin{cases} \varphi_y + \frac{\partial w_0}{\partial y} \\ \varphi_x + \frac{\partial w_0}{\partial x} \end{cases}, \quad \begin{cases} \gamma_{yz}^{(2)} \\ \gamma_{xz}^{(2)} \end{cases} = \left(\frac{-4}{h^2}\right) \begin{cases} \gamma_{yz}^{(0)} \\ \gamma_{xz}^{(0)} \end{cases} \quad (\text{A.2})$$

Appendix B

Displacement and rotational functions of FG-GRC plate with elliptical embedded delamination

(SSSS)

Out-of-plane displacement

$$\begin{aligned}
 W^{(1)} &= \sum_{m=0}^{M_1} \sum_{n=0}^{N_1} \left(x - \frac{L_1}{2}\right) \left(x + \frac{L_1}{2}\right) \left(y - \frac{b_1}{2}\right) \left(y + \frac{b_1}{2}\right) W_{mn}^{(1)} x^m y^n \\
 W^{(2)} &= W^{(1)} + \sum_{m=0}^{M_2} \sum_{n=0}^{N_2} \left(\frac{x^2}{a^2} + \frac{y^2}{b^2} - 1\right)^2 W_{mn}^{(2)} x^m y^n \\
 W^{(3)} &= W^{(1)} + \sum_{m=0}^{M_3} \sum_{n=0}^{N_3} \left(\frac{x^2}{a^2} + \frac{y^2}{b^2} - 1\right)^2 W_{mn}^{(3)} x^m y^n
 \end{aligned} \tag{B.1}$$

In-plane displacements

$$\begin{aligned}
 U^{(1)} &= \sum_{p=0}^{P_1} \sum_{q=0}^{Q_1} \left(x - \frac{L_1}{2}\right) \left(x + \frac{L_1}{2}\right) U_{pq}^{(1)} x^p y^q \\
 U^{(2)} &= U^{(1)} - \frac{4h_2^3}{3h_1^2} \left(\varphi_x^{(1)} + \frac{\partial W^{(1)}}{\partial x}\right) + h_2 \varphi_x^{(1)} + \sum_{p=0}^{P_2} \sum_{q=0}^{Q_2} \left(\frac{x^2}{a^2} + \frac{y^2}{b^2} - 1\right) U_{pq}^{(2)} x^p y^q \\
 U^{(3)} &= U^{(1)} - \frac{4h_3^3}{3h_1^2} \left(\varphi_x^{(1)} + \frac{\partial W^{(1)}}{\partial x}\right) + h_3 \varphi_x^{(1)} + \sum_{p=0}^{P_3} \sum_{q=0}^{Q_3} \left(\frac{x^2}{a^2} + \frac{y^2}{b^2} - 1\right) U_{pq}^{(3)} x^p y^q \\
 V^{(1)} &= \sum_{s=0}^{S_1} \sum_{r=0}^{R_1} \left(y - \frac{b_1}{2}\right) V_{sr}^{(1)} x^s y^r \\
 V^{(2)} &= V^{(1)} - \frac{4h_2^3}{3h_1^2} \left(\varphi_y^{(1)} + \frac{\partial W^{(1)}}{\partial y}\right) + h_2 \varphi_y^{(1)} + \sum_{s=0}^{S_2} \sum_{r=0}^{R_2} \left(\frac{x^2}{a^2} + \frac{y^2}{b^2} - 1\right) V_{sr}^{(2)} x^s y^r \\
 V^{(3)} &= V^{(1)} - \frac{4h_3^3}{3h_1^2} \left(\varphi_y^{(1)} + \frac{\partial W^{(1)}}{\partial y}\right) + h_3 \varphi_y^{(1)} + \sum_{s=0}^{S_3} \sum_{r=0}^{R_3} \left(\frac{x^2}{a^2} + \frac{y^2}{b^2} - 1\right) V_{sr}^{(3)} x^s y^r
 \end{aligned} \tag{B.2}$$

Rotational functions

$$\begin{aligned}
 \varphi_x^{(1)} &= \sum_{j=0}^{J_1} \sum_{k=0}^{K_1} \varphi_{x_{jk}}^{(1)} x^j y^k \\
 \varphi_x^{(2)} &= \varphi_x^{(1)} - \frac{4h_2^2}{h_1^2} \left(\varphi_x^{(1)} + \frac{\partial W^{(1)}}{\partial x} \right) + \sum_{j=0}^{J_2} \sum_{k=0}^{K_2} \varphi_{x_{jk}}^{(2)} \left(\frac{x^2}{a^2} + \frac{y^2}{b^2} - 1 \right) x^j y^k \\
 \varphi_x^{(3)} &= \varphi_x^{(1)} - \frac{4h_3^2}{h_1^2} \left(\varphi_x^{(1)} + \frac{\partial W^{(1)}}{\partial x} \right) + \sum_{j=0}^{J_3} \sum_{k=0}^{K_3} \varphi_{x_{jk}}^{(3)} \left(\frac{x^2}{a^2} + \frac{y^2}{b^2} - 1 \right) x^j y^k \\
 \varphi_y^{(1)} &= \sum_{i=0}^{I_1} \sum_{t=0}^{T_1} \varphi_{y_{it}}^{(1)} x^i y^t \\
 \varphi_y^{(2)} &= \varphi_y^{(1)} - \frac{4h_2^2}{h_1^2} \left(\varphi_y^{(1)} + \frac{\partial W^{(1)}}{\partial y} \right) + \sum_{i=0}^{I_2} \sum_{t=0}^{T_2} \varphi_{y_{it}}^{(2)} \left(\frac{x^2}{a^2} + \frac{y^2}{b^2} - 1 \right) x^i y^t \\
 \varphi_y^{(3)} &= \varphi_y^{(1)} - \frac{4h_3^2}{h_1^2} \left(\varphi_y^{(1)} + \frac{\partial W^{(1)}}{\partial y} \right) + \sum_{i=0}^{I_3} \sum_{t=0}^{T_3} \varphi_{y_{it}}^{(3)} \left(\frac{x^2}{a^2} + \frac{y^2}{b^2} - 1 \right) x^i y^t \tag{B.3}
 \end{aligned}$$

Displacement and rotational functions of FG-GRC plate with elliptical embedded delamination (CCCC)

Out-of-plane displacement

$$\begin{aligned}
 W^{(1)} &= \sum_{m=0}^{M_1} \sum_{n=0}^{N_1} \left(x - \frac{L_1}{2} \right)^2 \left(x + \frac{L_1}{2} \right)^2 \left(y - \frac{b_1}{2} \right)^2 \left(y + \frac{b_1}{2} \right)^2 W_{mn}^{(1)} x^m y^n \\
 W^{(2)} &= W^{(1)} + \sum_{m=0}^{M_2} \sum_{n=0}^{N_2} \left(\frac{x^2}{a^2} + \frac{y^2}{b^2} - 1 \right)^2 W_{mn}^{(2)} x^m y^n \\
 W^{(3)} &= W^{(1)} + \sum_{m=0}^{M_3} \sum_{n=0}^{N_3} \left(\frac{x^2}{a^2} + \frac{y^2}{b^2} - 1 \right)^2 W_{mn}^{(3)} x^m y^n \tag{B.4}
 \end{aligned}$$

In-plane displacements

$$\begin{aligned}
 U^{(1)} &= \sum_{p=0}^{P_1} \sum_{q=0}^{Q_1} \left(x - \frac{L_1}{2} \right) \left(x + \frac{L_1}{2} \right) U_{pq}^{(1)} x^p y^q \\
 U^{(2)} &= U^{(1)} - \frac{4h_2^3}{3h_1^2} \left(\varphi_x^{(1)} + \frac{\partial W^{(1)}}{\partial x} \right) + h_2 \varphi_x^{(1)} + \sum_{p=0}^{P_2} \sum_{q=0}^{Q_2} \left(\frac{x^2}{a^2} + \frac{y^2}{b^2} - 1 \right) U_{pq}^{(2)} x^p y^q
 \end{aligned}$$

$$\begin{aligned}
U^{(3)} &= U^{(1)} - \frac{4h_3^3}{3h_1^2} \left(\varphi_x^{(1)} + \frac{\partial W^{(1)}}{\partial x} \right) + h_3 \varphi_x^{(1)} + \sum_{p=0}^{P_3} \sum_{q=0}^{Q_3} \left(\frac{x^2}{a^2} + \frac{y^2}{b^2} - 1 \right) U_{pq}^{(3)} x^p y^q \\
V^{(1)} &= \sum_{s=0}^{S_1} \sum_{r=0}^{R_1} \left(y - \frac{b_1}{2} \right) V_{sr}^{(1)} x^s y^r \\
V^{(2)} &= V^{(1)} - \frac{4h_2^3}{3h_1^2} \left(\varphi_y^{(1)} + \frac{\partial W^{(1)}}{\partial y} \right) + h_2 \varphi_y^{(1)} + \sum_{s=0}^{S_2} \sum_{r=0}^{R_2} \left(\frac{x^2}{a^2} + \frac{y^2}{b^2} - 1 \right) V_{sr}^{(2)} x^s y^r \\
V^{(3)} &= V^{(1)} - \frac{4h_3^3}{3h_1^2} \left(\varphi_y^{(1)} + \frac{\partial W^{(1)}}{\partial y} \right) + h_3 \varphi_y^{(1)} + \sum_{s=0}^{S_3} \sum_{r=0}^{R_3} \left(\frac{x^2}{a^2} + \frac{y^2}{b^2} - 1 \right) V_{sr}^{(3)} x^s y^r
\end{aligned} \tag{B.5}$$

Rotational functions

$$\begin{aligned}
\varphi_x^{(1)} &= \sum_{j=0}^{J_1} \sum_{k=0}^{K_1} \left(x + \frac{L_1}{2} \right) \left(x - \frac{L_1}{2} \right) \varphi_{x_{jk}}^{(1)} x^j y^k \\
\varphi_x^{(2)} &= \varphi_x^{(1)} - \frac{4h_2^2}{h_1^2} \left(\varphi_x^{(1)} + \frac{\partial W^{(1)}}{\partial x} \right) + \sum_{j=0}^{J_2} \sum_{k=0}^{K_2} \varphi_{x_{jk}}^{(2)} \left(\frac{x^2}{a^2} + \frac{y^2}{b^2} - 1 \right) x^j y^k \\
\varphi_x^{(3)} &= \varphi_x^{(1)} - \frac{4h_3^2}{h_1^2} \left(\varphi_x^{(1)} + \frac{\partial W^{(1)}}{\partial x} \right) + \sum_{j=0}^{J_3} \sum_{k=0}^{K_3} \varphi_{x_{jk}}^{(3)} \left(\frac{x^2}{a^2} + \frac{y^2}{b^2} - 1 \right) x^j y^k \\
\varphi_y^{(1)} &= \sum_{i=0}^{I_1} \sum_{t=0}^{T_1} \left(y + \frac{b_1}{2} \right) \left(y - \frac{b_1}{2} \right) \varphi_{y_{it}}^{(1)} x^i y^t \\
\varphi_y^{(2)} &= \varphi_y^{(1)} - \frac{4h_2^2}{h_1^2} \left(\varphi_y^{(1)} + \frac{\partial W^{(1)}}{\partial y} \right) + \sum_{i=0}^{I_2} \sum_{t=0}^{T_2} \varphi_{y_{it}}^{(2)} \left(\frac{x^2}{a^2} + \frac{y^2}{b^2} - 1 \right) x^i y^t \\
\varphi_y^{(3)} &= \varphi_y^{(1)} - \frac{4h_3^2}{h_1^2} \left(\varphi_y^{(1)} + \frac{\partial W^{(1)}}{\partial y} \right) + \sum_{i=0}^{I_3} \sum_{t=0}^{T_3} \varphi_{y_{it}}^{(3)} \left(\frac{x^2}{a^2} + \frac{y^2}{b^2} - 1 \right) x^i y^t
\end{aligned} \tag{B.6}$$

Appendix C

$$W_{|x=-\frac{L_2}{2}}^{(1)} = W_{|x=-\frac{L_2}{2}}^{(2)} = W_{|x=-\frac{L_2}{2}}^{(3)} \quad , \quad \frac{\partial W^{(1)}}{\partial x} \Big|_{x=-\frac{L_2}{2}} = \frac{\partial W^{(2)}}{\partial x} \Big|_{x=-\frac{L_2}{2}} \\ = \frac{\partial W^{(3)}}{\partial x} \Big|_{x=-\frac{L_2}{2}}$$

$$W_{|x=\frac{L_2}{2}}^{(1)} = W_{|x=\frac{L_2}{2}}^{(2)} = W_{|x=\frac{L_2}{2}}^{(3)} \quad , \quad \frac{\partial W^{(1)}}{\partial x} \Big|_{x=\frac{L_2}{2}} = \frac{\partial W^{(2)}}{\partial x} \Big|_{x=\frac{L_2}{2}} = \frac{\partial W^{(3)}}{\partial x} \Big|_{x=\frac{L_2}{2}}$$

$$W_{|y=b_2}^{(1)} = W_{|y=b_2}^{(2)} = W_{|y=b_2}^{(3)} \quad , \quad \frac{\partial W^{(1)}}{\partial y} \Big|_{y=b_2} = \frac{\partial W^{(2)}}{\partial y} \Big|_{y=b_2} = \frac{\partial W^{(3)}}{\partial y} \Big|_{y=b_2}$$

$$U_{|x=-\frac{L_2}{2}}^{(2)} = U_{|x=-\frac{L_2}{2}}^{(1)} + h_2 \varphi_{x|_{x=-\frac{L_2}{2}}}^{(1)} - h_2^3 C_1^{(1)} \left(\varphi_{x|_{x=-\frac{L_2}{2}}}^{(1)} + W_{,x|_{x=-\frac{L_2}{2}}}^{(1)} \right)$$

$$U_{|x=\frac{L_2}{2}}^{(2)} = U_{|x=\frac{L_2}{2}}^{(1)} + h_2 \varphi_{x|_{x=\frac{L_2}{2}}}^{(1)} - h_2^3 C_1^{(1)} \left(\varphi_{x|_{x=\frac{L_2}{2}}}^{(1)} + W_{,x|_{x=\frac{L_2}{2}}}^{(1)} \right)$$

$$U_{|y=b_2}^{(2)} = U_{|y=b_2}^{(1)} + h_2 \varphi_{x|_{y=b_2}}^{(1)} - h_2^3 C_1^{(1)} \left(\varphi_{x|_{y=b_2}}^{(1)} + W_{,x|_{y=b_2}}^{(1)} \right)$$

$$U_{|x=-\frac{L_2}{2}}^{(3)} = U_{|x=-\frac{L_2}{2}}^{(1)} + h_3 \varphi_{x|_{x=-\frac{L_2}{2}}}^{(1)} - h_3^3 C_1^{(1)} \left(\varphi_{x|_{x=-\frac{L_2}{2}}}^{(1)} + W_{,x|_{x=-\frac{L_2}{2}}}^{(1)} \right)$$

$$U_{|x=\frac{L_2}{2}}^{(3)} = U_{|x=\frac{L_2}{2}}^{(1)} + h_3 \varphi_{x|_{x=\frac{L_2}{2}}}^{(1)} - h_3^3 C_1^{(1)} \left(\varphi_{x|_{x=\frac{L_2}{2}}}^{(1)} + W_{,x|_{x=\frac{L_2}{2}}}^{(1)} \right)$$

$$U_{|y=b_2}^{(3)} = U_{|y=b_2}^{(1)} + h_3 \varphi_{x|_{y=b_2}}^{(1)} - h_3^3 C_1^{(1)} \left(\varphi_{x|_{y=b_2}}^{(1)} + W_{,x|_{y=b_2}}^{(1)} \right)$$

$$V_{|x=-\frac{L_2}{2}}^{(2)} = V_{|x=-\frac{L_2}{2}}^{(1)} + h_2 \varphi_{y|_{x=-\frac{L_2}{2}}}^{(1)} - h_2^3 C_1^{(1)} \left(\varphi_{y|_{x=-\frac{L_2}{2}}}^{(1)} + W_{,y|_{x=-\frac{L_2}{2}}}^{(1)} \right)$$

$$V_{|x=\frac{L_2}{2}}^{(2)} = V_{|x=\frac{L_2}{2}}^{(1)} + h_2 \varphi_{y|_{x=\frac{L_2}{2}}}^{(1)} - h_2^3 C_1^{(1)} \left(\varphi_{y|_{x=\frac{L_2}{2}}}^{(1)} + W_{,y|_{x=\frac{L_2}{2}}}^{(1)} \right)$$

$$V_{|y=b_2}^{(2)} = V_{|y=b_2}^{(1)} + h_2 \varphi_{y|_{y=b_2}}^{(1)} - h_2^3 C_1^{(1)} \left(\varphi_{y|_{y=b_2}}^{(1)} + W_{,y|_{y=b_2}}^{(1)} \right)$$

$$V_{|x=-\frac{L_2}{2}}^{(3)} = V_{|x=-\frac{L_2}{2}}^{(1)} + h_3 \varphi_{y|_{x=-\frac{L_2}{2}}}^{(1)} - h_3^3 C_1^{(1)} \left(\varphi_{y|_{x=-\frac{L_2}{2}}}^{(1)} + W_{,y|_{x=-\frac{L_2}{2}}}^{(1)} \right)$$

$$V_{|x=\frac{L_2}{2}}^{(3)} = V_{|x=\frac{L_2}{2}}^{(1)} + h_3 \varphi_{y|_{x=\frac{L_2}{2}}}^{(1)} - h_3^3 C_1^{(1)} \left(\varphi_{y|_{x=\frac{L_2}{2}}}^{(1)} + W_{,y|_{x=\frac{L_2}{2}}}^{(1)} \right)$$

$$V_{|y=b_2}^{(3)} = V_{|y=b_2}^{(1)} + h_3 \varphi_{y|_{y=b_2}}^{(1)} - h_3^3 C_1^{(1)} \left(\varphi_{y|_{y=b_2}}^{(1)} + W_{,y|_{y=b_2}}^{(1)} \right)$$

$$\varphi_{x|_{x=-\frac{L_2}{2}}}^{(2)} = \varphi_{x|_{x=-\frac{L_2}{2}}}^{(1)} - 3h_2^2 C_1^{(1)} \left(\varphi_{x|_{x=-\frac{L_2}{2}}}^{(1)} + W_{,x|_{x=-\frac{L_2}{2}}}^{(1)} \right)$$

$$\begin{aligned}
\varphi_{x|_{x=\frac{L_2}{2}}}^{(2)} &= \varphi_{x|_{x=\frac{L_2}{2}}}^{(1)} - 3h_2^2 C_1^{(1)} \left(\varphi_{x|_{x=\frac{L_2}{2}}}^{(1)} + W_{x|_{x=\frac{L_2}{2}}}^{(1)} \right) \\
\varphi_{y|_{y=b_2}}^{(2)} &= \varphi_{y|_{y=b_2}}^{(1)} - 3h_2^2 C_1^{(1)} \left(\varphi_{y|_{y=b_2}}^{(1)} + W_{y|_{y=b_2}}^{(1)} \right) \\
\varphi_{x|_{x=-\frac{L_2}{2}}}^{(3)} &= \varphi_{x|_{x=-\frac{L_2}{2}}}^{(1)} - 3h_3^2 C_1^{(1)} \left(\varphi_{x|_{x=-\frac{L_2}{2}}}^{(1)} + W_{x|_{x=-\frac{L_2}{2}}}^{(1)} \right) \\
\varphi_{x|_{x=\frac{L_2}{2}}}^{(3)} &= \varphi_{x|_{x=\frac{L_2}{2}}}^{(1)} - 3h_3^2 C_1^{(1)} \left(\varphi_{x|_{x=\frac{L_2}{2}}}^{(1)} + W_{x|_{x=\frac{L_2}{2}}}^{(1)} \right) \\
\varphi_{y|_{y=b_2}}^{(3)} &= \varphi_{y|_{y=b_2}}^{(1)} - 3h_3^2 C_1^{(1)}
\end{aligned} \tag{C.1}$$

Appendix D

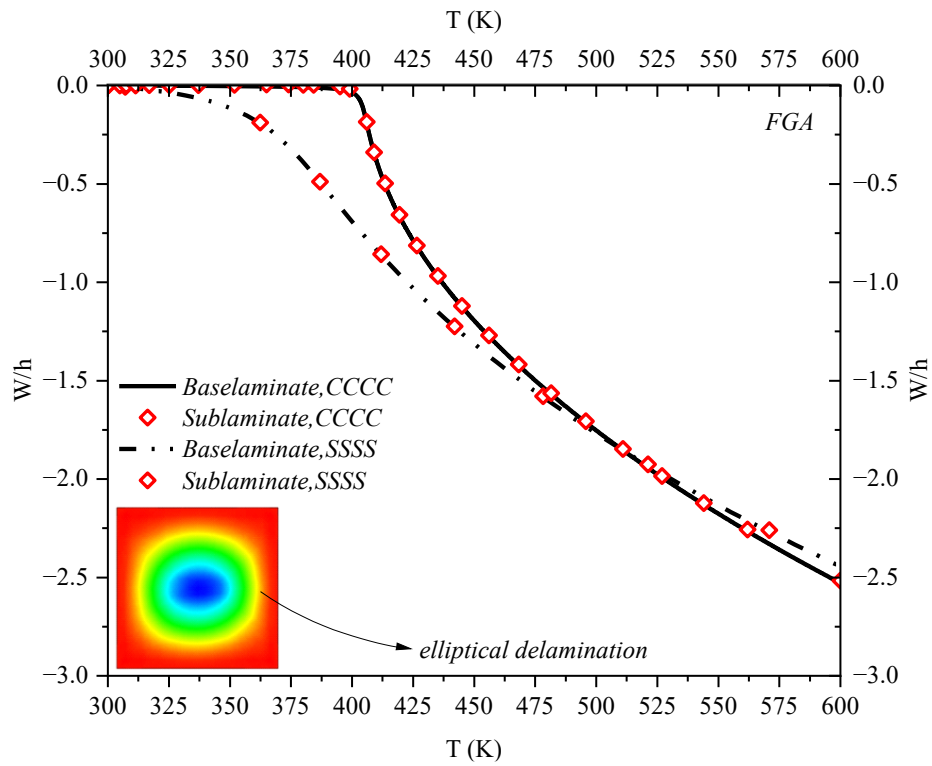


Figure D.1 Influence of clamped and simply-supported boundary conditions on the thermal equilibrium paths of FGA laminated plates with embedded elliptical delamination, $AD/A=0.25$, $\frac{h_s}{h} = 0.2$.

(a)

(b)

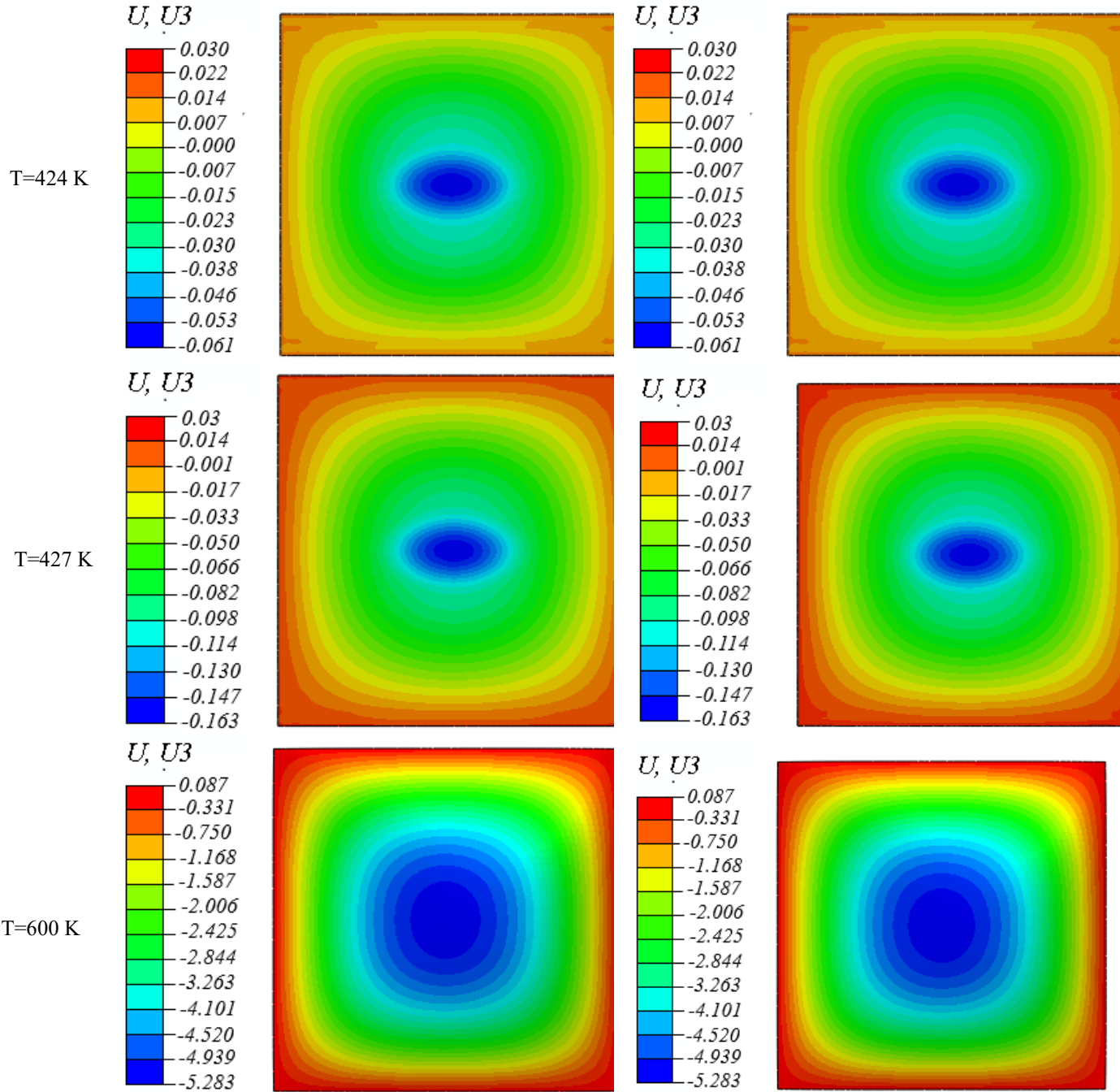


Figure D.2 Comparison of deflection through the sublaminates and baselaminates of FG-X plate with embedded elliptical delamination at three different temperatures $AD/A=0.25$, SSSS. (a) Sublaminate (b) Baselaminate

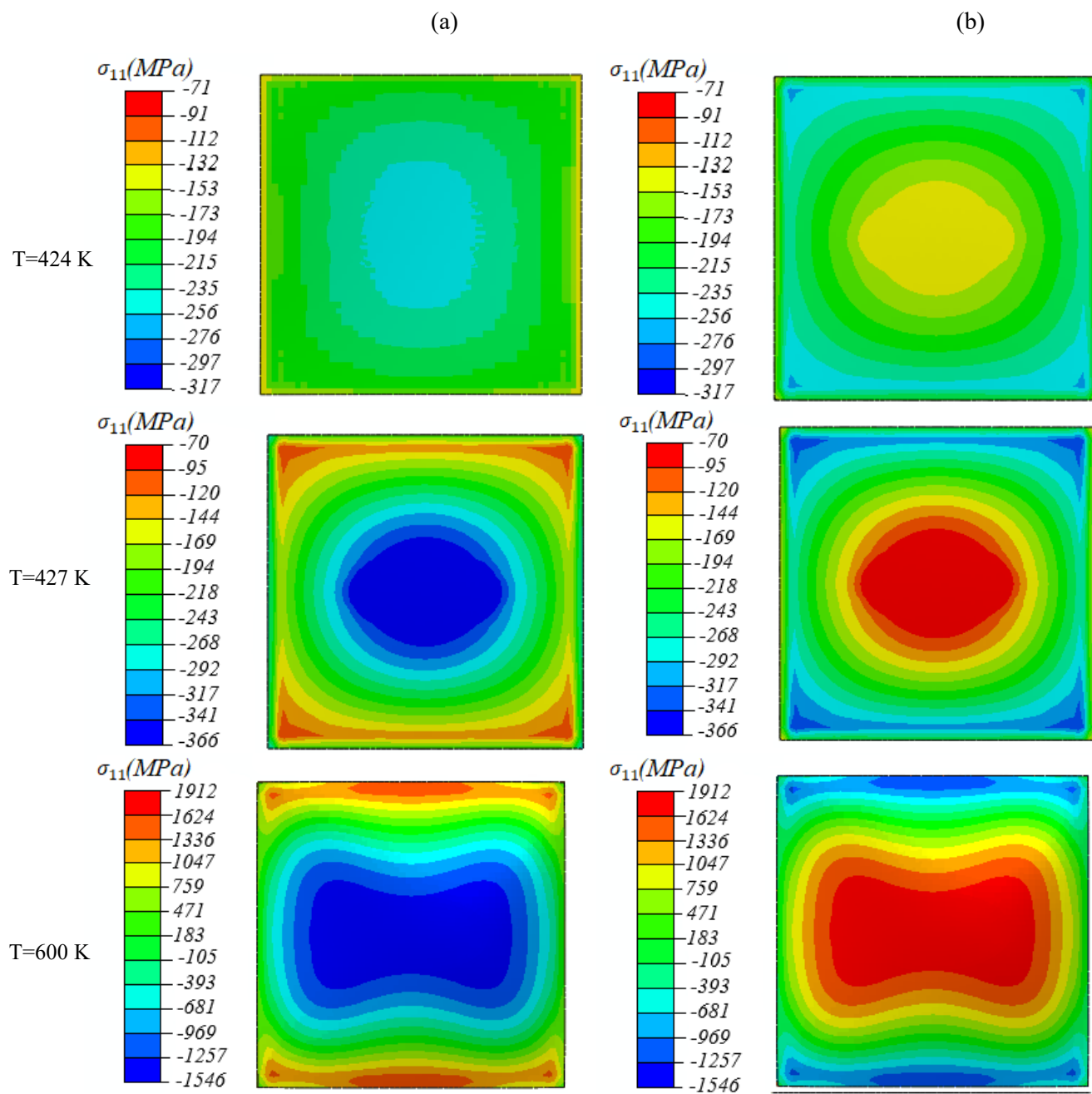


Figure D.3 Comparison of normal Stress (σ_{11}) through the sublaminates and baselaminates of FG-X plate with embedded elliptical delamination at three different temperatures $AD/A=0.25$, SSSS. (a) Sublaminates (b) Baselaminates